Limiting microcracks and hydrogen permeability in thermoplastic composites for LH_2 storage

MSc Thesis Aerospace Engineering

J.J.M. (Jens) van der Helm

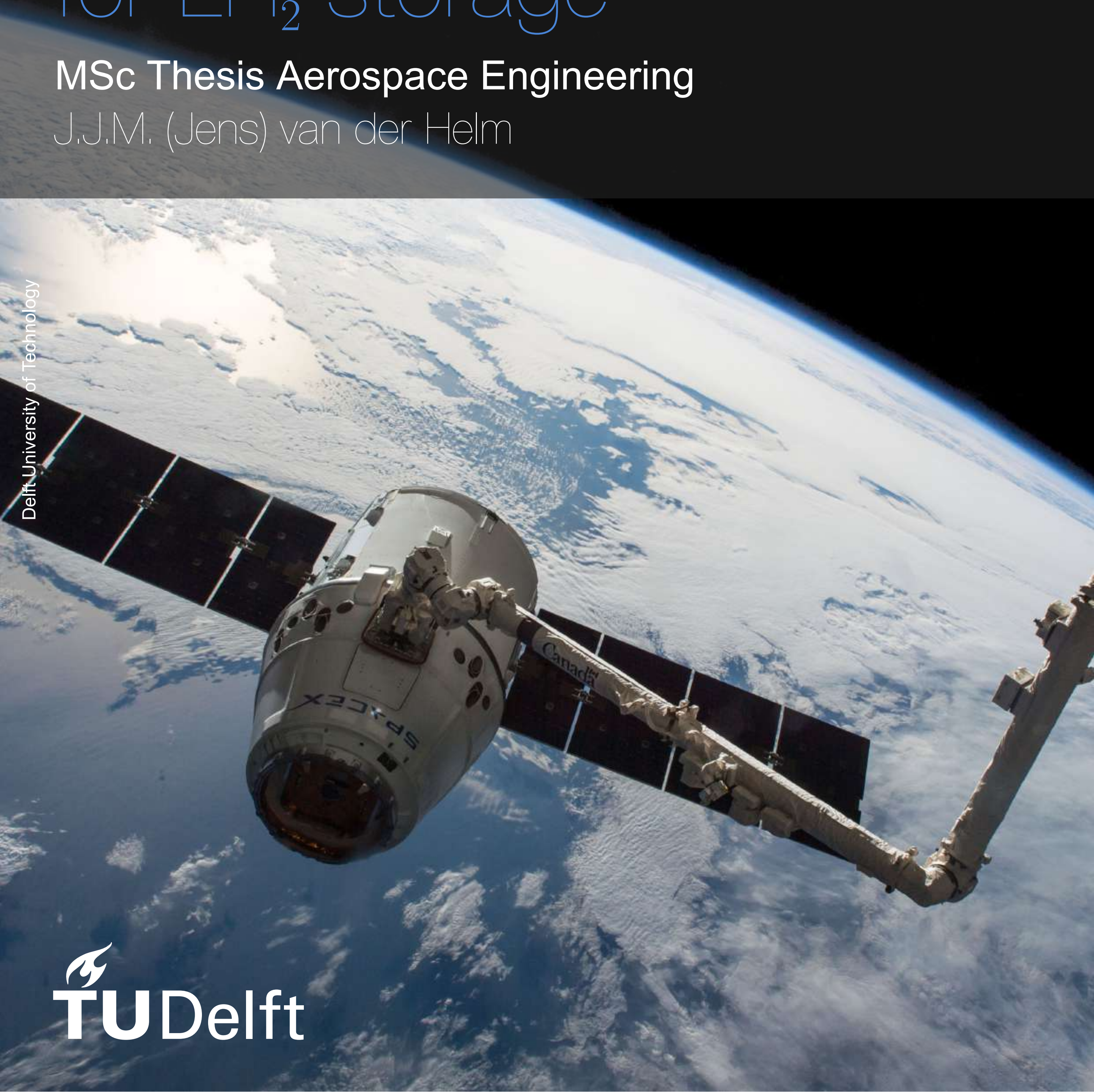

Delft University of Technology

TUDelft

Limiting microcracks and hydrogen permeability in thermoplastic composites for LH_2 storage

by

J.J.M. (Jens) van der Helm

Student Number
4482395

TU Delft Supervisors:	ir. Jos Sinke
	dr. Bilim Atli-Veltin
Company Supervisor:	ing. Henri de Vries
Project Duration:	May, 2022 - March, 2024
Faculty:	Faculty of Aerospace Engineering, Delft

Cover: Canadarm 2 Robotic Arm Grapples SpaceX Dragon by NASA under CC BY-NC 2.0 (Modified)

Style: TU Delft Report Style, with modifications by Daan Zwaneveld

Preface

This thesis forms the last milestone for my ± 4-year adventure in Delft, in which I combined my full time job at the RNLAF with the actual full time education program of this Master's program. While starting the first academic year mainly online, I still quickly got the chance to enjoy my student life like everyone else. To be able to finish my Master's program at NLR, where literally everything breathes their motto '*Dedicated to innovation in aerospace*', was a real highlight and a unique opportunity.

First of all, I want to thank my TU Delft supervisors, Jos Sinke and Bilim Atli-Veltin, and my NLR supervisor, Henri de Vries, for their expert guidance. Henri, to me you've shown to be a true subject matter expert in this field of research. Under your mentorship, every challenge appeared surmountable. Jos, your wealth of experience allowed me to navigate the entire thesis-writing process with ease and a sense of tranquility; you posed precisely targeted questions at the right moments. Bilim, your knowledge, fresh perspective on the matter, good suggestions throughout the thesis and your contacts in the field where crucial in realising this final result.

Furthermore, I would like to express my gratitude to the following individuals from TU Delft and NLR, who have provided advice to varying degrees during my thesis and/or have made it possible to carry out my testing program: Arshdeep Singh Brar, Amin Hosseini, Wubbo de Grave, Hosam Ebrahim, Jan Willem Wiegman, Ralf Creemers, Frank Hoekstra, Tom Janssens, Javier Ramirez Aldana and Marcel van der Kroeg. I also want to thank my employer, the RNLAF, for giving me time and space to follow this Master's program while this is actually uncommon for a person in his first phase contract, like me. Someone who also belongs on this list is Jordy Voges, RNLAF colleague and study buddy throughout the complete Master's program. We pulled each other through the study and always had each other to bounce ideas off of.

Finally, I want to express my deepest gratitude to my parents, my brother and his girlfriend, as well as to the rest of my family and friends for their unwavering support throughout the process of writing this thesis. I couldn't have accomplished it without your invaluable assistance.

J.J.M. (Jens) van der Helm
Delft, March 2024

Abstract

The Netherlands Aerospace Centre (NLR) together with Toray Advanced Composites and 12 other parties take part in the Netherlands liquid hydrogen (LH_2) composite tank consortium which is funded by the Netherlands research & development mobility (RDM) Fund. The goal of the RDM project NLR takes part in is to develop a long-life, fully composite LH_2 tank for civil aviation, with an ultimate goal of enabling zero-emissions aircraft. NLR is responsible for testing and selecting different thermoset and thermoplastic composite materials at 20 K, which is the boiling point of hydrogen.

The views of many researchers considering the mechanical and thermal behaviour differ, which indicates more need for research. Microcracking and the subsequent hydrogen permeation remain the biggest challenges. This study encompasses three fundamental facets: a comprehensive investigation into material behavior, the formulation of a Finite Element Method (FEM) model, and a partial experimental verification of said FEM model. The latter integral component involves an extensive testing system that includes room temperature and cryogenic tensile tests, permeability assessments, and microcrack evaluations facilitated by optical microscopy. During the experiments there is focused on the critical microcrack density and material selection criteria such as ply thickness.

It can be concluded that LM-PAEK / T700 UD-tape (Toray TC1225) is a suitable material choice, as it has met the permeability requirement of the consortium in all tested samples, regardless of the applied tensile load. It can be asserted based on the findings that an elevated microcrack density similarly does not impact permeability. Furthermore, it has demonstrated sufficient strength and stiffness in the tensile tests. Although the material is not entirely free of microcracks, based on the results, these scores appear to be adequate for LH_2 storage. Thin ply materials (<125 μm) perform less favorably than the regular ply materials, and for this reason, it is advised not to incorporate thin plies into the LH_2 tank design.

Contents

Preface i

Abstract ii

Nomenclature ix

1 Introduction 1
- 1.1 Background 1
- 1.2 Research objectives 1
- 1.3 Research questions 2
- 1.4 Scope of study 2
- 1.5 Report structure 2

2 Literature review and theory of mechanical behaviour 4
- 2.1 Background 4
- 2.2 Microcracks 6
  - 2.2.1 Origin of microcracks 6
  - 2.2.2 Microcrack parameters 8
  - 2.2.3 Limiting microcracks 13
- 2.3 Material properties for FEM model 18
- 2.4 Fracture mechanisms 19

3 Microcrack and permeability simulation methodology 22
- 3.1 Test program microcracks and permeability 23
  - 3.1.1 Stiffness non-linear behaviour 25
  - 3.1.2 Energy release rate analysis method 26
- 3.2 XFEM-SCZM model 28

4 Experimental set-up 34
- 4.1 Instron 5989 tensile tester 34
  - 4.1.1 Y series strain gauges 34
  - 4.1.2 OptimAE 35
- 4.2 Cryostat 35
- 4.3 Permeability set-up 36
- 4.4 Optical microscope 36
- 4.5 Python scripting in Abaqus 36

5 Experimental results and model validation 37
- 5.1 Basic FEM model 37
- 5.2 Experimental results 37
  - 5.2.1 RT tensile test 37
  - 5.2.2 Cryogenic tensile test 42
  - 5.2.3 Permeability 48
  - 5.2.4 Optical microscopy 50

6 Outcome and relevance of the results 57

7 Conclusion 70
- 7.1 Critical microcrack density 70
- 7.2 Material selection criteria 71
- 7.3 Recommendations 72

References 74

A Source Code XFEM-SCZM model 77

B Test proposal TC1225 microcracking 79
B.1 Test proposal 79
B.2 Machining panel drawing 90

C Permeability results 91

D Additional experimental results 93

E C-scan results 102
E.1 Panel 10793 102
E.2 Panel 11107 105
E.3 Panel 11169 108
E.4 Panel 11170 112

F TC1225 datasheet 116

List of Figures

2.1 NLR LH_2 tank promotional representation from 2021 showcasing a deep-vacuum double-walled tank with MLI. 5
2.2 Selection of main vacuum insulation deterioraters present in liquid hydrogen tanks. Taken from Schultheiss. [31] 6
2.3 Ultimate compressive strength (above) and E-modulus (below) versus temperature for E-glass/urethane: ⋄, x-direction; □, y-direction; △, z-direction; •, pure resin. Taken from Song and Vinson [36] 6
2.4 Numerically calculated diffusion energy barrier as a function of pore size. The fitting parameters A, b, and t are 0.143, −5.199, and 1.886 for H_2. Taken from Zhang et al. [43] 9
2.5 Micrograph of a gap and two transverse microcracks present in a tape-laid CF/PEEK QI specimen after exposure to a single cryogenic cycle. A permeability network can also be (partially) formed by means of gaps and/or voids. Scale 1:20. Taken from Grogan et al. [13] 10
2.6 Crack opening displacement and gap width measurement from cryogenic cycled tape-laid CF/PEEK QI specimens. Ply groups 1–9 refer to symmetric ply pairs. Taken from Grogan et al. [13] 12
2.7 Change in tensile strength and tensile modulus of different modified thermoset polymers with respect to the same pristine polymers. Experimentally determined, taken from Chen et al. [6] 13
2.8 Numerically determined transverse stress distribution for several lay-ups under a thermo-mechanical load consisting of a two-stage thermal load and an internal pressure ramp load. Taken from Grogan et al. [13] 15
2.9 Oblique fracture plane. Taken from Grogan et al. [13] 20
2.10 Mode I, II and III matrix fracture modes. 21

3.1 Ply stack plot of the suggested regular ply thickness triaxial lay-up 24
3.2 Strain field comparison after applying an uniformly distributed static step in length between a specimen with length 160 mm and a test section of 110 mm length (left), and a specimen with length 330 mm and a test section of 250 mm length (right). 25
3.3 Microcrack example on a LM-PAEK test specimen with fibres of 5 micron diameter. The transverse loading and cracking direction combined with the stress concentration points at the fiber-matrix interfaces are explanatory for the propagation of microcracks from fiber to fiber; this sample likely had a good quality of interfacial bonding given the fact that microcrack propagation along the fiber-matrix interface is actually not present. . . . 26
3.4 Indicative figure of stiffness in transverse direction. Test curve of an initial test laminate (0°, $\pm15°$ and $\pm60°$ for example) in transverse direction. 27
3.5 A unit cell of damage for microcracking in $[(S)/90_n]_s$ laminates. Taken from Nairn. [27] . 28
3.6 Representation of zero-thickness cohesive element inserted in transverse ply 90° and between the interface 0°/90° 29
3.7 Mesh refinement comparison between pure XFEM (a) and XFEM-SCZM approach (b). Taken from Grogan et al [12] 29
3.8 Coefficient of Thermal Expansion (CTE) of TC1225. Taken from Toray processing guidelines. [41] 30
3.9 Transverse matrix strength Weibull distribution for TC1225 for 1000 elements, σ_0 = 86 MPa and m = 12. 31
3.10 Knudsen number under three different conditions for 5 different fibre diameters in LM-PAEK. The fibre diameter of 7 μm is characteristic for TC1225 32
3.11 90 ° XFEM enrichment mesh generation. Taken from Brar. [34] 33

4.1 RT tensile test set-up consisting of the Instron 5989, AE sensors, strain gauges and one of the specimens . . . 35

5.1 Directly observed AE events in specimen 10793-5 from 0 kN to ∼30 kN during RT tensile test . . . 39
5.3 Directly observed AE events in specimen 11169-5 from 0 kN to ∼140 kN during RT tensile test . . . 39
5.2 Strain gauge results specimen 10793-5 . . . 40
5.4 Strain gauge results specimen 11169-5 . . . 40
5.5 Strain gauge results specimen 11107-5 . . . 41
5.6 Strain gauge results specimen 11170-4 . . . 41
5.7 Influence of AE sensor defects on sample 11170-4 with signal in [nm] on the y-axis and time in [s] on the x-axis. . . . 42
5.8 AE results consisting of events, load and cumulative events for the thin ply samples during RT tensile test. . . . 43
5.9 Directly observed AE events during RT tensile test, threshold of 0.195 nm . . . 44
5.10 Strain gauge results specimen 10793-1 . . . 45
5.11 Strain gauge results specimen 11169-2 . . . 45
5.12 Strain gauge results specimen 11170-1 . . . 47
5.13 Measured leak rate [mbarL/s] and helium pressure [bara] of specimen 10793-6 . . . 50
5.14 Measured leak rate [mbarL/s] and helium pressure [bara] of specimen 11169-6 . . . 50
5.15 Optical microscopy examination on microcracks of specimen 11107-5, which is a thermoplastic thick ply specimen loaded to 62.5 kN ($N_{ref} + 67$%). The microcracks can be distinguished as a lighter, whimsical pattern in the matrix in the middle of the figure, mainly on the fiber-matrix interfaces. . . . 51
5.16 Optical microscopy examination on microcracks of specimen 11170-4 [1/2]. The microcracks can be distinguished as a lighter, whimsical pattern in the matrix in the middle of the figure, mainly on the fiber-matrix interfaces. This should not be confused with the lighter color in the matrix which will be discussed later. . . . 52
5.17 Optical microscopy examination on microcracks (marked by the red capsules) of specimen 10793-1 [1/2]. The left microcrack displays a very large COD, while the upper microcrack's formed in a 30°-ply. Delamination as a result of the tensile load performed at CTD is also visible. . . . 53
5.18 Microscopic comparison of specimens 10793-3 and 11107-1 [1/2]. The fibers in the ±30-plies of 11107-1 show to have less ovality compared to 10793-3 which should potentially indicate for higher strain and more microcracks. The discoloration in the ±30-plies of 11107-1 could therefore be explained by plastic deformation just before microcrack initiation. . . . 55
5.19 Optical microscopy examination on microcracks of specimen 11169-3. The upper part of the microcrack extends cracking into a 30°-ply for which it can be considered to be a *crack* . . . 56

6.1 Microcrack density results of TEP/RT specimens . . . 58
6.2 Microcrack density results of MDB/CTD specimens . . . 58
6.3 Load versus experimentally found crack opening distance for RT and cryogenic temperature, thick ply and thin ply samples. For each circumstance the N_{ref} in question and the next two following measurements are plotted. . . . 59
6.4 Comparison of the moduli found for the thick ply CTD/MDB specimens at maximum load. The average moduli of the RT/TEP specimens are given as reference. . . . 61
6.5 Comparison of the moduli found for the thin ply CTD/MDB specimens at maximum load. The average moduli of the RT/TEP specimens are given as reference. . . . 61
6.6 Knudsen number under three different conditions making use of the found COD's in the samples that showed microcrack initiation, from left to right: 11169-6 (RT, thin ply), 11107-5 (RT, thick ply), 10793-3 (CTD, thick ply) and 11169-3 (CTD, thin ply); the filled circles in the figure depict the empirically determined values of COD. The fibre diameter of 7 μm is characteristic for TC1225 and is given as the far-right reference value in the figure. . . 63

6.7 Leak rate of CF-PEEK samples without and after cryogenic cycling showing the correlation between measured microcrack density and leak rate. Taken from Flanagan et al. [10] 69

B.1 Machining panel drawing 90

D.1 Cryogenic strain gauge results specimen 10793-3 93
D.2 RT strain gauge results specimen 10793-3 93
D.3 Cryogenic strain gauge results specimen 11107-1 94
D.4 RT strain gauge results specimen 11107-1 94
D.5 Cryogenic strain gauge results specimen 11170-2 94
D.6 Cryogenic strain gauge results specimen 11107-2 95
D.7 Optical microscopy examination on microcracks of specimen 11169-6. 95
D.8 Optical microscopy examination on microcracks of specimen 11170-6 [1/2]. This is the only specimen showing microcracks through the fiber, these types of cracks can be attributed to the abrasion and polishing of the material in preparation for microscopic assessment. 96
D.9 Optical microscopy examination on microcracks of specimen 11170-6 [2/2]. 96
D.10 Optical microscopy examination on microcracks of specimen 11170-4 [2/2]. 97
D.11 Optical microscopy examination on microcracks of specimen 10793-1 [2/2]. 97
D.12 Optical microscopy examination on microcracks of specimen 11107-1 [2/2]. 98
D.13 Optical microscopy examination on microcracks of specimen 11169-2 [1/2]. 98
D.14 Optical microscopy examination on microcracks of specimen 11169-2 [2/2]. 99
D.15 Optical microscopy examination on microcracks of specimen 11170-1. 99
D.16 Optical microscopy examination on microcracks of specimen 11107-2. 100
D.17 Optical microscopy examination on microcracks of specimen 11170-2 [1/2]. 100
D.18 Optical microscopy examination on microcracks of specimen 11170-2 [2/2]. 101

E.1 Attenuation C-scan (Reflector plate) of panel 10793 102
E.2 Reflection C-scan of panel 10793 103
E.3 TOF (thickness) of panel 10793 104
E.4 Attenuation C-scan (Reflector plate) of panel 11107 105
E.5 Reflection C-scan of panel 11107 106
E.6 TOF (thickness) of panel 11107 107
E.7 Attenuation C-scan (Reflector plate) of panel 11169 108
E.8 A-, B- and C-scan of indication (reflector plate) of panel 11169 109
E.9 Reflection C-scan of panel 11169 110
E.10 TOF (thickness) of panel 11169 111
E.11 Attenuation C-scan (Reflector plate) of panel 11170 112
E.12 A-, B- and C-scan of indication (reflector plate) of panel 11170 113
E.13 Reflection C-scan of panel 11170 114
E.14 TOF (thickness) of panel 11170 115

List of Tables

5.1 Specimen numbering conversion table TEP specimens 38
5.2 Specimen numbering conversion table MDB specimens 45
5.3 Summary of permeability results after RT tensile test 48
5.4 Summary of microcrack results after RT tensile test 52
5.5 Summary of microcrack results after cryogenic tensile test * If delamination is included, the max. crack length found in 10793-1 is 1760 μm 53
5.6 Fibre directions of the upper and lower outer ply for all assessed MDB specimens; the nominal direction is 30° 54

Nomenclature

Abbreviations

Abbreviation	Definition
AE	Acoustic Emission
AFP	Automated Fiber Placement
API	Application Programming Interfaces
ASTM	American Society for Testing and Materials
ATL	Automated Tape Laying
CD	Crack Density
CFRP	Carbon Fibre Reinforced Polymer
CG	Center of Gravity
CNT	Carbon NanoTubes
COD	Crack Opening Displacement
CPV	Composite Pressure Vessel
CT	Computed Tomography
CTD	Cryogenic Temperature Test Conditions
CTE	Coefficient of Thermal Expansion
DCOD	Delaminated Crack Opening Displacement
DDS	Diaminodiphenylsulphone
DSMC	Direct Simulation Monte Carlo
EP	Epoxy
FEA	Finite Element Analysis
FEM	Finite Element Method
FRP	Fibre Reinforced Polymer
GF	Glass Fibre
GO	Graphene Oxide
ILSS	Interlaminar Shear Strength
IPSS	In-Plane Shear Stress
MAWP	Maximum Allowable Working Pressure
MDB	Modified DogBone specimens
MLI	Multi-Layer Insulation
NASA	National Aeronautics and Space Administration
NLR	Netherlands Aerospace Centre (Nederlands Lucht- en Ruimtevaartlaboratorium)
PA	Polyamide
(LM)-PAEK	(Low Melt)- Polyaryletherketone
PC	Polycarbonate
PDA	Progressive Damage Analysis
PEEK	Polyetheretherketone
PEKK	Polyetherketonketone
PI	Polyimide
PP	Polypropylene
PUM	Partition of Unity Method
QI	Quasi-Isotropic
RDM	Research & Development Mobility
RGA	Rest Gas Analyser
RT	Room Temperature
RTD	Room Temperature Test Conditions

Abbreviation	Definition
SCF	Short Carbon Fibers
SCZM	Surface Cohesive Zone Model
SEM	Scanning Electron Microscopy
SHC	Specific Heat Capacity
SPC	Single Polymer Composites
TCS	Transverse Compressive Strength
TEP	TEnsion and Permeability specimens
TS	Technical Specification
TTS	Transverse Tensile Strength
UD	Unidirectional
WCM	Wound Composite Modeller
XCT	X-ray Computed Tomogram
XFEM	Extended Finite Element Method

Symbols

Symbol	Definition	Unit
A	Unit cross-sectional area	[m^2]
AR	Aspect ratio	
B	Boil-off time	[h]
$B*$	Laminate thickness	[mm]
b^f	Fiber thermal stress concentration factor	
b^m	Matrix thermal stress concentration factor	
C	Tank insulation	[W/K]
$C*$	Concentration gradient	[kg/m^3]
C_p	Specific heat capacity	[J g$^{-}1$ K$^{-}1$]
D	Diffusion coefficient	[m^2/s]
d	Molecular dynamic diameter	[Å]
d_m	Molecule diameter	[m]
E	Young's modulus	[MPa]
E_A	Effective axial modulus	[MPa]
E_b	Energy barrier	[eV]
E_{f1}	Fiber axial elastic modulus	[MPa]
E_m	Matrix elastic modulus	[MPa]
f	Weighing coefficient	
f_f	Fibre volume fraction	
G	Material conductance	[scc/s - cm^2]
G_{12}	In-plane shear modulus	[Pa]
G_{1c}	Critical strain energy release rate / Mode 1 fracture toughness	[J/m^2]
G_{2c}	Mode 2 fracture toughness	[J/m^2]
H	Enthalpy	J
J	Flux	[kg m^{-2} s^{-1}]
k	Permeability	[m^2]
k_m	Mechanical stiffness	[N/m]
k_{perm}	Ultimate permeability	[mol He/(m.s.Pa)]
k_{th}	Thermal stiffness	[Pa]
K_n	Knudsen number	
K_q	Fracture toughness	[MPa$\sqrt{m}$]
l	Length	[m]
M	Molar mass	[kg/kmol]
m	mass	[kg]

Symbol	Definition	Unit
N_A	Avogadro constant	[mol^{-}1]
N_θ	Circumferential force	[N]
P	Permeability coefficient	[mol/(m.s.Pa)]
p	Pressure	[Pa]
Q	Volumetric flow rate	[m^3/s]
Q_{leak}	Heat loss	[W]
Q_{perm}	Ultimate diffusion rate	[Pa.m^3/s]
q_G	Outgassing rate	[mbar l s^{-1} m^{-2}]
R	Universal gas constant	[J K^{-}1 mol^{-}1]
$R*$	Half of the closest separation of two fibers	[m]
R_m	Radius of curvature of the meridian	[m]
R_p	Radius of parallel circle	[m]
r	Fibre radius	[m]
r_{pore}	Pore diameter	[m]
S	Solubility constant	[mol/(m^3 Pa)]
S_a	Stress amplitude	[MPa]
S_{is}^L	In situ shear strength	[Pa]
S_m	Mean stress	[MPa]
T	Temperature	[K]
T_g	Glass temperature	[K]
T_m	Melting temperature	[K]
t	Time	[s]
t_l	Lamina thickness	[mm]
V	Volume	[L]
V_f	Fiber volume fraction	
V_m	Matrix volume fraction	
α_1	Longitudinal CTE	[K^{-}1]
α_2	Transverse CTE	[K^{-}1]
α_m	Matrix CTE	[K^{-}1]
β	Atom mobility coefficient	
δ	Average COD	
δ_p	Pressure gradient	[Pa]
ϵ	Strain	
η	Viscosity (of resin)	[Pa.s]
θ	Ply angle	[degr.]
θ_e	Effective surface porosity	
κ	Thermal conductivity	[W m^{-1} K^{-1}]
λ	Mean free path	[μm]
μ	Dynamic viscosity	[Pa.s]
ν	Poisson's ratio	
ρ	Density	[kg/m^3]
σ	Stress	[MPa]
τ	Tortuosity factor	
ϕ	Volume fraction of filler	

1

Introduction

1.1. Background

Back in the 1980's the Russian aircraft manufacturer Tupolev rebuilt one of their Tu-155 airplanes to run on liquid hydrogen (LH_2). LH_2 is a cryogenic fluid which means that it only exists at extremely low temperatures, more specifically below 20 K for the case of hydrogen. Tupolev proved that LH_2 could produce sufficient thrust to power a commercial aircraft. [42] With a 2.8 times higher energy to unit mass ratio compared to kerosene, LH_2 plays a significant role in the decarbonization of the aviation sector by 2050 and subsequently in reducing aviation's climate impact. It is predicted that a CO_2 reduction of up to 45% is within reach in 2050 in the efficient decarbonization scenario. [23]

Within the overarching research to liquid hydrogen as aviation fuel, the development of aircraft components is one of the main research sub-areas besides e.g. infrastructure and regulations. Composites in the form of Fiber Reinforced Plastics are very suitable material options for cryogenic tanks, especially when taking into account that most metals suffer from inherent brittleness at very low temperatures. [17]

The Netherlands Aerospace Centre (NLR) together with Toray Advanced Composites and 12 other parties take part in the Netherlands LH_2 composite tank consortium which is funded by the Netherlands research & development mobility (RDM) Fund. The goal of this consortium is to develop a long-life, fully composite LH_2 tank starting from December 2021. Within this consortium, NLR is responsible for testing and selecting different composite materials at 20 K, both thermosets and thermoplastics. The final demonstrator tank will eventually be tested in cyclic thermal and mechanical conditions to assess performance and durability. NLR's aim is not to make this cryogenic composite tank only applicable for their relatively small unmanned aerial vehicle (UAV), but also for commercial aircraft. [11]

1.2. Research objectives

The goal of the RDM project NLR takes part in is to develop a long-life, fully composite LH_2 tank for civil aviation, with an ultimate goal of enabling zero-emissions aircraft. Fully understanding and defining requirements for composite LH_2 tanks in order to meet aircraft requirements is one of the key developments in this project. As a subordinate work package material properties of thermoset and thermoplastic materials at cryogenic temperatures should be delivered; the thesis aims to contribute to this research field by research on material selection. As we've seen in the literature review, the views of many researchers considering the mechanical and thermal behaviour differ, which indicates more need for research. Microcracking and the subsequent hydrogen permeation remain the biggest challenges, which eventually leads to the research question. What is finally aimed for in the conclusion is summarized in the following two points:

- The critical microcrack density;
- Mechanical behaviour selection criteria for composite materials and/or permeation barriers.

1.3. Research questions

The following research question is formulated:

- **How can microcracking and hydrogen permeability for thermoplastic composites under tensile loading at deep cryogenic conditions be limited to a predefined level in order to fulfill the requirements for long-life, vacuum-insulated composite liquid hydrogen tanks for civil aviation?**

To answer this research question, several sub-questions have been formulated to give the research a clearly defined direction and to divide the research work into several work packages. Therefore, the following sub-questions are formulated:

1. What solutions can be conducted to limit transverse microcracks to a predefined level?
2. How can mechanical behavior of thermoplastic materials within the temperature envelope of 20 to 333 K be simulated by means of Finite Element Modeling (FEM)?
    (a) What material properties are necessary?
3. To what extent can experimental results contribute in the validation of the FEM model for thermal and mechanical loading conditions?
    (a) Can the effect of thin ply materials be demonstrated?
    (b) Are AE sensors of added value in determining microcrack initiation?
    (c) Can the influence of microcracks on permeability be proven?

1.4. Scope of study

Examining the various research inquiries outlined in the preceding section, this study encompasses three fundamental facets: a comprehensive investigation into material behavior, the formulation of a Finite Element Method (FEM) model, and a partial experimental verification of said FEM model. To enhance comprehension of the factors influencing microcrack formation, thermal stresses, and permeability, and to facilitate the determination of input parameters for the FEM model, the thesis initiates with an in-depth analysis of material behavior. This analysis, characterized by a synthesis of desk research and data analysis, aims to provide foundational insights. The FEM model which is going to be created next will be based on the novel XFEM (extended FEM) model as described by Grogan et al. [13] This model, of which the basis is already instantiated in Python code, serves the purpose of predicting intra- and inter-ply damage within an internally pressurized cryogenic tank. The third integral component involves an extensive testing system that includes room temperature and cryogenic tensile tests, permeability assessments, and microcrack evaluations facilitated by optical microscopy. This multifaceted approach is designed to contribute a comprehensive and rigorous examination of the selected research problem.

1.5. Report structure

This thesis starts with chapter 2, where a recap on the literature review and a more in-depth analysis of mechanical behaviour in the form of microcracks are given. Also the necessary properties for the FEM model and the most common fracture mechanisms will be discussed in this chapter. Besides that, chapter 3 elaborates on the methodology consisting of material selection, test program for the experimental part and the description of the XFEM-SCZM model. After that, chapter 4 discusses the experimental setup and chapter 5 the experimental results. Furthermore, in chapter 6 a preliminary analysis of the results is given leading to the answering of the sub-questions. Finally, in chapter 7 the conclusion and recommendations are given.

Additional information is given in the appendices. Appendix A shows the complete source code of the developed XFEM-SCZM model, appendix B the test proposal for TC1225 microcracking including technical drawings, appendix C the results of the permeability tests following from appendix B and appendix D presents additional experimental results considering the tensile tests and microscopic images for the microcrack assessment. Next to that, the C-scan results for common quality of the material used in the experiments is shown in appendix E and a data sheet of TC1225 provided by the manufacturer is finally given in appendix F.

2

Literature review and theory of mechanical behaviour

This chapter gives an overview of the most important theory that is built on during this research project, more specifically to answer subquestions (1) and (2.a). The cryogenic use of thermoplastic composites for containing liquid hydrogen presents several engineering challenges, with microcracks and permeability being particularly significant obstacles. The main focal point for the thesis is on microcracks, but because microcracks can create potential pathways for hydrogen leakage, permeability (a material property) is inextricably linked and intertwined throughout this chapter. First, a short background and state of the art is given based on the literature review [15]. The background is then followed by the sections about the occurrence and limitation of microcracks, material properties necessary for the FEM model and finally the differences in fracture mechanisms.

2.1. Background

The overall focus of using hydrogen as a fuel is currently on liquid hydrogen. Solid storage techniques are under development but are very premature and less interesting considering mass and cost. So far, spherical or cylindrical tanks are optimal to keep LH_2 cold and to prevent heat transfer and vaporization as much as possible. Looking purely from this heat transfer perspective, spherical tanks have the smallest surface to volume ratio and are therefore the smallest heat dissipators, especially when combined with (vacuum) insulation. [15].

The most development-dictating material properties of current composite LH_2 tanks are the formation of microcracks and the subsequent permeability. It is therefore no wonder that the trends here are to focus on permeation barriers, tank wall insulation and exploring different production methods. Considering tank wall insulation, a deep-vacuum double-walled insulation system is the main trend at the moment, see Figure (2.1). Additionally, Bubacz [4] confirms the preferred use of deep-vaccum double-walled tanks with MLI because adhesively bonded sandwich structures are susceptible to damage from low velocity impact. [15]

To prevent for permeation of H_2 through the inner tank, permeation barriers are used. As it stands, multiple metallic permeation barriers are already successfully produced and tested, like AL6061-T6. [8] The possible transition from metallic barriers to composite barriers is most dependent on the outgassing properties of a composite barrier. If it would not be possible to prevent this with composite alone, it would mean that a metallic permeation barrier would always be necessary. Coherent with the permeation barrier is the preventing of microcracks. This can either be done by thin ply technology: plies with a thickness below 125 μm to create less thermal stresses in a more homogeneous laminate and therefore limiting transverse crack propagation. Or this is done by using additives. [15]

Liquid hydrogen has a higher volumetric energy density than gaseous hydrogen. To compare, gaseous

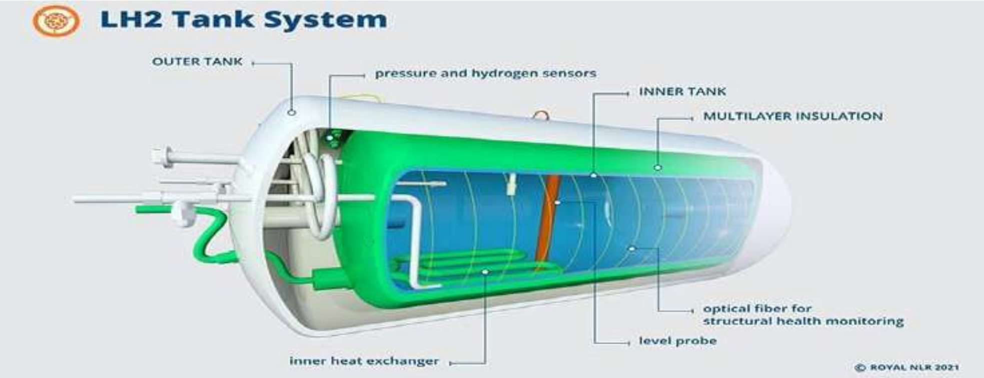

Figure 2.1: NLR LH_2 tank promotional representation from 2021 showcasing a deep-vacuum double-walled tank with MLI.

hydrogen has a volumetric energy density of 5.323 MJ/L and liquid hydrogen (after reheating to 298 K has a volumetric energy density of 10.044 MJ/L. In the case that liquid hydrogen starts evaporating to gas this would mean that the pressure increases, because of the big difference in volumetric density, and that therefore the gaseous hydrogen has to be released from the tank. This process of releasing is called boil-off. This given fact thus underlines the already mentioned importance of insulation. The importance of insulation however also operates bidirectionally. Liquid hydrogen namely expands rapidly when it absorbs heat. Therefore, it must be secured that as little as possible heat can come in. Besides creating the most optimal insulation to prevent the tank from exploding, the implementation of venting tubes are a necessity in the design of liquid hydrogen tanks. The consortium TS.14 [38] (fuel tank pressure control) agrees on this: venting should be effective under any normal flight condition. The minimum tank pressure should therefore always be at least 0.1 bar higher than ambient pressure to prevent air ingress. The boil-off rate for a LH_2 tank shall be less than 2%/day according to the TS, and, to achieve this, a thermal conductivity < 8$\times 10^{-4}$ $Wm^{-1}K^{-1}$. [38] [15]

Boil-off forms a serious challenge in developing LH_2 tanks because it can be caused by different factors next to external heat causing evaporation. Also the ortho- para-hydrogen conversion is an exothermal reaction, which thus stretches the need of maintaining a stable temperature environment inside the tank. Next to this, residual thermal leaks, often through support struts in the tank, are contributing to this challenge as well. *Sloshing* and *flashing* are known other contributors to boil-off, however these are not that important purely looking at the stage where LH_2 is already implemented in tank; these two factors are more likely to happen during transport of hydrogen. Sloshing is impact of hydrogen with the tank wall during transportation which on it turn converts impact energy to thermal energy and flashing occurs when LH_2 is transferred from a high pressure environment to a low pressure environment. [15]

Two other phenomena threatening the vacuum insulation are outgassing and leakage, also refer to Figure (2.2) for a visual overview. Leakage is the passage from hydrogen from the inner tank into the vacuum due to a defect in the tank. Outgassing is composed of two processes both coming down to the release of gas from a solid. Thermal outgassing on one hand means that after the conversion to gaseous hydrogen as a result of temperature increase, the gas diffuses and desorbs through the tank wall. Short-time outgassing on the other hand means that previously adsorbed particles by the wall (e.g. during vacuum venting), desorb again. Due to the small molecular size of hydrogen, the phenomenon of outgassing is very typical for hydrogen. [31] [15]

The interest in the use of composites for liquid hydrogen tanks is logical considering that metals are typically much heavier and also that most metals become very brittle when they are exposed to the extreme cold of liquid hydrogen. This, and also pores due to welded seams, create voids functioning as leak paths in the material. Permeability is also shown in Figure (2.2), as also composites face a challenge dealing with permeability. Requirements set up by the consortium for the RDM project in the Technical Specification (TS) TS.57 and TS.58 regarding permeability are that CFRP tank materials may not exceed a permeability larger than 1.0$\times 10^{-9}$ $molH_2/m.s.MPa$ at RT and also that permeation

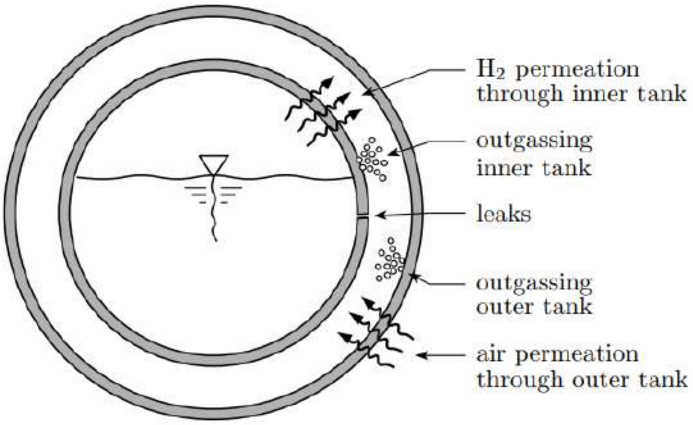

Figure 2.2: Selection of main vacuum insulation deterioraters present in liquid hydrogen tanks. Taken from Schultheiss. [31]

is not allowed as a result of thermal cycling between 4 K and ambient temperature. [38] [15] Although the latter specification is probably not completely realistic as there is always a certain minimum amount of hydrogen passage through the material.

2.2. Microcracks

Of the above mentioned main tank deterioraters, leaks are directly caused by microcracks, but permeation through the tank wall is also indirectly attributed to them. These microcracks act as potential pathways for gas permeation, including hydrogen. The cracks create open channels through which gases can migrate, compromising the integrity of the containment system. In this subchapter is zoomed in on the formation of and several countermeasures for microcracks, which for this reason also addresses permeability.

Figure 2.3: Ultimate compressive strength (above) and E-modulus (below) versus temperature for E-glass/urethane: ⋄, x-direction; □, y-direction; △, z-direction; •, pure resin. Taken from Song and Vinson [36]

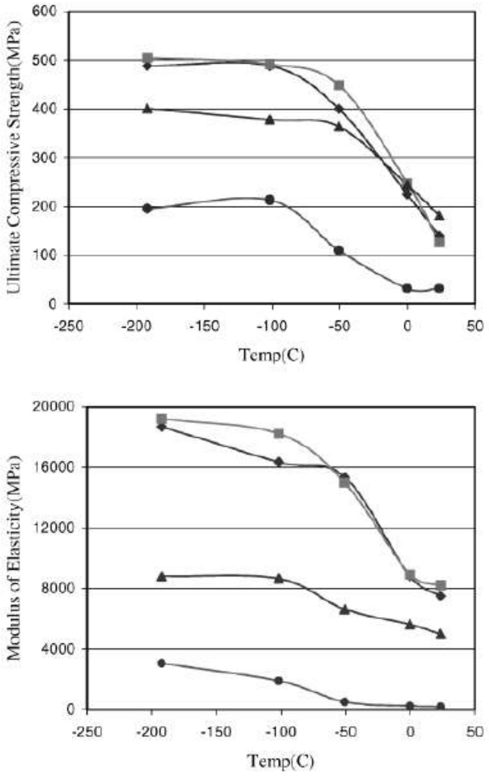

2.2.1. Origin of microcracks

In general it can be stated that the lower the temperature, the higher the Young's and shear moduli. The reason for the increase in Young's modulus can be found in the reduced polymer chain mobility which on its turn increases the binding forces between molecules. [30] Following that, also (tensile) strength increases but toughness decreases. The strength of a material can be described as the maximum amount of stress that can be applied on an element before it deforms permanently. Also, an increased stiffness (which is the resistance to imposed deformations) at decreasing temperatures can be witnessed, at least to a proven extent of 77 K which is the liquid nitrogen temperature; this is because stress relaxation can be completely arrested at low temperatures. [30] These developments are accompanied by a decrease in failure strain and embrittlement regarding impact strength and fracture toughness. Moreover, the strength of the fibers may also increase when the material is cooled down or thermocycled to cryogenic temperatures. Lastly, also the friction coefficient decreased in the cryogenic environment, at least when tested on PEEK at 77 K. [17] When talking about the friction coefficient for composites, this is about the amount of friction between the different material contact surfaces within that composite, e.g. matrix/matrix, matrix/fiber or fiber/fiber.

Song and Vinson [36] on the other hand experimentally found that, when cooling down, the ultimate compressive strength in x-, y- and z-direction of their E-glass/urethane cross-ply test specimen (V_f 48 %) was flattened at the temperature below of 173 K and also the E-modulus plateaued in the z-direction at 173 K, see Figure (2.3). Because the trendline only consists of a limited number of measuring points, it cannot be said with certainty however whether this conclusion is correct. On the other hand, in the same line of reasoning, Sapi [30] claims to observe a plateau for similar material properties versus temperature at 77 K. An explanation about the plateau at 77 K for different mechanical properties is suggested by Sapi [30]; it is possible that below 77 K internal stresses due to thermal expansion in the laminate become more critical than the internal stresses because of the mechanical loading.

When FRP's in a cryogenic regime are subjected to loads, also fatigue and delamination are proven design limits. To point out the fatigue behaviour, Kumagai et al. [24] performed uniaxial tension-tension fatigue tests on NEMA G-11, which is composed of E-glass and a bisphenol-A with a DDS (diaminodiphenylsulphone) with a V_f of 47% and had a crossply (0/90)-layup to also reveal the sensitivity of matrix dominated fatigue properties to low temperatures. The strain-to-failure of E-glass is 4.0 % at RT. A thermocouple was embedded in these specimens and tests were performed at room temperature, 77 K and 4 K. It was experimentally found that at both cryogenic temperatures the specimens had a fatigue limit of 200 MPa at 10^6 cycles, where the specimens at room temperature had a fatigue limit of only 100 MPa at 10^6 cycles. What distinguishes the results of the specimens at 4 K compared to the 77 K specimens, is that this colder temperature seems to lead to a more rapidly decreasing strength over the number of cycles. It is highly likely that this can be explained because material damage can grow faster and material degradation occurs sooner. An example of degradation is delamination occurring due to different CTE's, because each layer may expand or contract at a different rate when exposed to temperature variations. If these differences in expansion and contraction are significant, it can lead to internal stresses within the composite structure. Over time, these stresses may exceed the adhesive strength between the layers, causing the layers to separate or delaminate.

The above described, partly contradictory, results on the delamination modes on FRP's in a cryogenic environment have underlying reasons on microscopic level which also account for the found contradictions. Microcracks are main contributors to delamination and hydrogen permeability and are strongly dependent on the presence of thermal residual stresses in the composite. Because there is a difference in coefficient of thermal expansion (CTE) between fibres and matrix, both intralaminar and interlaminar residual stresses are developed when a FRP is thermocycled. When talking about the intralaminar scale (UD single-ply), no external mechanical load is even necessary for residual stresses to occur. This is a result of the higher stiffness of the fibres: the fibres are dominant over the matrix in thermal contraction in fibre direction when cooled down to cryogenic temperatures, forcing longitudinal mechanical strain and thus mechanical stress in the matrix. To behold a macroscopically stress free state of the composite, this ultimately leads to compressive residual stresses in the fibres. This is supported by Equation (2.1) as described by Huang [19]. In this Equation, V_f is the fiber volume fraction, b^f is the fiber thermal stress concentration factor, V_m is the matrix volume fraction and b^m is the matrix thermal stress concentration factor.

$$V_f\{b^f\} + V_m\{b^m\} = \{0\} \tag{2.1}$$

The residual stresses due to this anisotropy in thermal expansion in a single-ply are increased when combined on interlaminar level. Because the anisotropies of differently oriented stacked plies enlarge each other and this given is added to the already present anisotropy in a single-ply, the residual stresses are even larger on laminate-scale, mainly in the transverse direction. Hence, a cross-ply stacking is most vulnerable to thermally induced residual stresses considering their ultimate directional mismatch.

Ways to prevent or limit the influence of different CTE's can be found in for example the use of woven plies. Thermal expansion in woven plies occurs mainly out-of-plane. In-plane expansion is prevented due to the fibres who hold a kinematic constraint on the resin. Other options are using single polymer composites (where fibres and matrix hold the same CTE) or hybridising the laminate, for example in combining carbon and glass fibre plies. [30] Selection on SPC's (single polymer composites) should in this case be performed accurate, as not all SPC's hold the same CTE for both matrix and fiber. Atli-Veltin [1] on the other hand performed successful cryogenic tests with a polypropylene (PP) SPC where matrix and fiber had the same CTE; and in that way providing an advantage over other conventional composites.

It has to be noted that besides the already described residual stresses, also thermal shocking has a significant effect on the forming of microcracks. Thermal shocking means that a rapid thermal load is placed on the composite, e.g. a tank at ambient temperature which gets filled with liquid hydrogen. The big temperature difference causes the composite structure to cool down inhomogeneously. As a result a thermal strain is formed between two adjacent areas in the structure of different temperatures, leading to thermally induced stresses. [17] Shown by multiple researches, the formation of microcracks due to the combination of the different stresses after thermal shock is predominantly present during the first or first few thermocycles and is negligible during the following cycles, however the thermal cycles only ranged between roomtemperature and 77 K. Moreover, in another research performed by Hohe et al. [18], slow cooling thermocycles were used to the extent of 4.2 K on both UD as cross-ply laminates and no microcracks were found during the process. This development has a positive impact on the long term degradation characteristics.

Furthermore, the softening effects in the matrix are the effects that soften the matrix as a result of formed microcracks due to thermally induced residual stresses. This would mean that the strength and stiffness of a laminate should decrease with a decreasing temperature, contrary to previously made statements. The microcracks work as stress relaxation here; noteworthy is that permeability increases due to this phenomenon. This contradiction could be the explanation to all the contradictory results discussed before. [20]

2.2.2. Microcrack parameters

The most important size to prevent for hydrogen permeation is the maximum critical crack size needed for hydrogen to permeate. According to Liu et al. [25] this experimentally and numerically determined critical size lies below 2.1 Å (1 Å is equal to 1.0$\times 10^{-7} mm$), but he also states that it is unclear what the ultimate size of nanopores is to prevent for hydrogen permeation. Amongst other factors, temperature, pressure, crystallinity and gas-material interaction are main influencers on the permeability. It is for this reason that it is extremely difficult to determine the critical microcrack size and eventually critical microcrack density to prevent for LH_2 permeation. The experiments of Liu et al. were for instance performed at RT in order to find the optimal pore size for producing hydrogen i.e. separating H_2 from undesirable by-products. A membrane with 2.1 Å pore size functioned as an excellent barrier for all other gases, but at least until a pore size of 1.5 Å hydrogen permeation was still detected.

To compare: hydrogen can migrate through conductive materials both atomically and molecularly, the atomic radius of hydrogen is 0.25 Å and the kinetic diameter is 2.89 Å. The kinetic diameter expresses the likelihood that a molecule in a gas will collide with another molecule. It is for this reason that the critical crack size is not only dependent on the pore size of the tank material, but also on the diffusion energy barrier. According to Zhang [43], the numerically calculated diffusion energy barrier is 0.54 eV, dependent on the pore size.

Contradictory to microcracking, permeability is always present in a composite to a greater or lesser extent due to the (micro)porosity characteristics and the dynamic free volume of a material. In describing how hydrogen permeability through a composite works, it is important to understand what permeability actually is. Sapi et al. [30] describe permeability as both a molecular property in the form of diffusion but also as a microstructural property in the form of leakage. The previously described leak paths are a prerequisite for leakage whereas diffusion is based on atoms literally passing through a material. According to Bubacz [4], permeation is therefore logically dependent on as well the amount of voids as the dynamic free volume. The free volume or the so-called *free space* is the unoccupied space between and even within a molecule. Intuitively, a larger free volume is inherent to larger pore sizes. Zhang et al [43] found a relationship between energy barrier and the pore size. For three gas mixtures this is depicted in Figure (2.4) and for hydrogen the relationship is described by means of Equation 2.2 with the fitting parameters A, b and t already filled in.

$$E_b = 0.143 \cdot \times 10^{(d^2 - 5.199 \cdot d)/1.886} \tag{2.2}$$

Where:
E_b is the energy barrier in [eV];
d is the molecular dynamic diameter in [$\AA$].

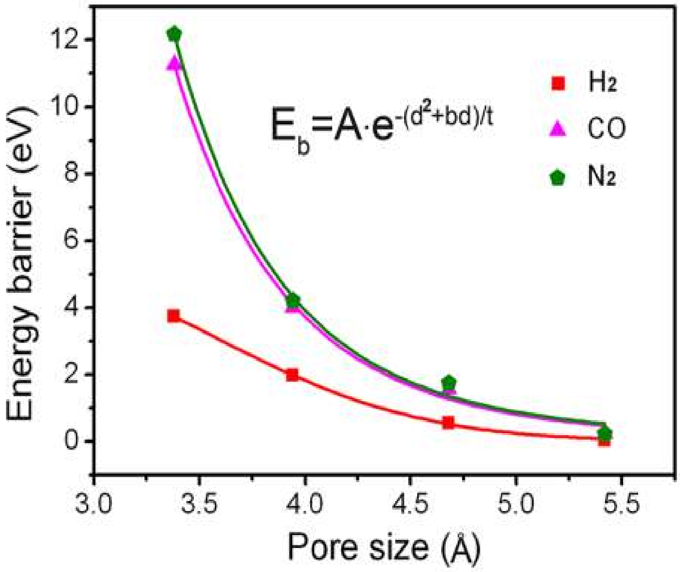

Figure 2.4: Numerically calculated diffusion energy barrier as a function of pore size. The fitting parameters A, b, and t are 0.143, −5.199, and 1.886 for H_2. Taken from Zhang et al. [43]

To prevent the possibility for a microcrack network to form, but also to guarantee structural integrity of the material, microcrack density is an important factor. Degradation of the composite at cryogenic temperatures does not stop when microcracks are formed; on the contrary, microcracks are main contributors to gas or fluid permeation. Chances are, that when intralaminar cracks are formed, they can get interconnected with each other and in that way form a flow path or leak path for the medium (LH_2 in this case) to pass through. Robinson et al. [29] even describes hydrogen permeability as 'the most unique requirement that affects the selection of materials for use in composite cryotanks.' The consortium prescribes (in TS.58 regarding permeability [38]) that CFRP tank materials may not exceed a permeability larger than 1.0$\times 10^{-9}$ $molH_2/m.s.MPa$ at RT.

Because the microcrack density determines for an important share in what order permeability will take place, it is one of the most important parameters to simulate and test. Grogan et al. [13], in their extended finite element method (XFEM) + surface cohesive zone model (SCZM) simulation, chose a mesh density for each ply in their model where at least 5 microcracks per every linear centimeter of the cylinder was allowed. This value is equal to the maximum crack density observed in heavily damaged

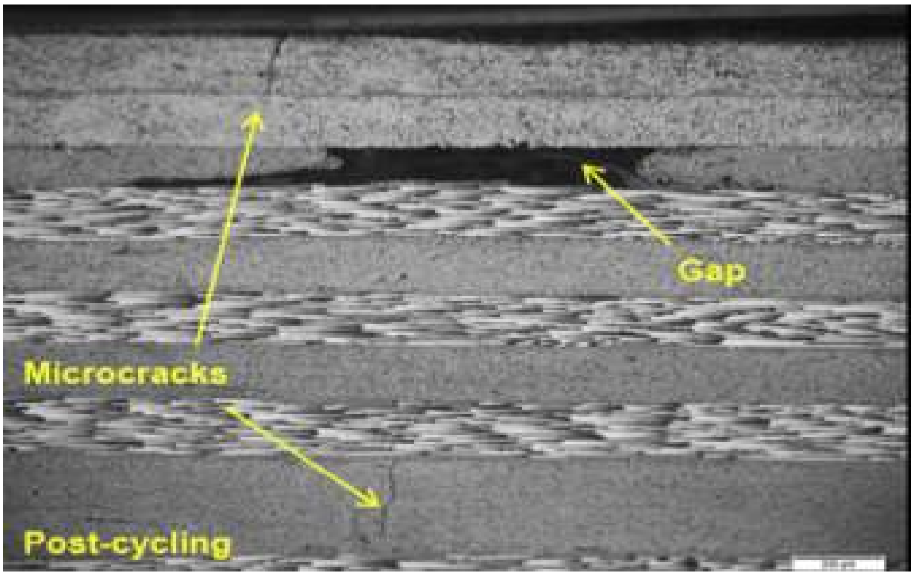

Figure 2.5: Micrograph of a gap and two transverse microcracks present in a tape-laid CF/PEEK QI specimen after exposure to a single cryogenic cycle. A permeability network can also be (partially) formed by means of gaps and/or voids. Scale 1:20. Taken from Grogan et al. [13]

cryogenically cycled CF/PEEK laminates. This will be discussed further in chapter 3.

As the strain energy can be used to predict the formation of microcracks, NASA [16] included this in their model to predict microcrack density. The critical strain energy release rate is described by Equation (2.3), keeping in mind that the modulus increases due to cooling and therefore the strain energy release rate G decreases. Despite the fact that this NASA-model does not take temperature dependence of CTE into account, they did take G_{1c} as a function of temperature into account. The research meanwhile did show a possible reason why thermal shocking caused most microcracking in the first or first few thermocycles. Because although the transverse plies are already the weaker compared to the longitudinal plies by means of ability to carry tensile stresses in longitudinal direction, this ability is lost much more at higher microcrack densities.

$$G_{1c} = \frac{Q\sigma^2 h}{E} \tag{2.3}$$

Where:
G_{1c} is the critical strain energy release rate in [J/m^2];
Q is a geometry factor;
σ is the stress in [MPa];
h is half the distance between cracks in [μm];
E is the modulus in [MPa].

Next, the crack opening displacement (COD) is a measure of the degree of opening of a microcrack and thus the fluid leak rate through a damaged ply and laminate. This distance between the surfaces of an open microcrack can be measured using optical micrographs. [13] A large COD would implicate that a contribution to a high leak rate is easily made. While this is true, the order of magnitude is completely different compared to the maximum critical crack size mentioned before. Grogan et al. measured the COD on ply level using micrographs on a quasi-isotropic tape-laid CF/PEEK specimen with $[45/-45/90/0/90/0/90/0/90]_S$ layup after cryogenic cycling. The experimentally found COD values per ply group (symmetric ply pairs, e.g. the two outer plies) ranged between 1.0 and 2.5 μm, however not in all ply groups microcracks occurred which caused a COD of 0 μm. The fact that the COD, when present in a ply, is many times larger than the kinetic diameter of hydrogen, makes it obvious that the total prevention of microcracks should be the main objective when permeability needs to be avoided.

The Knudsen number is an important measure as it can be used to relate the flow mechanism to the critical length of the microcrack. The Knudsen number, K_n, is the dimensionless ratio of the molecular mean free path to a representative physical length scale, and is represented by Equation (2.4). The mean free path is related to the kinetic diameter and is the average distance that a particle will travel without collision.

$$K_n = \frac{\lambda}{L} \tag{2.4}$$

Where L can be seen as the characteristic length of a microcrack in μm, or COD, and,

$$\lambda = \frac{\mu}{p}\sqrt{\frac{\pi RT}{2M}} \tag{2.5}$$

Where p is pressure in Pa, R is the universal gas constant in $kgm^2s^{-2}K^{-1}kmol^{-1}$, T is the temperature in K, M is the molar mass of the molecule in $kg/kmol$ and μ is the dynamic viscosity in $Pa.s$ and is given by:

$$\mu = \frac{2}{3\sqrt{\pi}}\frac{\sqrt{MRT}}{\pi N_A {d_m}^2} \tag{2.6}$$

In this Equation (2.6), d_m is the molecule diameter in m and N_A is the Avogadro constant in mol^{-1} . The Knudsen number tells us accordingly what type of flow mechanism applies to a specific situation. When $K_n < 0.1$, it means that diffusion by means of viscous and slip flow applies because collision mainly occurs between free gas molecules and not with the pore wall. Fick's law (Equation (2.7)) gives us the Fick diffusion coefficient D_f in [m^2/s] which on its turn leads to the effective Fick diffusion coefficient D_{fe}, also visible in Equation (2.8). In this Equation θ_e is effective surface porosity and τ is the tortuosity factor.

$$J = -RT\beta\nabla C* = -D_f\nabla C* \tag{2.7}$$

Where:
J is flux in [kg m^{-2} s^{-1}];
β is the atom mobility coefficient;
$C*$ is the concentration gradient in [kg/m^3].

$$D_{fe} = \frac{D_f\theta_e}{\tau} \tag{2.8}$$

When $K_n > 10$, the dominant collision is between gas molecules and the pore wall and leads to Knudsen diffusion. In this case, the Knudsen diffusion coefficient D_k in [m^2/s] is given by Equation (2.9). r_{pore} represents the average pore diameter in [m].

$$D_k = \frac{2}{3}r_{pore}\sqrt{\frac{8RT}{\pi M}} \tag{2.9}$$

When $0.1 < K_n < 10$, it means that the pore diameter is similar to λ (mean free path) and a transitional diffusion between viscous flow and Knudsen diffusion takes place, see Equation (2.10). [46]

$$\frac{1}{D_{Pe}} = \frac{1}{D_{fe}} + \frac{1}{D_{ke}} \tag{2.10}$$

Where:
D_{Pe} is transitional Knudsen diffusion coefficient in [m^2/s];
D_{fe} is effective Fick diffusion coefficient in [m^2/s];
D_{ke} is effective Knudsen diffusion coefficient in [m^2/s]

To account for flow transition between slip flow and Knudsen diffusion, a weighing coefficient, f, is introduced; a low weighing coefficient accounts for Knudsen diffusion. Zhang et al. [44] formulate f as:

$$f = \frac{1}{1 + (K_n/K_{n0.5})^{n-1}} \tag{2.11}$$

Where $K_{n0.5}$ and n are fitting parameters and have the value of:
$K_{n0.5}$ = 4.5 [33]
n = 5 [33]

Finally, the Knudsen number and the weighing factor can be used to generate a relation between the apparent permeability k_{app} in $[m^2]$ and the intrinsic permeability k_0 in $[m^2]$ according to Zhang, eventually leading to a dimensionless permeability model. See Equation (2.12) as described by Zhang. A correction which has to be made however is that in this relationship, both k_{app} and k_0 are a measurement of diffusion instead of permeability, given their unit.

$$\frac{k_{app}}{k_0} = (1 + 4K_n)f + \frac{64}{3\pi}K_n(1 - f) \tag{2.12}$$

In extension of the above mentioned about COD, Grogan et al. stress the facts that microcracking was found in thicker laminates post-processing and that crack opening in inner and off-axis ply groups was found to be significantly less than outer plies. Besides, quasi-isotropic laminates generally exhibited higher crack densities than cross-ply laminates.

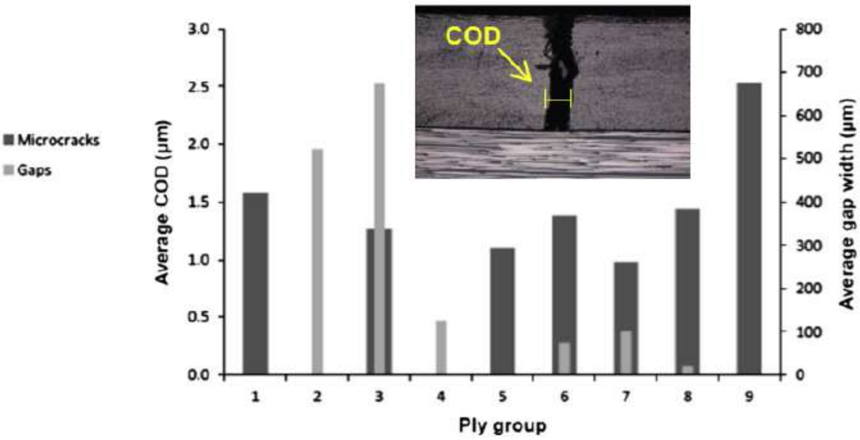

Figure 2.6: Crack opening displacement and gap width measurement from cryogenic cycled tape-laid CF/PEEK QI specimens. Ply groups 1–9 refer to symmetric ply pairs. Taken from Grogan et al. [13]

Furthermore, the pressure range hydrogen gets stored in its liquid state is between ambient pressure and 4 bar. Next to this pressure range the following pressures have to be taken into account when designing a LH_2 tank: design pressure, operating pressure, maximum allowable pressure and burst pressure. The design pressure is the pressure taken into account when designing a tank and is always above the operating pressure, because it is the operating pressure times a safety factor. In case of LH_2 tanks the design pressure lies around 10 bar and the operational pressure is kept at maximum 8,5 bar. However, the consortium strives for a larger safety factor; with a strived operating pressure of 4 bar, they still take 10 bar as design pressure. Furthermore, the maximum allowable working pressure (MAWP) is the maximum pressure to which a component is designed to be subjected to and which is the basis for determining the strength of the component under consideration. The MAWP is therefore close to the design pressure, but below failure of the tank and is for most tanks located between 10 and 10,1 bar; a pressure relief valve ensures that the MAWP is maintained as long as there is no decrease. [40] Finally, the burst pressure is the maximum pressure that can be applied without physically damaging the component. Burst pressure is considered the most important requirement for the tank according to Sippel [35], therefore the 10 bar burst pressure in this RDM project is an important design criterion.

2.2.3. Limiting microcracks

This chapter will describe certain design criteria and material modifications that can be made in order to limit microcracks to a level where the following permeability stays below 1.0$\times 10^{-9}$ $molH_2/m.s.MPa$ at RT. Moduli of polymeric matrix materials are in general very sensitive to change when exposed to thermally induced residual stresses. As mentioned, there is a general trend of an increasing modulus and therefore stiffness as a result of subjection to cryogenic temperatures. What is often seen in combination with the increasing modulus, is a decreasing strain to failure which on its turn is disadvantageous for high pressure applications and impact strength. Concluding, the strain to failure decrease as a result of cryogenic temperature often leads to brittle behavior of the material. [17]

A general tendency for thermosets is that strain to failure (or also called tensile fracture strain) decreases when stiffness increases as a result of cryogenic thermal cycling; therefore one should not per se aim for a tensile modulus that is multiple times higher after modification. On the other hand, fibers dictate the thermal contraction of a composite because of their higher stiffness. To create a better balance CTE-wise, it is worth investigating the value of a slightly higher modulus. Taking these givens into account and looking at Figure (2.7), in particular filler-modifications using carbon nanotubes (CNT's) and graphene draw the attention. Both additives cause just a slight increase in the tensile modulus and at the same time a promising tensile strength increase, for example compared to hyperbranched polyester (H30). What makes graphene even more interesting is the fact that the tensile modulus change decreases the colder it gets, what on its turn accounts for a little lower stiffness and thus a higher tensile fracture strain compared to other additives and to its own RT state.

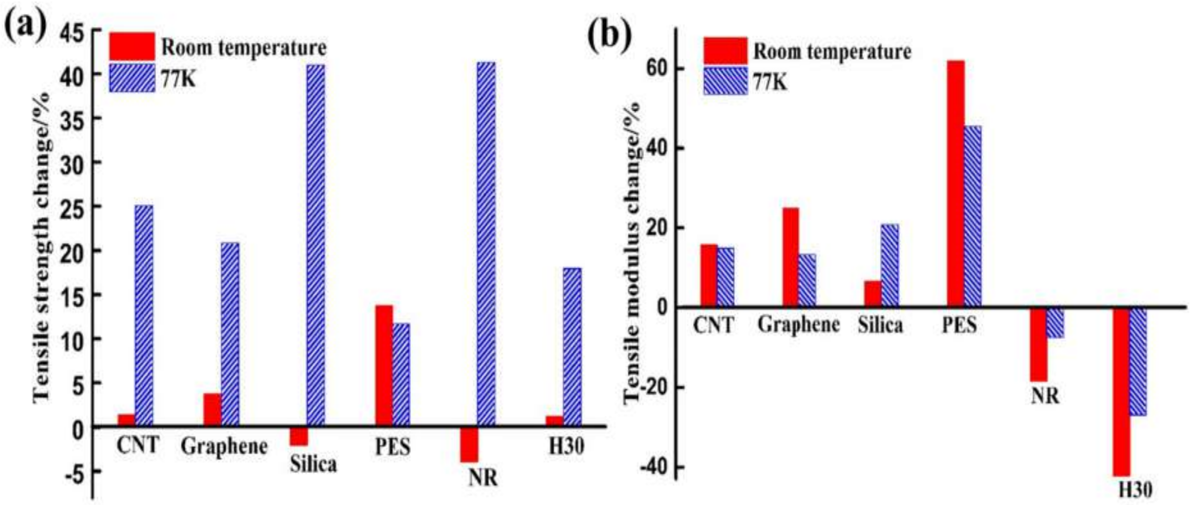

Figure 2.7: Change in tensile strength and tensile modulus of different modified thermoset polymers with respect to the same pristine polymers. Experimentally determined, taken from Chen et al. [6]

One of the characteristics of thermoplastics that offers chances for LH_2 tanks is their crystallinity in relation to permeability. Whereas thermosets are generally only present in the cross-linked amorphous appearance, some thermoplastics can be present in both amorphous and (semi-)crystalline. The percentage of crystalline regions can range from roughly 10% to 80% to call it a semi-crystalline. A large influence on permeability however is the free volume in the polymer through which particles can dissipate. One way to create better permeability barrier properties is by packing the polymer chains closer together in order to reduce the free volume available. In the semi-crystalline state this chainpacking occurs as a natural property in the lamellar crystals, because of the chain structure of the oriented polymer. Compared to amorphous polymers, where molecules are given a chance to permeate by means of the ’free volumes’ between the crosslinks, semi-crystalline polymers hold much better natural permeation barrier properties. [4]

Above is described why semi-crystalline thermoplastics could be a better choice because of their chain-packing, but next to this semi-crystalline plastics also have a better temperature stability compared to amorphous thermoplastics. One reason herefore is the fact that semi-crystalline thermoplastics can operate above their T_g: the crystalline regions in the material are namely characterized by a melting temperature (T_m) in addition to their T_g. At this point the material (region) transforms from glassy to a molten state. Because the T_m is always higher than the T_g the average operating temperature for semi-crystallines can be above their T_g. [6]

Although the options to modify thermoplastics are more limited compared to thermosets, there are a few options to do so. A number of researches are performed where nanofiller material was incorporated in the matrix. Known nanofillers of thermoplastics are carbon nanotubes (CNT’s), graphene oxide (GO) and short carbon fibers (SCF’s). Incorporation of CNT’s showed to cause a higher Young’s modulus and yield strength; as could be expected and wanted. Contradictory, this also caused a decrease of fracture strain at 77 K which is unwanted. [6] The use of CNT’s may offer opportunities for further research: for a CNT/polycarbonate composite it was found that fatigue live got extended but also that the composite could withstand a two times higher applied load at 77 K compared to RT while maintaining the same fatigue live.

Fibre direction

According to Sapi et al. [30] there are a few behavioural aspects of thermal conductivity which have to be kept in mind when creating an optimised design for a composite. One being the fact that composites have a higher thermal conductivity in the longitudinal fibre direction compared to the transverse direction, ranging from 10% to two orders of magnitude, dependent on what research is followed. Hohe [17] explains this as a result of the higher stiffness of the fibres: the fibres are dominant over the matrix in thermal contraction in fibre direction when cooled down to cryogenic temperatures, forcing longitudinal mechanical strain and thus mechanical stress in the matrix. To behold a macroscopically stress free state of the composite, this ultimately leads to compressive residual stresses in the fibres. This is supported by Equation (2.1) as described by Huang [19].

Lay-up

Hypothetically in a cylindrical tank shape, a unidirectional lay-up is most suited for the reduction of thermal stress on laminate level, but of course this is not practical for resisting internal pressurisation loads. A cross-ply stacking of UD-laminas as described in 2.2.1 should however not directly be seen as something negative with respect to microcracking. To prevent permeability it is important that the microcracks stay unconnected and do not form a network; cross-ply stacks are eminently important to prevent this as much as possible because the oriental ply-mismatch reduces the crack propagation. According to Sapi et al. [30] multiple researches have shown that quasi-isotropic and small-angle laminates have a higher crack density and a higher leak conductance (however a lower microcrack initiation), which favors the use of a cross-ply stacking to prevent the forming of microcrack networks. A cross-ply stacking is however most vulnerable to thermally induced residual stresses considering their ultimate directional mismatch.

Bechel et al. [3] extend this line of reasoning by stating that an unblocked laminate with relative thin plies is most desirable. In their research, Bechel et al, used laminates composed of only 0°, -45°, +45° and 90° plies; a blocked lay-up is a lay-up with adjacent plies of the same orientation. An important conclusion to include is: using a ply adjacent to the surface ply 90° out of phase with the surface ply. This is to arrest the many surface ply micro-cracks due to thermal stresses. Furthermore, once microcracks started to initiate in a block, they quickly penetrated the complete block in the thickness direction before being arrested. Although this happens in both surface blocks and inner-ply blocks, it is of higher importance to prevent blocked surface plies as these are more vulnerable for microcracking. This is because of the thermal gradient where the outer surface, being exposed to lower temperatures, tends to contract more than the inner layers, leading to increased tensile stresses on the surface plies and thus promotes microcracking. An option to completely prevent blocked plies is to use a laminate with an odd number of plies, e.g. $[90/0/90/0/90/0/90/0/90]$.

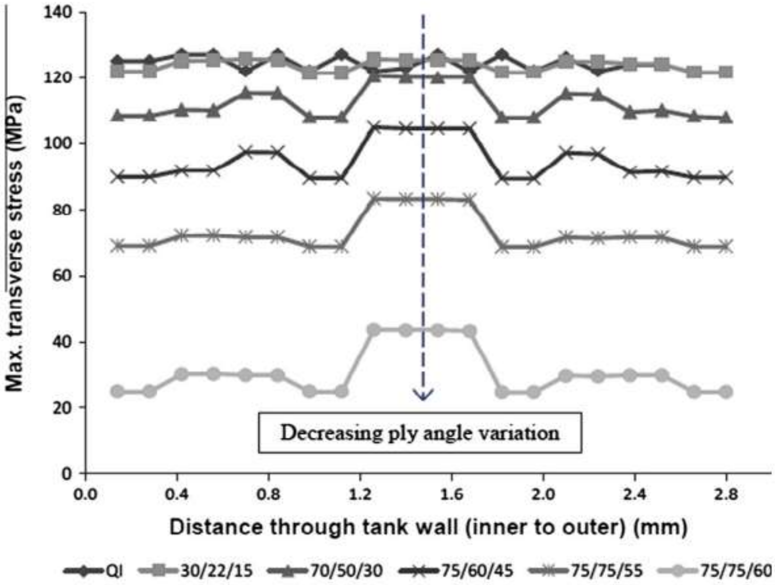

Figure 2.8: Numerically determined transverse stress distribution for several lay-ups under a thermo-mechanical load consisting of a two-stage thermal load and an internal pressure ramp load. Taken from Grogan et al. [13]

However, for cryogenic fuel storage, thermal stress is critical; axial stress is reduced by rotating the angles of specific hoop plies towards the axial direction. This pleads more against the use of a cross-ply laminate and thus a balance between unidirectional and cross-ply had to be found. Grogan et al. tested different lay-ups in Abaqus using the wound composite modeller (WCM). The starting point was the general lay-up $[90_2/\pm\theta/\pm\theta/90_2/\pm\theta_2]_S$, the aim to find the lay-up with the lowest maximum transverse stress. This was found to be $[90_2/\pm75/\pm75/90_2/\pm60_2]_S$ for an automated tape-laid CF/PEEK laminate under thermo-mechanical load, refer to Figure (2.8). This however goes against the theory to use thin plies in order to relieve thermal stresses. This lay-up should therefore possibly be considered as an option for the final tank design, while a QI lay-up would be suitable for experiments where the intention is to create microcracks.

Permeation barriers

One way to restrict the phenomena of permeation and outgassing on composite LH_2 tanks is by applying a permeation barrier, also called a liner when this barrier layer is a self supporting material. A popular way to construct a LH_2 tank is by using an inner tank and an outer tank with a vacuum in between. A liner is a thin layer of material with much better permeation resistance properties compared to the composite tank, metallic liners are for that reason researched more widely. According to Schultheiss [31] the liner has to be placed on one of the surfaces or inside the shell. The most straightforward location however is the surface of the inner tank which faces the vacuum, because the LH_2 gets encapsulated as close to its original state and location and also leakage and outgassing into the vacuum is (partly) captured.

Humpenoder in his research in 1998 [21] claimed that the usage of thin liners in the order of several micrometers did not noticeably decrease the permeability of composite materials. He tested the application of liners on GFEP (LY556/HY917 Ciba Geigy combined with E-glass, 67 vol%) and CFEP (LY556/HY917 Ciba Geigy combined with Toho HTA7, 60 vol%). As he only experimentally tested the gaseous hydrogen permeation in a temperature range between 77 K and 325 K, this data is not directly applicable to LH_2, but might at least give a good indication. It was found that thick liners, thicker than several micrometers, became mechanically unstable because the adhesive bond between the material and the liner would fail. On the other hand, when thin liners where used, there was almost no effect on the permeability; liners used here were polyimide (Kapton), amorphous hydrogenous carbon (aCH), titanium nitride and metals like copper, gold and silver. What Humpenoder however did find, is that when metal foils where embedded in the composites, no permeability at all was detected. This was tested with an aluminium foil of 0.24 mm and a tin foil of 0.25 and 0.1 mm. As the aluminium foils showed forms of delamination after thermal and mechanical cycling, embedded tin foils seemed to be a very interesting solution as permeation barrier. [21] Other materials drawing attention to function as permeation barrier are graphene, silver, phenoxy, PEEK films in combination with a metal and polyimide (PI). [15]

Fibre-volume fraction

The fact that the fibers have a higher stiffness and are therefore the dominant part of the ply which dictate the thermal contraction, is however limited to certain fibre volume fraction f_f in combination with the differing CTE's of the fibres and the matrix. The Equations for fibre volume fraction f_f, axial Young's modulus and transverse Young's modulus are given by (2.13), (2.14) and (2.15). From these, Equation (2.14) is also known as the rule of mixtures. r stands for the radius of a fibre with a circular cross-sectional area and $2R*$ stands for the closest separation of two fibre centers in a hexagonal array.

$$f_f = \frac{\pi}{2\sqrt{3}}(\frac{r}{R*})^2 \tag{2.13}$$

$$E_1 = E_f f_f + E_m f_m = E_f f_f + E_m(1 - f_f) \tag{2.14}$$

$$\frac{1}{E_2} = \frac{f_f}{E_f} + \frac{(1 - f_f)}{E_m} \tag{2.15}$$

Where:
f_f is the fibre volume fraction;
r is the fibre radius with a circular cross-sectional area in [m];
$R*$ is half of the closest separation of two fibre centers in a hexagonal array in [m];
E_1 is the longitudinal Young's modulus in [MPa];
E_2 is the transverse Young's modulus in [MPa];
E_f is the Young's modulus of the fiber in [MPa];
E_m is the Young's modulus of the matrix in [MPa];

In their study where Ran et al. [28] proposed a model to predict longitudinal and transverse CTE's of UD single plies, it was numerically found that the total CTE was dominated by the matrix when $V_f \leq 0.15$ and dominated by the fiber when $V_f \geq 0.50$. This uneven distribution on the V_f axis compared to the CTE is explained by the fact that the matrix usually holds a higher CTE than the fiber; Ran et al combined the total CTE in fiber direction of a UD single ply in Equation (2.16). In general, this directly means that the longitudinal CTE is dominated by the axial fibre CTE α_{f1} in [K^{-1}], whereas the transverse CTE is more of a combination between fibre and matrix CTE; this causes anisotropy on thermal behaviour on the intralaminar scale.

$$\alpha_1 = \frac{E_{f1} V_f \alpha_{f1} + E_m V_m \alpha_m}{E_{f1} V_f + E_m V_m} \tag{2.16}$$

Where:
α_1 is the longitudinal CTE in [K^{-1}];
E_{f1} is the fiber axial elastic modulus in [MPa];
V_f is the fiber volume fraction;
α_{f1} is the axial fibre CTE in [K^{-1}];

α_m is the CTE of the matrix in [K^{-1}];
V_m is the matrix volume fraction.

Ply thickness

Other microcrack-related influencers on the mechanical behaviour are the thickness of a ply (or a cluster of same-oriented plies). As a general rule of thumb it can be said that the thicker a ply is, the more microcracks occur in that ply. A laminate consisting of thin plies (<125 μm [8] or 70 g/m^2 [45]) is therefore preferred because these show a more homogeneous fibre distribution throughout the laminate. Subsequently, this causes less voids, less resin rich regions and a more uniform V_f and finally less permeation. Thin plies are besides also an outcome to suppress the onset and propagation of delamination because of their lower interlaminar stresses as a result of thermal cycling. [8] Whereas manufacturing always used to be a problem for thin plies, AFP/ATL methods nowadays seem promising. [45]

Numerous studies have shown that it is easier for a matrix crack to evolve on the surface than inside a laminate. This is because of the thermal gradient where the outer surface, being exposed to lower temperatures, tends to contract more than the inner layers, leading to increased tensile stresses on the surface plies and thus promotes microcracking. As matrix strength is also a function of the thickness of the laminate, Camanho et al. [5] developed an analytical relation between the thickness of the lamina and the in situ strength S_{is}^L in [Pa] of the matrix in the lamina. After deriving the Equation, the general expression for the in situ shear strength is given by Equation (2.17).

$$S_{is}^L = \sqrt{\frac{(1+\beta\phi G_{12}^2)^{1/2}-1}{3\beta G_{12}}} \tag{2.17}$$

In this Equation, β defines the non-linearity of the shear stress–shear strain relation, which is zero for a linear behavior, and G_{12} defines the in-plane shear modulus in [Pa]. Besides, ϕ is defined as follows for the different ply configurations:

$$\begin{aligned} \text{For a thick ply: } \phi &= \frac{12(S^L)^2}{G_{12}} + \frac{72}{4}\beta(S^L)^4 \\ \text{For a thin ply: } \phi &= \frac{48G_{IIc}}{\pi t_l} \\ \text{For an outer ply: } \phi &= \frac{24G_{IIc}}{\pi t_l} \end{aligned} \tag{2.18}$$

Where:
S^L is shear strength in [Pa];
G_{IIc} is mode 2 fracture toughness in [J/m^2];
t_l is thickness of a lamina in [mm].

Voids and resin-rich areas

Permeation is logically dependent on as well the amount of voids as the dynamic free volume, which dictates how often a molecule jumps from one void to a neighboring void. The presence of voids contributes to the formation of leak paths, and therefore a higher permeability, as a void will serve as connecting link between microcracks and/or delaminations; also the degradation of certain material properties like stiffness can be appointed to voids. Voids are often a result of manufacturing and are subsequently randomly distributed throughout the laminate, all having their own appropriate dimensions. When size ranges are known, for example from X-ray CT-scans, voids can be presented as ellipsoids with each their own Gaussian distributed random length, width and height, this is done by using the normal distribution. This probability density function $P(x)$, Equation (2.19), is used to express the distribution for x (length) in this case. μ represents the mean and σ represents the standard deviation in this Equation. [12]

$$P(x) = \frac{1}{\sigma\sqrt{2\pi}} \times 10^{-\dfrac{(x-\mu)^2}{2\sigma^2}} \tag{2.19}$$

By defining E_1 as the fibre direction modulus and E_2 and E_3 as the transverse moduli, this leads to reduced element stiffnesses (E_i^*) which are defined as follows:

$$E_1^* = (1 - \pi yz)E_1 \tag{2.20}$$

$$E_2^* = (1 - \pi xz)E_2 \tag{2.21}$$

$$E_3^* = (1 - \pi xy)E_3 \tag{2.22}$$

Resin-rich areas are to be considered as comparable troublesome as voids, because they also locally weaken the material properties like stiffness. For modelling purposes, resin-rich areas can be programmed in the same way as voids, with the only exception being the fact that the properties of the element will be altered to represent the discontinuity instead of reducing the stiffness of an element. This will lead to replacing the properties of an element by those of the polymer (when talking about large resin-rich areas). [12]

Exposed free edges

Bechel in his research found that sectioning of the samples revealed that the micro-cracks in the surface plies spanned the full width of the sample while many of the micro-cracks observed on the edge of the inner plies did not extend to the center of the samples. This implies that a rectangular specimen with exposed free edges may result in a significantly different micro-crack density than a sample without free edges. [3]

2.3. Material properties for FEM model

Chapter 3 will describe what methodologies will be used for this thesis. Part of the methodology is creating a FEM model in which microcrack initiation and growth is going to be modelled using X-FEM. As a prerequisite for this model a number of input variables are already listed below. The general build-up of the FEM model is based on the methodology as described by Grogan et al. [12]

General inputs for the Python code:

- Number of plies
- x- and y- length of ply in [mm]
- Number of elements in x- and y-direction per ply
- Number of elements in z-direction per ply
- Distance between two enriched X-FEM zones in a ply
- Ply orientation and lay-up
- Thickness of each ply in [mm]
- $F_{t_{mean}}$ in [N/mm] (mean value of transverse matrix strength)
- Shape of Weibull curve (Weibull parameter)
- m (Weibull modulus)
- F_s in [N/mm] (shear strength of matrix)

Grogan et al. [13] take a selected amount of temperature points for their temperature-dependent data. The complete set of input data over the temperature range is then interpolated and normalized using fitting functions. Below, the subscripts 1 and 2 refer to longitudinal and transverse directions.

- E_1, E_2, E_3 in [MPa] (elastic modulus)
- G_{12}, G_{13}, G_{23} in [GPa] (shear modulus)
- ν_{12}, ν_{13}, ν_{23} (Poisson's ratio)

- ρ in [kg/m3] (density)
- SHC in [J/kg.K] (specific heat capacity)
- α_1, α_2, α_3 in $[10^-6$ (m/m)/K] (CTE)
- κ_1, κ_2, κ_3 in [W/m.K] (thermal conductivity)
- TTS in [MPa] (transverse tensile strength)
- TCS in [MPa] (transverse compressive strength)
- $IPSS$ in [MPa] (in-plane shear strength)
- $ILSS$ in [MPa] (inter-laminar shear strength)
- G_{IC}, G_{IIC}, G_{IIIC} in [J/m2] (Mode 1, 2 and 3 fracture toughness)

The following variables will be added in order to predict permeability following the microcracking:

- r in $[\mu m]$ (fiber radius)
- f_f (fiber volume fraction)
- $2R$ in $[\mu m]$ (closest separation between two fibre centres)
- Crystallinity gradient
- Crystallization shrinkage
- Crack density in [cracks/cm]: corresponds to maximum crack density observed in heavily damaged cryogenically cycled laminates
- Void volume fraction
- Void dimensions in x-, y- and z-direction in $[\mu m]$ (mean and deviation)
- Permeability influencers: temperature in [K], pressure in [bar]
- (Diffusion) Energy barrier necessary for a hydrogen molecule to pass through the material
- Strain to failure
- σ_0 in [MPa] (mean fracture strength)
- Knudsen fitting parameters $K_{n0.5}$ and n

Tank properties
For future work, the representative volume element (RVE)-approach in the FEM model can possibly be extended to tank panels or even the complete tank; to do so at least the following variables should also be taken into account considering the tank position in the aircraft:

- Tank size
- H_2 fuel mass
- Tank packaging lay-out (placement of valves, fittings, instrumentation etc.)
- Center of gravity (CG) limits
- Acceptable boil-off rate
- Applicability of dormancy of the tank and/or aircraft
- Acceptable crashworthiness
- Acceptable fire resistance
- Fwd/aft side designs of tanks including attachment fittings
- Dimensions of LH_2 pipes

2.4. Fracture mechanisms

The cryotank to be obtained will be subject to complex thermo-mechanical load states. As a result, the failures that will occur will likely be mixed-mode compression-shear matrix failures. Microcracking can therefore be modelled using X-FEM because this is an intra-ply failure mode. According to Grogan et al. [13] the main matrix failures are:

- transverse tension;
- longitudinal shear;
- transverse compression;

- transverse shear;
- oblique fracture planes.

With oblique fracture planes a microcrack morphology is meant where the plane is oriented at a prescribed angle (α) and is parallel to the ply fibre angle (β), see Figure (2.9) for a visual representation. When these matrix failures are translated to the emergence of microcracks, it means that a crack initiates when a specific failure criterion, like Hashin, is exceeded.

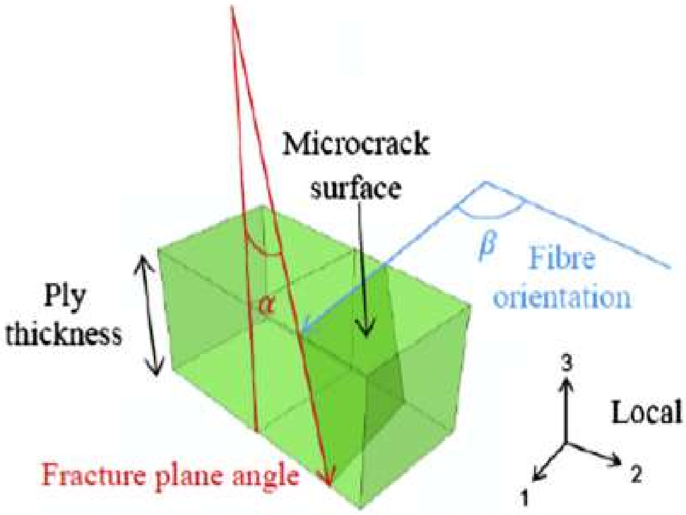

Figure 2.9: Oblique fracture plane. Taken from Grogan et al. [13]

Additionally, delamination is a known inter-ply fracture mechanism due to the complex multi-axial loading during cryogenic cycling. Grogan et al. [12] describe this damage evolution to a mixed-mode fracture, which is defined by combining energy release rates from all three fracture modes (G_I, G_{II}, G_{III}).

According to Sapi et al. [30] the use of thermoplastic resins instead of thermoset resins reduces permeability of composite laminates exposed to cryogenic temperatures. That is because of the increased fracture toughness and the following ability to reduce matrix cracking. It is known that the crystallinity of a material has a direct effect on the permeability of the material, with the general trend being a higher crystallinity percentage leading to reduced permeability. This can be explained by the matrix density increase as result of the crystallization and the following increased residual stress.

Translating this to fracture mechanisms means that semi-crystalline thermoplastics might be the sweet spot in a figurative sense regarding fracture mechanisms. Considering fracture toughness, mode I, II and III induced fractures and delaminations, thermoset composites have a lower resistance to crack initiation as a result of their higher crosslink density and higher crystalline thermoplastics on the other hand will show greater crystallization shrinkage and thus more fracture vulnerability. [32] [30] On the other hand, crystallization shrinkage and differences in CTE can be reduced to a certain extent by means of annealing. Annealing involves heating a material to a specific temperature and then cooling it slowly to allow the internal structure to reach a more thermodynamically stable state.

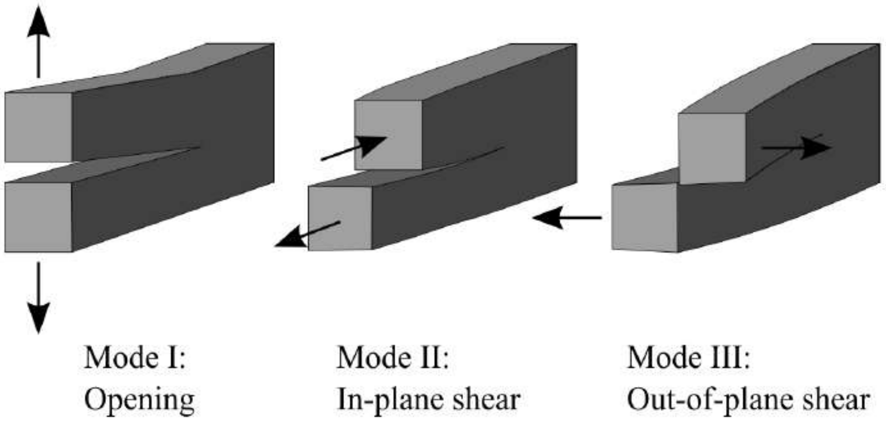

Figure 2.10: Mode I, II and III matrix fracture modes.

3

Microcrack and permeability simulation methodology

This chapter describes the methodology of the experiments that are carried out during this research project, as well as the methodology for an XFEM-SCZM model. The aim of the experiments described below is to 1. generate validated material property values, 2. experimentally determine the microcrack density, energy release rate and permeability and 3. serve as validation for the XFEM-SCZM model which will be used to model microcracking and leak rate in composite materials; in this model XFEM will be used to model microcrack growth.
In 2022, NLR performed mechanical tests on a selection of materials at $4K$ and RT. These mechanical tests consisted of tensile strength and modulus, in-plane shear strength, modulus and interlaminar shear strength. To ensure the quality of the manufacturing of the specimens, all test specimens have been checked by means of ultrasonic C-scan, refer to Appendix E. As thermoplastics polyetheretherketon (PEEK), polyetherketoneketone (PEKK) and low melt polyaryletherketone (LM-PAEK) were assessed and after evaluation by Toray and NLR it could be concluded that PEKK and LM-PAEK were amongst the better performers mechanically and that only PEEK showed lesser results. PEKK and LM-PAEK showed comparable results and both even showed better results at $4K$ than at RT, which is beneficial considering the cryogenic purpose.

For these thermoplastic materials no microcracks have been detected after thermal cycling. Thermal cycling involves subjecting a material to alternating cycles of heating and cooling within predefined temperature ranges. This controlled process is designed to mimic real-world conditions where materials may experience fluctuations in temperature due to environmental or operational factors. For this topic these fluctuations will take place between 20 K and ambient temperature at an estimated frequency of two times per year, for example for re-vacuuming or maintenance purposes. Because of industry interest, LM-PAEK / T700 UD-tape (Toray TC1225) was selected as the material to perform tests on at $20K$; standard average properties are displayed in appendix F.

Considering thermosets the following materials are selected to perform mechanical tests at $4K$ and at RT: TC-380, Toray 3900 and TC-346. Next to that, NLR performed permeability tests at RT without mechanical loading for these materials. Minimal microcracks were found in TC-380 and no microcracks were found in Toray 3900 and TC-346, however regarding permeability Toray 3900 and TC-346 are the better performers. An explanation for these results can be found in the toughening agents in TC-380, but also in the higher amount of crosslinking in Toray 3900 and TC-346. A higher amount of crosslinks accounts for more brittle behaviour but also for lower permeability. Because of the variety in these properties all three materials will still be tested mechanically and a choice in TS material will be made afterwards.

A choice is made to already further scope down on material choice. LM-PAEK/T700 is chosen because of its good results in the mechanical tests, the lack of microcracks after thermal cycling and industry interest. To be able to compare results and serve as a reference, also PEEK/AS4D will be considered.

AS4D is in its properties very comparable with the T700 fiber. In this case, PEKK will thus be the thermoplastic material that will not be incorporated in the model. As Toray 3900 is US-based, this material is difficult to obtain and will therefore not be considered. Given the fact that TC-346 is a non-aviation matrix material it is often used in combination with a stiffer fiber than T700; of the latter combination, no documentation is available and therefore also TC-346 will be out of scope for this research. Acquiring results of TC-380/T700 is planned by Toray, but not yet executed (at the moment only TC-380/IM7) and therefore also out of scope for this research at the time of writing.

3.1. Test program microcracks and permeability

This paragraph presents an experimental investigation into the microcracking and permeability of the selected LM-PAEK/T700: Toray Cetex TC1225 (hereafter TC1225) for liquid hydrogen storage tanks; the material is selected following mechanical test results performed by NLR, in association with Toray. As a reference material TC1200 will be used, which is a PEEK/AS4D composite, because this material is widely researched and a lot of reference material is available. The effects of cryogenic temperatures, tensile loading, lay-up, material defects, pressure, and thickness on the microcracking and permeability of numerous test specimens are investigated. Laminates are manufactured using AFP. Regarding permeability, the model can be validated at room temperature using the current test setup.

After a number of iterations, a test program is developed where test specimens will be assessed on their tensile behaviour at RT and cryogenic temperature, their microcrack resistivity and their microcrack-permeability relationship. The final test program can be found in Appendix B.

A comparison between two materials with three different lay-ups was aimed for initially.In the first instance, the test program would be executed on both Toray TC1225 and Toray PEEK/AS4D, each with 3 corresponding lay-ups: a triaxial (QI), a blocked cross-ply and an asymmetrical lay-up. It was hypothesized that the triaxial lay-up would show very few microcracks and decent permeability resistance, whereas the blocked cross-ply lay-up was hypothesized to show a significant amount of microcracks and permeability. The asymmetrical lay-up was thought of as a way to resemble a mechanical load like the eventual pressure from within the tank.; this would then make the asymmetrical lay-up suitable for thermal cycling. However, after FEM-analysis, it appeared that an asymmetrical lay-up did show a lot of deformation but the internal stresses where almost similar to the symmetrical lay-up. Also because the asymmetrical lay-up would not be suitable for the permeability test set-up, because of its curvature, this lay-up has been waived.

To limit cost and size of the test program, a choice is made to only perform the experiments on TC1225. The cost to test at 20 K has increased significantly due to the price increase of helium as a result of the Russo-Ukrainian war escalation since 2022. Also the blocked cross-ply laminate has been dropped, because this would introduce even more variables and thus a larger test matrix. The test program is therefore scoped to the influence of ply thickness. The QI triaxial lay-up that is chosen consists of 60-, 0-, and -60-plies; a variant is manufactured for regular ply thickness and a variant is manufactured for thin ply thickness in a way that total laminate thickness is comparable.

- Regular ply thickness triaxial lay-up: $[(60/{-60}/0)(60/{-60}/0)(60/{-60}/0/{-60}/60)(0/{-60}/60)(0/{-60}/60)]$ (2.38 mm and 17 plies = 140 μm per ply)
- Thin ply thickness triaxial lay-up: $[(60/-60/0)(60/-60/0)(60/-60/0)(60/-60/0/-60/60)(0/-60/60)(0/-60/60)(0/-60/60)]$ (2.53 mm and 23 plies = 110 μm per ply)

The triaxial QI lay-up is chosen over the most common QI lay-up consisting of -45-, 0-, 45- and 90-plies because this is also the proposed lay-up for the LH_2 tank. Due to the shape of the tank and the subsequent loading conditions, the lay-up will always have to consist of 0-plies and +/-XY-plies, where X and Y will always be between 55 and 70 degrees, this is necessary to distribute loads more evenly across the material and prevent localized stress concentrations. In order to keep internal stresses balanced, the triaxial lay-up is the most obvious option (X and Y will thus have the value of 60 and -60 degrees).

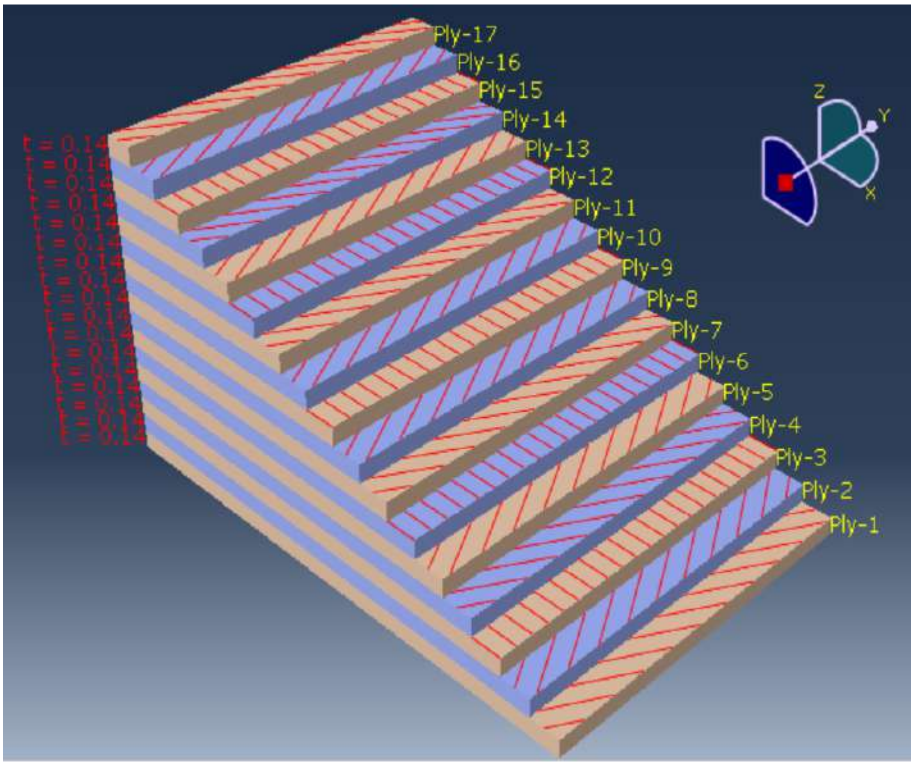

Figure 3.1: Ply stack plot of the suggested regular ply thickness triaxial lay-up

In order to create and track microcrack initiation and propagation, part of the test proposal consists of tensile tests, both at RT and 20 K. The standard that is largely followed here is ASTM D3039/D3039M - 17: Standard Test Method for Tensile Properties of Polymer Matrix Composite Materials. This test method determines the in-plane tensile properties of polymer matrix composite materials reinforced by high-modulus fibers. The standard actually requires a constant rectangular cross-section as shape for a balanced and symmetric tensile specimen, however the test proposal deviates from this geometry for the cryogenic tensile tests. Modified dogbone specimens are used to create the most optimal fit for the cryostat. [22] The reduced width is necessary in order to create a uniform temperature across the entire width of the specimen by means of the He-spray nozzle.

An interfering factor to keep track on during the tensile tests is the edge effect because of the off-axis plies in the laminates. The edge effect can be described as the concentrated occurrence of stress fields at the free edges in the interfaces between two layers of composite laminates. Premature failure caused by drastically underestimated strength and modulus for angle plies are a constant threat. The effect can be partly countered by incorporating significant 0° plies or by increasing the width. In this test proposal the latter is executed to a certain extent, while still keeping the specimens fit for the test set-up. [22]

The specimen dimensions are large enough in a way that the predicted strain distribution will not affect results significantly, but dimensions are also based on the dimensions of the produced laminates. Using FEM, it was found that the minimum length between the two grippers should be 250 mm. This specimen length creates a strain distribution which is uniform enough in width when subjected to a uniformly distributed static step in length; this can be seen in Figure (3.2).

As stated before, it is hypothesized that the triaxial lay-up will show very few microcracks when subject to a tensile load in the 0° direction, because part of the fibre direction is the same as the tensile load direction. Microcrack initiation is, however, necessary in order to deduct a proper microcrack-permeability relation. To overcome this, the laminate will be tested under 90°, while the tensile load will still be applied in the 0° direction, and can also be found in Appendix B.

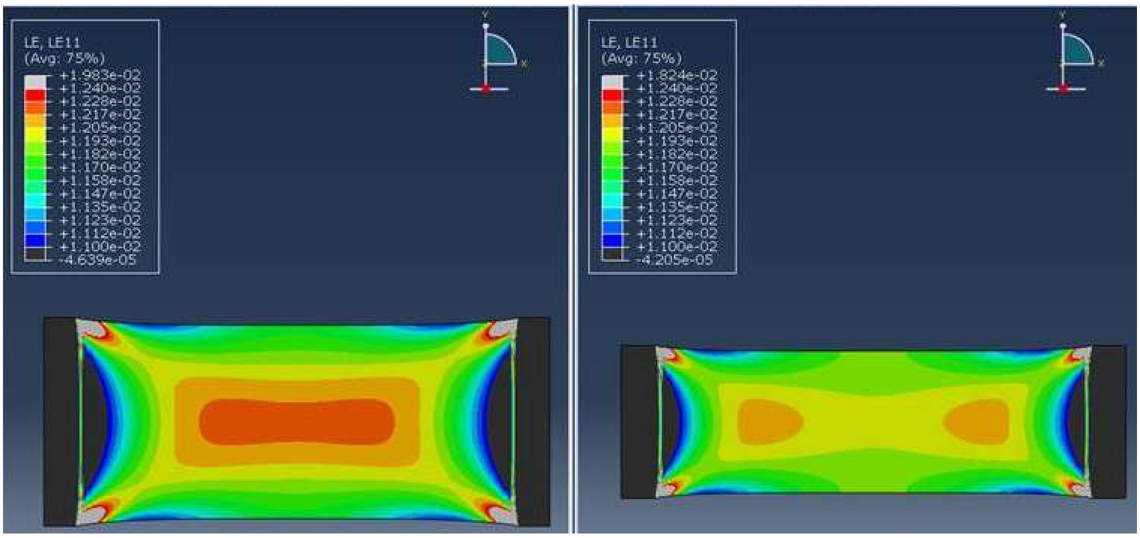

Figure 3.2: Strain field comparison after applying an uniformly distributed static step in length between a specimen with length 160 mm and a test section of 110 mm length (left), and a specimen with length 330 mm and a test section of 250 mm length (right).

Furthermore, initially there was aimed for defect determination and microcrack density determination by means of micro-CT scanning. After approaching several institutions, micro-CT scanning has been canceled from the test proposal. The highest resolution reachable with micro-CT was 1/1000 of the sample diameter. Figure 3.3 displays a typical example of a microcracked LM-PAEK specimen with 5 micron diameter fibres. The size of the crack, location in the matrix between two fibers and the transverse cracking direction make it almost certain to say that this is a microcrack. A resolution of approximately 0.5 micron is thus necessary to properly display microcracks. When the selected test specimens would have to be cut into smaller volumes of 0.5 mm diameter, this step in the test proposal would turn out completely cost- and time-ineffective. After the tensile test, and the permeability test for the RTD specimens, the specimens will be cut as described in Appendix B and an optical microscope will be used to determine microcrack density.

Regarding the cryogenic experiments it applies that thermal cycling in combination with tensile testing is no option due to cost restraints. Also permeability testing at cryogenic temperatures is no option at NLR at the time of writing. However, as the assigned specimens will get tested on their tensile properties under cryogenic circumstances first, the influence of testing on permeability at RT is limited. Both the cryostat set-up and permeability set-up will be discussed in Chapter 4.

3.1.1. Stiffness non-linear behaviour

It is hypothesized that both the RT tensile test and the cryogenic tensile test will result in a non-linear stress-strain behaviour. This hypothesis is substantiated by a NLR company confidential stress analysis of the HMAE1 wind tunnel model. Although that research was focused on a different deliverable, part of the analysis procedure of the material modelling is valuable for this research. Namely, in determining the stiffness of a GFRP laminate consisting of 0°, ±15° and ±60° plies, the laminate showed some kind of non-linear behaviour, especially in the transverse direction. As the report is confidential, no results can be shared but an indicative figure showing the expected development in stiffness in transverse direction is presented in Figure (3.4).

The non-linear behaviour is potentially caused by the development of mechanically induced matrix cracks in the laminate prior to failure. It is very plausible that the visible kink in the graph is the result of the matrix crack initiation in the 0° and ±15° plies in this example. It is imperative to bear in mind that fibers that are not in the load direction will rotate slightly to the loading direction, which is called

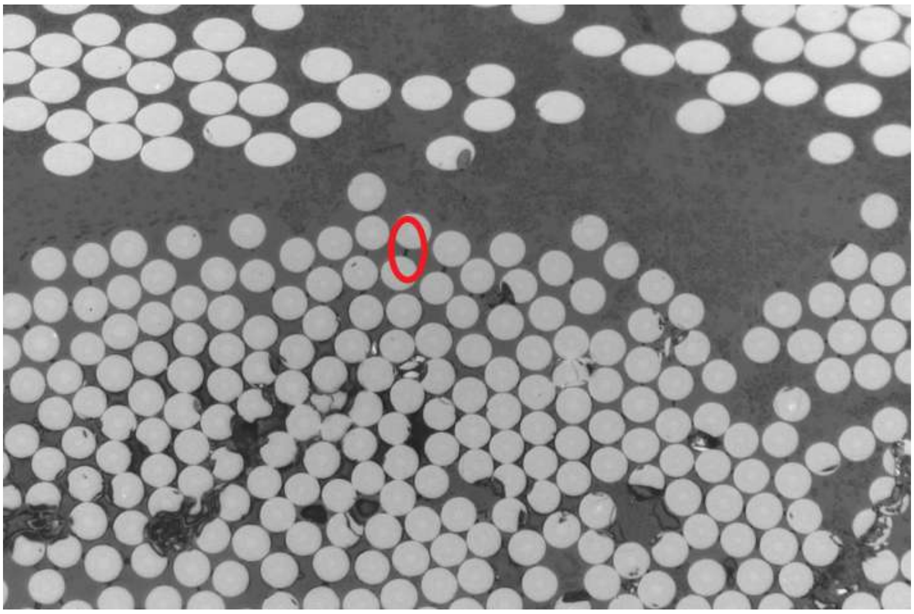

Figure 3.3: Microcrack example on a LM-PAEK test specimen with fibres of 5 micron diameter. The transverse loading and cracking direction combined with the stress concentration points at the fiber-matrix interfaces are explanatory for the propagation of microcracks from fiber to fiber; this sample likely had a good quality of interfacial bonding given the fact that microcrack propagation along the fiber-matrix interface is actually not present.

scissoring, and that this could also be a partial explanation of the kink in this graph. Figure (3.4) tells us that the matrix cracks do have some influence on the stiffness of the laminate, final failure of the laminate is however governed by the strength of the load-carrying fibres. Once these matrix cracks have been created (by loading the material up to a certain strain level) the material behaves linear during subsequent unloading and loading up to the previously attained strain level.

In addition to the strain gauges, the OptimAE Acoustic Emission (AE) sensors that will be used on the RT tensile test have as function to better detect this initiation of non-linear behaviour; in Appendix B this point is referred to as N_{ref}. In the before mentioned stress analysis of the HMAE1 wind tunnel model, visible assessment was an option too due to the laminate being a GFRP. As our laminate is a CFRP, visible assessment is no option and AE sensors are therefore necessary in this test program.

3.1.2. Energy release rate analysis method

The AE test results together with the microscopically determined microcrack density will serve as a prerequisite for an energy analysis method to understand and predict microcracking under a variety of conditions. The energy analysis method that will be used correlates most experimental results, makes use of a microcracking fracture toughness G_{mc}, and is described by Nairn [27]. In short, this method ties together existing experimental results and is based on the underlying principle that when energy released by a fracture event exceeds some critical value, microcracks form. The main objective of the optical microscopy is to determine the number of cracks or microcrack density as a function of applied load.

In this method of analysis, a simplification of the laminate is implemented. As the laminate is predominantly loaded with tensile loads perpendicular to the fibers in the 90° plies, there is focused on microcracking of the 90° plies. The microcracks that form in these plies typically span the entire cross-section of the 90° plies. Thus the potentially three-dimensional problem can be reduced to two dimensions by looking at the edge of the laminate.

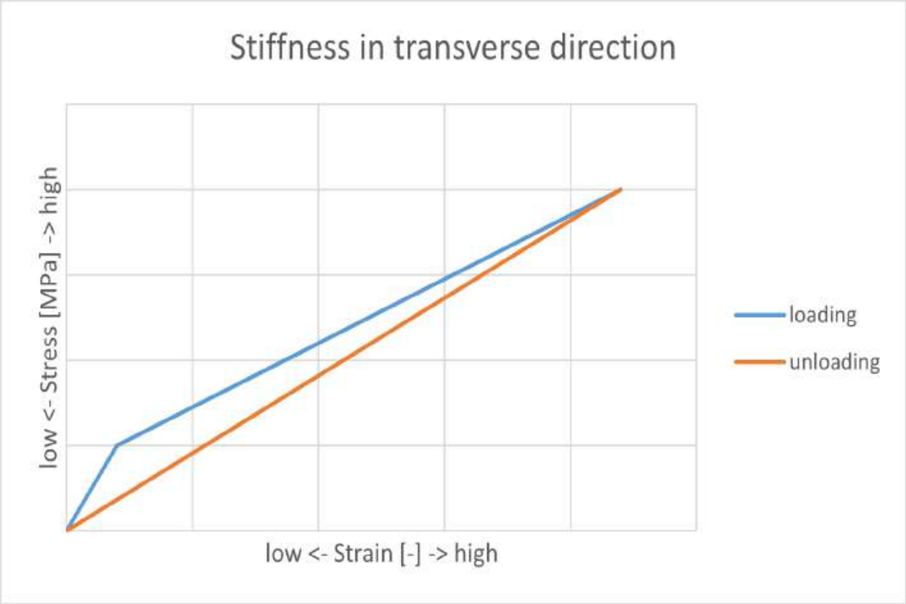

Figure 3.4: Indicative figure of stiffness in transverse direction. Test curve of an initial test laminate (0°, ±15° and ±60° for example) in transverse direction.

The goal of the energy release method is to calculate the total energy released per unit crack area due to the formation of the new microcrack in the unit cell of damage. While the energy release rate is denoted as G_m, the loading conditions can be expressed as both ε_0 (displacement control), or σ_0 (load control). As these experiments are a form of finite fracture mechanics with a finite amount of new crack area, G_m is dependent on the loading method. In this case, displacement control will be applied as the test program only consists of static tests (and no fatigue tests for example). G_m for displacement control conditions is given by Equation (3.1) as described by Nairn. [27] An important assumption to keep in mind is that this method is actually designed for microcracking in the the 90° plies in $[(S)/90]_s$ laminates, where (S) is any set of supporting plies.

$$G_m = -\frac{1}{2}ARB*\left(\frac{\sigma^0_{xx,1}}{E_{xx,1}}\right)^2 [E_A(AR/2) - E_A(AR)] \tag{3.1}$$

$$\text{where} \quad E_A(AR) = E_{A0} - \frac{E^2_{xx,1}\langle\delta(AR)\rangle}{\sigma^0_{xx,1}ARB*} \tag{3.2}$$

Where:
$\sigma^0_{xx,1}$ is the initial stress in the 90◦ plies at the location of the microcrack before any microcracks form in [MPa];
E_{A0} is the effective axial modulus in the absence of microcracks in [MPa];
$E_{xx,1}$ is the x-direction modulus of the 90° plies in [MPa];
$B* = 2h$ is the thickness of the laminate in [mm];
$AR = a/t_1$ is the aspect ratio of the microcracking interval.
$\langle\delta(AR)\rangle$ is the average COD for a microcrack in a unit cell of damage of aspect ratio AR in [mm].

$\sigma^0_{xx,1}$, $E_{xx,1}$, AR and $\langle\delta(AR)\rangle$ will eminently follow from the experiments as described in Appendix B. Equations (3.1) and (3.2) can be used to predict the formation of microcracks for a variety of $[(S)/90]_s$ laminates and for experiments under different loading conditions. In that line of reasoning, $G_{unit}(\rho)$ is the energy release for the formation of new microcracks in a unit cell (the next microcrack) when there is unit stress in the 90° plies and can be written as follows.

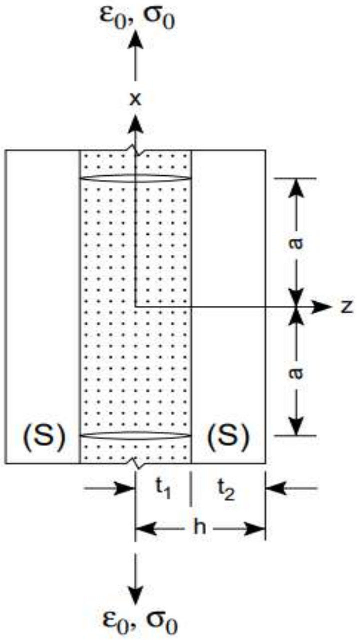

Figure 3.5: A unit cell of damage for microcracking in $[(S)/90_n]_s$ laminates. Taken from Nairn. [27]

$$G_m = (\sigma^0_{xx,1})^2 G_{unit}(\rho) \tag{3.3}$$

To predict microcracking in this method, G_m is equated to G_{mc} (the microcracking fracture toughness) and the following resulting equation, Equation (3.4), is solved for applied stress. This Equation gives the stress as a function of crack density, $D = 1/(2t_1\rho)$. When this result is inverted, crack density can be predicted as a function of applied load.

$$\sigma_0 = \frac{1}{k_{m,1}}\sqrt{\frac{G_m}{G_{unit}(\rho)}} - \frac{k_{th,1}}{k_{m,1}}\Delta T \tag{3.4}$$

Where:
$k_{m,1}$ is the mechanical stiffness for the 90° plies;
$k_{th,1}$ is the thermal stiffness for the 90° plies;
$\Delta T = T_s - T_0$ is the difference between the specimen temperature, T_s, and the stress-free temperature, T_0, in [K].

3.2. XFEM-SCZM model

The FEM-methodology used in this thesis follows the model described by Grogan et al. [12] and is based on a combined extended finite element method (XFEM) for microcrack initiation and propagation and a surface cohesive zone model (SCZM) for delamination. Conventional FEM requires a mesh that conforms to the geometry of the crack, which means that a crack is modelled along the edge or surface of the element. Besides, the mesh needs to be constantly updated to adapt to crack growth. XFEM extends the regular FEM in the fact that discontinuities are introduced in the element and thereby eliminating mesh conformity. By adding extra degrees of freedom in the element, a local enrichment function is created in the element. This is also called partition of unity method (PUM).

With more severe loadings, delaminations may develop, which in the end can be the connecting factor between microcracks in creating leak paths. As a delamination is an inter-ply failure mode, XFEM cannot be used solely here; this is also because XFEM is limited to one crack surface per element. The solution that is used is SCZM methodology, this method uses (additional) predefined delamination surfaces and in that way makes interaction between adjacent plies and and cracks possible. The way this is implemented in the model is by using zero-thickness cohesive elements in between the existing mesh elements, see Figure (3.6). Without further distorting the mesh under influence of XFEM, this SCZM method makes it possible to also have delamination surfaces in the mesh additional to microcrack surfaces inside the elements of the mesh. To illustrate the advantage the combination of XFEM and SCZM has considering the level of mesh refinement, Figure (3.7) shows a comparison between pure XFEM and the combined XFEM-SCZM.

The final source code of my XFEM-SCZM model can be found in Appendix A. The initial code is created by Singh Brar [34]. During this thesis, the code is expanded and made suitable for our thin ply, LM-PAEK material, with all constants already filled in.

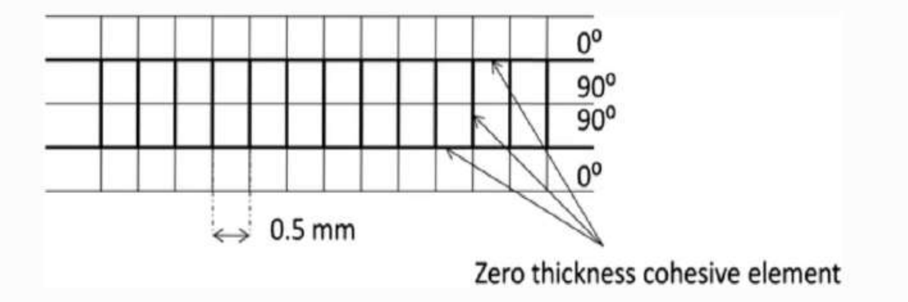

Figure 3.6: Representation of zero-thickness cohesive element inserted in transverse ply 90° and between the interface 0°/90°

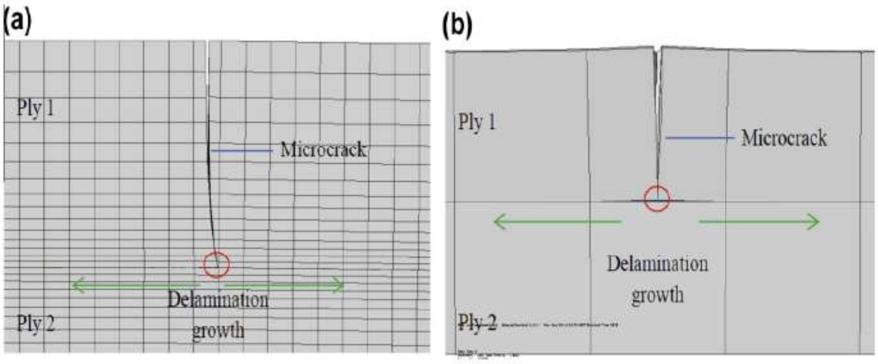

Figure 3.7: Mesh refinement comparison between pure XFEM (a) and XFEM-SCZM approach (b). Taken from Grogan et al [12]

Abaqus is chosen as the software to create the model because Abaqus provides the option to use Python scripting; python is therefore used to create the input file for the analysis. Within the meso-scale model, the section that is used for the finite element analysis is 10 x 10 mm with ply thicknesses dependent on the different testcases, but maximized at a total laminate thickness of 2.38 mm. The radius of curvature of the section is considered to be infinite (section is planar), because the radius of curvature of composite pressure vessels is significantly greater than the meso-scale model and therefore valid to do so. Next to that, the model focuses on the influence ply stacking and ply thickness have on microcracking and permeability; to accomplish this, it is assumed that each ply is homogeneous and anisotropic.

The material properties used in the model consist of elastic properties, temperature dependent conductivity, temperature independent CTE and specific heat amongst others. A temperature independent

CTE is chosen because for TC1225 the CTE is never measured to behave as temperature dependent below its T_g which is at 420 K. The model is therefore also only suitable when operated below the T_g of TC1225. Additionally, the CTE in fiber direction is negligible compared to the transverse and thickness direction which, in turn, is favourable for our homogeneous model, also refer to Figure 3.8.

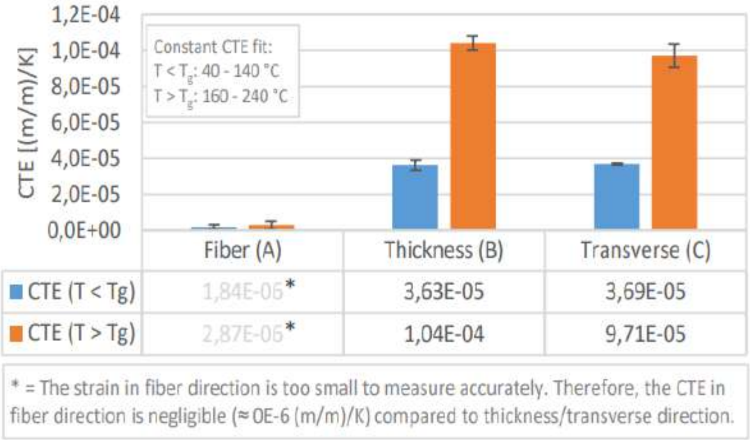

	Fiber (A)	Thickness (B)	Transverse (C)
🟦 CTE (T < Tg)	1,84E-06*	3,63E-05	3,69E-05
🟧 CTE (T > Tg)	2,87E-06*	1,04E-04	9,71E-05

* = The strain in fiber direction is too small to measure accurately. Therefore, the CTE in fiber direction is negligible (≈ 0E-6 (m/m)/K) compared to thickness/transverse direction.

Figure 3.8: Coefficient of Thermal Expansion (CTE) of TC1225. Taken from Toray processing guidelines. [41]

Simulating random microcrack initiation can be done by: 1) continuous probability Weibull distribution, 2) general elements representation of defects whereby voids are represented via reduced element stiffness throughout the finite element mesh. [12] Following the comparison study between these two methods performed by Singh Brar [34], a Weibull distribution is used to model a random distribution of fracture strengths and therefore a random occurrence of microcracks dependent on the applied load(s). Without random distribution, it would mean that all elements will fail at the same time and thus no crack density can be calculated. Crack density is preconditionary in calculating permeability later on in the model. The continuous Weibull distribution is given by Equation (3.5) for a given load σ. In the Equation, σ_{th} is the threshold stress below which failure does not occur, σ_0 is the normalised material strength and m is the Weibull parameter or also Weibull modulus. [12]

$$F(\sigma) = 1 - exp\left[-\left(\frac{\sigma - \sigma_{th}}{\sigma_0}\right)^m\right] \tag{3.5}$$

The Weibull parameter determines the shape of the strength distribution. Besides, the element strength is dictated by the transverse tensile matrix strength considering the cryogenic tank purpose; from the TC1225 datasheet σ_0 can be valued at 86 MPa. The Weibull parameter is set on the default value of 12, taken from literature. The random Weibull distributed element strength of TC1225 against the element number are presented in Figure (3.9), the figure is created using the Python command *'random.weibullvariate()'*.

A positive side effect of using a Weibull distribution is that the effect of mesh density on the number of elements below the mean fracture strength is shown to be invariant, within the bounds of normal statistical scatter, for element volumes below 0.01 mm^3. This volume corresponds to at least 10000 elements needed in the FE element mesh according to Grogan et al. [12] In other words this means that the number of low-strength elements remains constant for high mesh densities; Grogan confirmed this with a sensitivity study. While modifying the XFEM-SCZM model of Singh Brar [34] I therefore chose to use 40 elements in x- and y-direction and 1 element in z-direction per ply, meaning lay-ups of at least 7 plies are required for this model when mesh density should be out of influence.

Furthermore, voids, but also resin rich areas, can be represented as ellipsoids within an element volume. A possibility is created to implement these in the model by using their mean sizes and accompanying

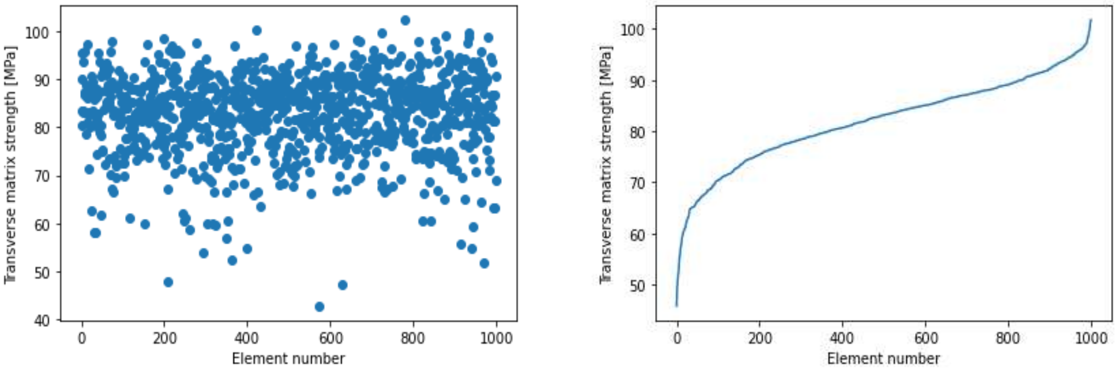

(a) Unsorted Weibull distribution

(b) Sorted Weibull distribution

Figure 3.9: Transverse matrix strength Weibull distribution for TC1225 for 1000 elements, σ_0 = 86 MPa and m = 12.

deviation on all three axis (following from e.g. a micro-CT scan) in combination with Equation (2.19). In practice however, it appeared that due to the random distribution of fracture strength from the Weibull parameter, implementing additional voids and resin rich areas had no significant effect. Considering that the effect of voids is to degrade various material properties and that this effect is already intrinsically included in the Weibull distribution, this is not worrisome. The void ratio is included however, because this is necessary as input for modelling permeability; the void ratio can follow from e.g. C-scan or micro-CT scan.

A hexagonal cell type is used while formulating the input values, as this is also suggested by Choi after empirical comparison. [7] The hexagonal unit cell is a better model for the micromechanics model to satisfy the transverse isotropy and can be considered as more realistic for fiber-reinforced composites. The type of cell used has an effect on the closest separation possible between two fibre centres and therefore the fibre volume fraction. For this reason, Equations (2.13), (2.14) and (2.15) are implemented in the model.

Translating this chosen finite volume to finite elements, the element type that is chosen from the Abaqus element library is DC3D8 which is a 8-node linear brick mass diffusion element. This element type is chosen because this is also used in linear steady-state mass diffusion analysis which solves Fick's law. [9] Another option was to use the C3D8, which is a 8-node linear brick stress/displacement element; however, for a coupled temperature-displacement analysis, this is less favourable.

In order to implement permeability as initial property in the XFEM model, six values of the fully saturated permeability, also called the hydraulic conductivity, ($\kappa_{11}, \kappa_{12}, \kappa_{22}, \kappa_{13}, \kappa_{23}, \kappa_{33}$) and the specific weight of the wetting liquid are included. The wetting liquid in this case is gaseous hydrogen at 293 K and 1 bara, which has the value of 811.95 N/m^3. [39] As the problem concerns low flow velocities, Darcy's law can be used in Abaqus instead of Forchheimer's law and therefore also the unknown velocity dependent term in Forchheimer's law can be omitted. [37] As hydraulic conductivity the ultimate k_{perm} for LM-PAEK of 1.07$\times 10^{-16}$ is taken divided by the total thickness of the laminate; this value is already retrieved from the thin ply permeability experiments performed later on in this thesis.

Of the six CTE coefficients, α_{11} = 0 (refer to datasheet TC1225), α_{22} and α_{33} are taken from the datasheet and have the values of 3.63×10^{-5} and 3.69×10^{-5} $(m/m)/K$ respectively. α_{12}, α_{13} and α_{23} are set at 0 because the material can be considered orthotropic and therefore thermal shearing coefficients are zero.

To define when a crack initiates, Grogan [13] makes use of the Hashin failure criteria for matrix failure for both tensile failure criterion (f_t) and compressive failure criterion (f_c).

For tensile matrix failure ($\sigma_{22} + \sigma_{33} > 0$), $f_t \geq 1 =$ failure

$$f_t = \frac{(\sigma_{22} + \sigma_{33})^2}{{Y_T}^2} + \frac{\sigma_{23}^2 - \sigma_{22}\sigma_{33}}{{S_{23}}^2} + \frac{\sigma_{12}^2 + \sigma_{13}^2}{{S_{12}}^2} \tag{3.6}$$

For compressive matrix failure ($\sigma_{22} + \sigma_{33} < 0$), $f_c \geq 1 =$ failure

$$f_c = \left[\left(\frac{Y_c}{2S_{23}}\right)^2 - 1\right]\left(\frac{\sigma_{22} + \sigma_{33}}{Y_c}\right) + \frac{(\sigma_{22} + \sigma_{33})^2}{4{S_{23}}^2} + \frac{\sigma_{23}^2 - \sigma_{22}\sigma_{33}}{{S_{23}}^2} + \frac{\sigma_{12}^2 + \sigma_{13}^2}{{S_{12}}^2} \tag{3.7}$$

Abaqus offers two different options for implementing permeability as a material property; with permeability is in this case referred to as the relationship between the volumetric flow rate per unit area of a particular wetting liquid through a porous medium and the gradient of the effective fluid pressure. In Abaqus this can be done by either Forchheimer's law or by Darcy's law. They differ in the use of a velocity dependent term which is present in Forchheimer's law but isn't in Darcy's law, that is because Forchheimer's law approximates Darcy's law as the fluid flow velocity reduces. To determine when to select which of the two, the Knudsen number is used as defined by Equation (2.4). Following the theory as described in chapter 2, Darcy's law will be applied when $K_n < 0.001$ and Forchheimer's law will be applied when $K_n > 0.001$. A result from the code is already given by Figure (3.10) in which the Knudsen number is plotted for different fibre diameters.

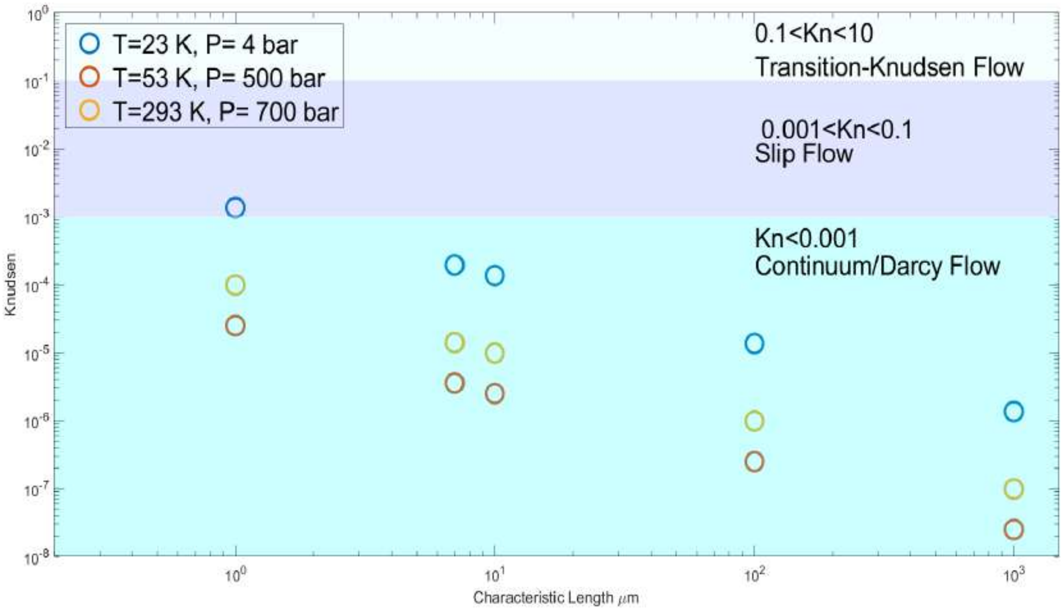

Figure 3.10: Knudsen number under three different conditions for 5 different fibre diameters in LM-PAEK. The fibre diameter of 7 μm is characteristic for TC1225

Subsequently, the right step has to be defined which makes it possible to incorporate both mechanical as thermal loads. A coupled thermal-stress analysis is needed because the stress analysis is dependent on the temperature distribution and vice versa. Abaqus offers a standard step for this, the *coupled temp-displacement step*, but it is known from literature that Abaqus cannot calculate crack initiation using XFEM for this step. The solution that is used is to define the temperature as a predefined field of a general static step, incorporating both the heat flux and convection boundary conditions. In this way the static analysis can be performed under a one-time cooling. Thermal cycling is thus not suited for this approach, but this shouldn't be a problem as for the experimental part in the cryostat thermal cycling is also out of scope.

As one of the last steps in the model, the XFEM regions have to be assigned. As stated before, in XFEM a local enrichment is created in the element. The enriched zones are constructed as lines parallel on the mesh in the 90 degree direction; the elements contained by these lines have degradation properties. For plies with fibres in another direction than 90, the lines are rotated by means of a linear Equation so that the lines always match the fiber direction and the distance between the lines remains the same. This distance, *d*, is set at a default value of 0.5 mm [34] and dictates the number of cracks i.e. crack density of the model. This can be explained because per enriched region, only one crack can form and this crack can only grow in between its own enriched region. Therefore, *d* is also the average spacing between a matrix crack. This is however a value that should preferably be checked experimentally.

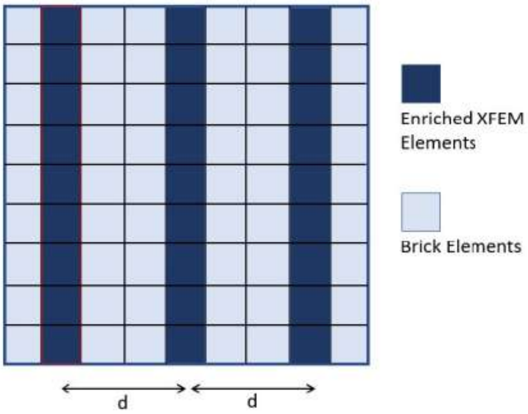

Figure 3.11: 90 ° XFEM enrichment mesh generation. Taken from Brar. [34]

As the last step of the XFEM-SCZM model, permeability calculations are carried out. This part of the code is built around Equation (3.8), an expression for material permeability β_0 for an N-ply composite laminate, and makes use of non-experimentally determined variables. Instead, the values of necessary key damage characteristics follow from the Abaqus .odb file generated by the previously described part of the code.

$$\beta_0 = G\left[\sum_{K=1}^{N}\left(\frac{\sin\theta}{CD_K CD_{K+1} DCOD_K DCOD_{K+1}}\right)\right]^{-1} \tag{3.8}$$

Where:
G is the material conductance in [$scc/s - cm^2$];
θ is the ply angle;
CD_K and CD_{K+1} are the crack densities of adjacent plies;
$DCOD_K$ and $DCOD_{K+1}$ are the delaminated crack opening displacements of adjacent plies in [mm].

In this model, the value for C is predefined at 3119.52 $scc/s - cm^2$ according to Grogan [12] and the ply angle is $60°$ for any set of adjacent plies. The crack densities and the DCOD's will follow from the FEM-model by incorporating the following steps.

1. Read nodal connectivity from mesh.
2. Read x, y, z nodal displacements from output database.
3. Cross reference connectivity with cracked XFEM elements.
4. DCOD calculation based on relative x, y, z displacements of adjacent nodes in crack elements.
5. Calculation of crack-overlap area for individual crack networks.
6. Sum over the entire laminate and calculate permeability. [12]

The complete implementation of the described XFEM-SZCM method can be found in the code displayed in Appendix A.

4

Experimental set-up

In this research, the sensitivity of microcracks in LM-PAEK will be investigated as a crucial aspect of understanding its mechanical behavior. The study aims to comprehensively examine the response of LM-PAEK to different loading conditions and temperatures, particularly focusing on its performance regarding microcrack initiation and propagation. To achieve this objective, the material will be subjected to static testing at various load levels under RT conditions and at 20 K. Additionally, permeability testing will be conducted on the RT specimens to assess their permeation characteristics in relation to the different loadings executed before. Furthermore, all specimens will undergo thorough cross-sectional analysis to evaluate the microcracks characteristics. By systematically analyzing these parameters, this study endeavors to provide valuable insights into the microstructural integrity and mechanical properties of LM-PAEK.

This chapter gives an overview of the main equipment used during the experimental phase of this thesis, how they're combined in the test set-up and how they are operated. All of the mentioned equipment originates from the testplan that is displayed in Appendix B.

4.1. Instron 5989 tensile tester

The tensile test bench that is used for the RT tensile tests is the Instron 5989, with a maximum loading capacity of 600 kN. This tester is a heavy-duty dual column floor model of 313x159x96 cm and 2516 kg, makes use of *Bluehill3* software and is shown in Figure (4.1). The room temperature and humidity are measured at the start with a calibrated rotronic hygrometer (A1-(C94/Pt100)) and should have values of 21 $^\circ C$ ± 3 $^\circ C$ and between 40% and 60%, respectively. All specimens were loaded with a constant cross head displacement of 0.5 mm/min. Besides, every tested specimen was equipped with two strain gauges and 2 AE sensors as standard; both of these are described below. Bluehill3 is used as software for analysis of the strain gauge results.

4.1.1. Y series strain gauges

Two standard foil strain gauges per specimen for the uniaxial stress state will be used. As there is dealt with a near homogeneous strain field and a normal temperature range, Y series linear gauges from HBK are being used. HBK also offers M- and C-series gauges for more extreme temperature ranges, but as these tests will all be performed at RT, Y series strain gauges are the right choice. The centers of the gages are located at 165 mm length and 40 and 70 mm width.

The strain gauges used are the HBK 1-LY66-6/350 (LY linear strain gauges with 1 measuring grid for composite). This strain gauge has a resistance of $R = 350\Omega \pm 0.35$%, a gage factor of $k = 2.34 \pm 1.0$% and a temperature coefficient of $\alpha = 10.8[10^{-6}/K]$.

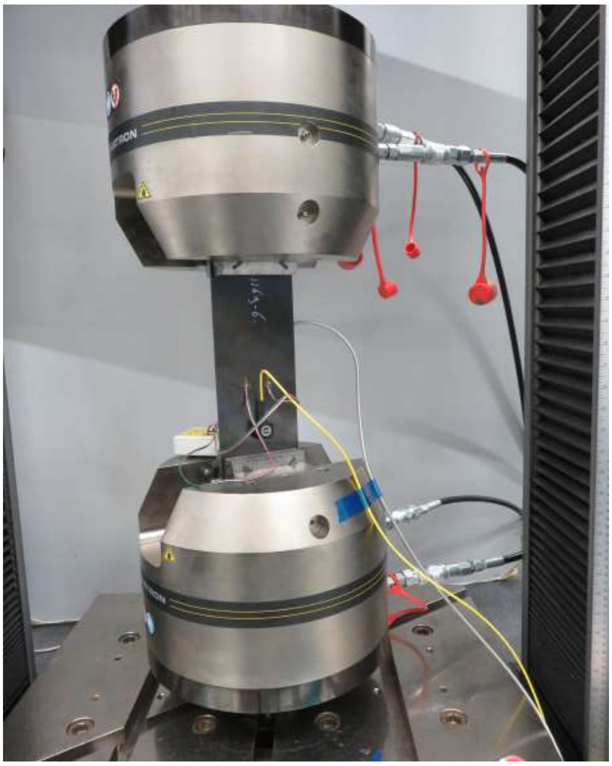

Figure 4.1: RT tensile test set-up consisting of the Instron 5989, AE sensors, strain gauges and one of the specimens

4.1.2. OptimAE

The AE measuring system that is used in order to determine initiation of damage, is OptimAE from *Optics11*. With combining the benefits of fiber optic sensing and state-of-the-art electric systems, OptimAE makes itself suitable for AE measurements in special conditions, ranging from extreme temperatures, high voltages, and radiation, to explosive hazardous areas. Unlike what is described in Appendix B, two different AE sensors are attached to the specimen, one at each side of the specimen approximately 3 cm below the strain gauges. The 6300-NC-045 sensor is placed on the frontside of the specimen (visible in Figure (4.1) attached to the yellow cable) and the 6300-1S-SST sensor is placed on the backside of the specimen. The latter one has previously been used as the standard sensor at NLR, but due to suspicions of recording too much noise, the 6300-NC-045 is also incorporated in this series of testing.

4.2. Cryostat

The cryostat employed in the experimentation is a bespoke apparatus designed exclusively for NLR by one of its industrial partners. Due to competitive considerations, specific details are not disclosed. This tailored configuration is implemented to facilitate precise temperature control within the cryostat, particularly at a designated temperature of 20K. In contrast to cryostats intended for broader user applications, which commonly utilize liquid helium immersion at 4K, the described cryostat employs a distinctive cooling approach. It employs liquid nitrogen for cooling until reaching 77K (the liquefaction temperature of nitrogen) and subsequently employs liquid helium to further cool the system to 20K, employing two distinct cooling techniques. Consequently, it can be ascertained that this cryostat is purposefully engineered for these specific testing scenarios, as operations at 4K are deemed excessively cold.

Furthermore, the cryostat serves a dual role as a vacuum chamber, utilizing a vacuum pump to mitigate heat leakage. The associated tensile tester is identified as an Instron 5900(R), characterized as a static tensile testing device with a maximal loading capacity of 100 kN. However, it is pertinent to note that the grips currently employed in conjunction with the apparatus possess a maximum loading capacity of approximately 50 kN. Bluehill3 is used as software for analysis of the strain gauge results.

One strain gauge per specimen (0°/90° T rosette) was used, but primarily only the uniaxial stress state (0° strain) will be looked at. As there is dealt with a near homogeneous strain field but at extreme temperatures, C series linear gauges are being used. The C series strain gauges of HBK are the low-cost specialists for temperatures up to $4K$ and $523K$. The center of the gage is located at 125 mm length and 15 mm width.

The strain gauges used are the HBK 1-XC11-3/350 (C series SG with 2 measuring grids, 0°/90° T rosette). This strain gauge also has a resistance of $R = 350\Omega \pm 0.35$%, a gage factor of $k = 2.34 \pm 1.0$% and a temperature coefficient of $\alpha = 10.8[10^{-6}/K]$.

4.3. Permeability set-up

The permeability test set-up and method of operation are described in Appendix B. The leak detector that is used is a PhoeniXL. Unfortunately, due to delay in delivery of materials at the time of writing, all permeability tests are conducted using helium instead of hydrogen.

4.4. Optical microscope

The optical microscope that is used for microcrack detection and microcrack characterization is a *Axioplan 2*, produced by Zeiss, the typical magnification that is used is 100x. The software used for analysis is *Axiovision 4.8*, also from Zeiss. Lastly, the digital camera used for imaging is the *Axicam* from Zeiss.

4.5. Python scripting in Abaqus

Abaqus provides an option to create a model using Python scripting, this is used in creating the XFEM-SCZM model. Python scripting in Abaqus refers to the capability of using Python to automate, customize, or extend the functionalities of Abaqus. This integration allows users to harness the power of Python to manipulate models, manage simulations, extract and process data, and create custom workflows within the Abaqus environment. To execute Python scripts within the Abaqus environment, the software provides an interface where users can input and run their scripts. Additionally, Abaqus offers a Python scripting interface that exposes a set of API's (Application Programming Interfaces) and modules specifically designed for interacting with Abaqus functionalities. It is therefore required to have a good understanding of the Abaqus modelling architecture.

5

Experimental results and model validation

5.1. Basic FEM model

Regrettably, due to unforeseen time constraints and the exigencies of the research timeline, it became impractical to conduct the anticipated testing phase for the FEM model within the scope of the allotted timeframe. The complex nature of the model, coupled with the intricacies involved in the testing process, demanded a more comprehensive and time-intensive approach than initially estimated. A recap on the model as well as the specifications the consortium sets that should be adhered to, are presented in chapter 6.

5.2. Experimental results

This chapter serves as the empirical cornerstone of this thesis, offering a comprehensive first analysis and presentation of the outcomes derived from the conducted experiments. Through a systematic exploration of the empirical findings, this section aims to illuminate the implications, trends, and correlations inherent in the data set, thereby contributing to a nuanced understanding of the research questions posed. The relevance of these results however, together with their link to theory, will be elaborated in chapter 6.

5.2.1. RT tensile test

The following conversion table (5.1) considering specimen numbering is used in the execution of this test. The first row of numbers originates from the test proposal in appendix B. Due to NLR practical considerations, the specimens are also indicated as shown on the second row. The actual applied loads during the two days of testing are also displayed. Some samples have been retested, the reason why is explained below. The maximum strain levels are also displayed, an analogous buildup similar to the load increase can be distinguished.

Specimen 10793-5 was the first to be subjected to the RT tensile test. The specimen failed around 140 kN due to grip-induced (slippage) failure. The first AE events were already measured at the load initiation, visible in Figure (5.1). This might be against the expectation, however, the amount of measured events is still very limited during the first seconds. With a total of 380 measured events during the first 15 seconds, and considering every event is a microcrack, this leads to a crack density of 0.0138 crack per mm^2. It is assumed that this does not effect permeability significantly.

A visible change in the graph that was expected to indicate microcrack initiation did not emerge clearly. In order to determine N_{ref}, the measured event count gives an interesting graph. From t=37.7 seconds one regularly sees a period with an event rate that is above 10 for a longer period of time and then drops back again. At that moment the load is 12.9 kN and the total amount of events 2236 (what would mean

Specimen nr. appendix B	Specimen nr. NLR	Ply thickness	Max. load 3-10-2023 [kN]	Max. load 6-12-2023 [kN]	Max. strain [μsn]
1	10793-4	Regular	N/A	N/A	N/A
2	10793-5	Regular	140.0	N/A	10931.32
3	10793-6	Regular	15.0	37.5 (N_{ref})	2948.77
4	11107-4	Regular	20.0	50.0 (N_{ref} + 33%)	3990.27
5	11107-5	Regular	25.0	62.5 (N_{ref} + 67%)	4995.89
6	11107-6	Regular	30.0	N/A	-
13	11169-4	Thin	N/A	N/A	N/A
14	11169-5	Thin	140.0	N/A	11530.16
15	11169-6	Thin	N/A	41.25 (N_{ref})	3452.67
16	11170-4	Thin	N/A	72.19 (N_{ref} + 75%)	5712.17
17	11170-5	Thin	N/A	51.56 (N_{ref} + 25%)	4225.37
18	11170-6	Thin	N/A	61.88 (N_{ref} + 50%)	5010.78

Table 5.1: Specimen numbering conversion table TEP specimens

a microcrack density of 8.1 cracks per mm^2).

A similar area of interest can be derived from the intensity graph: the intensity only seems to increase significantly above 15 kN. Based on these two graphs, there is chosen for an N_{ref} of 15 kN. Additionally, due to the lack of a clearly visible changing trend, the percentage step size is also increased from 5%, 10% and 15% to 33%, 67% and 100% for specimens 11107-4, -5 and -6 respectively. Afterwards, a 110x110 mm cut out off specimen 11107-6, which was thus subjected to a load of 30 kN, was made and directly imported in the permeability set-up; these first results are discussed in section 5.2.3.

Worth mentioning is that a load of 15 kN (approximately 57,3 MPa) should already be sufficient for proper operation of the tank NLR and the consortium strive for. The tank is namely dimensioned for four different maximum pressures with a coupled maximum microstrain, based on the working pressure of 5 bar and 1500 μsn. Consequently, the safety valves operate at 1.33 times the working pressure, or 6.67 bar. From there the burst pressure is strived for to be 1.5 times the safety valve pressure, or 10 bar. The proof pressure finally (the maximum pressure that can be applied without changing the performance within the specifications) is 1.5 times the working pressure, equal to 7.5 bar and 2250 μsn. Using these strain levels, it can be calculated that the tank is dimensioned for a maximum stress of 54 MPa at burst pressure at RT. As the working pressure is only halve of the burst pressure, this results in a stress of only approximately 27 MPa.

When compared to the permeability and strain results, the idea arose that the first N_{ref} value of 15 kN was too low and therefore not accurate enough for the regular ply thickness TEP specimens. For specimen 10793-5 the modulus is calculated in two different ways; the first one being stress divided by strain for every single generated datapoint from the strain gauges. The average strain is thereby calculated as the mean of the the two strain gauges, as the data showed that these did not differ significantly for the complete data range. Furthermore, the load application was paused multiple times above 70 kN, this has a direct effect on the results as a kind of elastic behaviour can be seen above 70 kN, refer to Figure (5.2).

The linear stress-strain relation result of this specimen leads to a smooth flattening modulus gradient from 0 to 70 kN. This trend changes when the modulus is not calculated for every datapoint separately. The second method namely, calculates the modulus for a databracket of 30 datapoints for each to highlight the actual progression more clearly. With this method, a clear kink is visible after when the modulus starts to decrease again. This result could indicate sudden damage in the material i.e. a possible clue for microcrack initiation. The moment the modulus starts decreasing is at an approximate load of 37,5 kN and an approximate strain of 2900 microstrain; based on this result, 37,5 kN is chosen as the adjusted N_{ref} for the regular thickness TEP specimens.

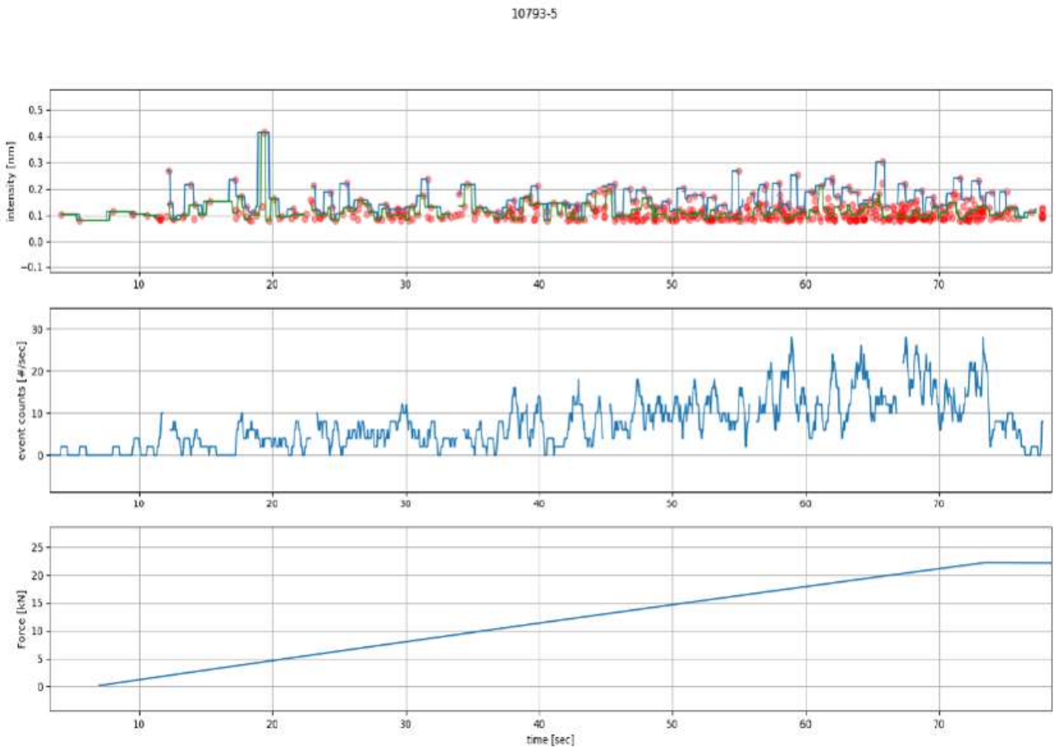

Figure 5.1: Directly observed AE events in specimen 10793-5 from 0 kN to ∼30 kN during RT tensile test

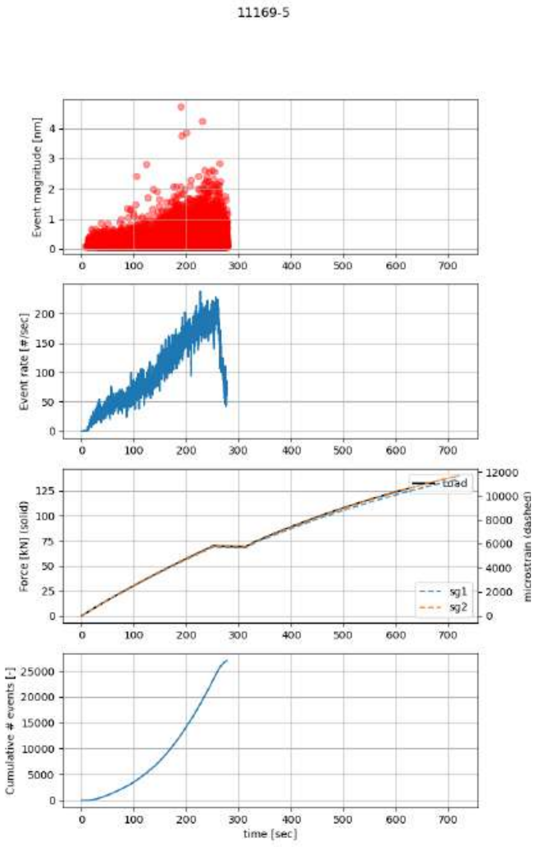

Figure 5.3: Directly observed AE events in specimen 11169-5 from 0 kN to ∼140 kN during RT tensile test

An analogous path has been followed for specimen 11169-5. The load application was maximized at 140 kN instead of failure, as N_{ref} for this material would most certainly be below 140 kN. Next to that, the AE sensors were removed at a load of 70 kN to protect the sensors. Similar to specimen 10793-5, this specimen also showed slippage in the grips, however in a much less significant amount than the 10793-5 as it appeared visually.

The strain gauge and AE results of specimen 11169-5 are shown in Figures (5.4) and (5.3). In particular, Figure (5.4) illustrates that the signal type indicates a deviation from the measured signal; there is (excessive) noise present in the signal. Furthermore, no extremely clear kink point is visible on the strain gauge graph, as is the case with the 10793-5 graph, for example. In a more zoomed view, two significant drops in stiffness appear in the strain gauge results after which the stiffness gradually increases again. This is firstly the case between 26 and 27 kN and secondly the case between 39 and 41 kN. In addition to that, a small kink in the AE event rate graph is visible at approximately 140 seconds what relates to a load of approximately 41,2 kN; taking into ac-

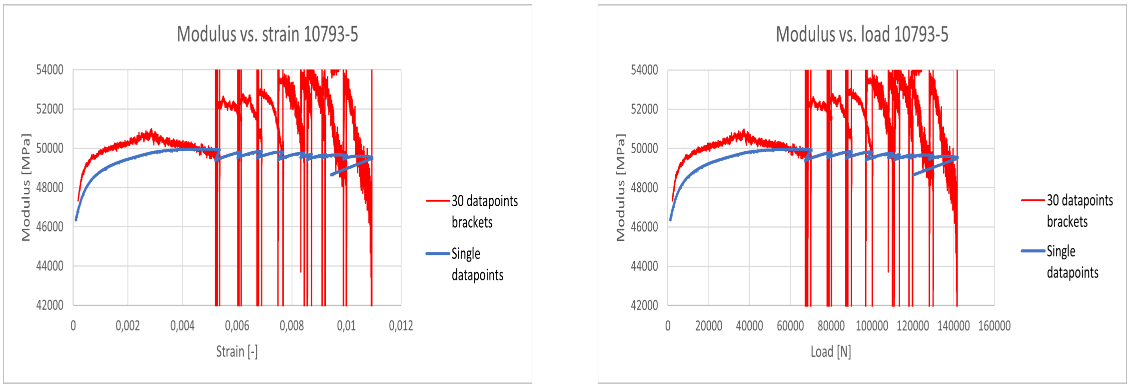

(a) Modulus vs. strain **(b)** Modulus vs. load

Figure 5.2: Strain gauge results specimen 10793-5

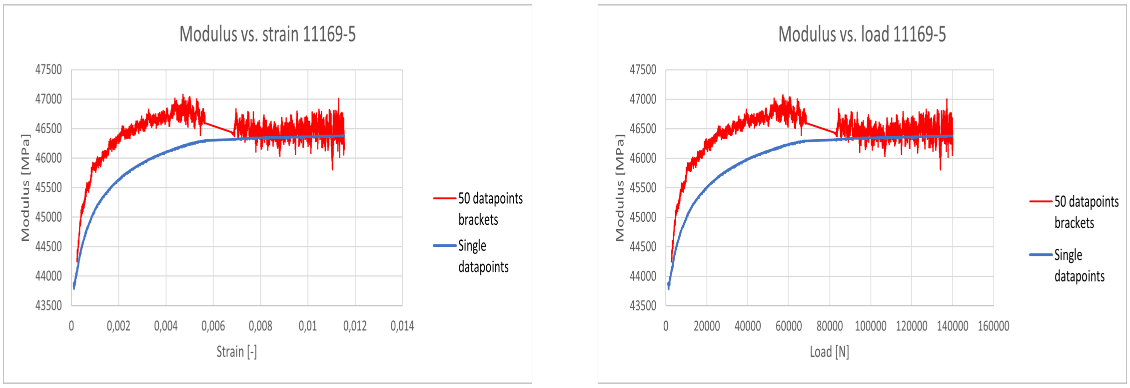

(a) Modulus vs. strain **(b)** Modulus vs. load

Figure 5.4: Strain gauge results specimen 11169-5

count that a small error in time tracking of the AE results is expected, both strain gauge and AE results seem to line up in determining N_{ref}. Based on this result, 41,25 kN is chosen as the adjusted N_{ref} for the thin ply thickness TEP specimens, 10% higher than N_{ref} for the regular thickness TEP specimens.

To validate N_{ref} for both ply configurations, the strain gauge results of specimens 11107-5 and 11170-4 are also elaborated and assessed. This is done because these specimens were subject to the highest loads and could therefore display results over the broadest range of load. The regular ply thickness specimen (Figure (5.5)) does not seem to show one clear N_{ref} as is the case for 10793-5; instead three significant stiffness drops appear at 30,5 kN, 37,5 kN and 49 kN. The second one seems to align with the stated N_{ref} which is positive for the validation. The other drops can possibly be attributed to the fact that this specimen is reused, the first loading being set at 25 kN. Because more damage has already slipped into the specimen, the extra damage during this test run could be magnified in other regions on the modulus-load graph.

For validation of the thin ply N_{ref} there is looked at specimen 11170-4. Zooming in on the modulus-load graph (Figure (5.6)) both an increase and decrease in stiffness occur. The increase starts right after a small decrease at approximately the same point as the predefined N_{ref}, 41,25 kN. This small decrease could be attributed to the initiation of microcracks, however it's not very convincing. The immediately following increase seems to be more significant, which is against intuition as modulus is expected to decrease when microcracks initiate. Further down the graph, a period of modulus consolidation appears between approximately 45 and 55 kN, this is a more or less comparable result as is seen in specimen 11169-5.

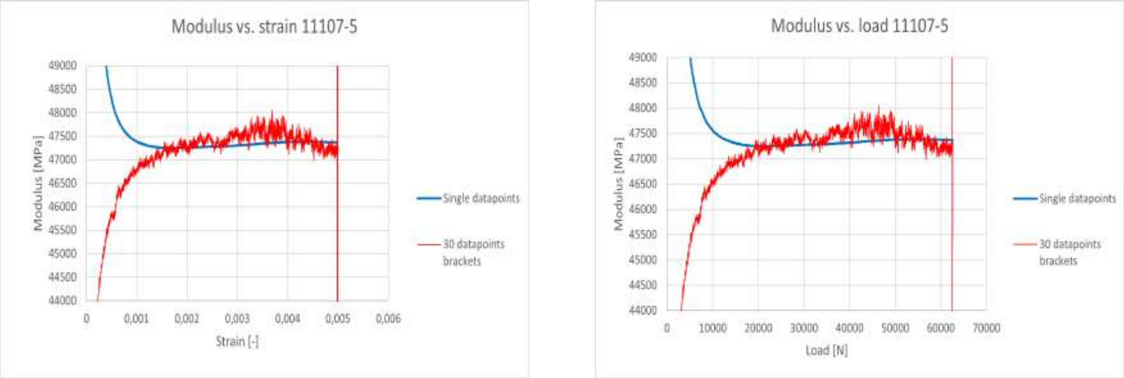

(a) Modulus vs. strain

(b) Modulus vs. load

Figure 5.5: Strain gauge results specimen 11107-5

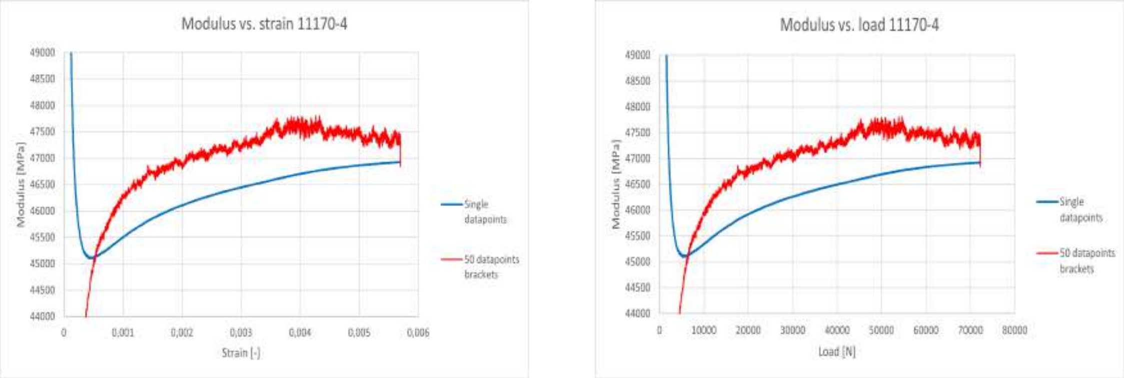

(a) Modulus vs. strain

(b) Modulus vs. load

Figure 5.6: Strain gauge results specimen 11170-4

The additional results coming from the AE sensors are unfortunately not sufficient. During the second day of testing the AE sensors broke down which lead to distorted results. This series of tests consisted of specimens 10793-6, 11107-4, 11107-5, 11169-6, 11170-4, 11170-5 and 11170-6. This lead to an increased noise level and also parts with data loss. These two defect modes are displayed in Figure (5.7), respectively. Due to the defect sensors, it was inevitable to work with (3) different thresholds to deduct the events from the raw signal, namely 0.08 nm, 0.1 nm and 0.195 nm. Because a specimen can only be compared to another specimen with the same specimen, the overall comparison has shrunk significantly.

Overall it can be stated that the thick ply samples generated comparable results with previous measurements on the first day of testing, despite the disturbed signals. The thin ply samples show large scatter in the amount of events in general, however it must be noted that specimen 11169-6 deviates from this. This was the first sample that was tested on the second day of testing; it appears that the AE sensor did not show any deviant behavior at that time. This lead to a significant lower amount of events compared to for example 11169-5, which could also indicate a high level of noise on the first day of testing (when 11169-5 was tested). The large scatter in the amount of events for all thin ply samples can be seen in Figure (5.8).

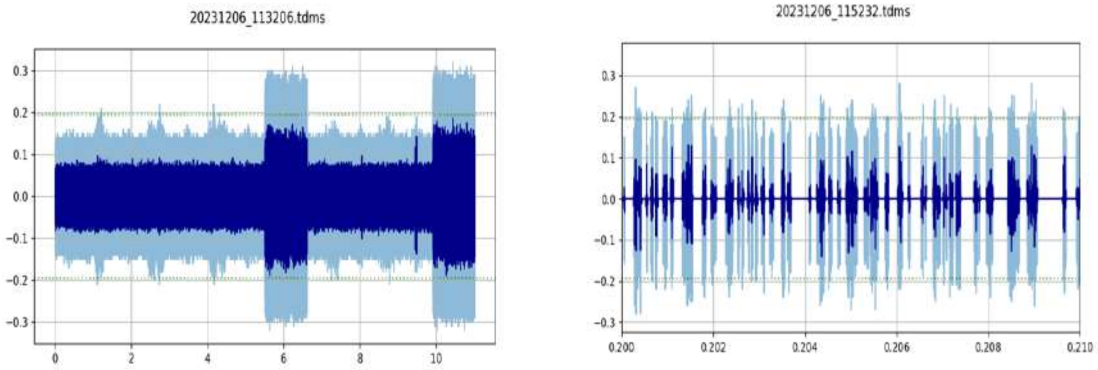

(a) Blocks of increased noise **(b)** Increased noise leading to sections of dataloss

Figure 5.7: Influence of AE sensor defects on sample 11170-4 with signal in [nm] on the y-axis and time in [s] on the x-axis.

Similar to the strain gauge results, also the AE measurements of specimens 11107-5 and 11170-4 are displayed in Figure (5.9) and analyzed. By drawing trendlines through the event rate graph of 11107-5, a kink appears roughly at 39 kN, although this kink is not very convincing which could be due to the broken sensor. It is therefore close to the stated N_{ref} of 37,5 kN. Based on this analysis, the combination of strain gauges and AE sensors seems preconditional to detect (initiation of) damage.

Just like the strain gauge results, also the AE results of the thin ply samples are less convincing compared to the thick ply samples. When trendlines are drawn through the AE event rate graph of 11170-4, a kink appears approximately at 51 kN. This significant deviation of the stated N_{ref} of 41,25 kN, combined with the broken sensor, make that the AE measurements for these thin ply samples are not usable. On the other hand, the lower amount of events in Figure (5.9b) compared to Figure (5.9a) could be indicative for less damage detection in the laminate and therefore favor the use of thin ply materials.

5.2.2. Cryogenic tensile test

The cryogenic tensile tests were carried out different compared to the RT tensile tests. In terms of sensors, only one strain gauge in longitudinal direction is used due to the dimensions of the specimen. Two temperature sensors have been used too, one on the specimen and one on one of the walls of the cryostat. After the sensors and the specimen are installed, the cooldown process starts. A preload of 5 kN for 10793-1 and 11169-2 and a preload of 1.6 kN for all other samples is used during this cooldown, to make sure that shrinkage of the material has minimum effect on the grips. As described in chapter 3, a two-stage cooling is used; during the first stage of cooling a vacuum pump is used to create a pressure of approximately 0,5 bar. During the second stage of the cooling the pressure is again increased to atmosphere, after which the load is lowered again to almost 0 N. When the temperature of 20 K is then reached, the strain gauges are balanced (to get rid of thermal stress of the strain gauge) and the test starts with 0,5 mm/minute. A corrected k-factor for the strain gauge of 2,52 is used due to the cryogenic temperature.

Similar to the RT tensile tests, the applied loads and some specimen numbers deviate slightly in some cases from what is proposed in appendix B, the number conversion table accompanied by the actual executed loads and found strain levels are given below in table (5.2). Unlike the RT tensile test with the TEP specimens, the analogous strain buildup similar to the load increase cannot be distinguished. As it appears, the '-2' samples induce this deviation with their lower strain levels, this can possibly be explained because of their position on the panel during manufacturing. This will be discussed more in paragraph 5.2.4 and chapter 6.

Specimens 10793-2 and 11169-2 were originally designated for loading until failure. However, an op-

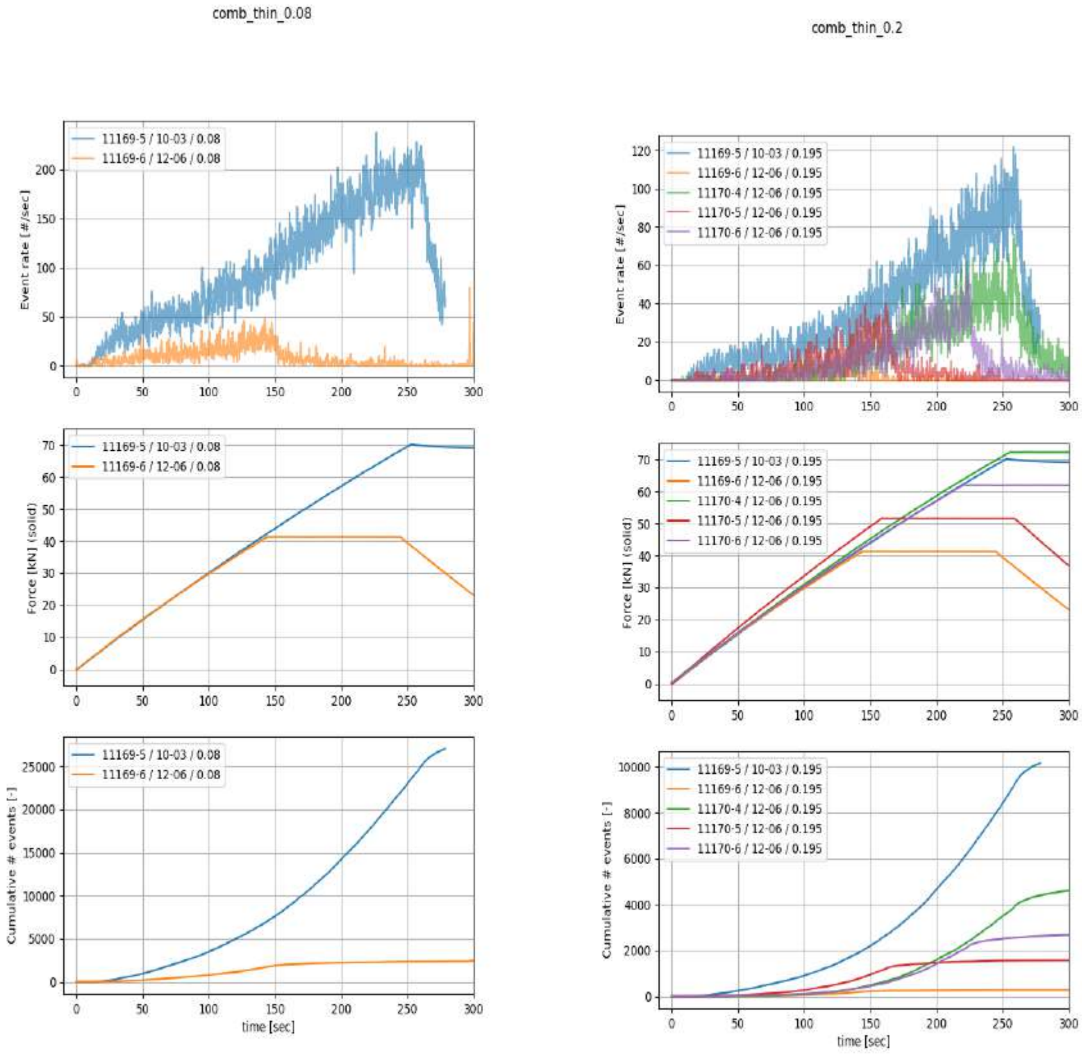

(a) Measurements without increased noise, threshold of 0.08 nm

(b) All thin ply measurements, threshold of 0.195 nm

Figure 5.8: AE results consisting of events, load and cumulative events for the thin ply samples during RT tensile test.

erational error in the testing apparatus resulted in the fracture of specimen 10793-2, necessitating its replacement with specimen 10793-1. Subsequently, challenges arose due to slippage of the specimens from the grips. Following adjustments to the setup and specimen preparation, the loads at which slippage occurred were recorded as 16.10 kN for specimen 10793-1 and 17.82 kN for specimen 11169-2. Although the specimens did not actually fail in the cryogenic test bench and the anticipated failure loads were expected to be higher, these recorded loads at slippage are deemed adequate for conducting the subsequent cryogenic tests, notwithstanding the fact that neither of these two specimens underwent failure.

Taking the thick ply specimen 10793-1 as example, 16,10 kN is deemed adequate for the testprogram after this was compared with the RT tensile test of specimen 10793-5. There is made use of Equation (5.1) and Equation (5.2) [15], where $E(T_2)$ is the calculated modulus for 10793-1 based on 10793-5 and $E(T_1)$ is the maximum modulus of 10793-5. α is the CTE of TC1225 = 3,63$\times 10^{-5}$ (m/m)/K and width and thickness are taken from the experimental results. This results in a strain level of 10308 μsn,

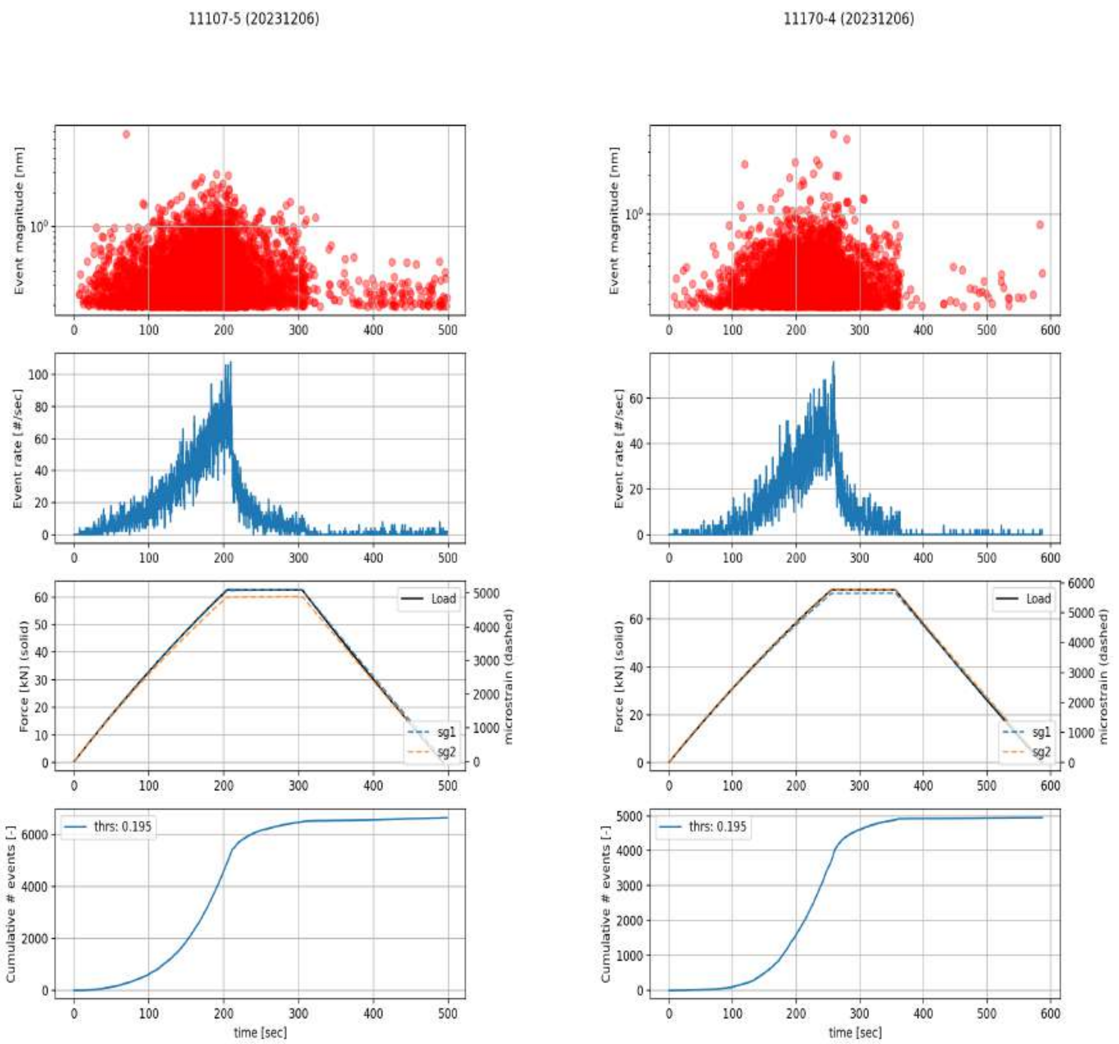

(a) Specimen 11107-5, maximum load of 62,5 kN **(b)** Specimen 11170-4, maximum load of 72,19 kN

Figure 5.9: Directly observed AE events during RT tensile test, threshold of 0.195 nm

comparable with a load of 133,9 kN. As this value is comparable with the failure load of 140 kN for the RT tensile specimens, the value of 16,10 kN is deemed adequate to allow it to proceed with the cryogenic tensile tests.

$$\epsilon = \frac{\sigma}{E(T_2)} = \frac{N_{max}/A}{E(T_2)} \tag{5.1}$$

$$E(T_2) = E(T_1)(1 + \alpha(T_2 - T_1)) \tag{5.2}$$

The expected N_{ref20K} values are calculated in advance based on the N_{ref} values from the RT tensile tests. This was done to see if the value calculated in advance aligns with the experimentally found value. Similar to the failure load, Equation's (5.1) and (5.2) have also been used to calculate N_{ref20K} for the thick ply and thin ply samples and had the following value

- N_{ref20K} Regular ply thickness samples: 4,518 kN
- N_{ref20K} Thin ply thickness samples: 5,387 kN

Specimen nr. appendix B	Specimen nr. NLR	Ply thickness	Max. load 17-1-2024 [kN]	Max. strain [μsn]
7	10793-1	Regular	16.10	11858.15
8	10793-2	Regular	Execution failure	N/A
9	10793-3	Regular	5.54 (N_{ref20K})	4922.25
10	11107-1	Regular	7.37 (N_{ref20K} + 33%)	7482.86
11	11107-2	Regular	9.25 (N_{ref20K} + 67%)	5278.56
12	11107-3	Regular	N/A	N/A
19	11169-1	Thin	N/A	N/A
20	11169-2	Thin	17.82	9370.84
21	11169-3	Thin	5.87 (N_{ref20K})	6493.12
22	11170-1	Thin	7.81 (N_{ref20K} + 33%)	9430.93
23	11170-2	Thin	9.80 (N_{ref20K} + 67%)	5771.42
24	11170-3	Thin	N/A	N/A

Table 5.2: Specimen numbering conversion table MDB specimens

With the use of the strain gauge results along the longitudinal axis, the determination of the modulus of elasticity for specimens 10793-1 and 11169-2 is undertaken and plotted as a function of applied load and as a function of resulting strain, similar to the RT tensile tests. These results are presented in Figures (5.10) and (5.11).

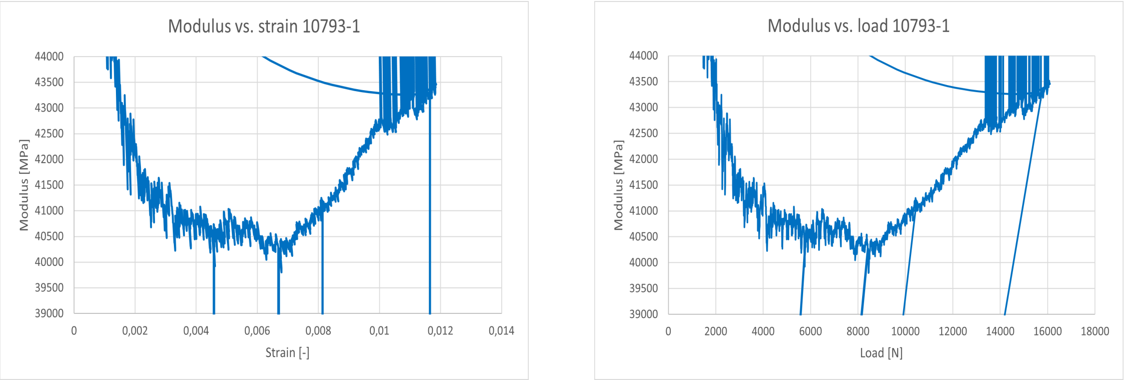

(a) Modulus vs. strain **(b)** Modulus vs. load

Figure 5.10: Strain gauge results specimen 10793-1

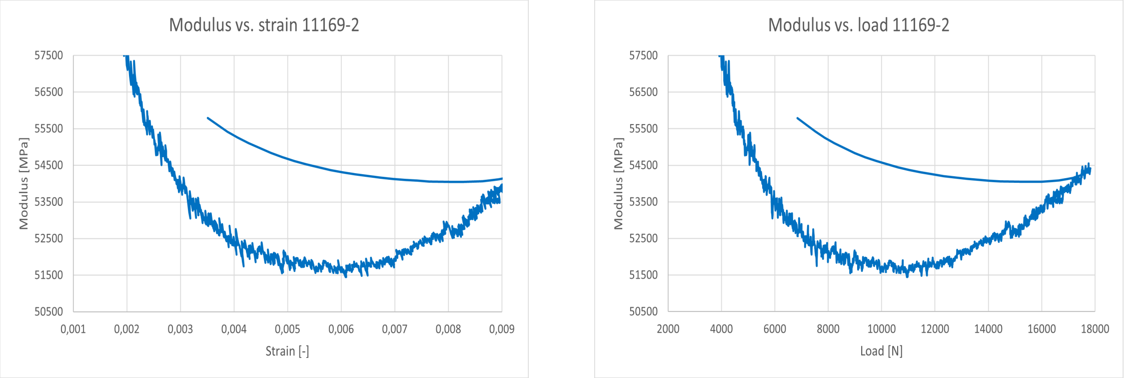

(a) Modulus vs. strain **(b)** Modulus vs. load

Figure 5.11: Strain gauge results specimen 11169-2

What directly stands out in the graphs of specimens 10793-1 and 11169-2, is that the modulus doesn't reach a constant stable level; instead roughly three phases of modulus decrease, stabilization and increase can be distinguished. The decrease at lower loads can most likely be explained by the fact that the sample is pre-loading between the 90 and ± 30 plies. This has to be done, because there are no fibers stretching from grip to grip. When tensile loading is applied, the fibers within the specimen may undergo initial deformations due to shear forces before they are fully stretched. These initial deformations can lead to a reduced effective modulus at low loads, as the fibers are not yet fully extended and contributing to the stiffness of the material. As the load increases, the fibers are further stretched, reducing the effect of the shear forces, which may cause the modulus to increase again.

It is no surprise that this effect of pre-loading has such a visual result compared to the RT tested samples, this can be mainly dedicated to the specimens dimensions. In smaller specimens, a larger portion of the composite material is near the edges, where interfacial bonding between the fibers and the matrix is more prominent. Consequently, any preloading-induced effects on the fibers, such as initial deformations due to shear forces, may have a more significant impact on the overall mechanical behavior of the smaller sample compared to wider ones.

The results in Figures (5.10) and (5.11) are not conclusive enough to make any assertions regarding potential crack initiation. Nevertheless, there is still aimed to determine N_{ref20K} for both ply configurations by looking for any kinks or anomalies in the graphs. For specimen 10793-1 a kink is expected close to 4,518 kN (calculated on beforehand). Zooming in on the graphs, a first kink is found at approximately 5,54 kN / approx. 4300 μsn and a second kink is found at approximately 7,65 kN / approx. 6000 μsn.

What is very noticeable to see is that, compared to the RT tensile results, the moduli of these specimens develop in a different way. Where during the RT tensile tests the thick ply TEP samples had a modulus of approximately 50 GPa at the stable part of the graph, the modulus of the thick ply sample 10793-1 decreased under influence of cryogenic temperatures to approximately 40,5 GPa. Contrary for the thin ply specimen 11169-2, the modulus increased under influence of cryogenic temperatures (to approximately 51,5 GPa) compared to modulus found under room temperature (approximately 47 GPa). In any case, the measurements are not robust enough to attach such conclusions, as the modulus will always increase at colder temperatures due to the reduced polymer chain mobility (and strain to failure will decrease). The load measurement results appear unreliable due to the flexible bellows; this is addressed in Chapter 6. Additionally, as will be addressed in paragraph 5.2.4, the -1 specimens cannot be directly compared to the -2 and -3 specimens due to fiber angular deviations.

To enhance comprehension, 10793-3 and 11107-1 are subject to an additional strain measurement. After the cryogenic tensile test had been conducted (table 5.2) the specimens were not instantly removed from the clamps when the setup had returned to RT, but an additional strain measurement to 2,5 kN at RT was conducted. Both cryogenic test results and RT test results of specimens 10793-3 and 11107-1 can be found back in appendix D. This resulted in a lower modulus at RT, as expected initially.

A possible explanation for the lower modulus at cryogenic temperature could be the gauge factor *k* of the strain gauge. Looking at the strain gauge Equation $\Delta R/R = k\epsilon$, a higher corrected gauge factor would lead to a lower strain and thus a higher modulus. Another influence on the modulus could also be the edge effect. Because the MDB specimens have much smaller (width) dimensions compared to the TEP specimens, the edge effect plays a relatively more significant role in the behaviour of the specimens during tensile testing. Notwithstanding the foregoing, these explanations would also be expected to apply to the thin ply sample 11169-2.

A more realistic explanation for the deviating behaviour of the thick ply samples 10793-1, 10793-3 and 11107-1 is most probably that an event occurs with respect to the strain gauge during cooldown. Specimen 10793-3 shows a cryogenic modulus of approximately 39 GPa and from the additional RT strain measurement follows a modulus of approximately 34 GPa. Similar, specimen 11107-1 shows a cryogenic modulus of approximately 33 GPa and from the additional RT strain measurement follows a modulus of approximately 28 GPa. The found moduli at cryogenic temperature of these three thick ply

MDB specimens (10793-1, 10793-3 and 11107-1) are thus all significantly lower than the RT modulus found from the TEP specimens strain measurements, but in direct comparison with themselves at RT, the cryogenic moduli are higher than the RT moduli which matches the expectation. Next to the fiber angular deviations (paragraph 5.2.4), one of the theories is that the strain gauge glue partly disbonds during cool down on some samples because of the temperature and may be also because of the vacuum that causes expansion of entrapped air in the bond line. This phenomenon becomes visual in the graphs by means of more scatter or a noisy signal, e.g. in sample 11107-2 as can be seen in Figure (D.6). When this sample is compared with sample 11170-1 (Figure (5.12)) for example, it becomes apparent that there's a significant difference in the stability of the measured signals.

At approximately 6470 μsn / 6.4 kN, specimen 11107-1 shows slippage in the grips. A sudden rise in modulus of approximately 500 MPa in 1.6 seconds occurs, refer to Figure (D.4). Because suddenly more strain is measured at this point, it could also be that a physical shift of the entrapped air in the bond line takes place causing a sudden increase in the operation of the strain gauge; due to the strong rise in a very short time bracket this is highly unlikely. Also the previously described scissoring effect may contribute to this increase.

Another plausible explanation for this phenomenon resides in the concept of strain hardening. As the load is increased, the sample undergoes plastic deformation, causing the material to strain harden, in other words an increase in material stiffness and strength as plastic deformation progresses. This behavior may be caused due to reduced thermal activation of dislocation motion. This increased strain hardening can lead to a sudden rise in modulus as the load is increased during the tensile test. A similar deformation behavior is e.g. found by Bai et al. [2] in their research to an in-situ Ti-based metallic glass matrix composite. Subsequently, the strain hardening can be preliminary for reduced matrix softening, already explained in chapter 2.2.1, which causes a stiffer matrix, enhanced load transfer and therefore an increase in modulus. [20]

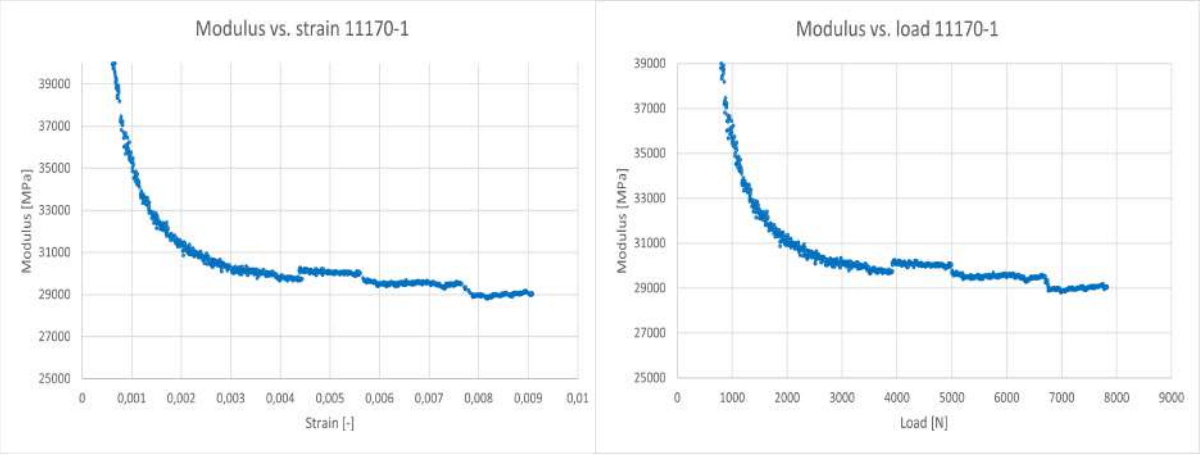

(a) Modulus vs. strain **(b)** Modulus vs. load

Figure 5.12: Strain gauge results specimen 11170-1

Following the analysis of the thick ply specimens, attention is directed towards the examination of the thin ply specimens. As previously noted, sample 11169-2, subjected to testing until slippage occurred, exhibited a modulus higher than that observed in the thin ply TEP specimens during the RT tensile test, a phenomenon consistent with anticipated behavior. However, it is noteworthy that sample 11170-1 demonstrated the highest strain among all thin ply cryogenic samples, despite being subjected to a load approximately 10 kN less than sample 11169-2. Intriguingly, this elevated strain in sample 11170-1 corresponded to a lower modulus, approximately 29 GPa. Such divergence in strain and modulus from expected trends aligns with observations made in the analysis of the three previously discussed thick ply specimens (10793-1, 10793-3, and 11107-1). Taking into consideration that the dimensions of all specimens are comparable, the derived loads and strains provide a reliable basis for estimating the moduli. Consequently, it is reasonable to anticipate that sample 11169-3 will similarly manifest a relatively diminished modulus.

The final results obtained from specimens 11107-2 and 11170-2 marked a noteworthy development within the study. Graphical representations of these specimens are provided in appendix D for further scrutiny. Specimen 11107-2 exhibited a modulus approximately measuring 48 GPa, notably surpassing those of other thick ply MDB specimens while almost equalling the modulus of the RT TEP thick ply modulus, which stands at approximately 50 GPa. Similarly, specimen 11170-2 demonstrated a notably elevated modulus of approximately 51 GPa, placing it in close proximity to the modulus of specimen 11169-2 and exceeding that of the RT TEP thin ply modulus, which stands at 47 GPa.

Based on the observed strain and modulus outcomes, a discernible inference emerges suggesting that the specimens denoted with '-2' suffixes exhibit a higher degree of reliability compared to their '-1' and '-3' counterparts. Notably, the proximity of these latter specimens to the edge of the panel, as delineated in the machining panel drawing provided in appendix B, appears to exert a pronounced influence on their performance. This phenomenon will be thoroughly addressed in paragraph 5.2.4 and chapter 6. Moreover, the cryogenic modulus recorded for specimen 11107-2, while elevated, remains lower than the analogous thick ply specimens subjected to RT tensile testing. This discrepancy lends credence to the previously posited assertions regarding gauge factor, edge effect, expansion of entrapped air in the bond line, and strain hardening, all of which are purported to impact the modulus characteristics of the specimens under consideration.

5.2.3. Permeability

As previously mentioned in chapter 4, all permeability tests are conducted using helium instead of hydrogen. Delay in the delivery of materials, but also limited experience with hydrogen permeability testing at NLR, were driving factors in this consideration. Next to that, other NLR samples made of LM-PAEK were already tested with helium, which in turn is beneficial in comparing the results. The purpose of the permeability tests is to establish a baseline level of permeability for both materials (thin ply and thick ply) and subsequently monitor the effect of an increased tensile load on permeability. The complete overview of permeability results of all tested specimens can be found in appendix C and a summary is given in table 5.3.

Specimen	Ply config.	Applied load [kN]	Ultimate Qperm [mbarL/s]	Ultimate kperm [mol He/(m.s.Pa)]
10793-4	Thick	0	3,18E-07	5,10900E-17
11107-6	Thick	30	4,93E-07	8,02789E-17
10793-6	Thick	37,5	3,55E-07	5,61042E-17
11107-4	Thick	50	4,49E-07	7,32414E-17
11107-5	Thick	62,5	4,50E-07	7,23117E-17
10793-5	Thick	140	3,64E-07	5,78762E-17
11169-4	Thin	0	7,04E-07	1,07747E-16
11169-6	Thin	41,25	6,15E-07	9,75179E-17
11170-5	Thin	51,56	6,41E-07	1,01232E-16
11170-6	Thin	61,88	7,44E-07	1,18700E-16
11170-4	Thin	72,19	6,93E-07	1,12844E-16
11169-5	Thin	140	6,67E-07	1,06645E-16

Table 5.3: Summary of permeability results after RT tensile test

The RT tensile tests were conducted on two different dates, see Table 5.1. After the first day of tensile testing, only specimen 11107-6 was isolated to be tested on permeability, this was done to validate and at the same time see the effect on permeability for the initial N_{ref} in the RT tensile test, being set at 15 kN. The effect on permeability was insignificant for this specimen, see table 5.3. Therefore the thick ply specimens 10793-6, 11107-4 and 11107-5 were retested with a higher RT tensile load on the second day of tensile testing. Considering the fact that both the UL-200 leaktester and the PhoeniXL leaktester were options to conduct the permeability tests in at NLR, both were used for 11107-6.

The first indicated results, accompanied by calibration tests of the leaktesters, showed that the UL-200 produced results that were a factor ~1000 [$molHe/(m.s.Pa)$] off compared to results from literature and experimentally tested comparable materials at NLR. This may be due to a deviation in the set-up in combination with this specific specimen. On the other hand, the PhoeniXL showed results for 11107-6 as expected and is therefore chosen as the main leaktest set-up. The permeability tests are typically executed under a 2.33$\times 10^{-7}$ MPa deep vacuum and at 293 K. Furthermore, a measurement stability criterion has been used: when the quotient of the leak rate at 50% of the measurement time divided by the leak rate at 100% of the measurement time was $>$0.9, a measurement was considered stable.

The permeability set-up expresses the diffusion rate as a result. The ultimate permeability K_{perm} is calculated by making use of the diffusion rate Q_{perm} expressed in [$mbar.L/s$]; multiplying by 100 and dividing by 1000 leads to Q_{perm} in [$Pa.m^3/s$]. This leads to the following Equation:

$$K_{perm} = \frac{Q_{perm} * d}{A * Pa} \frac{\rho_{He,295K}}{m * 100000} \tag{5.3}$$

Where:
K_{perm} is the ultimate permeability in [$molHe/(m.s.Pa)$];
Q_{perm} is the ultimate diffusion rate in [$Pa.m^3/s$];
d is the laminate thickness in [m];
A is the surface area in [m^2];
Pa is the helium pressure in [Pa];
$\rho_{He,295K}$ is the helium density at 295 K in [kg/m^2];
m is the mass of 1 mol He in [kg].

For specimen 11107-6 the measured leak rate was 4.93$\times 10^{-7}$ $mbarL/s$ leading to a permeability of 8.03$\times 10^{-17}$ $molHe/(m.s.Pa)$. When this permeability rate is compared to measurements performed by Schultheiss [31] in 2007 for example, our current material looks very promising. With 8.03$\times 10^{-17}$ $molHe/(m.s.Pa)$ this sample has a lower permeability than almost all measured thermoplastics permeabilities measured by Schultheiss.

Subsequently, specimen 11169-4 was the first thin ply sample to be tested on permeability. Conflicting with the RT tensile test results and expectations, sample 11169-4 (unloaded, thin ply) showed a higher permeability than sample 11107-6 with 1.08$\times 10^{-16}$ $molHe/(m.s.Pa)$. Worth mentioning is the speed with which the helium passes the sample. After 12 hours the maximum leak rate was already reached, this is approximately twice as fast as sample 11107-6.

What can be noticed immediately is that there seems to be no clear effect of the applied load on the permeability for the thin ply samples, and also that the thin ply specimens show a higher permeability compared to the thick ply specimens. Contrary, the effect the applied load has on the thick ply specimens is minimal but noticeable; the unloaded specimen 10793-4 showed the lowest permeability of the thick ply samples.

The N_{ref} value seems to have a minor positive effect on reducing permeability as well: specimen 10793-6 has the lowest permeability of the thick ply samples, specimen 10793-4 excepted, and specimen 11169-6 has the lowest permeability of the thin ply samples. Although for both configurations it applies that this effect is minimal. On the contrary, all results fall within an expected range of variation, and a considerable spread may occur when multiple measurements are performed on the same sample. Therefore, it is recommended to further investigate the potential variation in permeability results on the same sample.

Figures (5.13) and (5.14) represent the leak rates of these N_{ref} specimens and are exemplary for a typical expected measurement. It is implicit that the thin ply samples attained their steady-state leakrate prior to the thick ply samples. Further analysis and the relevance of these results will be discussed in chapter 6.

Figure 5.13: Measured leak rate [mbarL/s] and helium pressure [bara] of specimen 10793-6

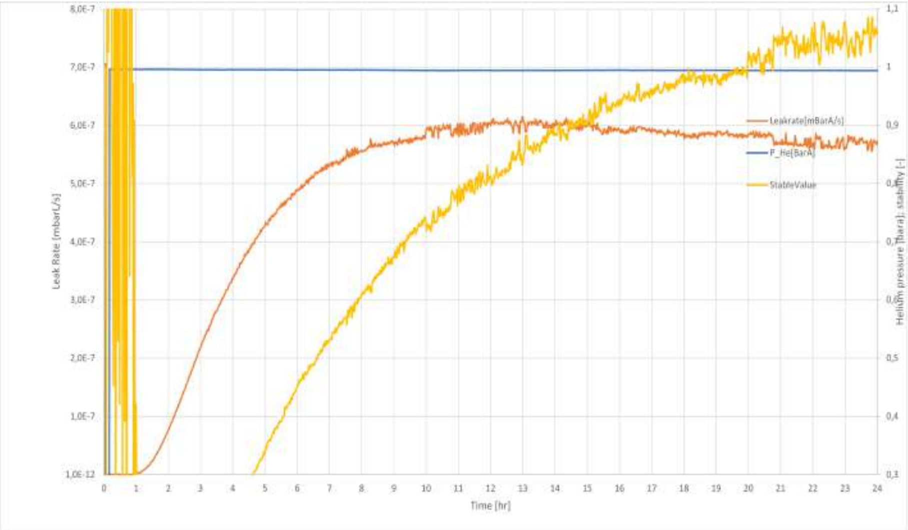

Figure 5.14: Measured leak rate [mbarL/s] and helium pressure [bara] of specimen 11169-6

5.2.4. Optical microscopy

TEP specimens

All specimens are cut once through the middle in longitudinal direction, in a way that the cut surface is perpendicular to the 90 degrees fibres. This is done as these fibres are expected to be the first to show microcracks. The assessed area is 40 mm over the complete thickness. The following specimens are assessed on microcraks using the optical microscope:

- 10793-6, RTD, Thick ply, N_{ref}
- 11107-4, RTD, Thick ply, N_{ref} + 33%
- 11107-5, RTD, Thick ply, N_{ref} + 67%

- 11169-6, RTD, Thin ply, N_{ref}
- 11170-6, RTD, Thin ply, N_{ref} + 50%
- 11170-4, RTD, Thin ply, N_{ref} + 75%

The investigation involved assessing the mere presence of microcracks, the dimensions of microcracks such as COD and crack length, and ultimately, also examining microcrack density. It appeared that 10793-6 and 11107-4 were free of microcracks which is obviously a positive result for the LH_2 tank application. Specimen 11107-5, which was loaded well above the chosen N_{ref}, however did show a microcrack in a 90 degrees ply as the only thick ply sample, as can be seen in Figure (5.15). The formation of the first crack is seen as the initiation of microcracking in this thesis. [27] The characteristic results of the microcracks are presented in table 5.4 while further analysis is provided in chapter 6.

The thin ply samples demonstrated significantly poorer performance regarding microcracks compared to the thick ply samples. Initially, microcracks were observed in each of the examined thin ply samples (even at the lowest loading of N_{ref}), with the quantities of cracks being significantly higher and the COD's wider. Furthermore, it is noteworthy to observe discoloration in certain sections of the matrix material, possibly indicative of material degradation. This is likely attributed to the fact that the thin ply material is an experimental material with a higher wt% matrix.

Sample 11169-6 thus already showed microcracks, these were not standing wide open and contribution to increased permeability is therefore unlikely, but it at least confirms the chosen N_{ref}. In general, a gradual buildup in COD and microcrack density can be distinguished parallel to the loading buildup, as could be expected. Specimen 11170-4, which faced the highest tensile loads, also showed the most microcrack related damage and the largest crack length as can be seen in Figure (5.16). Also for the thin ply samples, the characteristic results of the microcracks are presented in table 5.4 and appendix D, while further analysis is provided in chapter 6.

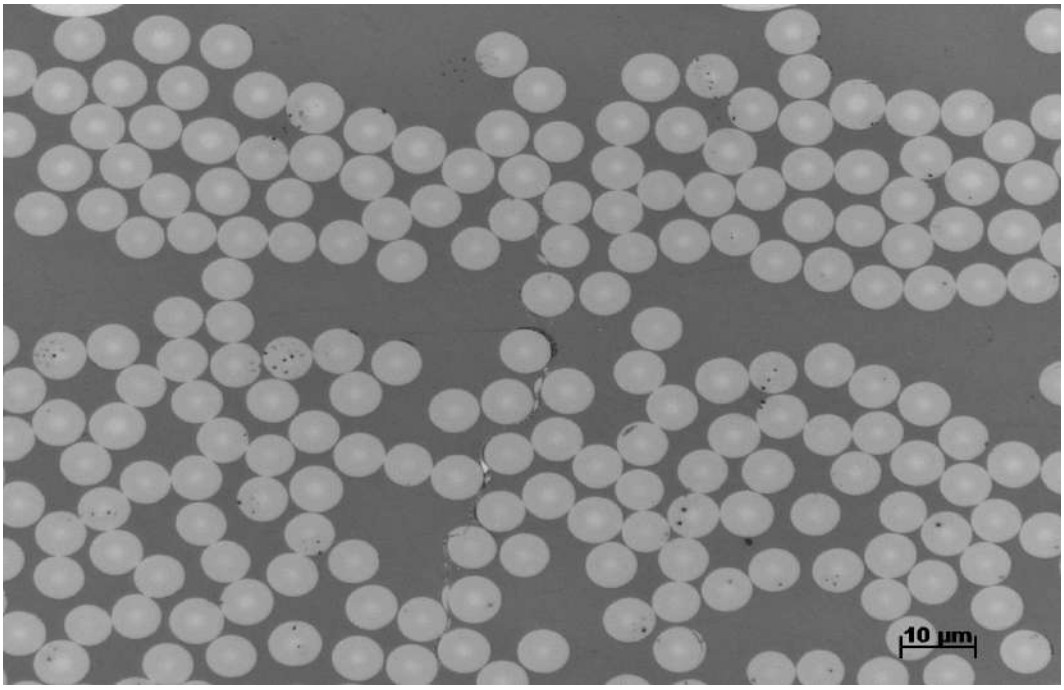

Figure 5.15: Optical microscopy examination on microcracks of specimen 11107-5, which is a thermoplastic thick ply specimen loaded to 62.5 kN ($N_{ref} + 67$%). The microcracks can be distinguished as a lighter, whimsical pattern in the matrix in the middle of the figure, mainly on the fiber-matrix interfaces.

Specimen	Cracks found	Amount	Max. crack length [μm]	Max. COD [μm]	Density [mm^{-2}]
10793-6	N	N/A	N/A	N/A	N/A
11107-4	N	N/A	N/A	N/A	N/A
11107-5	Y	1	4.25	1.0	0.0104
11169-6	Y	1	21.5	0.33	0.0106
11170-6	Y	2	12.5	1.1	0.0212
11170-4	Y	3	29.0	2.0	0.0305

Table 5.4: Summary of microcrack results after RT tensile test

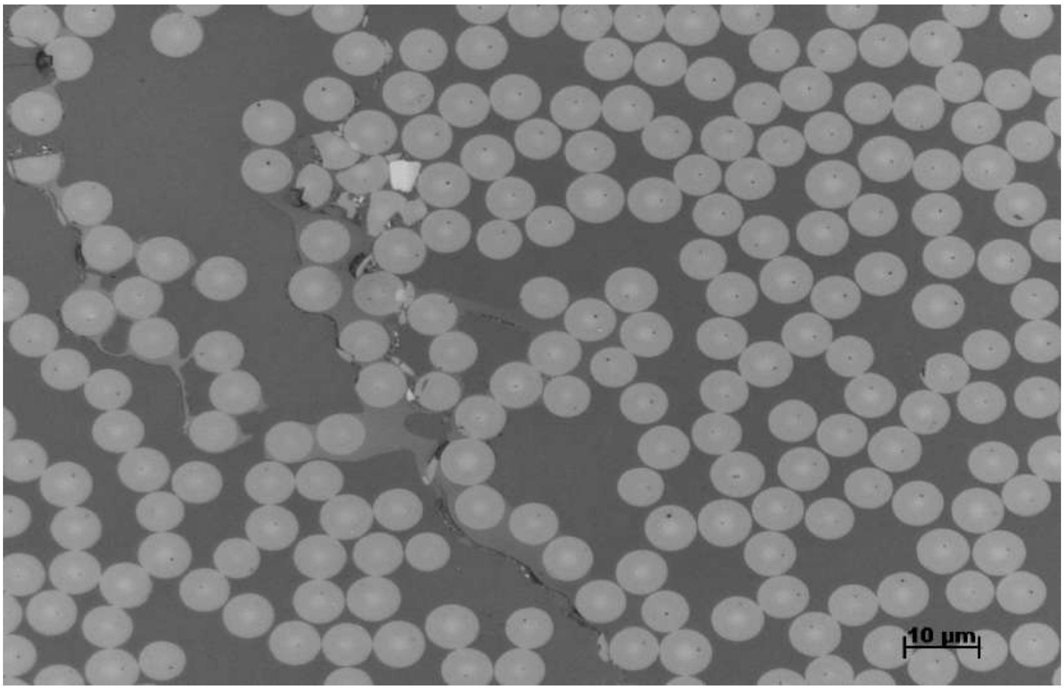

Figure 5.16: Optical microscopy examination on microcracks of specimen 11170-4 [1/2]. The microcracks can be distinguished as a lighter, whimsical pattern in the matrix in the middle of the figure, mainly on the fiber-matrix interfaces. This should not be confused with the lighter color in the matrix which will be discussed later.

MDB specimens

Like the TEP specimens, all MDB specimens are cut once through the middle in longitudinal direction of the test section, in a way that the cut surface is perpendicular to the 90 degrees fibres. The assessed area is 40 mm over the complete thickness. All tensile loaded specimens mentioned in table (5.2) are assessed on microcraks using an optical microscope. The characteristic results of the microcracks are presented in table (5.5).

Looking at the amount and density of microcracks in table (5.5), some similarities to table (5.4) can be distinguished. A gradual buildup in microcrack density after N_{ref20K} can be distinghuished for the thin ply specimens parallel to the loading buildup. The thick ply specimens 11107-1 and 11107-2 form an interesting exception which will be discussed below; also the thin ply samples perform seemingly less on microcracks compared to the thick ply samples again. Although specimen 10793-1 suffered from slippage in the grips, Figure (5.17) confirms that it was most likely close to its failure load, as expected, due to the high amount of microcracks present. Compared to specimens seen before, this specimen shows immense crack length and COD, while at the same time even cracks in the ±30-plies and delamination were detected. The delamination occurs once a microcrack reaches the ply boundary and continues to develop on an interply level.

Specimen	Cracks found	Amount	Max. crack length [μm]	Max. COD [μm]	Density [mm^{-2}]
10793-1	Y	>50	146.7*	12.5	0.5987
10793-3	Y	15	127.0	1.1	0.1838
11107-1	Y	5	102.6	2.0	0.0610
11107-2	Y	3	97.5	3.75	0.0318
11169-2	Y	10	116.0	1.0	0.1072
11169-3	Y	10	141.0	1.25	0.1338
11170-1	Y	30	132.5	1.1	0.3794
11170-2	Y	74	164.0	2.2	0.7819

Table 5.5: Summary of microcrack results after cryogenic tensile test
* If delamination is included, the max. crack length found in 10793-1 is 1760 μm

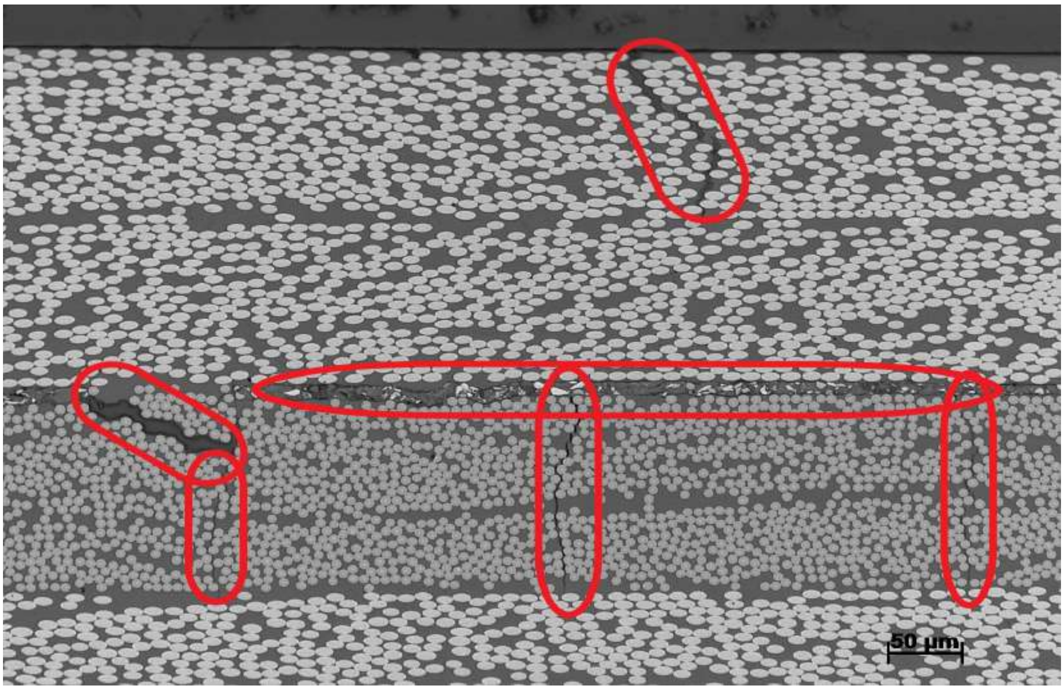

Figure 5.17: Optical microscopy examination on microcracks (marked by the red capsules) of specimen 10793-1 [1/2]. The left microcrack displays a very large COD, while the upper microcrack's formed in a 30°-ply. Delamination as a result of the tensile load performed at CTD is also visible.

Specimen 11169-2 presents an intriguing anomaly concerning microcrack formation. Despite enduring the most substantial load, it demonstrates a relatively low incidence of microcracks compared to the other thin ply specimens. This unexpected outcome may be attributed, in part, to its notably high modulus, approximately 51.5 GPa, as determined from the cryogenic tensile test. The influence of this high modulus is suggested by considerations such as those articulated in Equation (3.2), wherein the deduction from the effective axial modulus to compute $E_{a(\rho)}$ is contingent upon factors such as the aspect ratio and COD of microcracks. As described before, high strains (and thus low moduli) lead to more microcracks.

From this perspective, it is contended that the assessment of strains holds greater promise as an indicator for microcrack formation compared to the examination of applied loads. However, comparing the data presented in tables 5.2 and 5.5 concerning the thin ply specimens, such a proposition encounters ambiguity, particularly in the case of specimen 11170-2. Despite registering the lowest strain among the tested thin ply specimens, this particular specimen manifested the highest incidence of microcracks. In light of the thin ply specimens, it becomes apparent that while specimen 11169-2 deviates as an outlier when correlating microcrack formation with load escalation, specimen 11170-2 emerges as an outlier when associating microcrack formation with elevated strain levels.

Several other potential explanations exist for this counterintuitive result of specimen 11169-2. Firstly, it is conceivable that damage initiation occurred beyond the confines of the tested region, possibly originating at the clamps, thereby concentrating all damage accumulation at those locations. It is recommended to further investigate this for every specimen. Alternatively, while transverse microcracks may indeed be present, their detection could have been hindered by limitations in the surface area under examination. This possibility suggests that damage propagation might have occurred at locations further from the longitudinal center, thus eluding direct observation on the viewing surface. To eliminate this possibility, the microscopic sample underwent an additional sanding process of approximately 2 mm in depth. Despite this additional treatment, the resulting findings remained consistent with those obtained previously, thereby lending credence to the characterization of the sample as an outlier.

The interesting exception of specimen 11107-1 and 11107-2 mentioned before relates to the amount of microcracks which was expected to be more than 10793-3. The thick ply samples exhibit a distinctive trend wherein the formation of microcracks appears to diminish progressively as the applied load increases. In comparison to each other, samples 11107-1 and 11107-2 do, however, exhibit the expected trend in accordance with the measured strain levels, as elucidated above for the thin ply specimens.

Just like the anomalous findings on the cryogenic tensile test results, the origin from the edge of the panel (for all '-1' and '-3'-samples, refer to appendix B) could also be of influence here. By means of visual inspection of the surface plies (both upper and lower ply) the deviations in fibre direction compared to the nominal value of 30° for all assessed specimens is presented in table 5.6.

Specimen number	Fibre direction upper ply	Fibre direction lower ply	Avg. fibre direction outer plies
10793-1	33°	33°	33°
10793-3	36°	35°	35.5°
11107-1	37°	36°	36.5°
11107-2	30°	31°	30.5°
11169-2	29°	28°	28.5°
11169-3	38°	37°	37.5°
11170-1	31°	31°	31°
11170-2	32°	31°	31.5°

Table 5.6: Fibre directions of the upper and lower outer ply for all assessed MDB specimens; the nominal direction is 30°

Combining the results from table 5.6 with the comparison in Figure (5.18), it seems to be accurate that the $\pm$30°-plies of sample 11107-1 are shifted to approximately $\pm$36.5°-plies which is presented in the figure by a little less ovality than 10793-3. Although on the surface plies, these two specimens only differ approximately 1°, it could well be that the inner plies differ on a broader scale. By making use of (part of) the XFEM-SCZM model, E_x and E_y are calculated for these thick ply laminates with both the original layup $(30, -30, 90)_2(30, -30, 90, -30, 30)(90, -30, 30)_2$ and the same layup where all $\pm$30°-plies are replaced with $\pm$36°-plies. As expected, mainly E_x is influenced by changing this fibre direction: a decrease from 53444.9 MPa to 39826.6 MPa, or 25.48%, resulted for E_x when the $\pm$36°-plies were implemented. E_y on the other hand increased from 46908.0 MPa to 47645.3 MPa, or 1.57%. Comparing samples 10793-3 and 11107-2, this decrease in E_x can be used as the explanation why 10793-3 has more microcracks, taking into account that the loads (and therefore external stress) were applied as planned and that for a lower modulus a higher strain (i.e. more microcracks) is thus prerequisite.

This explanation does not seem to apply for specimen 11107-1 while this sample had both a lower E_x and a relatively high measured strain. The changed ovality of the specimen leads the non-90-plies to being closer to 90° than they should be. Because the specimens are loaded in the 0°-direction, this would mean that the sample most likely has lower thermal stress, and could be able to endure a larger strain first before showing signs of microcracks. On a critical note: because specimen 10793-3 and 11107-1 both have a significant deviation in fibre direction, but specimen 11107-2 doesn't, this explanation does not offer a satisfactory account for the observed trend in the development of microcracks in the thick ply specimens. In appendix D it's also clearly visible that the ±30°-plies of 11107-2 are much more oval.

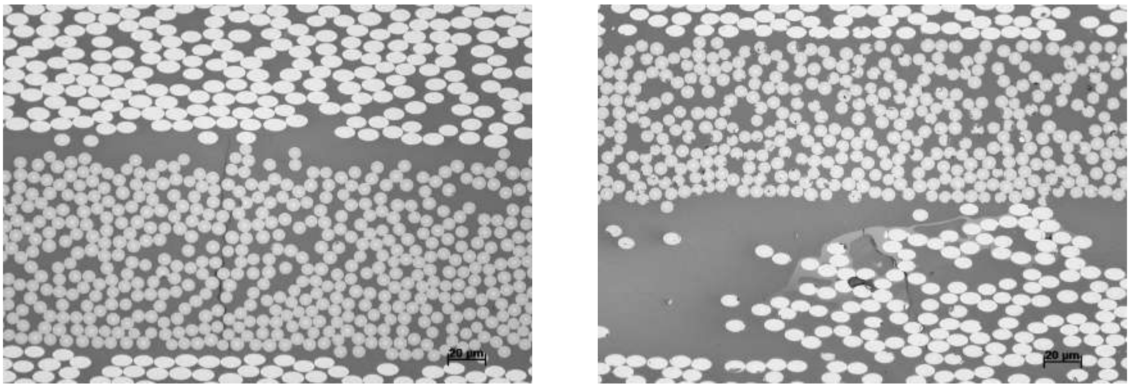

(a) 10793-3 **(b)** 11107-1 [1/2]

Figure 5.18: Microscopic comparison of specimens 10793-3 and 11107-1 [1/2]. The fibers in the ±30-plies of 11107-1 show to have less ovality compared to 10793-3 which should potentially indicate for higher strain and more microcracks. The discoloration in the ±30-plies of 11107-1 could therefore be explained by plastic deformation just before microcrack initiation.

Sample 11107-1 and 11107-2 present an additional noteworthy observation alongside the observed low incidence of microcracks. As depicted in Figure (5.18b) and in appendix D, material discoloration within the matrix is evident. Until now, such matrix discoloration had exclusively been observed in thin ply samples (RT and CTD). This phenomenon may imply plastic deformation of the matrix immediately preceding microcrack formation. This can be due to the fact that both samples experienced slippage in the grips as discussed before, and therefore temporarily deal with an increased strain and modulus causing the material to yield and deform plastically. Consequently, this observation may advocate for the quality of the thin ply samples, counter to the initial assumption attributing the discoloration solely to material degradation inherent in the experimental nature of the thin ply laminates. Notably, the thick ply laminates, deemed non-experimental, and the supplementary C-scans in Appendix E don't give a reason for any additional irregularities within this material. This observation of specimens 11107-1 and 11107-2 is in line with the observation of plastic deformation, strain hardening and matrix softening for these specimens as described in paragraph 5.2.2.

It is pertinent to note that crack growth rate is independent of crack length and that it's only a function of the distance to the pre-existing neighboring microcracks. [27] A microcrack is therefore also only defined as a microcrack when it's an intraply damage; when it would stretch over multiple plies or continues cracking in between plies, the damages are called *cracks* and *delamination* respectively. Delamination of specimen 10793-1 has already been discussed above, but also an example of a microcrack developing into a crack is found in specimen 11169-3, as can be seen in Figure (5.19). These damages are therefore also not included in table 5.5.

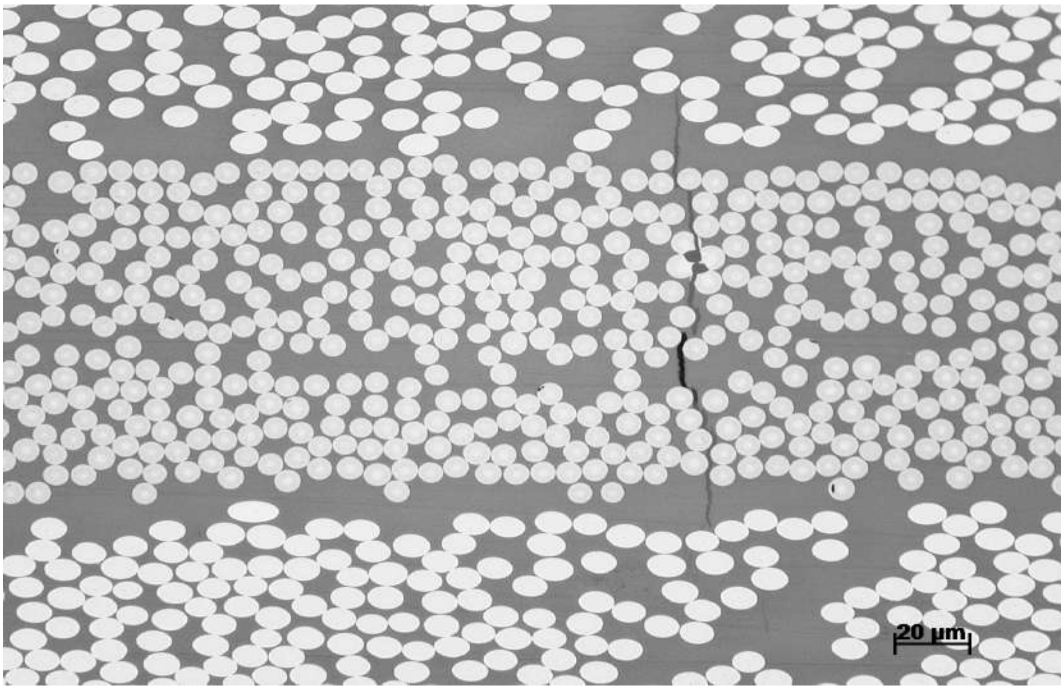

Figure 5.19: Optical microscopy examination on microcracks of specimen 11169-3. The upper part of the microcrack extends cracking into a 30°-ply for which it can be considered to be a *crack*

6

Outcome and relevance of the results

The obtained results hold significance in the context of this thesis, as they constitute the empirical foundation upon which the sub-questions will be addressed. The identified patterns and trends within the data provide crucial insights into the nuanced aspects of LH_2 storage. The analysis of the results will serve as a key analytical tool to unravel the complexities outlined in the sub-questions, and are presented in this chapter.

1. What solutions can be conducted to limit transverse microcracks to a predefined level?
A major interest in studying microcracking is to be able to predict the microcracking process and to be able to design laminates that are resistant to microcracking, in this case especially focused on cryogenic purposes. [27] In chapter 2 a number of issues in relation to microcracks have been reviewed for this purpose, of which a selection is experimentally tested in chapter 5.

Fibre direction, lay-up, permeation barriers, fibre-volume fraction, ply thickness, voids and resin-rich areas and exposed free edges were the main identified design criteria. Of these, ply thickness (in combination with lay-up) was the focal point in the microcrack test program and is therefore solely covered in answering this subquestion. It was hypothesised that the use of thin plies would be less sensitive to microcracking, because they have a lower thermal mass, and therefore a more uniform temperature distribution, minimized thermal stresses and thus a reduced risk of microcracks. The consortium [38] states no specific maximum microcrack density for the LH_2 tank, but does state that the materials must be microcracking resistant.

The experimentally found microcrack results in chapter 5 indicated that microcrack initiation and growth could be more dependent on the combination of found modulus and strain level rather than the load which was controlled on the samples. This is explained by the fact that the strain level at which microcrack initiation occurs can vary depending on the material properties, such as reaction to cryogenic temperatures, but also the material having certain higher stress concentrations (e.g. as a result of the scissoring effect) and a different strain energy release rate. For that reason the microcrack density for all measured samples is plotted against both load and maximum strain in Figure (6.1) and Figure (6.2), respectively.

It can be concluded that, for the samples tested at room temperature, the thin ply samples perform less on microcracks compared to the thick ply samples, while both types of samples develop in a way that was predicted. The increasing microcrack density at increasing load develops in a similar manner as the increasing microcrack density at increasing strain. This is explainable because of the facts that e.g. molecule rearrangement due to cryogenic reaction is not present and because the dimensions of the specimens are sufficient to not let the edge effect or scissor effect play a significant role.

On the contrary for the cryogenically tested specimens, this increasing microcrack development can only be distinguished for the thin ply specimens at increasing load, with exception of the highest load

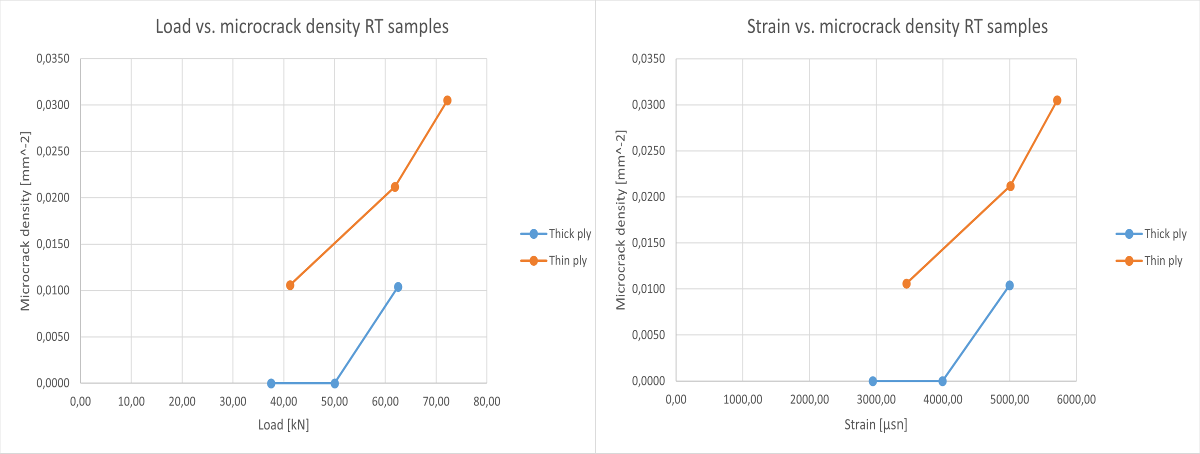

(a) Load vs. microcrack density

(b) Strain vs. microcrack density

Figure 6.1: Microcrack density results of TEP/RT specimens

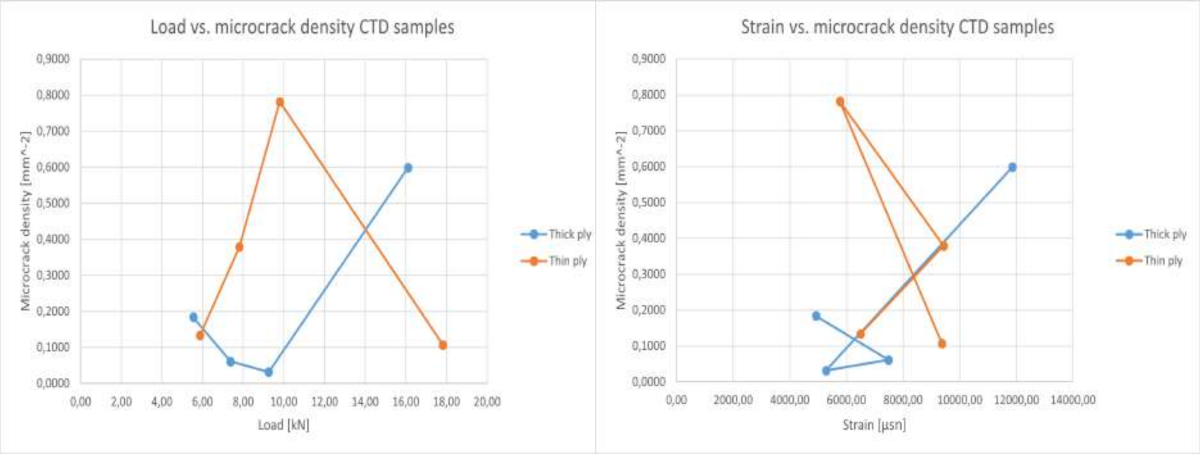

(a) Load vs. microcrack density

(b) Strain vs. microcrack density

Figure 6.2: Microcrack density results of MDB/CTD specimens

applied (sample 11169-2: a thin ply sample loaded to 17.82 kN (failure/slippage). It can be concluded however that also for the tested cryogenic samples, the thin ply specimens perform poorer compared to the thick ply specimens on microcrack development, for both load increase and strain increase. The divergent results on the load graph are possibly influenced by a pressure difference on the bellows caused by vaporized helium in the cryostat that seeks a way to escape. There is no discernible pattern in the progression of microcrack development as the strain level increases, evident in both the thick ply and thin ply samples. Given the expectation of accurate strain measurements, it is plausible that there is a discrepancy in the strain data, indicating also a potential issue with the insufficient number of tested specimens.

The experimentally found microcrack density can now also be used to assess whether it conforms to the threshold value used in the XFEM-SCZM model. Grogan et al. [13], in their extended finite element method (XFEM) + surface cohesive zone model (SCZM) simulation, chose a mesh density for each ply in their model where at least 5 microcracks per cm of cylinder width or circumference were allowed. This value is equal to the maximum crack density observed in heavily damaged cryogenically cycled CF/PEEK laminates. Translated to this testprogram, the issue boils down to a maximum allowed microcrack density of 0.3571 mm^{-2} for the thick ply specimens and 0.4545 mm^{-2} for the thin ply specimens. The amount of plies, ply thickness and assessed area in the microscope are taken into account to calculate these densities. When compared to the results in tables 5.4 and 5.5, it appears that only specimens 10793-1 (CTD, thick ply, loaded until failure) and 11170-2 (CTD, thin ply, loaded until $N_{ref20K} + 67\%$ exceed this allowed value with a microcrack density of 0.5987 mm^{-2} and 0.7819 mm^{-2}, respectively. It has to be stressed that specimen 10793-1 showed an ultimate stress of 515.29 MPa, but that the tank is dimensioned at a maximum stress of 54 MPa at burst pressure at RT. The working pressure is only halve of the burst pressure, resulting in a stress of only approximately 27 MPa at 1500 μsn. Hence, considering the stress value in this situation as a realistic scenario is not truly viable. It can thus be concluded that mesh density used in the XFEM-SCZM model is suitable for the purpose for which it was designed. On this aspect there is no favor of utilizing thin ply laminates or thick ply laminates.

A second aspect of microcracks that was assessed on, was the Crack Opening Distance (COD). The COD results of the samples are displayed in Figure (6.3). It becomes clear that the cryogenic temperature mainly has an effect on the thick ply samples, because the cryogenic COD's increase significantly with multiples of the RT COD. Conversely, the crack opening distance of the thin ply samples appears to be only minimally affected by the cryogenic temperature. This is explained by the fact that the thin ply samples experience lower thermal stresses and also lower thermal contraction because of the lower material volume. Grogan et al. [14] found that COD was greater in general for thicker laminates, however the results in this experiment do not seem to support that for RT samples.

Compared to other studies where COD's of up to 25 μm were found (for example in Grogan et al. [14]), the lay-up of the specimens have proven themselves considering the fact that all measured COD's are relatively small which is due to the constantly varying ply orientation and lack of ply blocking. This is a valuable conclusion as the chances on formation of a microcrack network are very much limited because of this. [13]

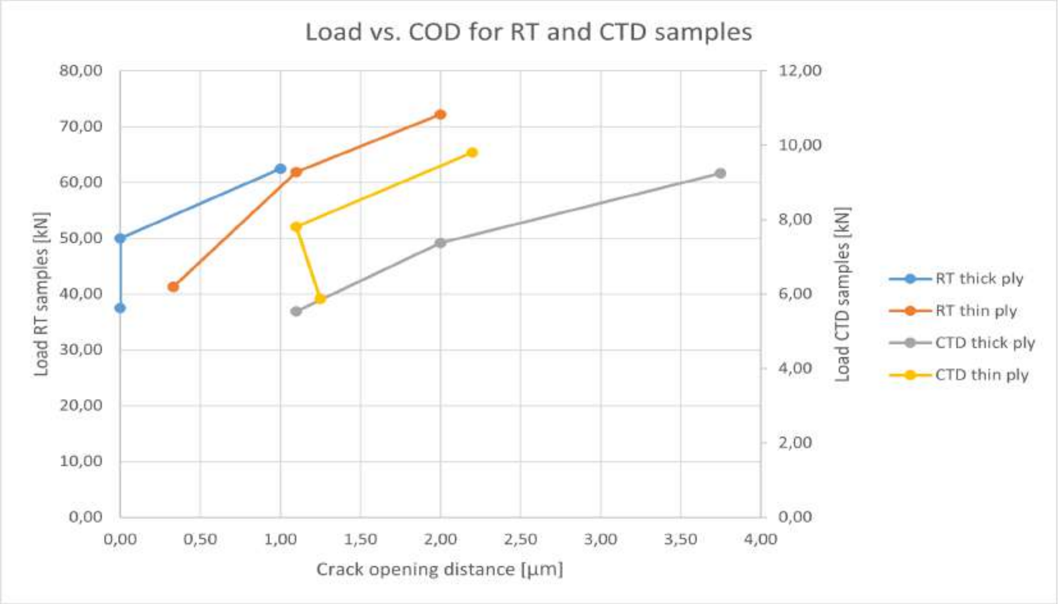

Figure 6.3: Load versus experimentally found crack opening distance for RT and cryogenic temperature, thick ply and thin ply samples. For each circumstance the N_{ref} in question and the next two following measurements are plotted.

Besides the two RT, thick ply samples that were microcrack-free, the smallest COD is found in specimen 11169-6 (thin ply sample loaded to 41.25 kN (N_{ref})): 0.33 μm. This value is equal to 3300 Å, which is orders of magnitude greater than the critical crack size to prevent for permeation (2.1 Å) [25] and the kinetic diameter of hydrogen (2.89 Å). As already stated in chapter 2: the fact that the COD, when present in a ply, is many times larger than the kinetic diameter of hydrogen, makes it obvious that the total prevention of microcracks should be the main objective when permeability needs to be avoided. Strictly interpreted, only the thick ply specimens tested until N_{ref} at RT fulfill the consortium's requirement of a microcracking resistant material. However, zooming in on the microcrack-permeability relation (which will be discussed below in subquestion 3), the mere presence of the microcracks and their COD do not seem to influence the permeability of the laminate significantly. It is therefore worthwhile to consider whether microcrack density could be a more precise requirement for the consortium to assess microcrack characteristics for the LH_2 tank.

Furthermore, the analysis considers the relation between the Young's modulus and the microcrack characteristics of the specimens, this is e.g. already covered in Figure (2.3). The expected general trend of a higher modulus at lower temperatures can partly be confirmed. Sapi et al. [30] explain the higher modulus because of the reduction in polymer chain mobility, increasing the binding forces between the molecules and therefore the strength of the material. Additionally, the lower the stress, the more time it takes for stresses to relax (principle of time-temperature superposition). This results in the fact that the stress relaxation can almost be completely arrested at cryogenic temperatures, which results in increased stiffness.

By comparing the found moduli in Figures (6.4) and (6.5), the presumption made in the preceding chapter appears to be substantiated, namely, that specimens ending in -2 exhibit a higher modulus (and therefore a decreasing strain to failure and decreasing strain energy release rate) at cryogenic temperatures. It could also be argued that only specimens subjected to higher loads meet the anticipated higher modulus; however, due to the divergent result of specimen 10793-1 (thick ply sample loaded to 16.10 kN (failure/slippage)), this does not seem to hold true. Based on the (limited) number of tested specimens, it can be concluded that the origin position of the specimens within their panel significantly influences the modulus and that no relation between modulus and microcrack density can be distinguished.

Still, the materials and measurement methods were assessed separately and no abnormality's were found, which makes it likely that e.g. slippage takes place causing a sudden increase in the operation of the strain gauge. The microscopic assessment confirms this line of reasoning as both the thick and thin ply samples show significantly more microcracks at cryogenic temperature and are all affected by higher thermal stresses; it is likely that the low modulus samples therefore also actually experienced a higher modulus and thus lower strain to failure because more microcracks are witnessed at cryogenic temperature, unlike what the strain gauge results are telling us. As a consequence, it would appear that strain is not such a reliable predictor for microcrack density, considering that the moduli observed in this experiment are primarily influenced by the identified strains. This is illogical, leading to the conclusion that the strain or load data is (partially) incorrect.

Having a higher modulus may not necessarily be preferable if the goal is to prevent the formation of microcracks. A higher modulus typically indicates greater stiffness and less deformation capability, which could lead to increased stress concentrations at localized regions within the material. This, in turn, may promote the initiation and propagation of microcracks, particularly in regions where stress is not evenly distributed.

In the XFEM-SCZM model, the difference in behaviour between thick and thin ply specimens is programmed using Equations (2.17) and (2.19) by Camanho et al. [5] Equation (2.17) expresses the in-situ shear strength, which is often represented as ILSS. Higher ILSS values indicate stronger bonding between laminae, which can enhance the overall mechanical performance of the composite, including resistance to microcrack initiation. Looking at the Equation, a high value for the parameter ϕ is beneficial if microcracks want to be prevented. When β is assumed to be 3.6×10^{-8} MPa^{-3} for a CFRP as suggested by Camanho et al. [5], the substitution of the Equations with data from appendix A and F yields the following:

$$\text{For a thick ply: } \phi = \frac{12(S^L)^2}{G_{12}} + \frac{72}{4}\beta(S^L)^4 = \frac{12(152)^2}{4.3\times10^3} + \frac{72}{4}3.6\times10^{-8}(152)^4 = 410.38$$

$$\text{For a thin ply: } \phi = \frac{48G_{IIc}}{\pi t} = \frac{48*2.6}{\pi 0.110} = 361.14 \qquad (6.1)$$

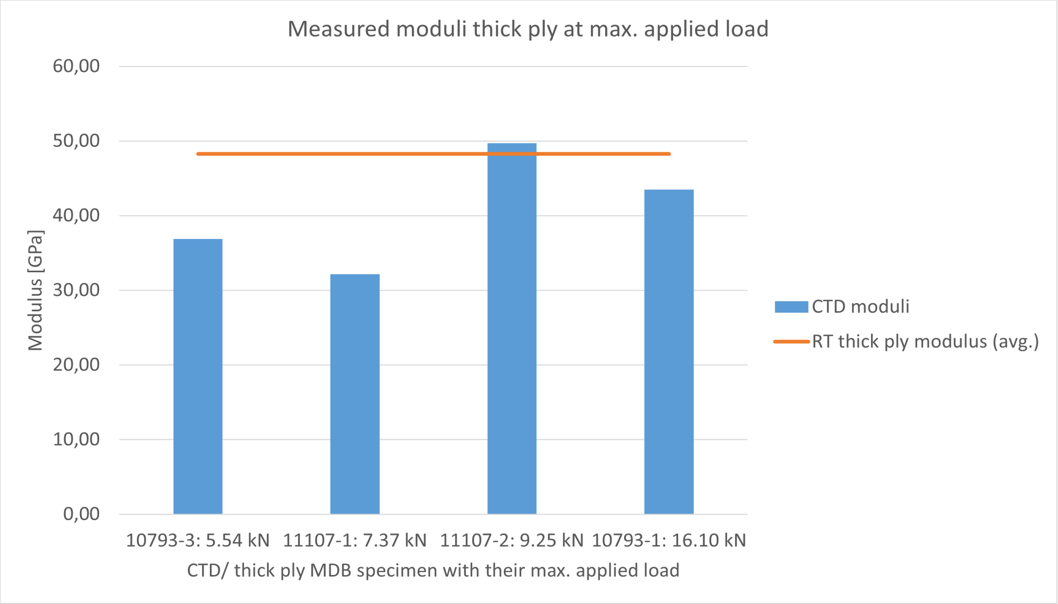

Figure 6.4: Comparison of the moduli found for the thick ply CTD/MDB specimens at maximum load. The average moduli of the RT/TEP specimens are given as reference.

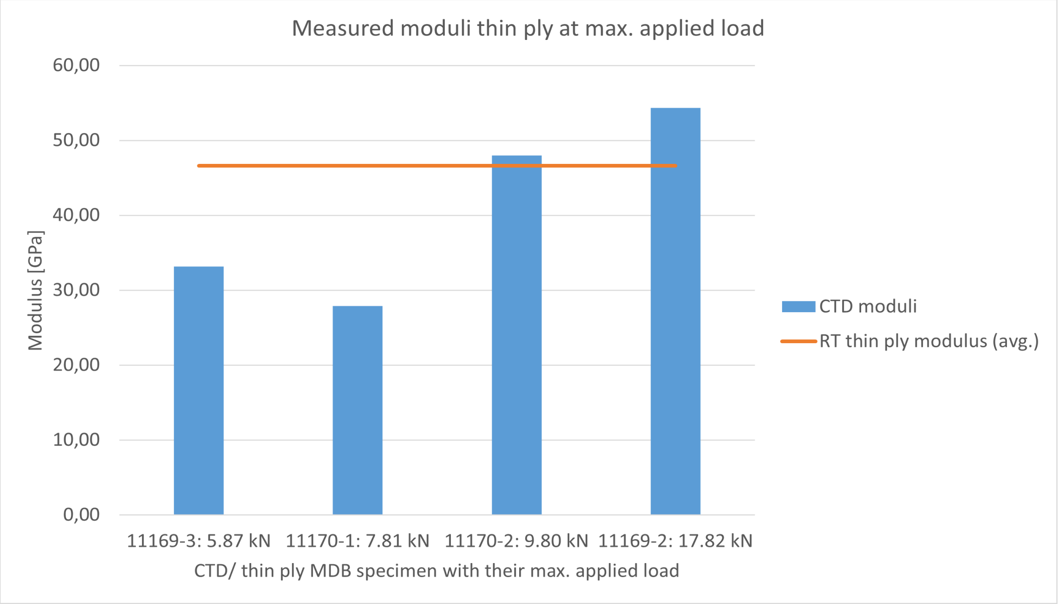

Figure 6.5: Comparison of the moduli found for the thin ply CTD/MDB specimens at maximum load. The average moduli of the RT/TEP specimens are given as reference.

Taking into account that β should be determined more accurately specifically for TC1225 and also that it is preferred to confirm S^L in an experimental way, the determination of the in situ shear strengths in relation to microcracks advocates for the use of thick ply laminates over thin ply laminates. It could however still be recommended to further investigate or improve this part of the XFEM-SCZM model.

The relationship between the identified microcracks and the alteration in permeability will be primarily addressed in subquestion 3 below. However, based on the microcrack findings, the following two observations can already be considered. Firstly, the formation of a flow path, denoting the interconnection between microcracks and/or delamination, was observed solely in sample 10793-1. This specimen was subjected to a tensile load of 16.10 kN at cryogenic temperature, which can be construed as the threshold load or 'failure' load in this context. This outcome is notable, particularly given the apparent absence of a correlation between microcracks in the RT specimens and the permeability results. Accordingly, it is inferred that, except for sample 10793-1, no significant increase in permeability is anticipated for the cryogenically loaded specimens. Secondly, microcracks in the CTD loaded specimens frequently extended across the entire thickness of the 90° ply, whereas those in the RT loaded specimens exhibited notably shorter average crack lengths. Given that neither the occurrence of flow paths nor the presence of extensive microcrack lengths could be elicited through the RT loaded specimens, it is advisable to develop an adapted permeability test configuration suitable for the smaller MDB specimens. Such modifications would enable a more accurate assessment of the experimental impact of flow paths and increased crack lengths.

In retrospect, the method employed for determining microcrack initiation raises doubts regarding the reliability of the outcomes. This method involved identifying a deviation in the evolution of modulus versus applied load to ascertain the reference load (N_{ref}). The outcomes obtained from the RT specimens appear to exhibit greater fidelity to this methodology compared to those from the cryogenic specimens. This discrepancy arises from the fact that the specimens loaded to the designated N_{ref} were 10793-6 (thick ply sample loaded to 37.5 kN (N_{ref})) and 11169-6 (thin ply sample loaded to 41.25 kN (N_{ref})), harboring 0 and 1 microcrack(s) respectively, suggesting an effective prediction of microcrack initiation. However, when applying the same methodology to the cryogenic specimens, the specimens loaded to the designated N_{ref20K} were 10793-3 (thick ply sample loaded to 5.54 kN) and 11169-3 (thin ply sample loaded to 5.87 kN), with 15 and 10 microcracks respectively. Such instances clearly deviate from the concept of microcrack initiation. Consequently, it is advisable to utilize the predicted N_{ref20K} derived from the N_{ref} values for forthcoming experiments. As elaborated in Chapter 5, the predicted N_{ref20K} for the thick ply specimens (4.518 kN) deviated by 18.4% from the experimentally chosen N_{ref20K} of 5.54 kN, while for the thin ply specimens, the deviation was 8.2%, with a predicted N_{ref20K} of 5.387 kN versus an experimentally chosen N_{ref20K} of 5.87 kN. Further experimental investigations are warranted to assess whether the calculation of N_{ref20K} based on N_{ref} can enhance the accuracy of predicting microcrack initiation.

2. How can mechanical behavior of thermoplastic materials within the temperature envelope of 20 to 333 K be simulated by means of Finite Element Modeling (FEM)?

The method uses XFEM for random microcrack initiation and propagation (intra-laminar failure) and SCZM for the delamination between plies (inter-laminar failure). In order to create the XFEM-SCZM model displayed in appendix A, the process of doing so was preceded by material and mesh characterization. A mesh with a simulated area of 100 mm^2 and 1600 elements per ply was chosen, combined with a distance of 0,5 mm between two enriched XFEM zones (*d*). It is likely that these values will have to be adjusted after checking experimentally, as *d* influences the enrichment of the mesh. The mechanical behaviour from the model is strongly dependent on the random distribution of fracture strengths and the simulation of random microcrack initiation by means of the Weibull distribution. Also, the difference in mechanical behaviour between thin ply material and thick ply material is dependent on the in situ shear strength of the matrix in the lamina as formulated by Camanho et al. [5] Next to the elastic material properties, also CTE and thermal conductivity for a temperature range of 292-493 K are already included.

Thermal conductivity (κ) is an important factor when dealing with boil-off. The more efficient the thermal conductivity of the composite namely is, the more effective the insulation becomes. The thermal conductivity is therefore a temperature-dependent material property and thermal behaviour of a composite is often measured by strength and stiffness ratios to thermal conductivity. The consortium TS.36 [38] about insulation design prescribes a thermal conductivity lower than 8E-04 $Wm^{-1}K^{-1}$. As the input value for thermal conductivity in z-direction at cryogenic temperatures is hard to determine, experiments to better determine this value are preconditional. The focal point for thermal conductivity is especially focused on the z-direction as permeability in z-direction over the thickness of the laminate is expected to be the main contributor to permeability in general.

Additionally, the calculation of the Knudsen number for different materials under different circumstances is added, an important addition to the code as it relates the flow mechanism to the critical length of microcracks. Looking at Equation (2.4), L and λ can be deducted from the experimental part of this thesis for both the RT and cryogenic conditions used. The pressure that was used was 1 bar and the temperatures were 20 K and 293 K respectively, leading to the mean free path λ = 4,7323 nm for the cryogenically loaded specimens and λ = 68,8478 nm for the RT loaded specimens; Equation (2.5) is used to calculate these values.

All maximum microcrack lengths and crack opening distances (COD's) of all the tested samples are covered in chapter 5.2.4. COD is the determining factor that influences the Knudsen number and is therefore chosen as the value of L. From the four conditions (RT and CTD, thick ply and thin ply), three of them showed microcrack initiation at the N_{ref}-load, except for the RT thick ply specimens where the first microcracks initiated at N_{ref}+67% (specimen 11107-5). As one of the aims of the thesis is to determine the critical microcrack density, the COD of this specimen and the other three N_{ref} loaded specimens are selected for Knudsen assessment. The values of L are set at 1.0 μm (11107-5: RT thick ply sample loaded to 62.5 kN ($N_{ref} + 67\%$)), 0.33 μm (11169-6: RT thin ply sample loaded to 41.25 kN (N_{ref})), 1.1 μm (10793-3: CTD thick ply sample loaded to 5.54 kN (N_{ref20K})) and 1.25 μm (11169-3: CTD thin ply sample loaded to 5.87 kN (N_{ref20K})), leading to the Knudsen numbers presented in Figure (6.6) below. Next to the two test conditions, also the condition under which the LH_2 will finally operate is presented: 20 K at a working pressure of 5 bar.

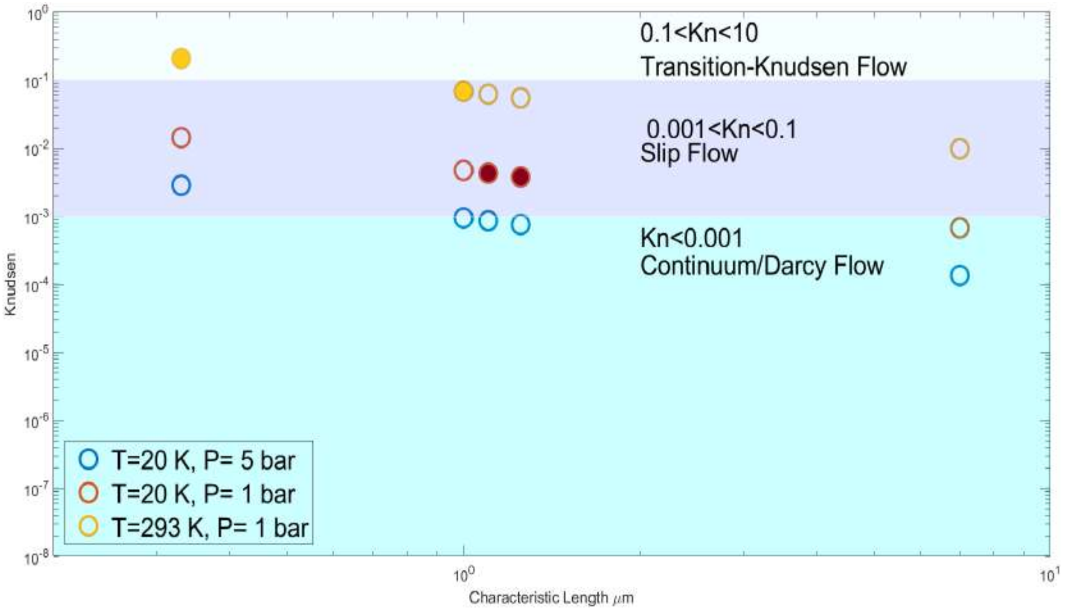

Figure 6.6: Knudsen number under three different conditions making use of the found COD's in the samples that showed microcrack initiation, from left to right: 11169-6 (RT, thin ply), 11107-5 (RT, thick ply), 10793-3 (CTD, thick ply) and 11169-3 (CTD, thin ply); the filled circles in the figure depict the empirically determined values of COD. The fibre diameter of 7 μm is characteristic for TC1225 and is given as the far-right reference value in the figure.

The Knudsen results tell us that using thin plies or thick plies leads to a different flow mechanism for the RT samples, but not for the CTD samples. However, the temperature under which the tensile test is executed is of bigger influence on the flow mechanism, because the cryogenic specimens are low in the slip flow area but close to each other and the RT specimens are in the slip flow area and in the transition-knudsen flow area, but also close to each other. By increasing the pressure to the working pressure of 5 bars, it appears that for these laminates the flow mechanisms will be on the interface of slip flow and continuum/Darcy flow. It is however recommended to execute a tensile test first under these conditions to confirm the hypothesis.

These Knudsen results at least tell that it is not desirable to only include flow by Darcy's law in the

XFEM code. Continuing, also Forchheimer's law alone is not sufficient to program transition-Knudsen flow and slip flow, because in Knudsen flow, the flow behavior is dominated by molecular interactions rather than viscous effects and Forchheimer's law does not take these molecular interactions into account. It is therefore already a recommendation to investigate a more suitable way of programming the flow mechanism in the XFEM-SCZM model, for example by using the Direct Simulation Monte Carlo (DSMC) method. [26]

The Knudsen results should be interpreted cautiously. Primarily, the manner in which the COD's are measured lacks precision, as it relies on manual assessment using microscopic images. Additionally, employing COD as the characteristic length scale presents potential challenges, as it is intrinsically linked to the mechanical properties of the material, notably in fracture mechanics contexts, rather than directly relevant to gas or liquid flow characteristics. Furthermore, there is no established consensus regarding if it is correct to implement the Knudsen number by means of Darcy's law and Forchheimer's law in order to determine the critical microcrack density.

As described in chapter 3 the boundary conditions are set in a way that the model is suitable for the scope of this thesis: uniaxial mechanical loading and one-time thermal cooling. The boundary conditions therefore include temperature as a predefined field, heat flux and convection, but also symmetry about the x- and y-plane and loading on the opposite edges. Examples of a biaxial loading concept as well as a thermal cycling concept are given in the code below, in case this is desired for future purposes. Finally, when void and inclusion content is incorporated in the FEM model it is important to compare this with the experimentally found void and inclusion content. This is possible with e.g. 3D X-ray computed tomography (CT). [13]

```python
# -*- coding: utf-8 -*-
"""
Created on Tue May  2 11:32:58 2023

@author: jensv
"""

#Biaxial loading concept
compositeModel.XsymmBC(createStepName='Step-1', localCsys=None, name=
    'BC-1', region=compositeModel.rootAssembly.sets['Set-1'])
compositeModel.rootAssembly.Set(faces=
    compositeModel.rootAssembly.instances['Part-1-1'].faces.getSequenceFromMask(
    ('[#8 ]', ), ), name='Set-2')
compositeModel.YsymmBC(createStepName='Step-1', localCsys=None, name=
    'BC-2', region=compositeModel.rootAssembly.sets['Set-2'])
compositeModel.rootAssembly.Surface(name='Surf-1', side1Faces=
    compositeModel.rootAssembly.instances['Part-1-1'].faces.getSequenceFromMask(
    ('[#2 ]', ), ))
compositeModel.Pressure(amplitude=UNSET, createStepName='Step-1',
    distributionType=UNIFORM, field='', magnitude=-300.0, name='Load-1',
    region=compositeModel.rootAssembly.surfaces['Surf-1'])
compositeModel.rootAssembly.Surface(name='Surf-2', side1Faces=
    compositeModel.rootAssembly.instances['Part-1-1'].faces.getSequenceFromMask(
    ('[#4 ]', ), ))
compositeModel.Pressure(amplitude=UNSET, createStepName='Step-1',
    distributionType=UNIFORM, field='', magnitude=-300.0, name='Load-2',
    region=compositeModel.rootAssembly.surfaces['Surf-2'])

compositeModel.fieldOutputRequests['F-Output-1'].setValues(variables=(
                'S', 'U', 'E', 'RF', 'CSTRESS', 'CDISP', 'CSDMG', 'MAXSCRT',
                'PHILSM', 'PSILSM', 'STATUSXFEM', 'SDEG'))

# Thermal cycling concept
compositeModel.SurfaceHeatFlux(createStepName='Heat transfer step',
    magnitude=5.15, name='Load-1', region=
    compositeModel.rootAssembly.surfaces['Surf-1'])

compositeModel.Temperature(createStepName='Initial',
    crossSectionDistribution=CONSTANT_THROUGH_THICKNESS, distributionType=
    UNIFORM, magnitudes=(20.0, ), name='Predefined Field-1', region=
```

```
    compositeModel.rootAssembly.sets['Set-1'])
del compositeModel.loads['Load-1']
compositeModel.rootAssembly.Surface(name='Surf-2', side1Faces=
    compositeModel.rootAssembly.instances['Part-1-6'].faces.getSequenceFromMask(
    ('[#10 ]', ), ))
compositeModel.SurfaceHeatFlux(createStepName='Heat transfer step',
    magnitude=5.15, name='Load-1', region=
    compositeModel.rootAssembly.surfaces['Surf-2'])
```

Looking at solver settings and post-processing, the current Python scripted code creates an Abaqus model subject to a load and with microcracks initiated; the permeability calculations however still miss. One wants to use the result (like nodal displacement) directly from the Abaqus result (.odb) generated by the first part of the Python XFEM-SCZM model code. It is only needed to know the structure of the file to access the required information, dedicated knowledge is needed in some cases to extract parameters. For example, to access the name of instances/steps in the odb.-file the following commands can be used: *odb.rootAssembly.instances.keys()* and *odb.steps.keys()[0]*.

Validation and optimization of this XFEM-SCZM model are the last steps in answering this sub-question. These steps can be applied to include fibre direction in relation to thermal gradient, lay-up in relation to thermal gradient, effect of barriers, fibre volume fraction, ply thickness and resin rich areas. According to the consortium TS.57 and TS.58 [38] the following specifications regarding microcracks and permeability should be met in relation to this research.

- Composite materials must be microcracking resistant (permeability is not allowed to increase due to thermal cycling (>40 cycles) between 4K and ambient temperature);
- Mechanical properties may not deteriorate due to thermal cycling within the operational temperature window of the LH_2 tank;
- Carbon fiber composite materials for tank structures, possibly in combination with surface materials, shall exhibit a diffusion coefficient not larger than 1×10^{-12} m^2/s for helium at room temperature (293 K);
- Regarding hydrogen permeation, carbon fiber composite materials for tank structures, possibly in combination with surface materials, shall exhibit a permeability not larger than 1×10^{-9} $molH_2/(m.s.MPa)$ at room temperature (293 K).

3. To what extent can experimental results contribute in the validation of the FEM model for thermal and mechanical loading conditions?
In this section the following sub-sub-questions will be answered in order to answer the stated sub-question.

1. Can the effect of thin ply materials be demonstrated?
2. Are AE sensors of added value in determining microcrack initiation?
3. Can the influence of microcracks on permeability be proven?

- **Can the effect of thin ply materials be demonstrated?**

In this thesis, an attempt has been made to demonstrate the effect of thin ply laminates by utilizing the results pertaining to microcracks and permeability. A preliminary exploration of the relationship between the effect of thin plies and the microcrack characteristics has been provided in the response to sub-question 1.

The first promising aspect of thin ply samples that was encountered was the determination of predicted microcrack initiation, or N_{ref}, for the RT samples which was higher than the thick ply samples, thus indicating a more microcrack-resistant material. This can be seen in Figures (5.2) and (5.4). However, because the measured strains were even higher relative to this, the moduli for the thin ply samples at RT turned out lower than the thick ply samples, refer to Figures (6.4) and (6.5). Purely based on the strain measurements on the RT samples that thus implicated for a slightly lower modulus and higher fracture strain for the thin ply samples, no clear preference for one of the two thicknesses exists as the difference is marginal. Additionally, it could, however, be concluded that considering microcracks (density and dimensions) the thin ply samples performed poorer meaning they showed a higher density and larger dimensions; therefore, for RT purposes, thick or regular ply laminates (>125 μm) are preferred.

In the cryogenic environment, the calculated value and experimentally determined value for N_{ref20K} was higher for the thin ply samples relative to the thick ply samples, which also resulted in higher strains for the thin ply samples. Due to uncertainties regarding the reliability of the load and strain data, the most appropriate approach for comparing moduli would be to examine specimens 11107-2 (thick ply sample loaded to 9.25 kN ($N_{ref20K} + 67$%)) and 11170-2 (thin ply sample loaded to 9.80 kN ($N_{ref20K} + 67$%)). Both specimens exhibit a higher modulus than at RT, with specimen 11107-2 demonstrating slightly superior performance. Given that the differences are once again marginal, there is no preference for either thick ply or thin ply laminates in this aspect.

Considering the microcrack characteristics in the cryogenic environment, the thick ply samples demonstrated to have a smaller amount of microcracks, a smaller microcrack density and a smaller found crack length than the thin ply samples. Conversely, the crack opening distance of the thin ply laminates is in general smaller than the thick ply samples, especially at the higher loads. In line with that, delamination, which is detrimental to the formation of leak paths, is only found in the thick ply sample 10793-1 (loaded to 16.10 kN (failure/slippage)). The thin ply laminates show discoloration due to plastic deformation on a greater regularity than the thick ply samples and could therefore be preferred looking at material quality. This is supported by fact that strain to microcrack initiation increases as ply thickness decreases, as described by Nairn et al. [27] In addition, it is not advised to make the (90°-)plies as thick as possible; this is for example suggested by the quadratic failure criterion as described in the same research by Nairn. [27] This research, compared with the results from this thesis, imply that thickening the plies too much increase the strain to microcrack initiation too much. An optimal ply thickness is therefore advised between 125 μm and 200 μm.

In conclusion, it can be stated that both thicknesses entail advantages and disadvantages. A larger COD and delamination significantly contribute to permeability, while conversely, a higher microcrack density increases the likelihood of forming a network of leak paths. Considering that the LH_2 tank will predominantly operate around lower tested loads in practice, delamination and high COD are essentially non-issues at this level. Therefore, purely in terms of microcrack density, thick ply laminates are favored for their microcrack characteristics at cryogenic temperatures.

With regard to permeability, thick ply laminates have a lower permeability than thin ply laminates, although the differences are not extremely significant (in general in the range of $\times 10^{-17}\ molHe/(m.s.Pa)$ for thick ply vs. $\times 10^{-16}\ molHe/(m.s.Pa)$ for thin ply). The explanation for this can mainly be attributed to the higher matrix percentage of thin ply laminates, which is characteristic of higher permeability because addition of fibres to the matrix usually decreases permeability. [10] [21] Looking at Fick's law, a deviating permeability dependent on ply thickness is also not expected. This is unlike leak rate, which was expected to be lower for the thick ply samples [10]; this can also be confirmed looking at Table (5.3). However, both thicknesses of laminates meet the permeability requirement of the consortium. Nonetheless, the thick ply samples are preferred once again. An interesting finding is that the sample exhibiting the lowest permeability for both laminates is the sample subjected to N_{ref} loading. This can be explained by the scissoring effect where the fibers are pulled more in length, thus densifying the free volumes, albeit without reaching the point of microcrack initiation.

It should be noted that the permeability results remain indicative. No cryogenic samples have been tested for permeability, hence the effect of thermal stresses and residual stresses on permeability is not known based on our results. To reassure, permeability is generally reduced upon exposure to cryogenic temperatures. [10] Additionally, testing was conducted with helium instead of hydrogen, which can certainly influence permeability, particularly in relation to microcrack characteristics. This point will be further discussed in addressing sub-sub-question 3 below.

Finally, when incorporating the found microcrack results in the strain energy Equation (2.3), it appears that the thin ply samples guarantee for a lower strain energy release rate, because the microcrack density is greater and hence the distance between cracks is lower. The thick ply samples with a thus relative higher strain energy release rate are preferred once again. A high strain energy release rate helps to resist the initiation and propagation of microcracks by requiring more energy for crack growth, thereby improving the overall fracture toughness and reliability of the composite material. [16]

- **Are AE sensors of added value in determining microcrack initiation?**

Unfortunately, assessing the added value of AE sensors has been significantly hindered by the fact that the AE sensors malfunctioned on the second test day. As a result, only specimens 10793-5 (thick ply sample loaded to 140.0 kN (failure/slippage)) and 11169-5 (thin ply sample loaded to 140.0 kN (failure/slippage)) can be considered for this purpose, both of which were pulled to failure with the AE sensors connected up to 70 kN.

Since the AE sensors register every acoustic event as an event, and microcracks develop well before the total failure of a laminate, it is most accurate to approach each recorded event as a potential microcrack. However, as indicated in chapter 5, the drawback is that the first AE events were observed immediately upon load initiation. At lower loads, this is likely attributable to fiber rearrangements; however, such distinction cannot be deduced from the results at present. Therefore, it is recommended for further research to explore whether these two events can be differentiated in the AE results, for instance, by isolating the two types in separate experiments, comparing the signal amplitudes, and ultimately considering fiber rearrangement as noise.

Due to the aforementioned reason, it is not sufficient to solely rely on the AE results to infer microcrack initiation. Conversely, the cumulative number of events at a specific load could serve as an indicator of the eventual formation/amount of microcracks. To achieve this, the number of AE events has been converted into an event density across the specimen. Given that the only thick ply specimen exhibiting microcracks (11107-5) was loaded at 62.5 kN, the cumulative number of events at this load, as measured in specimen 10793-5 (thick ply sample loaded to 140.0 kN (failure/slippage)), was selected for analysis. At 62.5 kN, the AE sensors registered a cumulative amount of 120728 events on specimen 10793-5 on a total volume of 65477.5 mm^3 (this excludes the clamped areas of the specimen). This translates to an event density of 1.8438 mm^{-3} or 4.3901 mm^{-2} in the case when the events are divided by solely the width (110 mm) and length (250 mm) of the testsection. In table 5.4 a microcrack density in specimen 11107-5 of 0.0104 mm^{-2} was found, more than 422 times less than indicated by the AE sensors.

A similar approach was followed for the thin ply samples: by making use of the applied load of specimen 11170-6 (thin ply sample loaded to 61.88 kN ($N_{ref} + 50$%)), the cumulative number of events at 61.88 kN was selected for analysis in the AE results of specimen 11169-5 (thin ply sample loaded to 140.0 kN (failure/slippage)). At 61.88 kN, the AE sensors registered a cumulative amount of 865160 events on specimen 11169-5 on a total volume of 65477.5 mm^3 (this excludes the clamped areas of the specimen). However when the threshold of 0.08 nm is used, due to the defect sensors as mentioned in chapter 5, a cumulative amount of only 17281 events is found. These results translate to an event density of 13.2131 mm^{-3} / 31.4604 mm^{-2} without the threshold and 0.2639 mm^{-3} / 0.6284 mm^{-2} with the threshold. In table 5.4 a microcrack density in specimen 11170-6 of 0.0212 mm^{-2} was found, still more than 29 times less than indicated by the AE sensors while already making use of the threshold value.

It can thus be said that using a threshold value is recommended to partly eliminate noise events, however the deviations between the AE results and the found microcrack densities are immense. The differences are mainly caused by the registration of noises, other damages or material events (like the rearrangements of fibers), events happening in the clamps, environmental noise and also because the microscopic assessment has been performed on a smaller section of which it is not said to be the most damaged area of the specimen. The latter argument could be different for the MDB specimens however. In conclusion, it can be stated that the AE sensors did not provide any added value in determining microcrack initiation, and unfortunately, they also failed to offer a realistic prediction for microcrack density. However, it is recommended to repeat the experiments with functional AE sensors on dogbone-shaped specimens and to employ a threshold, to be determined, to cancel out the aforementioned noise.

- **Can the influence of microcracks on permeability be proven?**

In chapter 2 it was already explained that permeability is both a molecular property in the form of diffusion but also as a microstructural property in the form of leakage. [30]. The amount and characteristics of microcracks mainly influence the latter part. To provide an initial insight, all tested samples meet the consortium's requirement for a permeability of no more than 1$\times 10^{-9}$ $molH_2/(m.s.MPa)$ at room temperature (293 K) under various loads.

There is first zoomed in on the edge-effect, which as we've seen played an influential role in the microcrack results of especially the MDB specimens. The edge effect is mainly explained by the mismatch of the elastic material properties between two adjacent dissimilar laminate layers, the free-edge effect is characterized by the concentrated occurrence of three-dimensional and singular stress fields at the free edges in the interfaces between two layers of composite laminates. The large width of the specimens is what counters the edge effect as good as possible, however as the lay-up does not contain significant 0 degree plies, edge effect still is a factor that has to be taken into account in this analysis.

Specimen 11170-6 (thin ply sample loaded to 61.88 kN (N_{ref}+50%)) is with a permeability of 1.187$\times 10^{-16}$ $molH_2/(m.s.MPa)$ the most permeable specimen of all the tested TEP specimens, but that sample thus significantly exceeds the requirement set by the consortium with the measured value. Compared with the samples that were microcrack free, this sample is approximately only two times more permeable. However, as stated by Flanagan et al. [10], leakage caused by gas flow through connected micro-cracks is typically multiple orders of magnitude higher than leakage caused by diffusion alone. This given implies that the (small) amount of microcracks found in samples 11107-5 (thick ply sample loaded to 62.5 kN ($N_{ref}+67$%)), 11169-6 (thin ply sample loaded to 41.25 kN (N_{ref})), 11170-6 (thin ply sample loaded to 61.88 kN ($N_{ref}+50$%)) and 11170-4 (thin ply sample loaded to 72.19 kN ($N_{ref}+75$%)) do not influence the helium permeability.

Next to the small amount of microcracks found in the assessed specimens, which prevent the formation of leak paths, there are a few other explanations for these results. First, no microcracks stretching over multiple plies were found, limiting the formation of a leak path. Next to that, looking at the visual appearance of the microcracks (appendix D) combined with the fact that the biggest COD found in the TEP specimens is only 2.0 μm, a possibility that the microcracks may not be sufficiently open to facilitate effective permeation is implied. In addition to that, there is tested with helium which has an atomic radius that is almost 5 times as large as hydrogen (1.20*Å* vs. 0.25*Å*) and a molecular diameter approximately also 5 times as large as hydrogen (3-5*Å* vs. 0.74*Å*). However as the kinetic diameters of H_2 and He are comparable (2.89*Å* vs. 2.60*Å*), it is not expected that the larger Helium molecules would encounter more difficulty in leaking through the microcracks compared to hydrogen molecules. This is however not the case for the diffusion part of permeability, where the size difference would have a significant impact.

The slightly higher permeation for the thin ply samples also depends mainly on the diffusional part of permeability. The explanation is sought in the higher matrix percentage of thin ply laminates, which is characteristic of higher permeability because addition of fibres to the matrix usually decreases permeability. [10] [21] But in conclusion, the influence of microcracks on permeability cannot be proven for the experiments executed in this thesis.

Based on literature, there however certainly should be a correlation between microcrack density and leak rate. This can e.g. be seen in Figure (6.7). Because the microcrack densities found for the MDB specimens are much larger than the TEP specimens, it is highly recommended to conduct the permeability testing with a TC1225 sample that has a microcrack density of at least 0.2 mm^{-2} as this is comparable with the microcrack density found in specimen 10793-3 (thick ply sample loaded to 5.54 kN (N_{ref20K})) which did not even experienced the highest applied load.

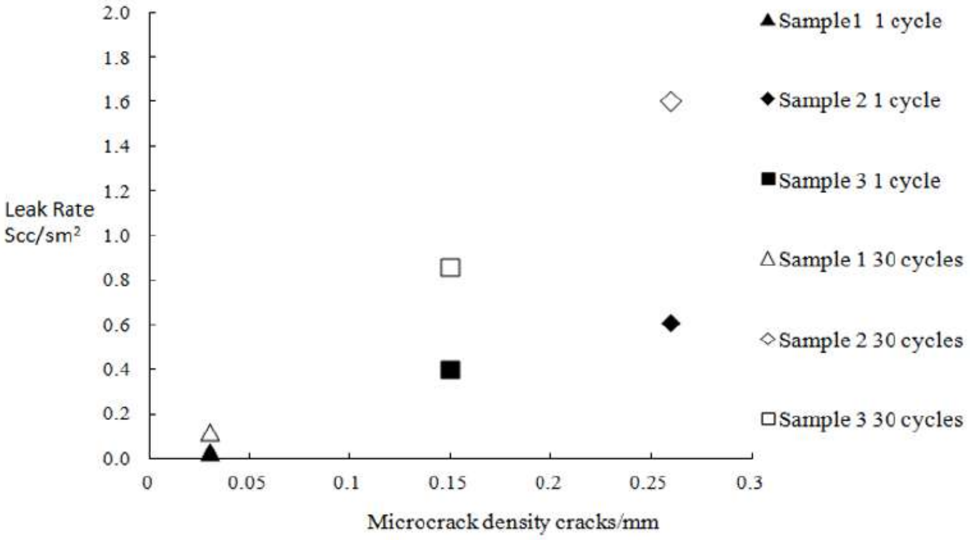

Figure 6.7: Leak rate of CF-PEEK samples without and after cryogenic cycling showing the correlation between measured microcrack density and leak rate. Taken from Flanagan et al. [10]

7

Conclusion

This chapter will present the conclusions from this research and provide an answer to the research question and next to that, a number of recommendations will be given. To do so, there is made use of the answers to the sub-questions provided in chapter 6. For convenience of the reader the research question is repeated first.

- **How can microcracking and hydrogen permeability for thermoplastic composites under tensile loading at deep cryogenic conditions be limited to a predefined level in order to fulfill the requirements for long-life, vacuum-insulated composite liquid hydrogen tanks for civil aviation?**

The final aim for the conclusion is to answer the research question by looking at the critical microcrack density and the mechanical behaviour selection criteria for composite materials. For this reason, the conclusion has been divided into the respective sections.

7.1. Critical microcrack density

What is meant with the critical microcrack density is the density following from the experiments from where poorer mechanical performance of the LM-PAEK composite and a greater contribution to permeability can be witnessed. The consortium [38] states no specific maximum microcrack density for the LH_2 tank, but does state that the materials must be microcracking resistant. In addition, the consortium does state a maximum allowable permeability of $1 \times 10^{-9}\ molH_2/(m.s.MPa)$ at room temperature (293 K) and a diffusion coefficient not larger than $1 \times 10^{-12}\ m^2/s$ for helium at room temperature (293 K).

It can be concluded that all tested RT specimens fulfill the requirement for permeability and diffusion. This compliance is regardless the load they were subjected to. There is no clear relation between increasing load and the development of permeability, and besides all thick ply samples had a lower permeability than the thin ply samples (although it was expected otherwise). However, for the RT samples, a correlation between increasing load and increasing microcrack density is proven for both thick and thin ply samples. It can be asserted based on these findings that an elevated microcrack density similarly does not impact permeability. An explanation is that the microcrack density for the RT samples is too low to contribute to permeability in any case.

The CTD samples showed a higher microcrack density than the RT samples, as expected. Contrary to the hypothesis, the thin ply samples showed to have more microcracks than the thick ply samples. The explanation is sought in the higher matrix percentage of thin ply laminates as described in chapter 6. Based on the load and strain data it can be concluded that the higher microcrack density at cryogenic temperatures will also not account for a higher permeability for this TC1225 laminate. This relation should however be confirmed experimentally.

Despite thorough verification of the entire measurement circuit and the correctness expected in strain measurements (including parallel measurements conducted at room temperature within the open cryostat to neutralize any pressure differentials affecting the bellows), it is evident that there are discrepancies in the load or strain data. Based on the observed deviations in fiber direction in both the top and bottom plies, all moduli should theoretically yield values exceeding 40 GPa. Lastly, it can be concluded that microcracks from fiber to fiber, like in Figure 3.3, are more absent than the microcracks along the fiber-matrix interface for all samples. This indicates an interfacial bonding of TC1225 that could be improved.

7.2. Material selection criteria

Considering the large variety of material selection criteria, this research is narrowed down to composite material choice, lay-up and ply thickness. During the exploratory phase of the research, the decision to utilize thermoplastics over thermosets was already made based on literature and exploratory research performed by NLR. This is mainly supported by the fact that crystallinity of a material has a direct influence on the permeability, because of the increased fracture toughness and the related ability to reduce matrix cracking. Because of industry interest, LM-PAEK / T700 UD-tape (Toray TC1225) was selected as the material to perform tests on at $20K$. Following from the thesis results it can be concluded that TC1225 is a suitable material choice, as it has met the permeability requirement of the consortium in all tested samples, regardless of the applied load. Furthermore, it has demonstrated sufficient strength and stiffness in the tensile tests. Although the material is not entirely free of microcracks, based on the results, these scores, particularly for the thick ply variant, appear to be adequate for LH_2 storage.

The QI triaxial lay-up consisting of ±30°-plies and 90°-plies was chosen, because a QI lay-up gives a balance between an UD and a crossply lay-up considering the loading conditions for the tank and to prevent for high thermal stresses. To keep internal stresses balanced and looking at the shape and loading conditions of the tank, the triaxial lay-up is the obvious choice. What can be concluded about the lay-up is that our triaxial lay-up demonstrates robust performance throughout the testing program. The dimensions of the specimens are sufficient to not let the edge effect or scissor effect play a significant role. There is gained valuable insight in the relation between fine-tuning the fiber orientation on one hand and the modulus and microcrack density on the other hand. Despite a significant inconsistency in the results, all samples with an angular deviation of approximately 6 to 7 degrees exhibited a markedly reduced modulus in the ±30°-plies, as expected. Since there is no direct correlation observed between angular deviation and microcrack density, it can be concluded that the laminate consisting of ±30°-plies and 90°-plies still remains preferable, given its higher modulus.

In this thesis two different ply thicknesses are assessed, being a thin ply variant of 0.11 mm and a regular/thick ply variant of 0.14 mm. For any load case, the thin ply specimens showed to form more microcracks, both at RT and at cryogenic temperature. The main explanations are the higher ratio of resin to fiber, increased interlaminar shear stress and possibly also manufacturing defects, because thin ply TC1225 is still an experimental material. Poor ply bonding and fiber misalignment could also be expected for the thin plies leading to more microcracks, but these do not seem to play a significant role, respectively looking at the fact that delamination/microcracks on the interfaces between plies is only found in specimen 10793-1, which is a thick ply specimen (loaded until slippage); and looking at Table 5.6 where the thin ply samples do not exhibit more extreme fiber angular deviations on the top and bottom layers compared to the thick ply samples.

A positive result for the thin ply specimens is that they exhibit a smaller COD at cryogenic temperatures and they also possessed a higher N_{ref} (load at which microcracks initiate). On the other hand, the thin ply specimens in general showed higher strains, higher microcrack density, larger crack lengths, lower strain energy release rate and almost two times more permeability. It can be concluded that the thin ply materials (<125 μm) perform less favorably than the regular ply materials, and for this reason, it is advised not to incorporate thin plies into the LH_2 tank design. In addition, it is not advised to make the (90°-)plies as thick as possible, because this will increase strain to microcrack initiation again too much. An optimal ply thickness is therefore advised between 125 μm and 200 μm.

7.3. Recommendations

After the completion of this research it is recommended to further investigate the following topics:

1. Make the XFEM-SCZM model suitable for cryogenic cycling: Grogan et al. [12] use a two-stage thermal load with different convection coefficients consisting of a processing thermal profile from the start and a tank fuelling thermal profile; the latter one is accompanied by an internal pressure ramp load being applied from the start of the fuelling profile. The intended LH_2 tank for the RDM project should however be capable of withstanding two thermal cycles per year, this should therefore be implemented in the FEM-model.

2. Adjusting 'd' (enrichment mesh generation distance) in the XFEM-SCZM model after checking experimentally.

3. Check if the used Weibull paramater in the XFEM-SCZM model needs to be adjusted based on the experimental results.

4. XFEM-SCZM model: β should be determined more accurately specifically for TC1225 and also it is preferred to confirm S^L in an experimental way, refer to the in-situ shear strength, Equation (2.17).

5. Knudsen number: By increasing the pressure to the working pressure of 5 bars, it appears that for these laminates the flow mechanisms will be on the interface of slip flow and continuum/Darcy flow. It is however recommended to execute a tensile test first under these conditions to confirm the hypothesis.

6. Investigate a more suitable way of programming the flow mechanism in the XFEM-SCZM model, for example by using the Direct Simulation Monte Carlo (DSMC) method.

7. Repeat the experiments with functional AE sensors on dogbone-shaped specimens and to employ a threshold, to be determined, to cancel out the aforementioned noise (refer to chapter 6).

8. Perform tensile and permeability experiments after cryogenic cycling. Literature like Flanagan et al. [10] show a different correlation between microcrack density and leak rate after both 1 and 30 cycles, also refer to Figure (6.7).

9. Assess if Progressive Damage Analysis (PDA) can become a reliable tool to analyse microcracking and hydrogen permeability for the used conditions in this thesis.

10. Use the 2 MDB spare specimens (thick ply specimen 11107-3 and thin ply specimen 11170-3) to be tensile tested at a lower load: the predicted/calculated N_{ref} to see if it's valuable to calculate N_{ref}'s before having to test cryogenically and if N_{ref} guarantees for a microcrack free result in the cryogenic environment. For the thick ply sample this load is 4.518 kN and for the thin ply sample this load is 5.387 kN.

11. Only utilize samples ending in -2, i.e., samples taken from the center of a plate rather than the edges, due to the observed deviant fiber angles which appear to influence the moduli.

12. Assess the effect of different preloadings on the specimens to gain insight in the effect preloading has on the edge effect and the scissoring effect.

13. Perform the permeability experiments with hydrogen.

14. Redo the permeability test with a TC1225 sample with a higher microcrack density of minimum 0.2 mm^{-2}, ideally creating TC1225 samples with a microcrack density similar to the MDB specimens and consequently test on permeability.

15. Further investigate the potential variation in permeability results on the same sample by performing multiple permeability tests on the same sample.

16. Perform a C-scan after the cryogenic tensile test to further investigate if damage initiation occurred beyond the confines of the tested region, possibly originating at the clamps, thereby concentrating all damage accumulation at those locations.

17. Implement a more precise way to determine microcrack density (e.g. micro-CT), because manual assessment, as performed in this thesis, is less accurate.

18. Confirm if a relation between the higher microcrack density at cryogenic temperatures will also not account for a higher permeability for this TC1225 laminate by performing the permeability test on the cryogenic tensile tested specimens. It is recommended to make the permeability set-up suitable for smaller specimens, as this is more realistic than adjusting the cryostat for wider specimens.

19. Use two longitudinal strain gauges on MDB specimens (both sides) instead of one longitudinal and one transverse; this could contribute to less deviating results.

20. Redo the cryogenic tensile test with more specimens to exclude differences in resin content and different residual stresses after annealing as much as possible.

21. Verify applied loads during the cryogenic tensile test by conducting the cryogenic tensile tests using specimens composed of alternative materials (such as aluminum).

References

[1] B. Atli-Veltin. “Cryogenic performance of single polymer polypropylene composites”. In: *Cryogenics* 90 (2018), pp. 86–95. ISSN: 0011-2275. DOI: `https://doi.org/10.1016/j.cryogenics.2018.01.009`. URL: `https://www.sciencedirect.com/science/article/pii/S0011227517302023`.

[2] J. Bai et al. “Tensile deformation mechanisms of an in-situ Ti-based metallic glass matrix composite at cryogenic temperature”. In: *Scientific Reports* 6 (Aug. 2016), p. 32287. DOI: `10.1038/srep32287`.

[3] V.T. Bechel et al. “Effect of stacking sequence on micro-cracking in a cryogenically cycled carbon/bismaleimide composite”. In: *Composites Part A: Applied Science and Manufacturing* 34.7 (2003), pp. 663–672. ISSN: 1359-835X. DOI: `https://doi.org/10.1016/S1359-835X(03)00054-X`. URL: `https://www.sciencedirect.com/science/article/pii/S1359835X0300054X`.

[4] M. Bubacz. “Permeability and flammability study of composite sandwich structures for cryogenic applications”. In: (Jan. 2006).

[5] P.P. Camanho et al. “Prediction of in situ strengths and matrix cracking in composites under transverse tension and in-plane shear”. In: *Composites Part A: Applied Science and Manufacturing* 37.2 (2006). CompTest 2004, pp. 165–176. ISSN: 1359-835X. DOI: `https://doi.org/10.1016/j.compositesa.2005.04.023`. URL: `https://www.sciencedirect.com/science/article/pii/S1359835X05002526`.

[6] D. Chen et al. “A Review of the Polymer for Cryogenic Application: Methods, Mechanisms and Perspectives”. In: *Polymers* 13 (Jan. 2021), p. 320. DOI: `10.3390/polym13030320`.

[7] S. Choi. “Micromechanics, fracture mechanics and gas permeability of composite laminates for cryogenic storage systems”. In: (Jan. 2005).

[8] F. Duvekot. “Storage of Liquid Hydrogen in Composite Structures”. PhD thesis. May 2021.

[9] M. Ebermann et al. “Analytical and numerical approach to determine effective diffusion coefficients for composite pressure vessels”. In: *Composite Structures* 291 (2022), p. 115616. ISSN: 0263-8223. DOI: `https://doi.org/10.1016/j.compstruct.2022.115616`. URL: `https://www.sciencedirect.com/science/article/pii/S0263822322004019`.

[10] M. Flanagan et al. “Permeability of Carbon Fibre PEEK Composites for Cryogenic Storage Tanks of Future Space Launchers”. In: *Composites Part A: Applied Science and Manufacturing* 101 (June 2017). DOI: `10.1016/j.compositesa.2017.06.013`.

[11] G. Gardener. *Demonstrating composite LH2 tanks for commercial aircraft*. 2022. URL: `https://www.compositesworld.com/articles/demonstrating-composite-lh2-tanks-for-commercial-aircraft` (visited on 12/06/2022).

[12] D.M. Grogan, C.M. Ó Brádaigh, and S.B. Leen. “A combined XFEM and cohesive zone model for composite laminate microcracking and permeability”. In: *Composite Structures* 120 (2015), pp. 246–261. ISSN: 0263-8223. DOI: `https://doi.org/10.1016/j.compstruct.2014.09.068`. URL: `https://www.sciencedirect.com/science/article/pii/S0263822314005169`.

[13] D.M. Grogan et al. “Damage and permeability in tape-laid thermoplastic composite cryogenic tanks”. In: *Composites Part A: Applied Science and Manufacturing* 78 (2015), pp. 390–402. ISSN: 1359-835X. DOI: `https://doi.org/10.1016/j.compositesa.2015.08.037`. URL: `https://www.sciencedirect.com/science/article/pii/S1359835X15003085`.

[14] D.M. Grogan et al. “Damage characterisation of cryogenically cycled carbon fibre/PEEK laminates”. In: *Composites Part A: Applied Science and Manufacturing* 66 (2014), pp. 237–250. ISSN: 1359-835X. DOI: `https://doi.org/10.1016/j.compositesa.2014.08.007`. URL: `https://www.sciencedirect.com/science/article/pii/S1359835X14002401`.

[15] J.J.M. van der Helm. “Application of composite materials for liquid hydrogen storage”. Unpublished literature study. 2022.

[16] A.J. Hodge. *Evaluation of Microcracking in Two Carbon-Fiber/Epoxy-Matrix Composite Cryogenic Tanks*. NASA/TM-2001-211194. NASA Center for AeroSpace Information, 7121 Standard Drive, Hanover, MD 21076-1320: Marshall Space Flight Center, Alabama, 2001.

[17] J. Hohe et al. “Performance of fiber reinforced materials under cryogenic conditions—A review”. In: *Composites Part A: Applied Science and Manufacturing* 141 (2021), p. 106226. ISSN: 1359-835X. DOI: `https://doi.org/10.1016/j.compositesa.2020.106226`. URL: `https://www.sciencedirect.com/science/article/pii/S1359835X20304620`.

[18] J. Hohe et al. “Validation of Puck’s failure criterion for CFRP composites in the cryogenic regime”. In: *CEAS Space Journal* 13 (Sept. 2020), pp. 1–9. DOI: `10.1007/s12567-020-00335-3`.

[19] Z.M. Huang. “Strength formulae of unidirectional composites including thermal residual stresses”. In: *Materials Letters* 43.1 (2000), pp. 36–42. ISSN: 0167-577X. DOI: `https://doi.org/10.1016/S0167-577X(99)00227-X`. URL: `https://www.sciencedirect.com/science/article/pii/S0167577X9900227X`.

[20] D. Hui and P.K. Dutta. “Cryogenic Temperature Effects on Performance of Polymer Composites”. In: *Proc. of the 5th Conference on Aerospace Materials, Processes, and Environmental Technology*. Composite Materials. 2002, pp. 1–26.

[21] J. Humpenöder. “Gas permeation of fibre reinforced plastics”. In: *Cryogenics* 38.1 (1998), pp. 143–147. ISSN: 0011-2275. DOI: `https://doi.org/10.1016/S0011-2275(97)00125-2`. URL: `https://www.sciencedirect.com/science/article/pii/S0011227597001252`.

[22] ASTM International. *2021 Annual book of ASTM standards*. Vol. 15.03. 100 Barr Harbor Drive, West Conshohocken, PA, USA: ASTM International, 2021.

[23] Clean Sky 2 JU and FCH 2 JU. “Hydrogen-powered aviation: A fact-based study of hydrogen technology, economics, and climate impact by 2050”. In: May 2020. ISBN: 978-92-9246-342-7. DOI: `10.2843/471510`.

[24] S. Kumagai, Y. Shindo, and A. Inamoto. “Tension–tension fatigue behavior of GFRP woven laminates at low temperatures”. In: *Cryogenics* 45.2 (2005), pp. 123–128. ISSN: 0011-2275. DOI: `https://doi.org/10.1016/j.cryogenics.2004.06.006`. URL: `https://www.sciencedirect.com/science/article/pii/S0011227504001572`.

[25] Q. Liu, L. Cheng, and G. Liu. “Enhanced Selective Hydrogen Permeation through Graphdiyne Membrane: A Theoretical Study”. In: *Membranes* 10 (Oct. 2020), p. 286. DOI: `10.3390/membranes10100286`.

[26] “Direct Simulation Monte-Carlo (DSMC) Method”. In: *Rarefied Gas Dynamics: Fundamentals, Simulations and Micro Flows*. Ed. by D. Mewes and F. Mayinger. Berlin, Heidelberg: Springer Berlin Heidelberg, 2005, pp. 275–315. ISBN: 978-3-540-27230-4. DOI: `10.1007/3-540-27230-5_8`. URL: `https://doi.org/10.1007/3-540-27230-5_8`.

[27] J. Nairn. “Matrix Microcracking in Composites”. In: *Polymer Matrix Composites* 2 (June 2000). DOI: `10.1016/B0-08-042993-9/00069-3`.

[28] Z. Ran et al. “Determination of thermal expansion coefficients for unidirectional fiber-reinforced composites”. In: *Chinese Journal of Aeronautics* 27.5 (2014), pp. 1180–1187. ISSN: 1000-9361. DOI: `https://doi.org/10.1016/j.cja.2014.03.010`. URL: `https://www.sciencedirect.com/science/article/pii/S1000936114000429`.

[29] M. Robinson et al. “Trade Study Results for a Second-Generation Reusable Launch Vehicle Composite Hydrogen Tank”. In: Apr. 2004. ISBN: 978-1-62410-079-6. DOI: `10.2514/6.2004-1932`.

[30] Z. Sápi and R. Butler. “Properties of cryogenic and low temperature composite materials – A review”. English. In: *Cryogenics* 111 (Oct. 2020). ISSN: 0011-2275. DOI: `10.1016/j.cryogenics.2020.103190`.

[31] D. Schultheiß. “Permeation Barrier for Lightweight Liquid Hydrogen Tanks”. PhD thesis. Oct. 2007.

[32] B. Seers, R. Tomlinson, and P. Fairclough. “Residual stress in fiber reinforced thermosetting composites: A review of measurement techniques”. In: *Polymer Composites* 42 (Jan. 2021). DOI: `10.1002/pc.25934`.

[33] J. Shi et al. “Diffusion and Flow Mechanisms of Shale Gas through Matrix Pores and Gas Production Forecasting”. In: *SPE Unconventional Resources Conference, Canada* (Nov. 2013). DOI: `10.2118/167226-MS`.

[34] A. Singh Brar. “A Step towards permeability modelling of Composites”. PhD thesis. Aug. 2021.

[35] M. Sippel et al. “Advanced Cryo-Tanks Research in CHATT”. In: July 2013.

[36] Shunjun Song, Jack R. Vinson, and Roger M. Crane. “Low-Temperature Effects on E-glass/Urethane at High Strain Rates”. In: *AIAA Journal* 42.5 (2004), pp. 1050–1053. DOI: `10.2514/1.9598`.

[37] Washington University in St. Louis. *Abaqus Scripting Reference Manual*. URL: `https://classes.engineering.wustl.edu/2009/spring/mase5513/abaqus/docs/v6.6/books/ker/default.htm?startat=pyi04.html` (visited on 05/20/2023).

[38] *Technical Specification (TS) - LH2 Storage System*. Toray Advanced Composites Netherlands B.V., ADSE B.V., Airborne, Bold Findings B.V., Cryoworld B.V., Fokker Aerostructures B.V., IT’s Engineering, Kok & Van Engelen Composites Structures B.V., NLR, PhotonFirst Technologies B.V., Technische Universiteit Delft / SAM|XL, Somni Solutions B.V., TANIQ B.V., 2021.

[39] The Engineering ToolBox. *Hydrogen - Density and Specific Weight vs. Temperature and Pressure*. 2018. URL: `https://www.engineeringtoolbox.com/hydrogen-H2-density-specific-weight-temperature-pressure-d_2044.html`.

[40] Hydrogen Tools. *Liquid Storage Vessels*. URL: `https://h2tools.org/bestpractices/liquid-storage-vessels#:~:text=Cryogenic%20tanks%20are%20vacuum%2Dinsulated,850%20kPa%20(~123%20psi)..`

[41] Toray advanced composites. *Product Toray Cetex TC1225*. 2022. URL: `https://www.toraytac.com/product-explorer/products/gXuK/Toray-Cetex-TC1225`.

[42] N. Van Zon. “Liquid Hydrogen Powered Commercial Aircraft: Analysis of the technical feasibility of sustainable liquid hydrogen powered commercial aircraft in 2040”. PhD thesis.

[43] H. Zhang et al. “Tunable Hydrogen Separation in sp–sp2 Hybridized Carbon Membranes: A First-Principles Prediction”. In: *The Journal of Physical Chemistry C* 116 (July 2012), pp. 16634–16638. DOI: `10.1021/jp304908p`.

[44] P. Zhang et al. “A multi-flow regimes model for simulating gas transport in shale matrix”. In: *Géotechnique Letters* 5 (Sept. 2015), pp. 231–235. DOI: `10.1680/geolett.15.00042`.

[45] H. Zheng et al. “The Application of Carbon Fiber Composites in Cryotank”. In: Mar. 2018. ISBN: 978-953-51-3905-8. DOI: `10.5772/intechopen.73127`.

[46] J. Zhou et al. “Chapter Eleven - Enhanced gas recovery technologies aimed at exploiting captured carbon dioxide”. In: *Sustainable Natural Gas Reservoir and Production Engineering*. Ed. by D.A. Wood and J. Cai. Vol. 1. The Fundamentals and Sustainable Advances in Natural Gas Science and Eng. Gulf Professional Publishing, 2022, pp. 305–347. ISBN: 978-0-12-824495-1. DOI: `https://doi.org/10.1016/B978-0-12-824495-1.00010-3`. URL: `https://www.sciencedirect.com/science/article/pii/B9780128244951000103`.

A

Source Code XFEM-SCZM model

The initial code is created by Singh Brar [34]. During this thesis, the code is expanded and made suitable for our thin ply, LM-PAEK material, with all constants already filled in. The codebase for this thesis project is published on a GitHub repository, ensuring transparency and accessibility for fellow researchers and enthusiasts. This step not only promotes collaboration but also enhances the reproducibility of the findings. Additionally, I've utilized 4TU.ResearchData to make the repository citable and to provide persistent, long-term preservation. 4TU.ResearchData is a reliable platform for preserving and sharing research data, to securely store supplementary datasets and materials associated with e.g. a thesis. Next to the code, the datasets on these two platforms also consist of the *Apache 2.0* license and a README.md. The README.md acts as the first point of contact for anyone who visits the repository, helping them understand the purpose of the project and how they can engage with it effectively.

The source code is available at:

- Github: `https://github.com/jensvdhelm/XFEM-SCZM-microcracks`
- 4TU.ResearchData: `https://data.4tu.nl/datasets/4303d493-d687-4ded-981b-b1714619097a`
- 4TU.ResearchData DOI: 10.4121/4303d493-d687-4ded-981b-b1714619097a

```
# -*- coding: utf-8 -*-
"""
Created on Sat Feb 11 10:05:04 2023

@author: Jens van der Helm, Arshdeep Singh Brar
@owner: TU Delft
"""

"""

XFEM-SCZM-microcracks



Copyright 2024 <Arshdeep Singh Brar, Jens van der Helm>



Licensed under the Apache License, Version 2.0 (the "License");

you may not use this file except in compliance with the License.

You may obtain a copy of the License at



    http://www.apache.org/licenses/LICENSE-2.0

```

```


Unless required by applicable law or agreed to in writing, software

distributed under the License is distributed on an "AS IS" BASIS,

WITHOUT WARRANTIES OR CONDITIONS OF ANY KIND, either express or implied.

See the License for the specific language governing permissions and

limitations under the License.

"""
```

B

Test proposal TC1225 microcracking

B.1. Test proposal

Dedicated to innovation in aerospace

TO *(action)*:

TO (info):

SPOKEN TO:

FROM:
Jens van der Helm
SUBJECT:
Test proposal TC-1225 microcracking

COMPANY:

DEPARTMENT:
NLR/AVST
CODE / ORDERNUMBER:
1292207 .2.5
DATE:
11-7-2023
PAGE:
1 / 10

Composite LH2 tank project, TC1225 microcracking

Together with Toray Advanced Composites and 12 other parties, NLR takes part in the Netherlands LH2 composite tank consortium which is funded by the Netherlands RDM (research & development mobility) Fund. The goal of this consortium is to develop a long-life, fully composite LH2 tank starting from December 2021 and ultimately to enable zero-emissions aircraft. Within this consortium, NLR is responsible for testing and selecting different composite materials at 20 K: the "ST_129207_Composiet_LH2_tank " project.

Within this research, a thesis is written where a FEM-model is compared and validated with experimental research focused on microcrack initiation and the relationship with permeability at room temperature (RT) and 20 K. This document presents the experimental investigation into the microcracking and permeability of TC1225 for liquid hydrogen storage tanks. The effects of cryogenic temperatures, tensile loading, material defects, and ply thickness on the microcracking and permeability of numerous test specimens are investigated; This will be accomplished by performing tensile tests at RT and 20 K and by performing permeability tests at RT. The test instruction is based on ASTM D3039 - Standard Test Method for Tensile Properties of Polymer Matrix Composite Materials.

The aim of the experiments described below is to 1. generate input values, and 2. serve as validation for an XFEM-SCZM model which will be used to model microcracking and leak rate in composite materials; in this model XFEM will be used to model microcrack growth. The results of these simulations could be used to model leakage of LH_2 using computational fluid dynamics. Regarding permeability, the model can be validated at room temperature using the current test setup.

Materials

From the thermoplastic screening and determination phase in 2022, Toray LM-PAEK / T700 (TC1225) was selected for further research. As the influence of ply thickness on microcracking and permeability is one of the research objectives, the same material in two different ply thicknesses is selected. The cured ply thickness of the regular panel is about 0.14 mm. The cured ply thickness of the thin ply panel is about 0.11 mm.

- **Toray LM-PAEK / T700 (TC1225)**: Cetex TC 1225 PAEK CW 0145 305 34 220 SLIT to ¼"

Ref. 1	ST_1292207-25-WI-020-0-RG
Ref. 2	ST_1292207-25-WI-027-0-RG
Ref. 3	ST_1292207-25-WI-051-0-RG
Ref. 4	ST_1292207-25-WI-052-0-RG

Additionally, in the thin ply variant:

- **Toray TC1225 / T700G / 36**: Cetex TC 1225 PAEK CW 0100 305 36 156 SLIT to ¼"

Ref. 5	ST_1292207-25-WI-055-0-RG
Ref. 6	ST_1292207-25-WI-056-0-RG

Ref. 7 ST_1292207-25-WI-057-0-RG
Ref. 8 ST_1292207-25-WI-058-0-RG

The material has a T_m of 305 °C and has a typical process window of 340-360 °C. The panels are manufactured by means of AFP.

Lay-up

For the proposed tests in this proposal, two different lay-ups will be used, one for the regular ply thickness laminate and one for the thin ply thickness laminate. For the regular panel, a triaxial quasi-isotropic and symmetric lay-up is chosen: $(30,-30,90)_2(30, -30, 90, -30, 30)(90, -30, 30)_2$. Hypothesised is that this lay-up will show microcrack initiation when subjected to a 0 degree tensile test and besides that this lay-up can provide decent resistance to (extreme) thermal stresses. With an average ply thickness of 0.14 mm, this will give a base material of 2.38 mm.

In order to create comparable results for a thin ply laminate, it is important to create a lay-up with comparable total thickness. The thin ply laminate therefore has the following lay-up: $(30,-30,90)_3(30, -30, 90, -30, 30)(90, -30, 30)_3$. With an average ply thickness of 0.11 mm, this will give a base material of 2.53 mm.

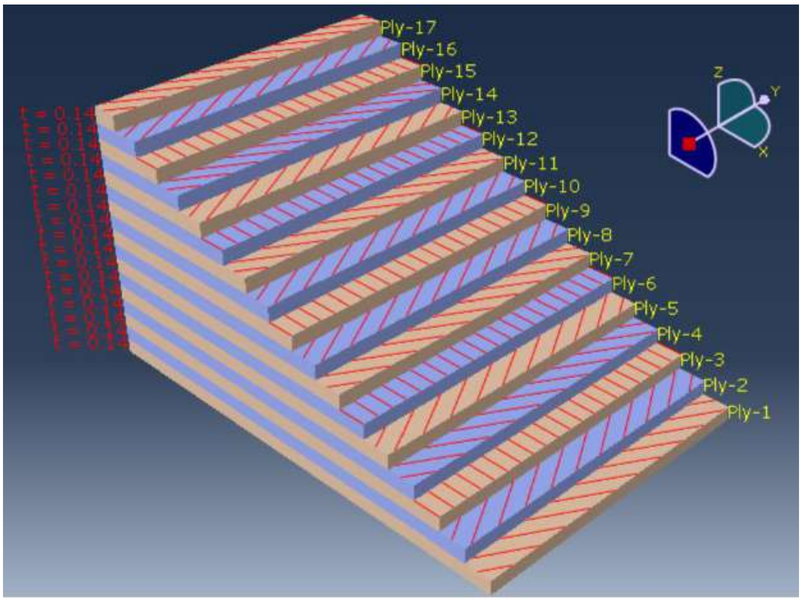

Figure 1: Ply stack plot of the regular thickness ply laminate, y-axis being the 0° tensile

Test conditions

A part of the specimens will be exposed to cryogenic temperatures. To make sure that no discontinuities or material defects are measured and no batch effects, also one reference specimen of each same panel/batch will be tested at room temperature; besides, all specimens will be checked on quality by means of C-scan. The following conditions will be tested:

RTD: The specimens will be manufactured and half of them will be tested in the “as received” condition at room temperature of 21 ±3 ºC for both microcracking and permeability. Since all specimens will be tested within week(s) after the manufacturing, the specimens are considered dry. No additional drying is proposed.

CTD: The specimens will be manufactured and half of them will be tested at the cryogenic temperature of -253 ºC for only microcracking. For each of these specimens it concerns a one-time cooldown, so thermal cycling is not applicable. Since all specimens will be tested within week(s) after the manufacturing, the specimens are considered dry. No additional drying is proposed.

Test specimens

Microcracks frequently represent one of the primary modes of damage initiation in composite laminates, specifically in plies off-axis to loading directions (transverse cracks). An additional problem microcracks hold for cryogenic tanks, is that microcracks can get interconnected with each other and create a leak path contributing to a higher permeability. To induce this phenomenon, all tensile test in this proposal will be performed in 0°. As the lay-ups are composed of -30, 30 and 90 plies, it is expected that microcracks will quickly occur in the 90-plies.

As the RT tensile test specimens will be tested on permeability and the permeability setup requires specific specimen dimensions, these specimens differ from the cryogenic tensile test specimens. The latter ones namely have the modified dogbone shape (250 x 30 mm) following ASTM D3039, however these dimensions are not feasible in the permeability setup.

For the tensile tests at RT acoustic emission sensors will be used; the first specimen will be subjected to a uniaxial tensile load until failure. Then, it is hypothesized that a certain strain level N_{ref} and N_{ref20K} can be deducted from the acoustic emission graph: the strain which is responsible for the initial accumulated matrix cracking. The following specimens will be subject to an increasing strain level above N_{ref} and N_{ref20K}.

The following specimens will be used:

Tension and permeability (TEP): Rectangular specimens of 330 mm length and 110 mm width; test section of 250 x 110 mm for tension, reduced to 110 x 110 mm for permeability. The dimensions are deviating from ASTM D3039 because of the required specimen dimensions for the permeability setup. Two strain gauges per specimen for the uniaxial stress state will be used. As there is dealt with a near homogeneous strain field and a normal temperature range, Y series linear gauges are being used, centers of the gages located at 165 mm length and 40 and 70 mm width.

- HBK 1-LY66-6/350 (LY Linear Strain Gauges with 1 Measuring Grid for composite)

Modified dogbone (MDB): Specimens shaped like a dogbone, based on ASTM D3039 for a balanced and symmetric tensile specimen, but slightly modified to 250 mm length and 30 mm width; test section of 40 x 15 mm. One strain gauge per specimen (0°/90° T rosette) will be used, but only for the uniaxial stress state. As there is dealt with a near homogeneous strain field but at extreme temperatures, C series linear gauges are being used, center of the gage located at 125 mm length and 15 mm width.

- HBK 1-XC11-3/350 (C series SG with 2 measuring grids, 0°/90° T rosette, $\alpha = 10.8$ [10^{-6} /K])

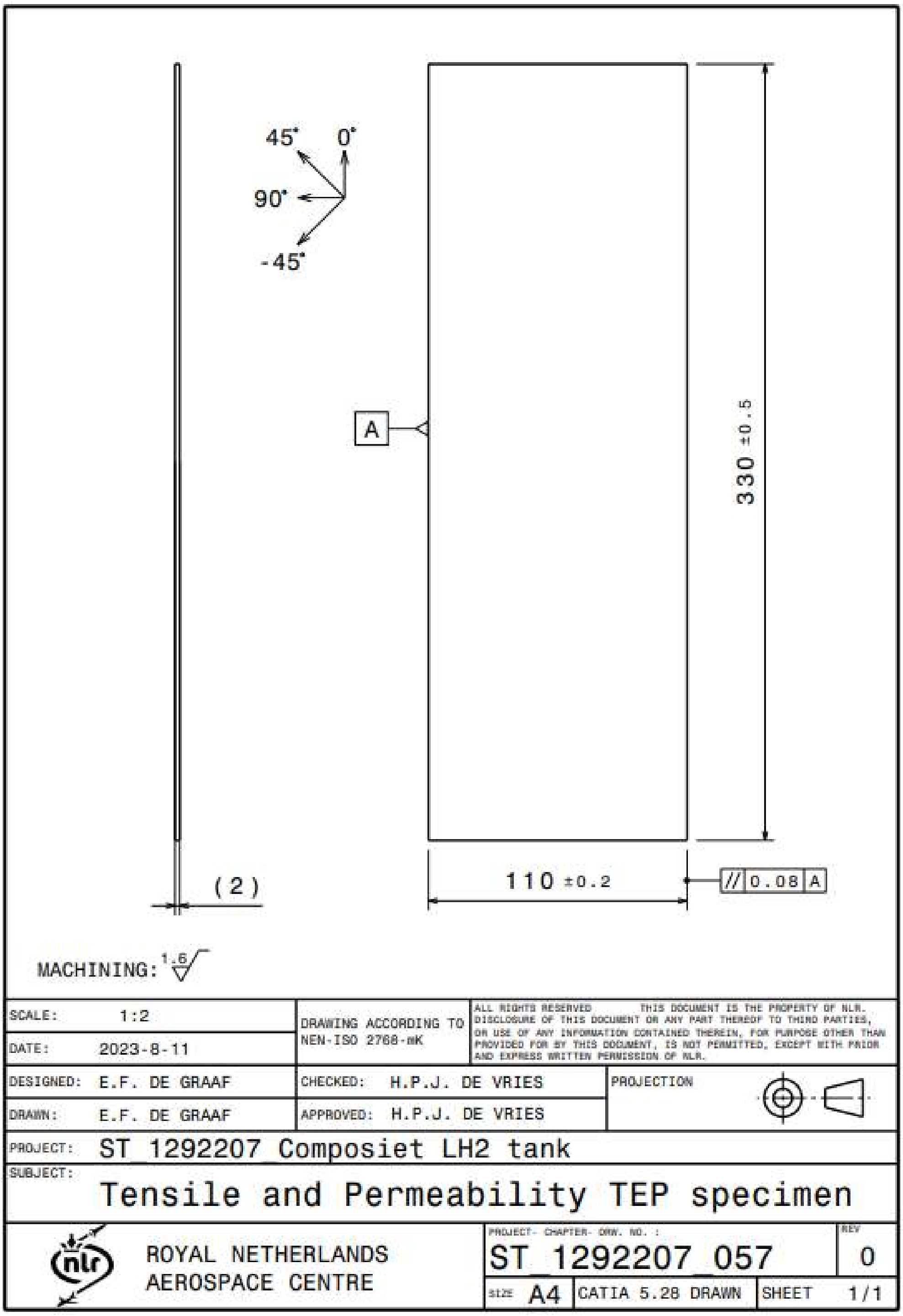

Figure 2: Drawing of TEP specimen

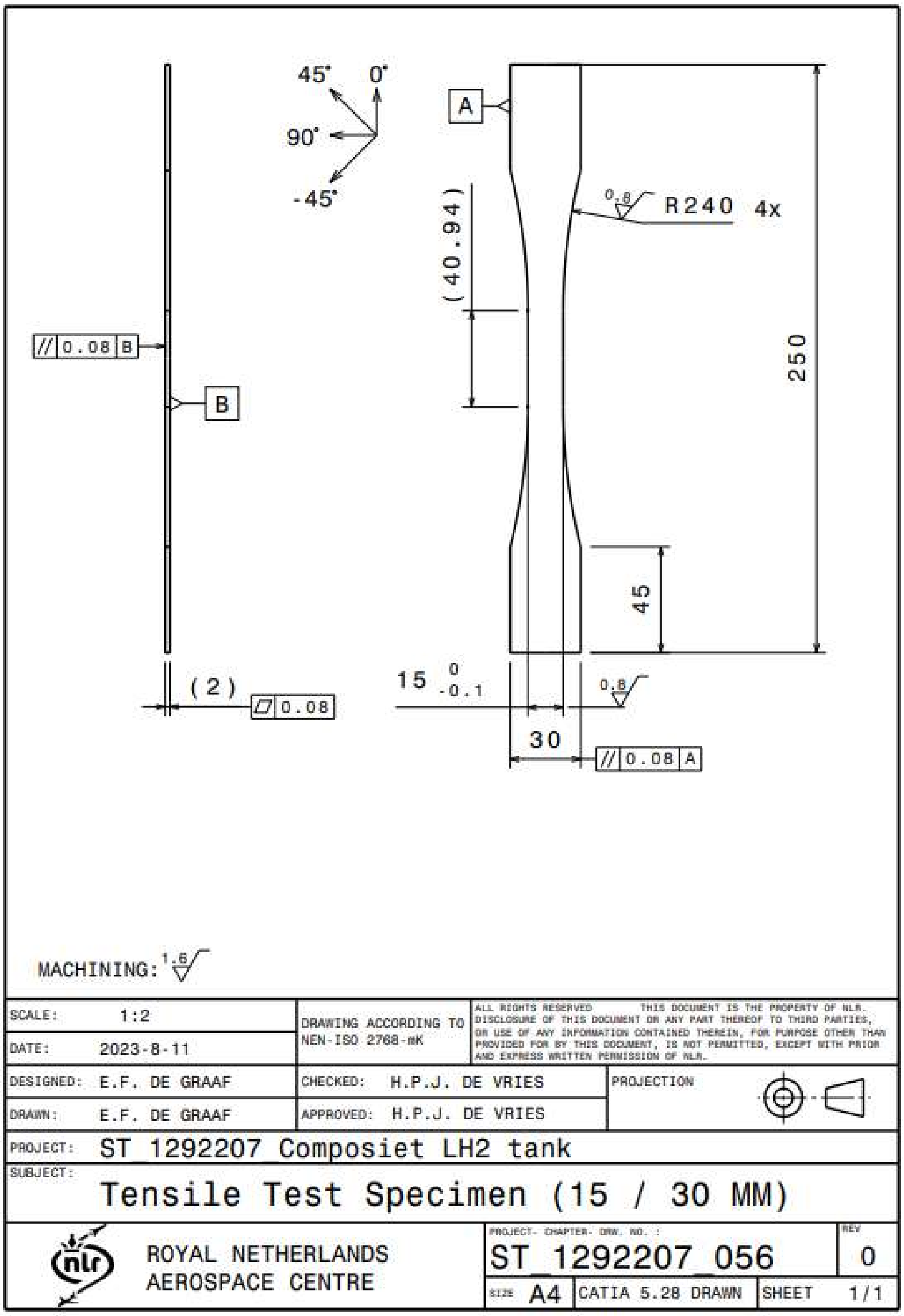

Figure 3: Drawing of MDB specimen

Test method

The test method consists of four parts, of which three apply for the TEP specimens and two apply for the MDB specimens. Below the tests are described and subsequently in Table 1 the test matrix for TEP specimens is displayed and in Table 2 the test matrix for MDB specimens is displayed. Also the two different conditions, RTD for room temperature and CTD for cryogenic temperature, are incorporated into these test matrices.

RT tensile test: The specimens will be tested according to ASTM D3039. No tabs will be used in this test as the specimens are not UD in length direction, therefore the tensile forces will not be extremely high and grip-induced failure is not expected. Besides, no conditioning is necessary. Next to a strain gage located in the coupon gage section, also (2) Acoustic Emission (AE) sensors VS900-M will be applied. These AE sensors have a diameter of 20.3 mm and will be located 10 mm off each gripper on the central length axis. The large distance between the AE sensors is suggested to localize the defect with high accuracy. The large width of the specimens is what counters the edge effect as good as possible, however as the lay-up does not contain significant 0° plies, edge effect still is a factor that has to be taken into account when analyzing results.

Cryo tensile test: The specimens will be tested according to ASTM D3039. This test will be executed at -253 ºC. To prevent for heat convection from the grippers, these specimens will be provided with glass/epoxy tabs of 1.5 mm; in this way the tabs serve as isolation for the specimens which will be sprayed upon with liquid helium. For this test only a strain gage located in the coupon gage section will be applied. The AE sensors are no option here as these are unsuitable for the cryostat and the AE signal cannot be transferred outside the cryostat. Instead the RT tensile test AE graph will be coupled with the accompanying RT strain curve. The cryo tensile test strain curve will then be compared with the RT strain curve.

The modified larger specimen width of 30 mm instead of 25 mm of the specimens is what counters the edge effect as good as possible, however as the lay-up does not contain significant 0° plies, edge effect still is a factor that has to be taken into account when analyzing results.

Permeability: After the RT tensile test, the test section of 110 x 110 mm will be cut out of the centre of the specimens. Additionally, these specimens will be tested on hydrogen permeability following the method described in Annex 1.

Optical microscopy: The test sections of 110 x 110 mm for the RT tensile test / permeability test specimens will be cut to 80 x 80 mm and subsequently will be cut into three sections. Together with the Cryo tensile test specimens (cut out test sections of 40 x 15 mm), these specimens will be placed under an optical microscope and will be manually assessed on (the amount of) microcracks. The microcracks will be counted in the order of amount cracks per mm.

Ply thickness	Specimen nr.	Reference	Product nr.	C-scan UT	Condition	RT tensile test	Permeability	Optical microscopy
Thick (140 µm)	1 / 10793-4	x	10793	x	RTD		(x)	
Thick (140 µm)	2 / 10793-5		10793	x	RTD	x, failure		
Thick (140 µm)	3 / 10793-6		10793	x	RTD	x, Nref*	x	x
Thick (140 µm)	4 / 11107-4		11107	x	RTD	x, Nref+33%		
Thick (140 µm)	5 / 11107-5		11107	x	RTD	x, Nref+67%	x	x
Thick (140 µm)	6 / 11107-6		11107	x	RTD	x, 30 kN	x	
Thin (110 µm)	13 / 11169-4	x	11169	x	RTD		x	
Thin (110 µm)	14 / 11169-5		11169	x	RTD	x, failure		
Thin (110 µm)	15 / 11169-6		11169	x	RTD	x, Nref	x	x
Thin (110 µm)	16 / 11170-4		11170	x	RTD	x, Nref+25%		
Thin (110 µm)	17 / 11170-5		11170	x	RTD	x, Nref+50%	x	x
Thin (110 µm)	18 / 11170-6		11170	x	RTD	x, Nref+75%		

*N_{ref}: the strain which is responsible for the initial accumulated matrix cracking

Table 1: Test matrix TEP specimens

Ply thickness	Specimen nr.	Reference	Product nr.	C-scan UT	Condition	Cryo tensile test	Optical microscopy
Thick (140 µm)	7 / 10793-1	x	10793	x	RTD		
Thick (140 µm)	8 / 10793-2		10793	x	CTD	x, failure	
Thick (140 µm)	9 / 10793-3		10793	x	CTD	x, Nref20K*	x
Thick (140 µm)	10 / 11107-1		11107	x	CTD	x, Nref20K+10%	x
Thick (140 µm)	11 / 11107-2		11107	x	CTD	x, Nref20K+(t.b.d.)%	T.b.d.
Thick (140 µm)	12 / 11107-3		11107	x	CTD	Spare	
Thin (110 µm)	19 / 11169-1	x	11169	x	RTD		
Thin (110 µm)	20 / 11169-2		11169	x	CTD	x, failure	
Thin (110 µm)	21 / 11169-3		11169	x	CTD	x, Nref20K*	x
Thin (110 µm)	22 / 11170-1		11170	x	CTD	x, Nref20K+10%	x
Thin (110 µm)	23 / 11170-2		11170	x	CTD	x, Nref20K+(t.b.d.)%	T.b.d.
Thin (110 µm)	24 / 11170-3		11170	x	CTD	Spare	

*N_{ref20K}: the strain which is responsible for the initial accumulated matrix cracking at 20 K

Table 2: Test matrix MDB specimens

Annex 1: Permeability measurements

The NLR performed helium permeability measurements on multiple composite samples the past several months. The goal is to perform similar permeability tests with hydrogen gas in the near future. A main difference between helium and hydrogen permeability testing is a persistent elevated level of hydrogen in the test apparatus of about 3*10-6 mbarL/s of hydrogen measured with a leak detector, whereas the helium background level is <1*10-12 mbarl/s. This persistent elevated level of helium in the test apparatusis caused by the break-up of water molecules into atomic hydrogen and OH molecules and the formation of H2 molecules from the atomic hydrogen inside the mass spectrometer of the leak detector and prevents permeability measurements on samples with low permeability. To reduce the high hydrogen background level the vacuum side of the test setup has to be baked-out to reduce the amount of water molecules here, which is not possible with a leak tester.

For this reason a hydrogen permeability measurement setup with a RGA (Rest Gas Analyser) is proposed (see figure underneath for an impression). This setup consist of a vacuum part (red) with a RGA, high vacuum sensor, temperature sensors, heaters, external insulation (TBD), turbo pump and a sample holder (with a sample support if needed). This part can be bake-out at a TBD temperature (e.g. 100°C, depending on the used materials such as O-rings and insulation materials) by means of the heaters and the RGA can be degassed, both to remove water from their (internal) surfaces.

The second part of the hydrogen permeability measurement setup is the gas containing part (green), consisting of a small volume filled with hydrogen with the required pressure (e.g. 1 or 2.5 bara), a pressure sensor, rough vacuum pressure sensor, temperature sensors, the other side of the sample holder and several valves for evacuating, filling and flushing this part.
The sensitivity of the RGA is not calibrated. Ideally the setup including the RGA is calibrated with a calibrated H2 leak. The NLR however does not possess such leak and they are difficult to get and are expensive. Later on it might be worth to acquire such a leak but on short notice the following procedure is proposed:

1. Measure the hydrogen back-ground level of the RGA setup.
2. Bake-out the test setup
3. Re-measure the hydrogen back-ground level of the RGA setup.
4. Measure the calibrated helium leak with the leak detector to check the calibrated leak.
5. Exchange the calibrated helium leak with the adjustable leak and a gas reservoir
6. Fill the gas reservoir with helium at a TBD pressure.
7. Set the helium peak measured with the RGA setup with the adjustable leak to the same level as measured at step 4 while measuring it with the leak detector.
8. Measure the helium level of the calibrated NLR helium leak with the RGA setup
9. Exchange the calibrated helium leak with the adjustable leak and the filled gas reservoir
10. Check if the helium peak measured with the RGA setup has the same value as the calibrated leak
11. Replace the helium gas in the gas reservoir with hydrogen gas at the same pressure
12. Measure the hydrogen peak with the RGA setup.

With this procedure the hydrogen sensitivity of the RGA setup can be established. All needed items to perform this procedure are available at the NLR TVL.

The sensitivity of the RGA can now also be compared with the leak detector at other leak values with the adjustable leak, e.g. 100x lower and 100x higher leak level.

Another issue with hydrogen is of course the high flammability of hydrogen. To perform the hydrogen permeability measurements safely the amount of hydrogen inside the setup will be minimalized. The worst case scenario for the needed amount of hydrogen is testing a (thick) sample with pronounced permeability through which the hydrogen molecules permeates slowly. If a maximum leak rate of 5*10-6 mbarl/s is assumed for a test duration of four days, an amount of approximately 1.3 mbarl/0.12 mgr of hydrogen will permeate the sample. If a hydrogen pressure decrease of 1% on the hydrogen side of the sample is allowed the reservoir will need to contain 130 mbarl/12 mgr of hydrogen. This amount is regarded to be safe to handle in a normal laboratory environment (the total amount of released energy at combustion is about 1650 J or 0.46 Wh). The fill procedure for this hydrogen reservoir is TBD.

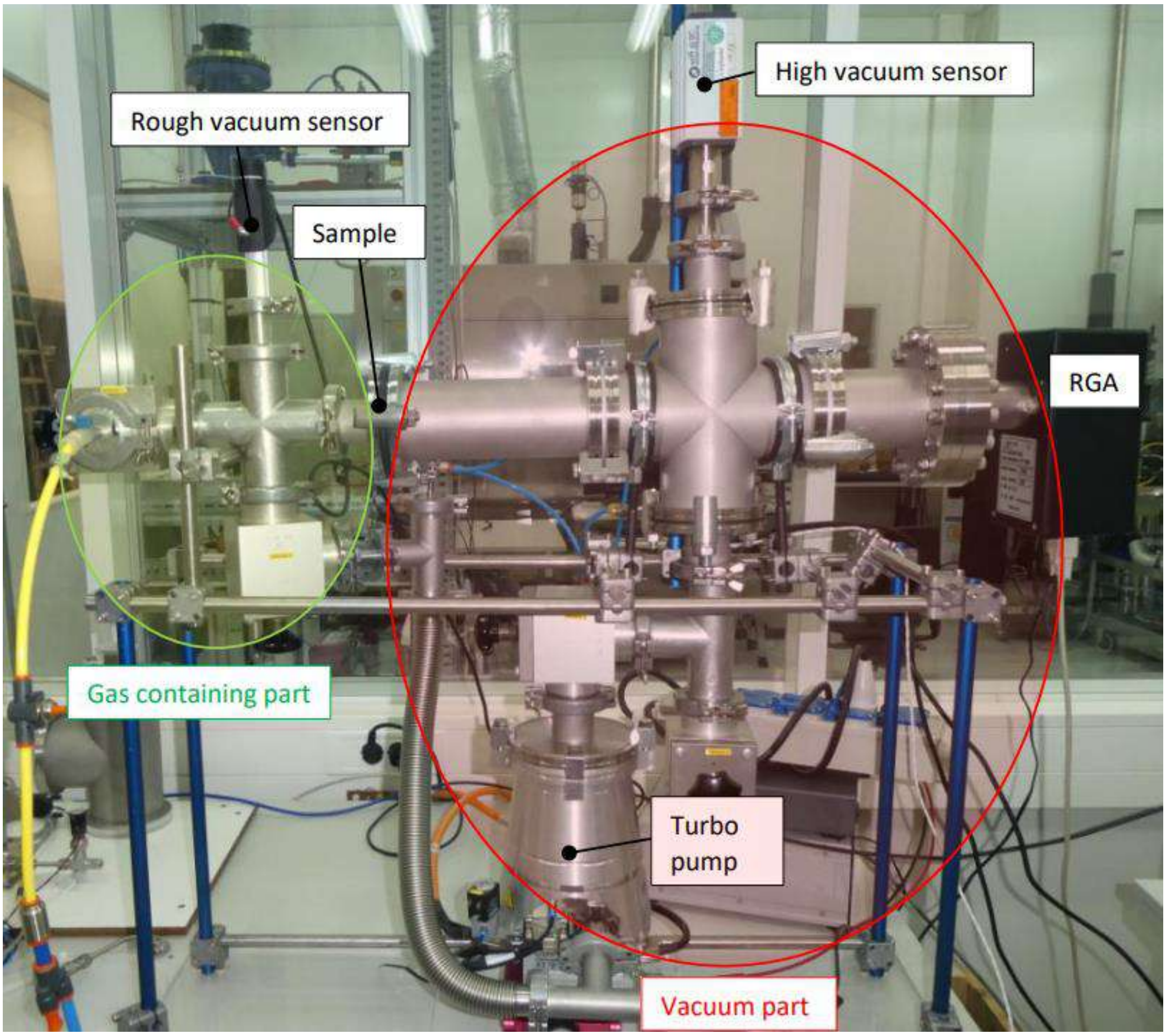

Figure A.1: Permeability test set-up with the RGA

B.2. Machining panel drawing

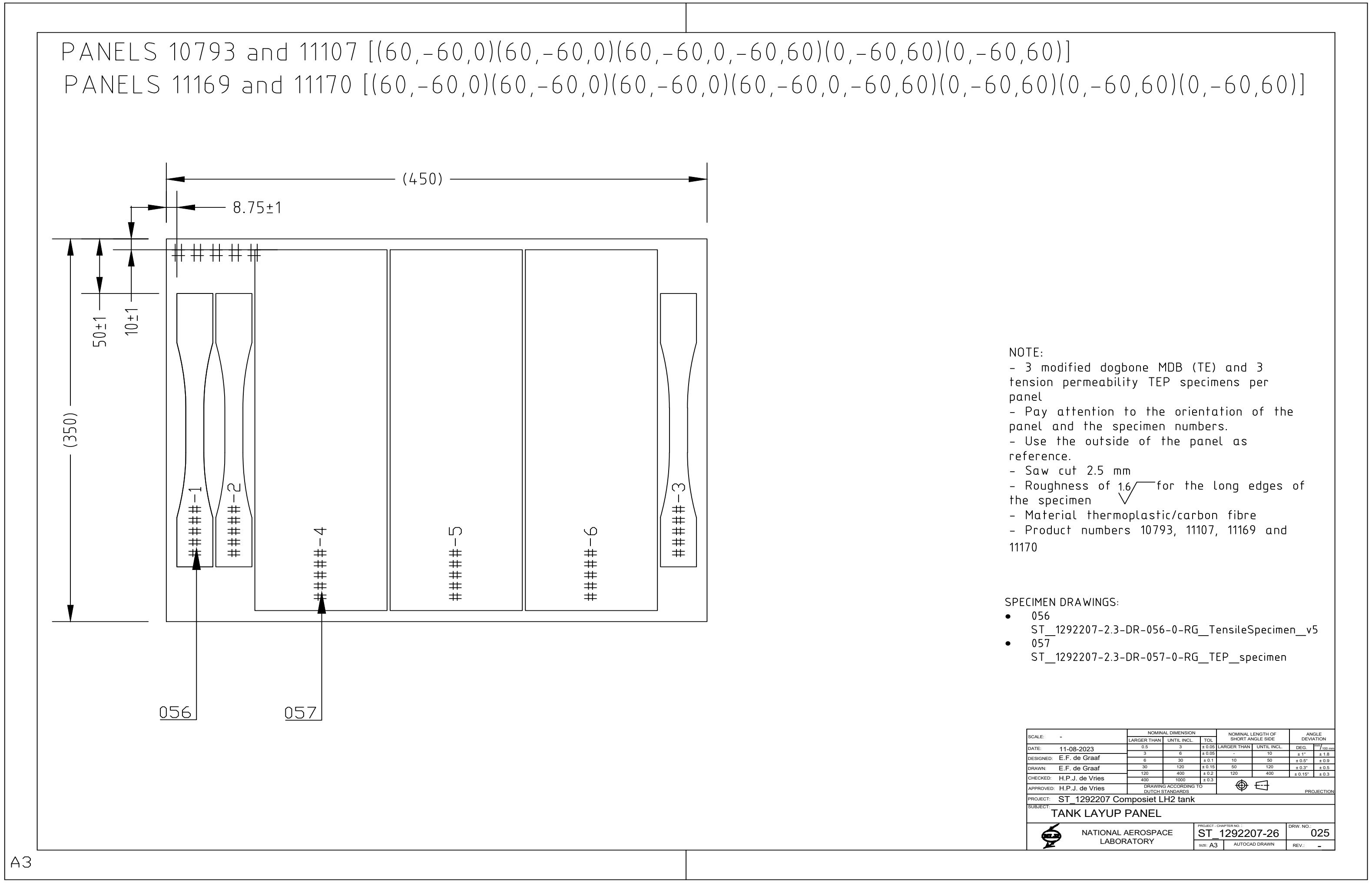

PANELS 10793 and 11107 [(60,-60,0)(60,-60,0)(60,-60,0,-60,60)(0,-60,60)(0,-60,60)]
PANELS 11169 and 11170 [(60,-60,0)(60,-60,0)(60,-60,0)(60,-60,0,-60,60)(0,-60,60)(0,-60,60)(0,-60,60)]

NOTE:
- 3 modified dogbone MDB (TE) and 3 tension permeability TEP specimens per panel
- Pay attention to the orientation of the panel and the specimen numbers.
- Use the outside of the panel as reference.
- Saw cut 2.5 mm
- Roughness of 1.6√ for the long edges of the specimen
- Material thermoplastic/carbon fibre
- Product numbers 10793, 11107, 11169 and 11170

SPECIMEN DRAWINGS:
- 056 ST__1292207-2.3-DR-056-0-RG__TensileSpecimen__v5
- 057 ST__1292207-2.3-DR-057-0-RG__TEP__specimen

		NOMINAL DIMENSION			NOMINAL LENGTH OF SHORT ANGLE SIDE		ANGLE DEVIATION	
SCALE:	-	LARGER THAN	UNTIL INCL.	TOL				
DATE:	11-08-2023	0.5	3	± 0.05	LARGER THAN	UNTIL INCL.	DEG.	mm/100 mm
DESIGNED:	E.F. de Graaf	3	6	± 0.05	-	10	± 1°	± 1.8
		6	30	± 0.1	10	50	± 0.5°	± 0.9
DRAWN:	E.F. de Graaf	30	120	± 0.15	50	120	± 0.3°	± 0.5
CHECKED:	H.P.J. de Vries	120	400	± 0.2	120	400	± 0.15°	± 0.3
		400	1000	± 0.3				
APPROVED:	H.P.J. de Vries	DRAWING ACCORDING TO DUTCH STANDARDS			PROJECTION			

PROJECT: ST_1292207 Composiet LH2 tank
SUBJECT: TANK LAYUP PANEL
NATIONAL AEROSPACE LABORATORY
PROJECT - CHAPTER NO.: ST_1292207-26
DRW. NO.: 025
SIZE: A3
AUTOCAD DRAWN
REV.: -

Figure B.1: Machining panel drawing

C

Permeability results

Action	10793-4	11107-6	10793-6	11107-4	11107-5	10793-5
Ply configuration	Thick	Thick	Thick	Thick	Thick	Thick
Applied load RT tensile test [kN]	0	30	37,5	50	62,5	140
Date	9-1-2024	10-11-2023	18-12-2023	15-12-2023	11-12-2023	21-12-2023
Time	17:03	09:37	09:20	09:24	09:24	09:55
Pressure Helium reservoir [mbar]	992	987	1001	1002	1001	999
End pressure leaktester [mbar]	3,67E-03	3,33E-03	2,00E-03	2,00E-03	2,30E-03	2,30E-03
Start leak rate [mbarL/s]	1,01E-12	1,00E-12	4,80E-10	1,00E-10	1,00E-10	4,35E-10
End leak rate [mbarL/s]	3,18E-07	4,93E-07	3,56E-07	4,50E-07	4,50E-07	3,64E-07
End date	11-1-2024	11-11-2023	19-12-2023	16-12-2023	12-12-2023	22-12-2023
End time	10:02:54	17:33:10	08:43:36	07:05:04	09:29:56	04:54:19
Measurement time [hrs]	40,99	31,93	23,39	21,68	24,09	18,98
Ultimate Qperm [mbarL/s] (= Diff. rate)	3,18E-07	4,93E-07	3,56E-07	4,50E-07	4,50E-07	3,64E-07
Remark (MP = measurement period)						
Ultimate Qperm [Pa m3/s]	3,18E-08	4,933E-08	3,55627E-08	4,49968E-08	4,50E-08	3,63915E-08
Pa = Helium Pressure [Pa]	99218,499	98691,36751	100134,7134	100209,1449	100093,1824	99876,52396
d = Wall thickness [m]	0,00239	0,00241	0,00237	0,00245	0,00241	0,00238
Ult. kperm = Qpermxd/(AxPa) [m2/s]	1,26E-13	1,98E-13	1,38E-13	1,81E-13	1,78E-13	1,43E-13
Ultimate kperm: [kg/(m.s.bar)]	2,04E-14	3,21E-14	2,24E-14	2,93E-14	2,89E-14	2,32E-14
Ultimate kperm: [mol He/(m.s.Pa)]	5,109E-17	8,03E-17	5,61042E-17	7,32414E-17	7,23117E-17	5,78762E-17

Action	11169-4	11169-6	11170-6	11170-5	11170-4	11169-5
Ply configuration	Thin	Thin	Thin	Thin	Thin	Thin
Applied load RT tensile test [kN]	0	41,25	51,56	61,88	72,19	140
Date	21-11-2023	12-12-2023	19-12-2023	13-12-2023	14-12-2023	20-12-2023
Time	16:17	09:37	09:47	10:41	10:24	10:26
Pressure Helium reservoir [mbar]	1018	994	998	1011	1006	996
End pressure leaktester [mbar]	4,67E-03	1,70E-03	2,70E-03	1,70E-03	1,50E-03	2,00E-03
Start leak rate [mbarL/s]	1,00E-12	1,05E-09	6,21E-10	1,00E-10	7,33E-10	4,69E-10
End leak rate [mbarL/s]	7,04E-07	6,15E-07	6,41E-07	7,44E-07	6,93E-07	6,67E-07
End date	22-11-2023	13-12-2023	20-12-2023	14-12-2023	15-12-2023	21-12-2023
End time	09:56:39	10:27:51	04:46:37	09:58:24	05:09:59	05:29:31
Measurement time [hrs]	17,65	24,83	18,99	23,28	18,76	19,05
Ultimate Qperm [mbarL/s] (= Diff. rate)	7,04E-07	6,15E-07	6,41E-07	7,44E-07	6,93E-07	6,67E-07
Remark (MP = measurement period)						
Ultimate Qperm [Pa m3/s]	7,042E-08	6,15E-08	6,41132E-08	7,44E-08	6,93E-08	6,67237E-08
Pa = Helium Pressure [Pa]	101808,1497	99374,32376	99753,86799	101106,9849	100620,8329	99589,29835
d = Wall thickness [m]	0,00234	0,00236	0,00236	0,00242	0,00246	0,00239
Ult. kperm = Qpermxd/(AxPa) [m2/s]	2,66E-13	2,40E-13	2,49E-13	2,93E-13	2,78E-13	2,63E-13
Ultimate kperm: [kg/(m.s.bar)]	4,31E-14	3,90E-14	4,05E-14	4,75E-14	4,51E-14	4,27E-14
Ultimate kperm: [mol He/(m.s.Pa)]	1,08E-16	9,75179E-17	1,01232E-16	1,187E-16	1,12844E-16	1,06645E-16

Action	Constants
A = Surface area [m2]	0,00608
Mass of 1 mol H2 [kg]:	0,002
Mass of 1 mol He [kg]:	0,004
Density H2 at 295 K [kg/(bar*m3]	0,0821
Density helium at 295 K [kg/(bar*m3]	0,1623
Max kperm required: [mol/(m.s.Pa)]	1E-15
Max kperm required: [kg He/(m.s.Pa)]	4,00E-18

D

Additional experimental results

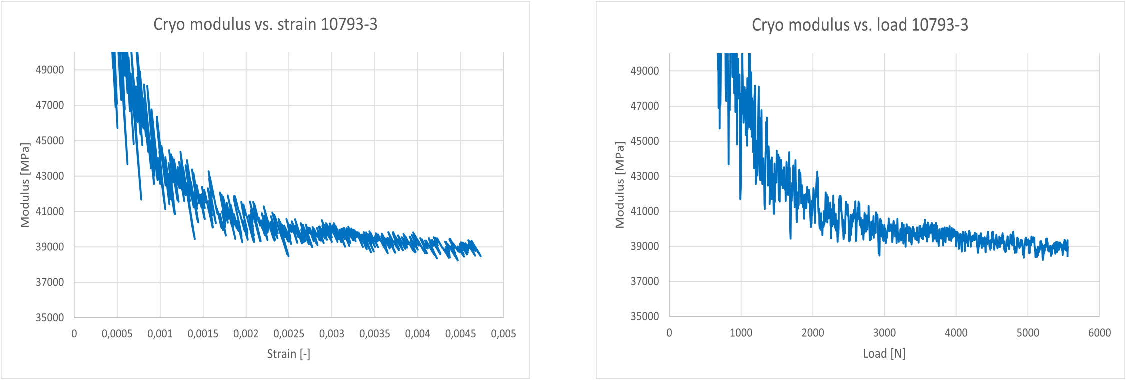

(a) Modulus vs. strain

(b) Modulus vs. load

Figure D.1: Cryogenic strain gauge results specimen 10793-3

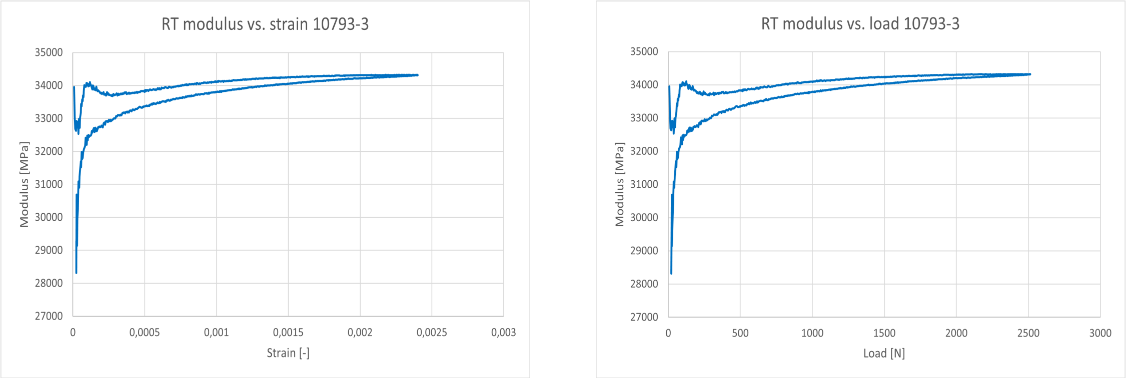

(a) Modulus vs. strain

(b) Modulus vs. load

Figure D.2: RT strain gauge results specimen 10793-3

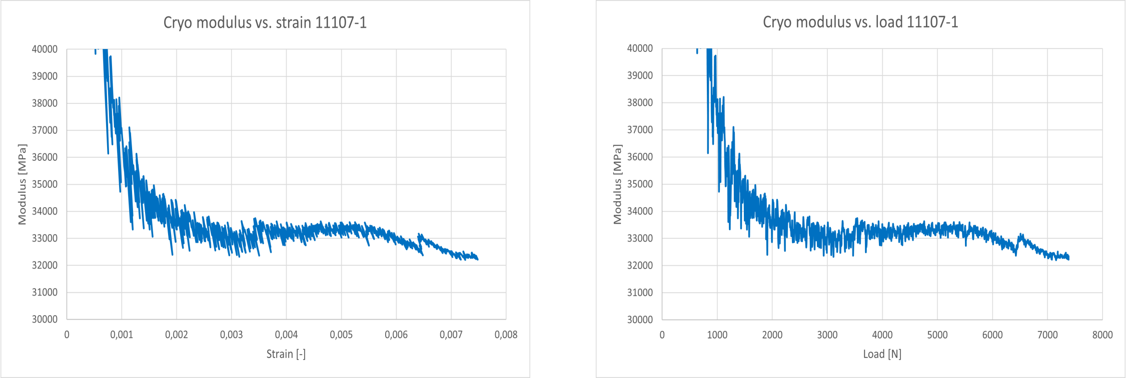

(a) Modulus vs. strain

(b) Modulus vs. load

Figure D.3: Cryogenic strain gauge results specimen 11107-1

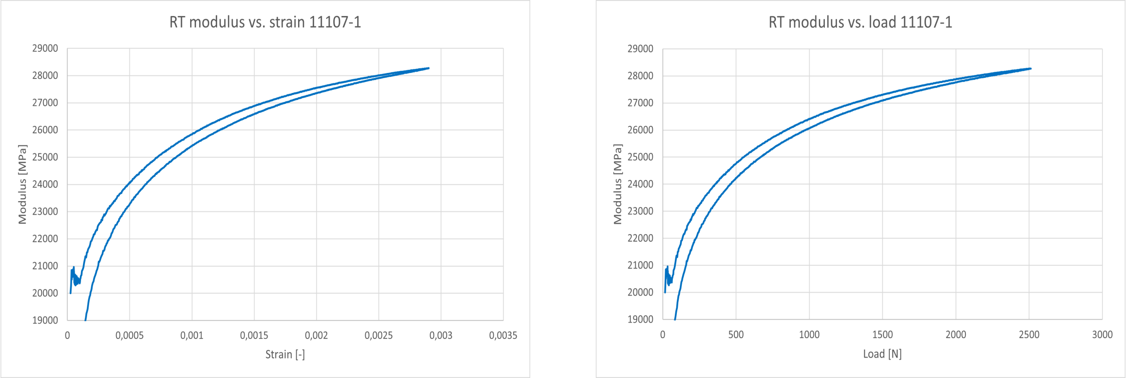

(a) Modulus vs. strain

(b) Modulus vs. load

Figure D.4: RT strain gauge results specimen 11107-1

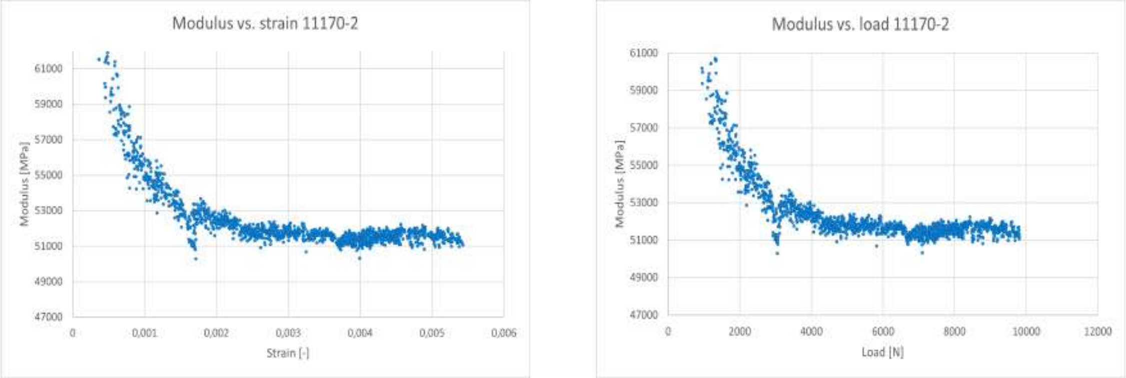

(a) Modulus vs. strain

(b) Modulus vs. load

Figure D.5: Cryogenic strain gauge results specimen 11170-2

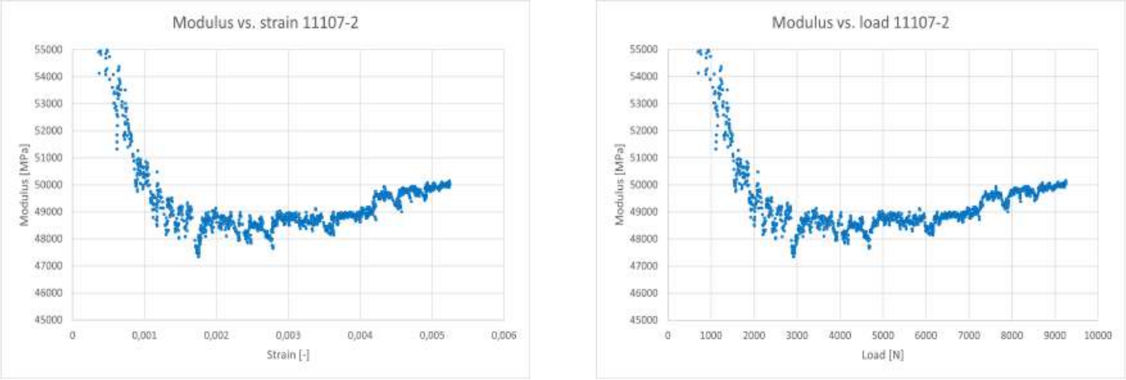

(a) Modulus vs. strain **(b)** Modulus vs. load

Figure D.6: Cryogenic strain gauge results specimen 11107-2

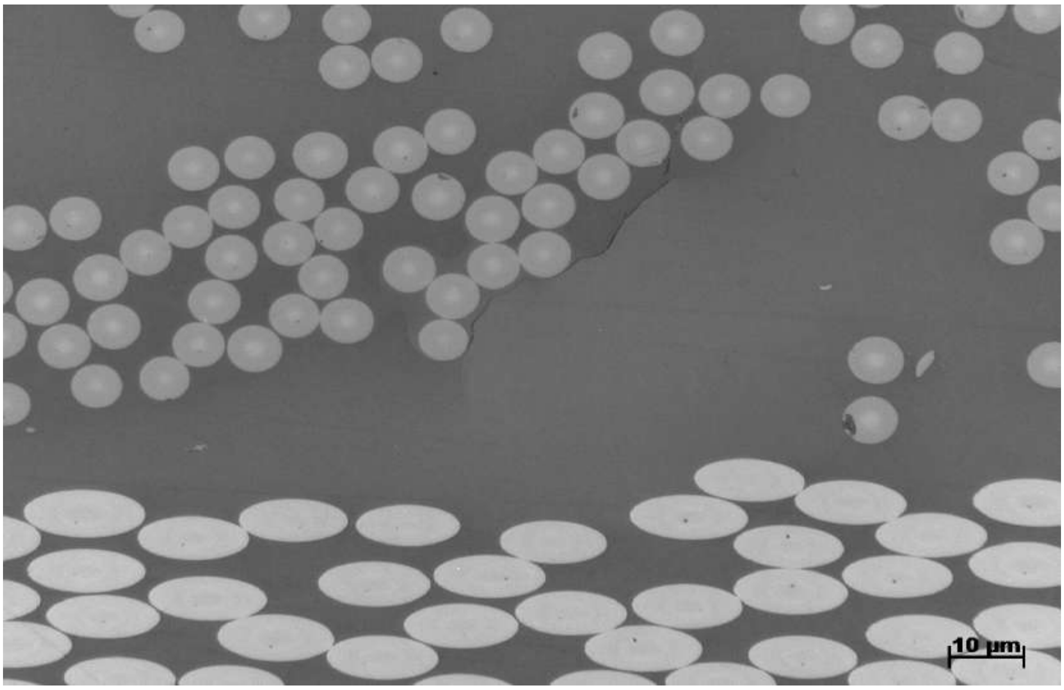

Figure D.7: Optical microscopy examination on microcracks of specimen 11169-6.

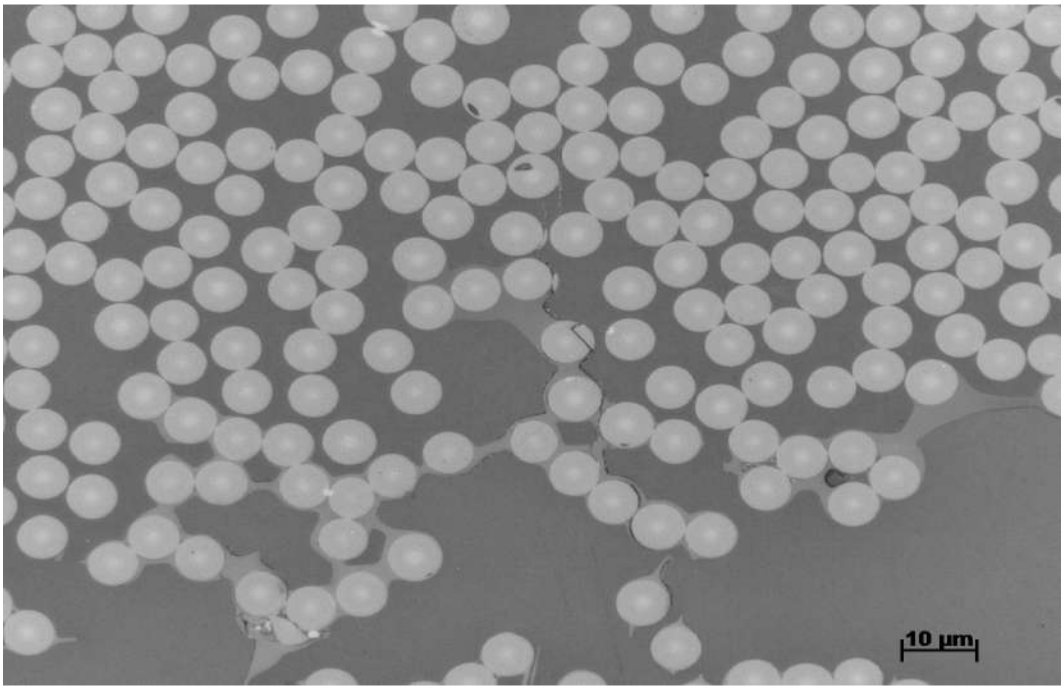

Figure D.8: Optical microscopy examination on microcracks of specimen 11170-6 [1/2]. This is the only specimen showing microcracks through the fiber, these types of cracks can be attributed to the abrasion and polishing of the material in preparation for microscopic assessment.

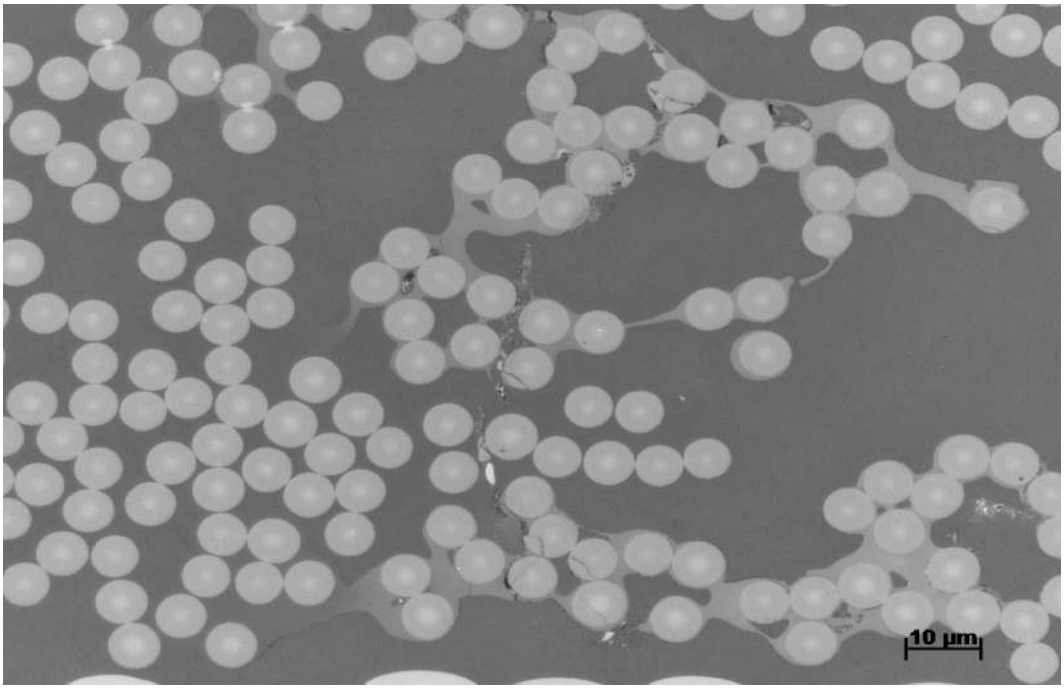

Figure D.9: Optical microscopy examination on microcracks of specimen 11170-6 [2/2].

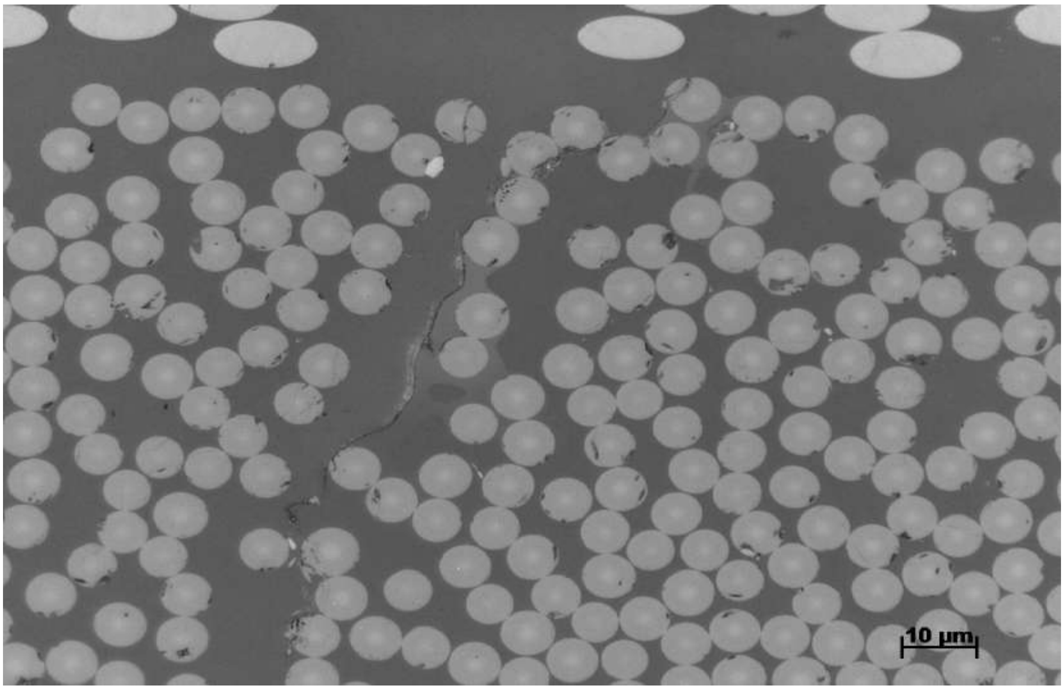

Figure D.10: Optical microscopy examination on microcracks of specimen 11170-4 [2/2].

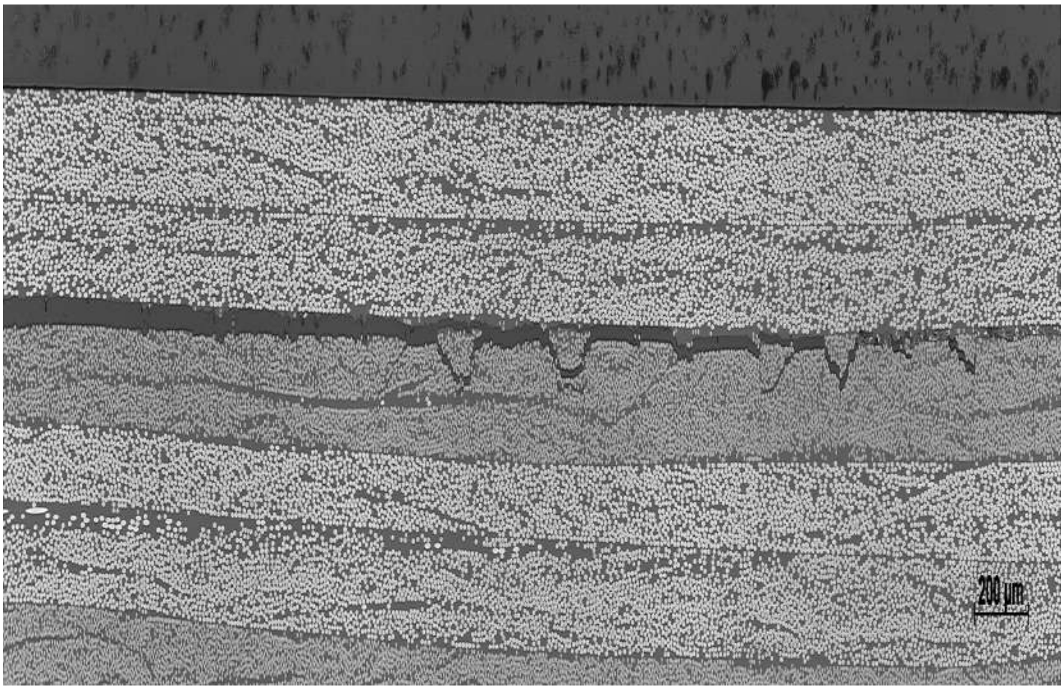

Figure D.11: Optical microscopy examination on microcracks of specimen 10793-1 [2/2].

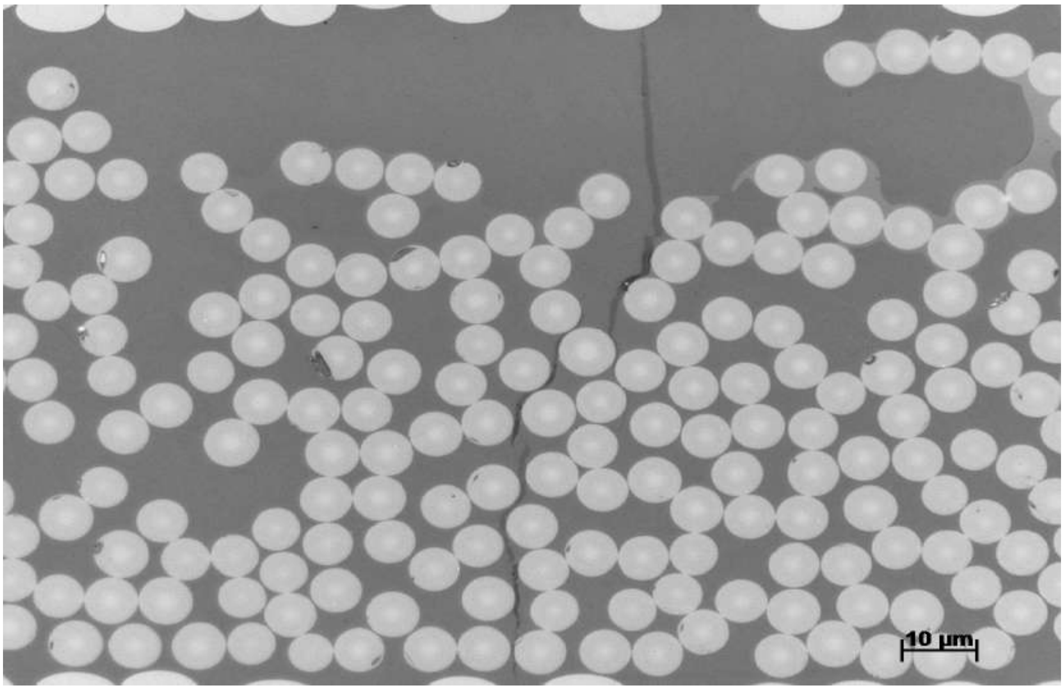

Figure D.12: Optical microscopy examination on microcracks of specimen 11107-1 [2/2].

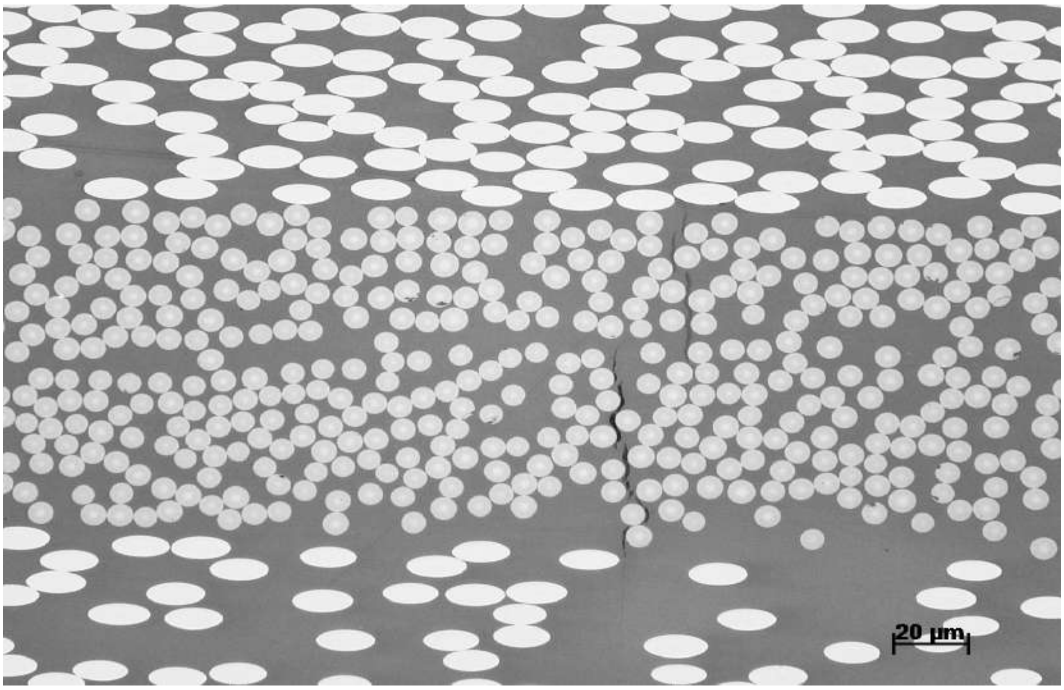

Figure D.13: Optical microscopy examination on microcracks of specimen 11169-2 [1/2].

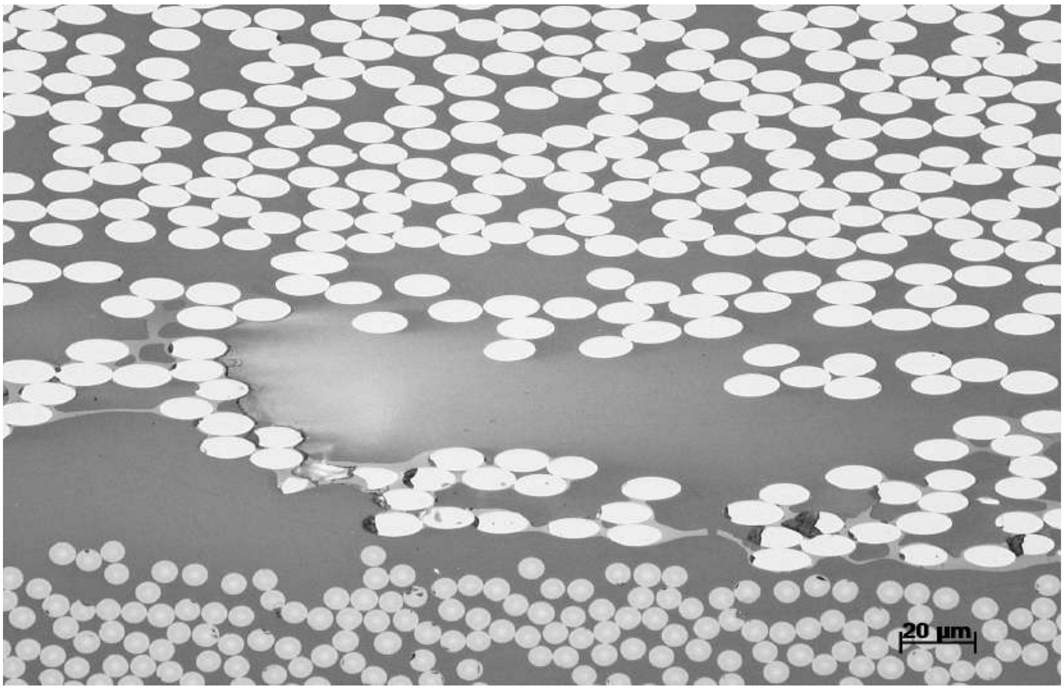

Figure D.14: Optical microscopy examination on microcracks of specimen 11169-2 [2/2].

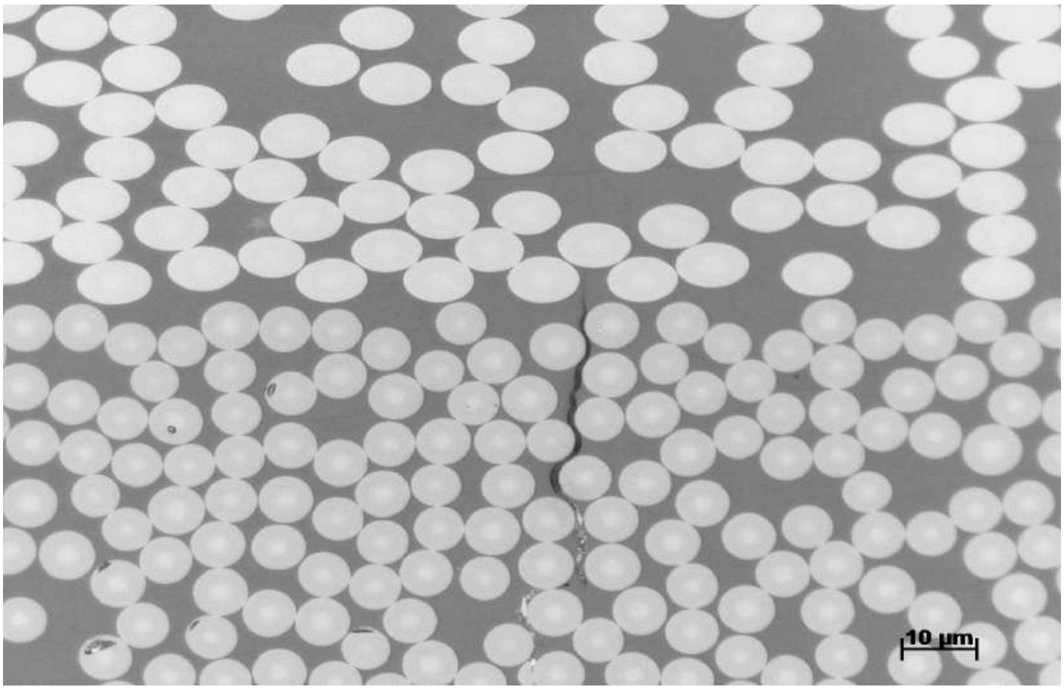

Figure D.15: Optical microscopy examination on microcracks of specimen 11170-1.

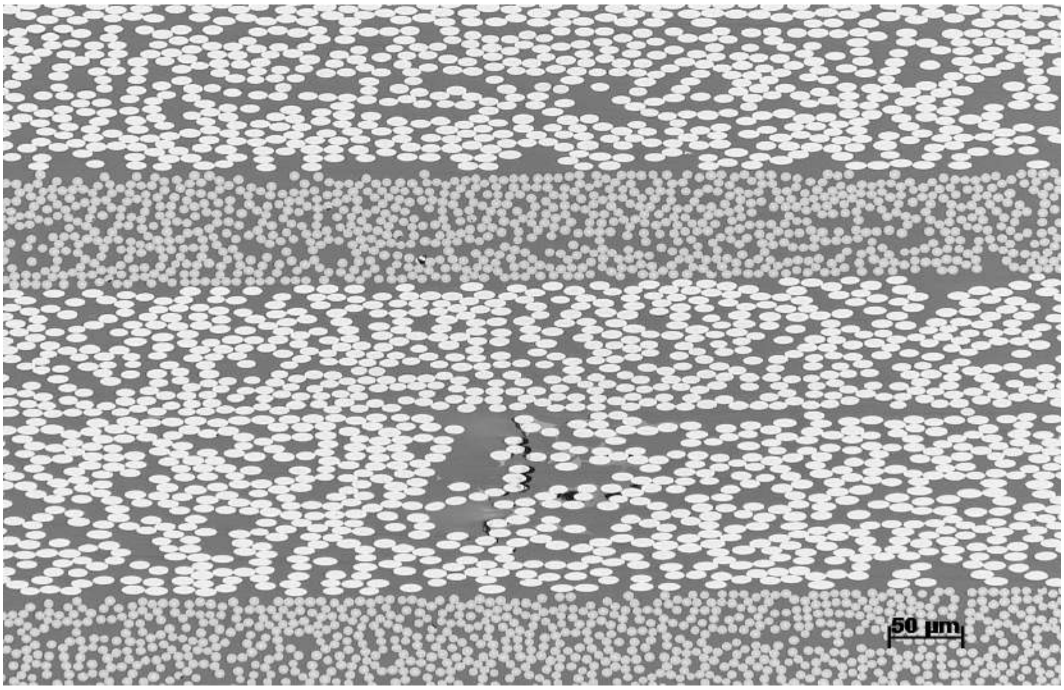

Figure D.16: Optical microscopy examination on microcracks of specimen 11107-2.

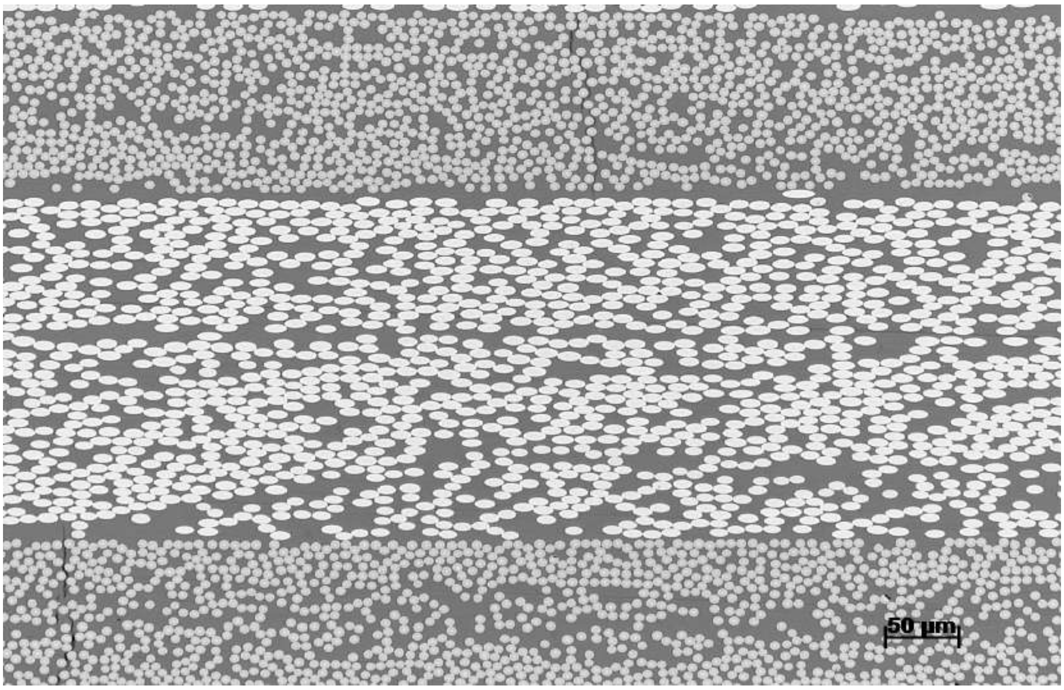

Figure D.17: Optical microscopy examination on microcracks of specimen 11170-2 [1/2].

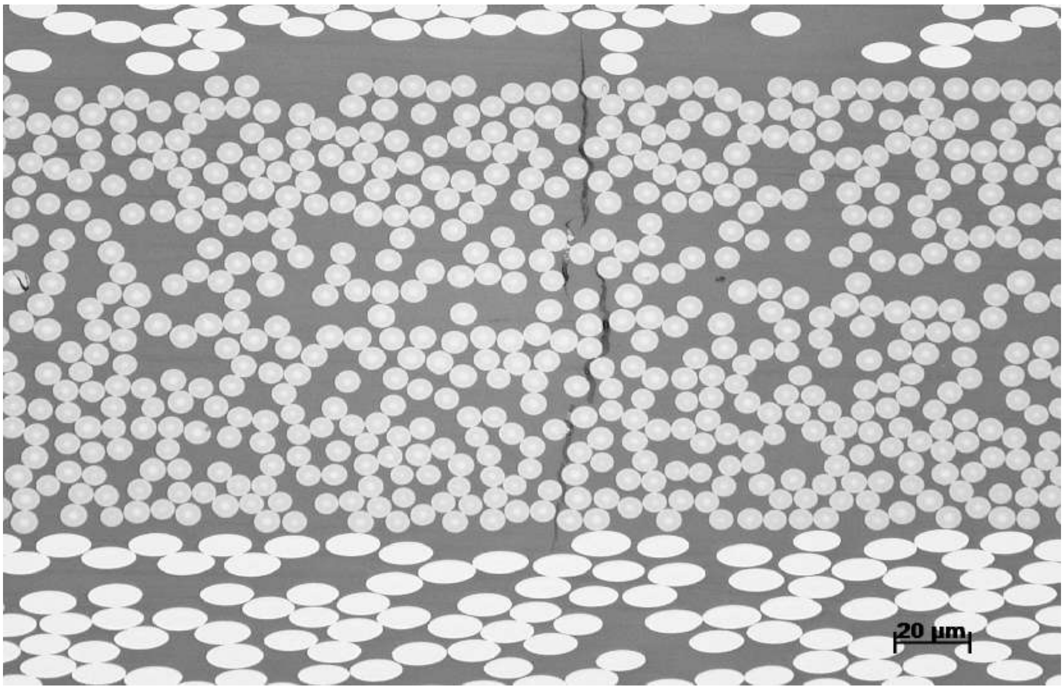

Figure D.18: Optical microscopy examination on microcracks of specimen 11170-2 [2/2].

E

C-scan results

E.1. Panel 10793

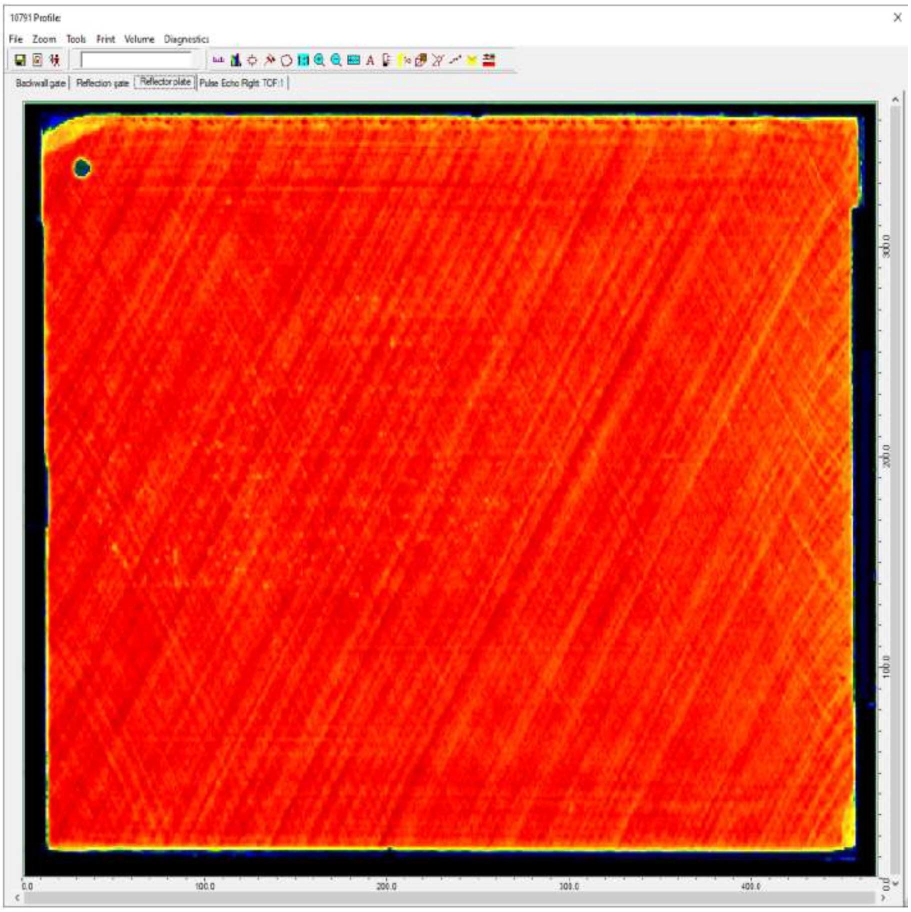

Figure E.1: Attenuation C-scan (Reflector plate) of panel 10793

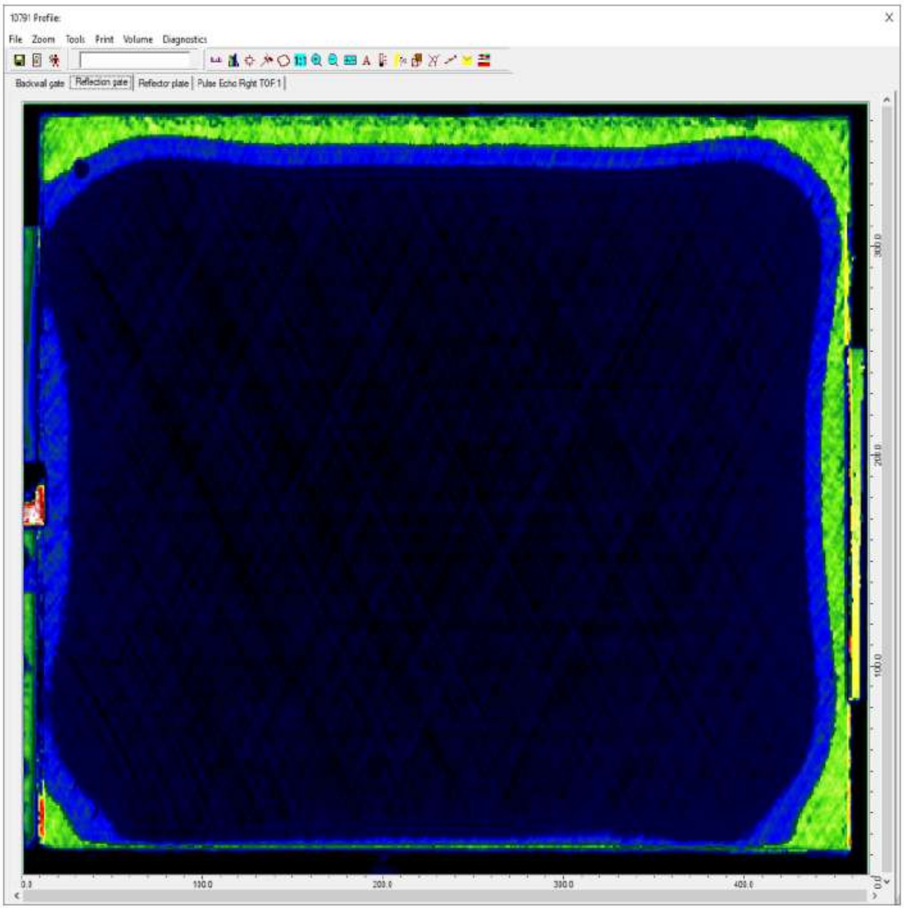

Figure E.2: Reflection C-scan of panel 10793

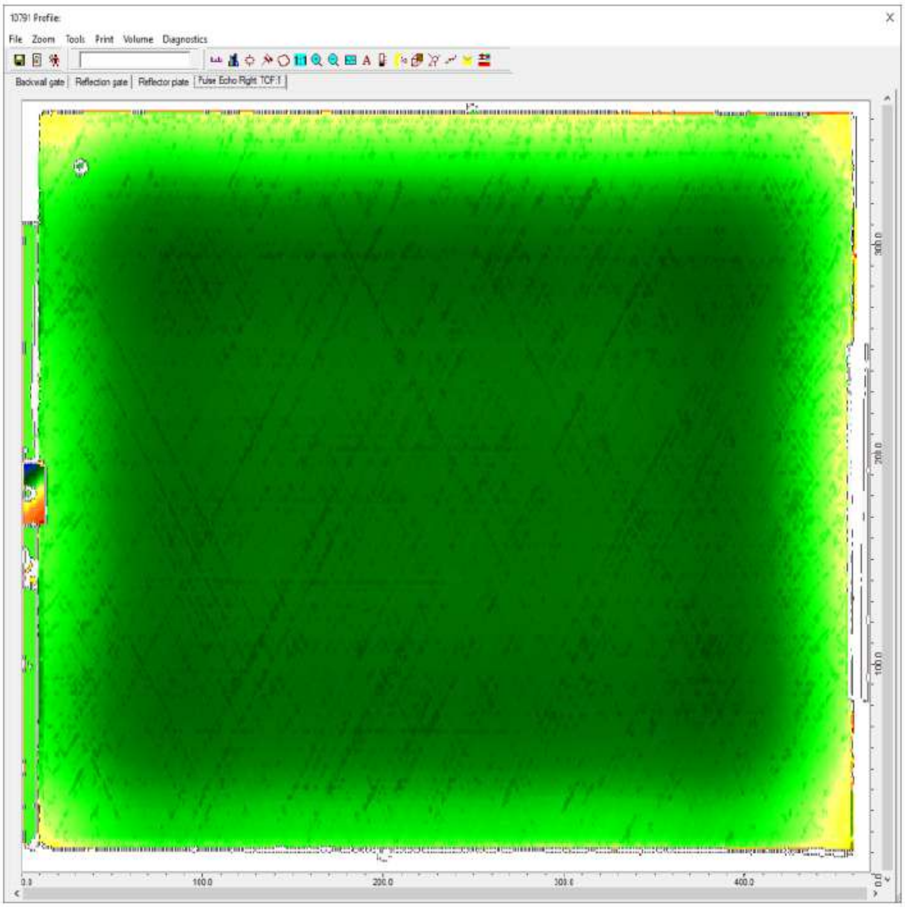

Figure E.3: TOF (thickness) of panel 10793

E.2. Panel 11107

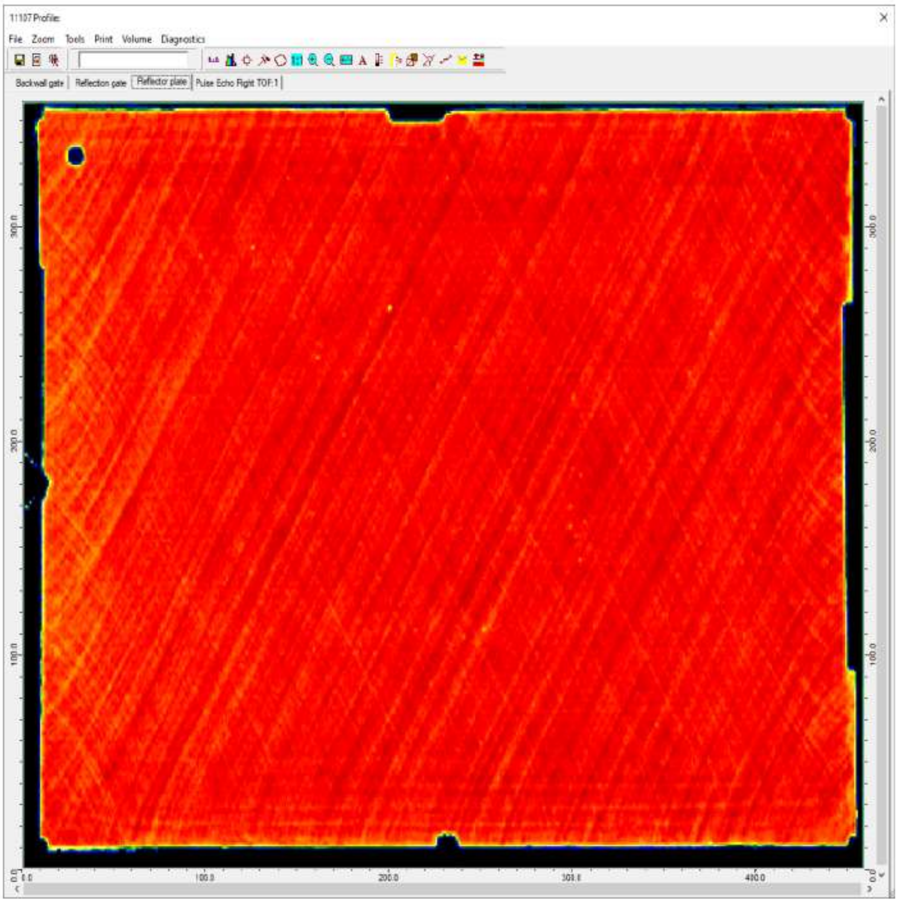

Figure E.4: Attenuation C-scan (Reflector plate) of panel 11107

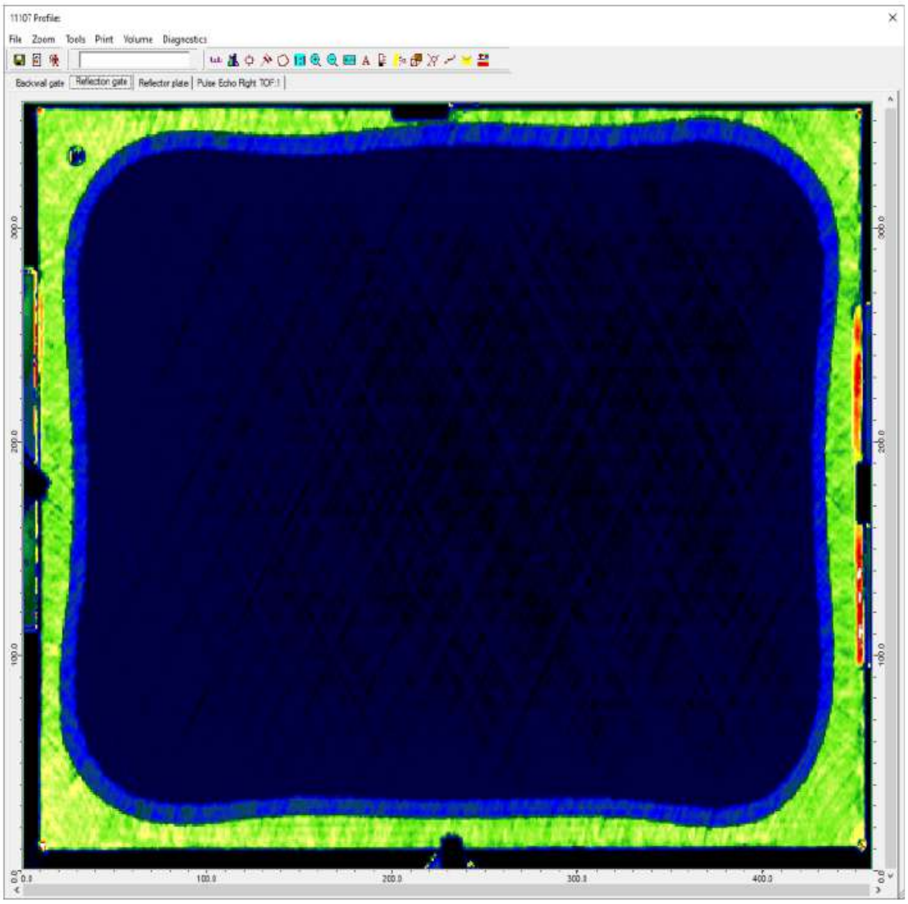

Figure E.5: Reflection C-scan of panel 11107

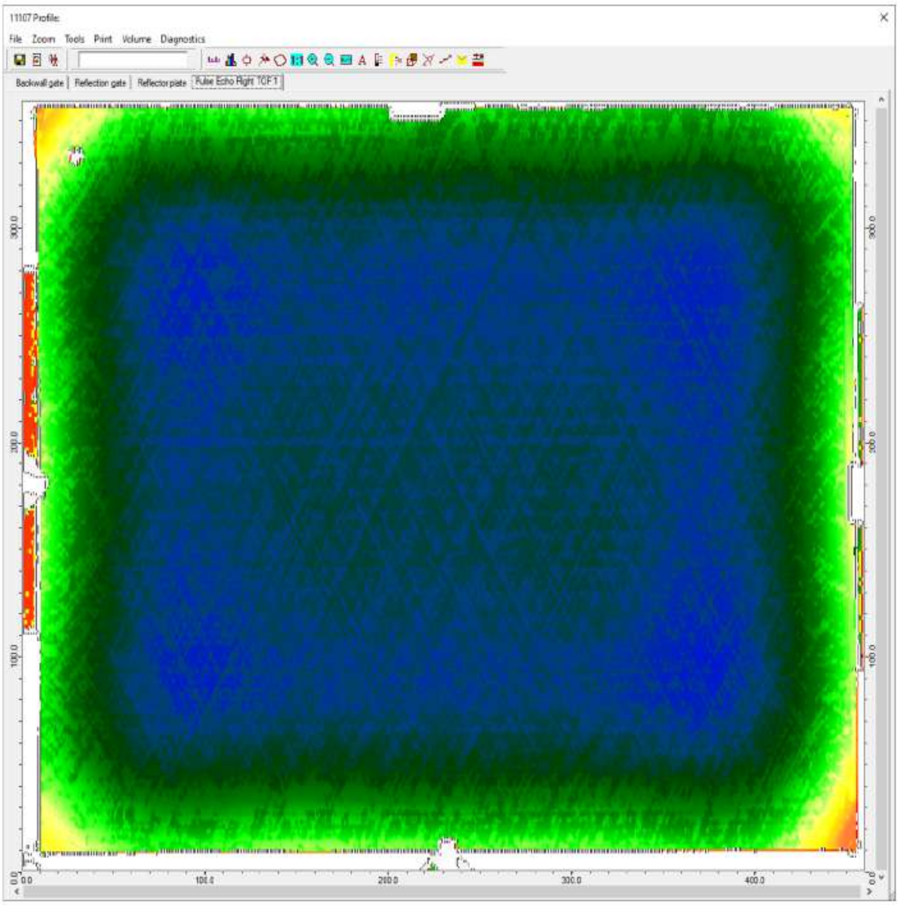

Figure E.6: TOF (thickness) of panel 11107

E.3. Panel 11169

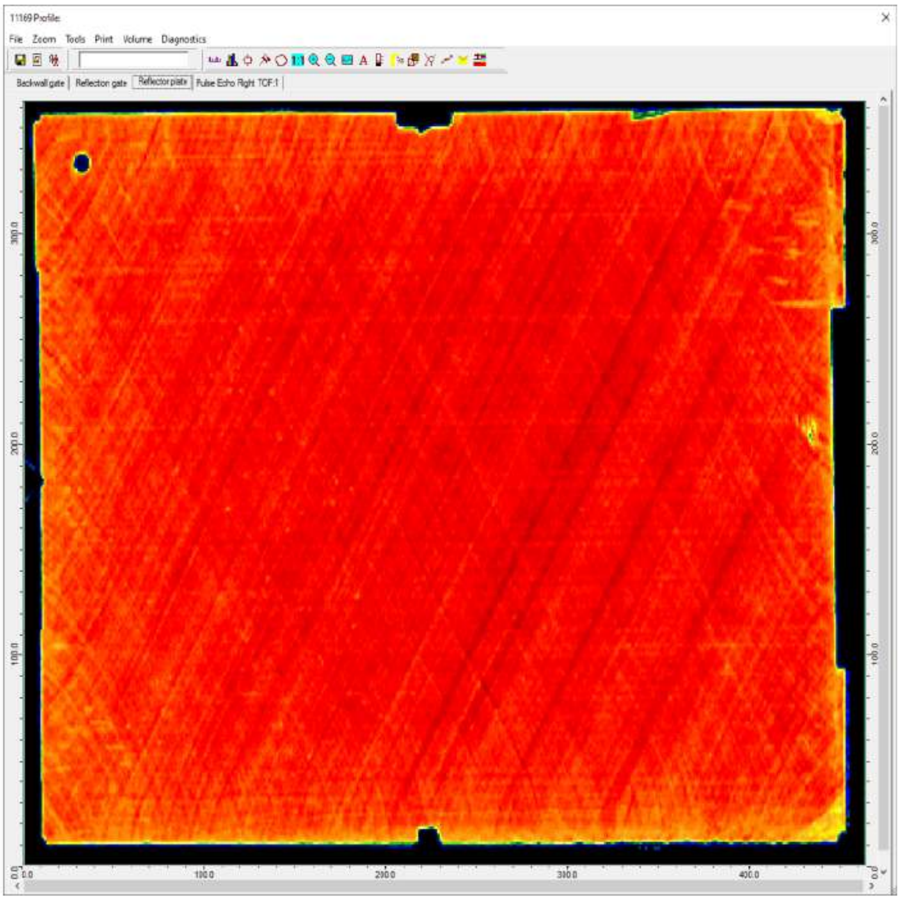

Figure E.7: Attenuation C-scan (Reflector plate) of panel 11169

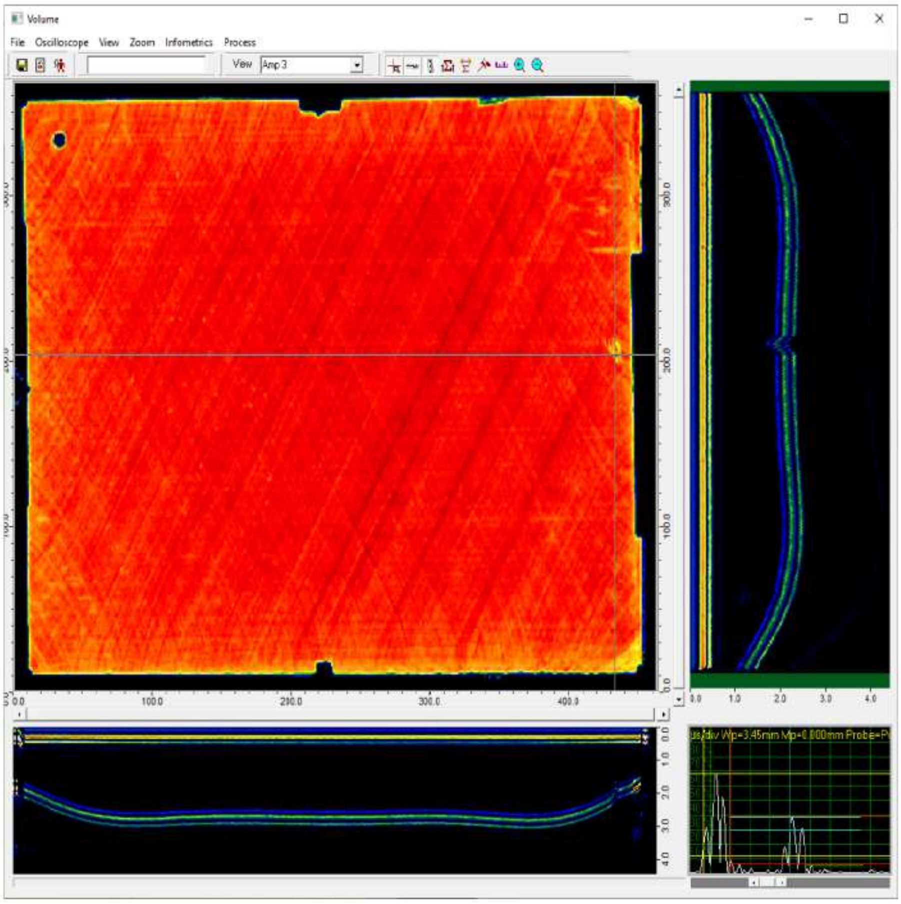

View: Amp 3

```
us/div Wp=3.45mm Mp=0.000mm Probe=P
```

Figure E.8: A-, B- and C-scan of indication (reflector plate) of panel 11169

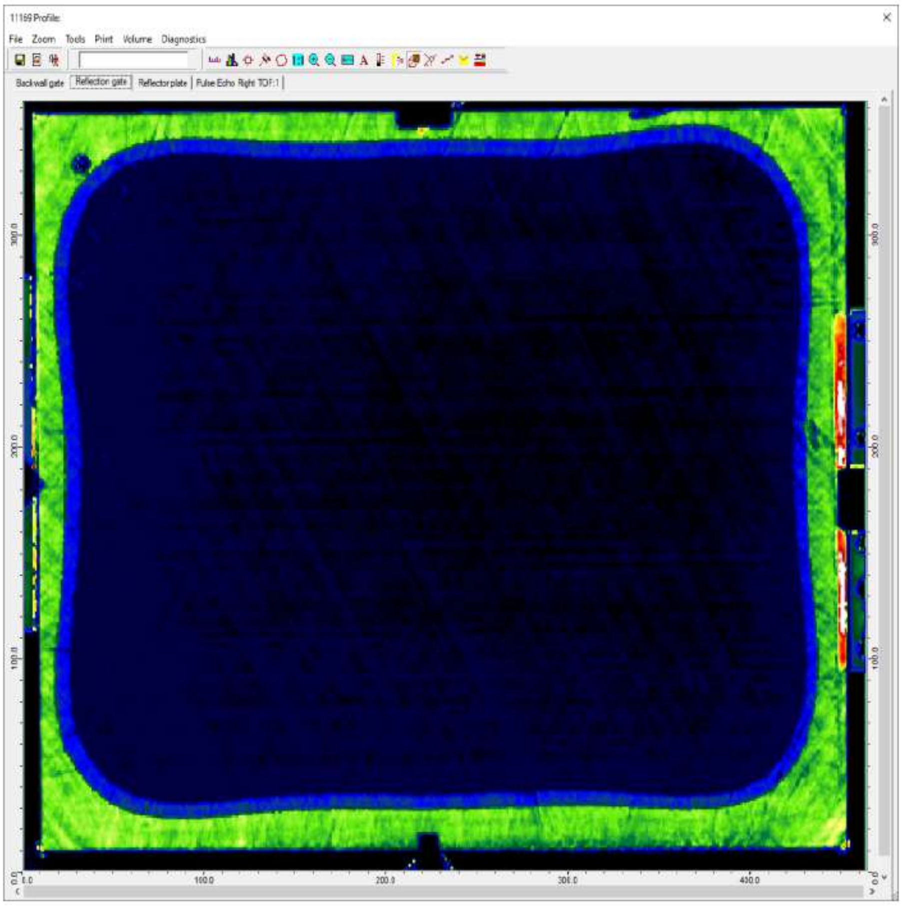

Figure E.9: Reflection C-scan of panel 11169

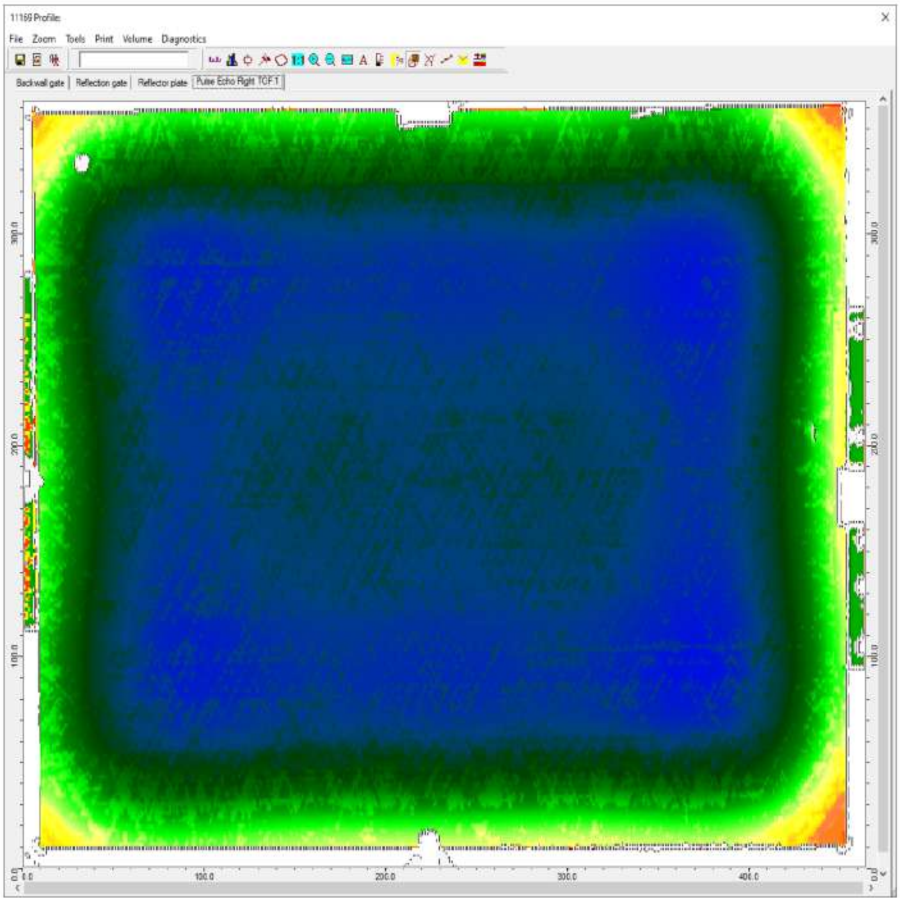

Figure E.10: TOF (thickness) of panel 11169

E.4. Panel 11170

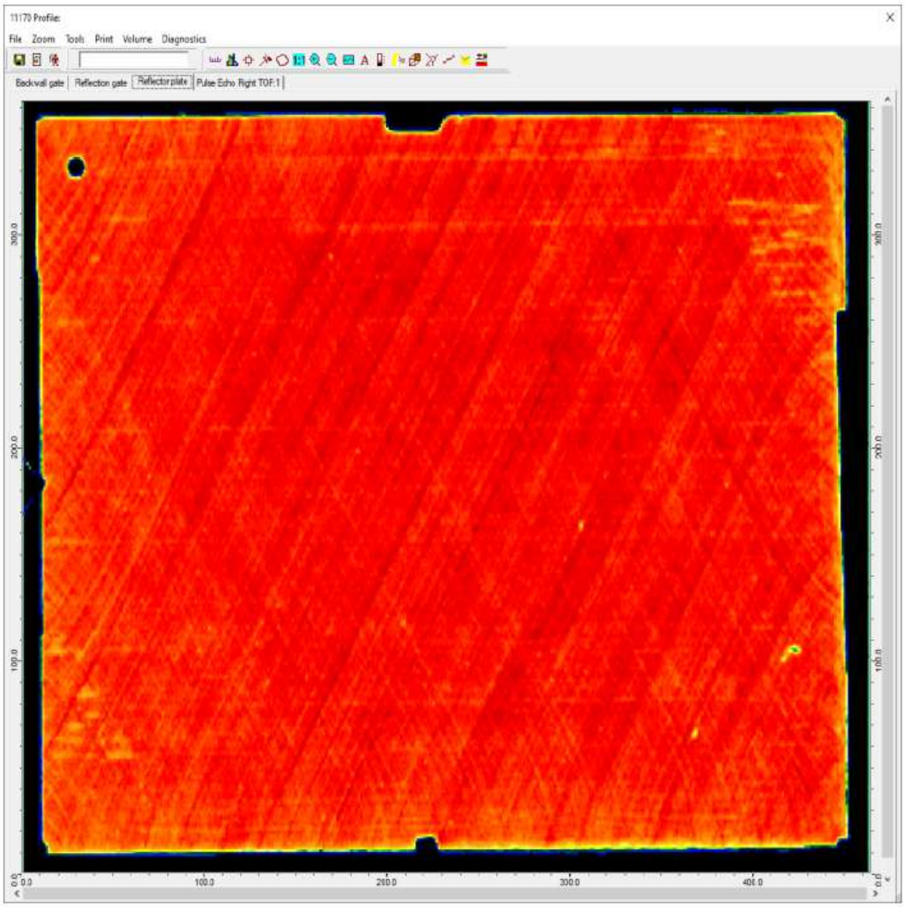

Figure E.11: Attenuation C-scan (Reflector plate) of panel 11170

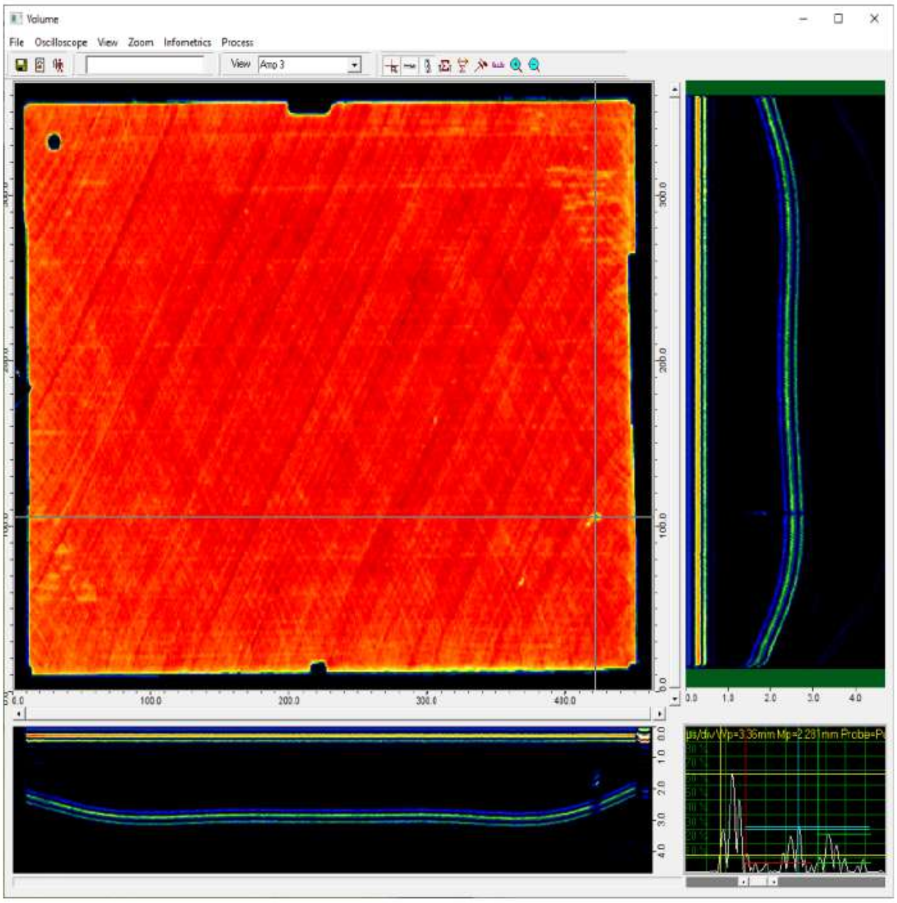

```
µs/div Wp=3.36mm Mp=2.281mm Probe=P
```

Figure E.12: A-, B- and C-scan of indication (reflector plate) of panel 11170

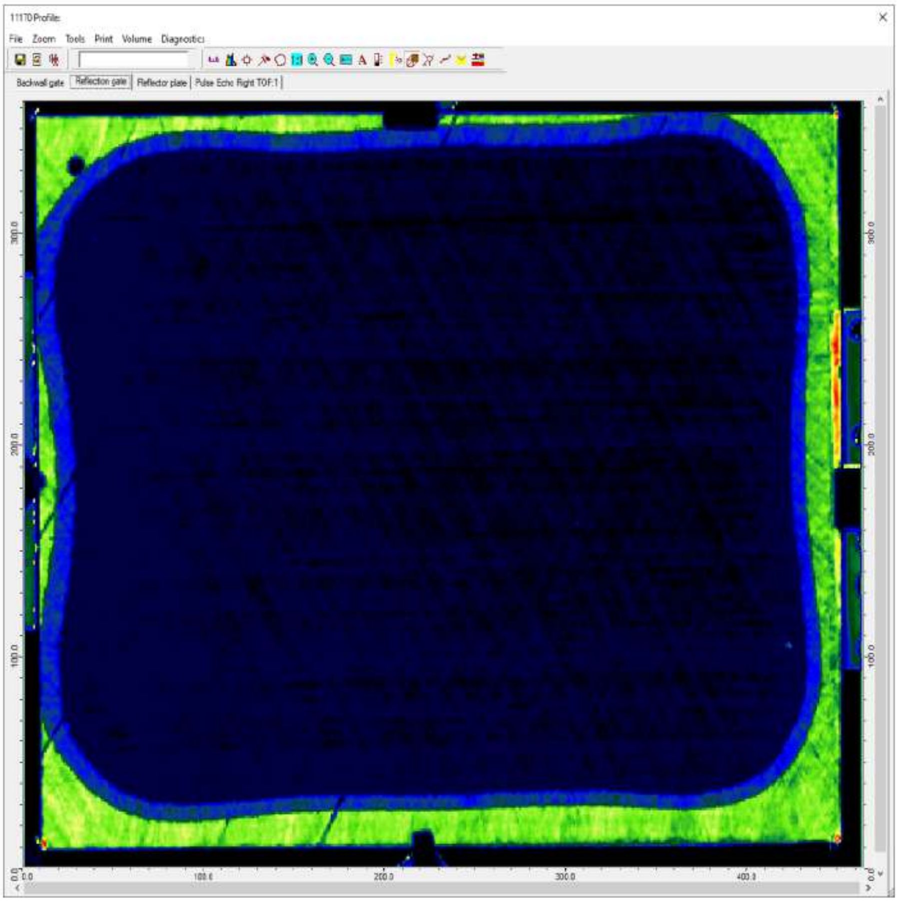

Figure E.13: Reflection C-scan of panel 11170

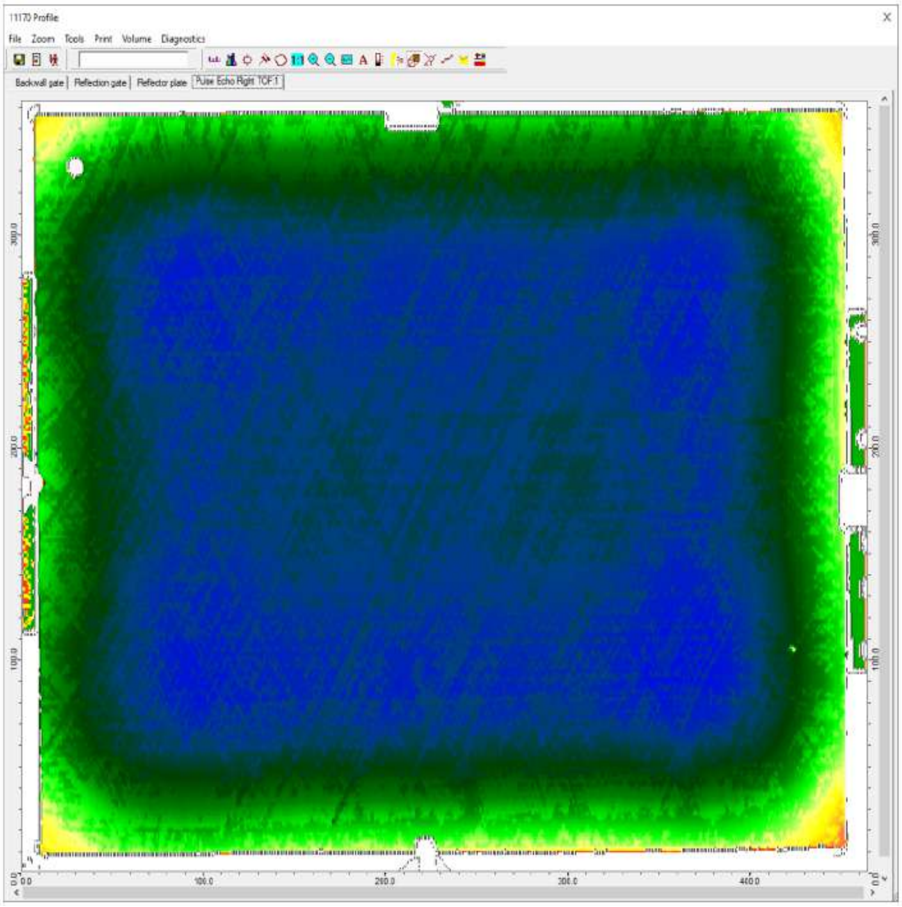

Figure E.14: TOF (thickness) of panel 11170

F

TC1225 datasheet

The material properties of TC1225 used in this thesis and in Appendix A originate from the Toray datasheet presented here.

Toray Cetex® TC1225

LMPAEK™

'TORAY'

Toray Advanced Composites

PRODUCT DATA SHEET

DESCRIPTION

Toray Cetex® TC1225 is a high-end thermoplastic composite material, utilizing a semi-crystalline low-melt PAEK resin for excellent mechanical performance. The distinctive value of Toray Cetex® TC1225, over other composites with a PAEK family matrix, is its superior processability due to a low-melt viscosity and reduction in processing temperature of up to 60°C (140°F)*. Toray Cetex® TC1225 doesn't only yield a high-quality product used in ATL/AFP processes, it also speeds up cycle times enabling cost-efficient production in all available formats.

Additionally, Toray Cetex® TC1225 is an ideal composite to be overmolded with neat or short fiber reinforced PEEK resin, creating a very strong bond. Overmolding, integrating continuous fiber reinforced composites in an injection molding process, combines the strength of high-end composites with the design freedom and complexity of injection molding parts.

Toray Cetex® TC1225 is available as a UD tape, a fabric prepreg, and as reinforced thermoplastic laminates (RTLs) of varying thicknesses. RTLs can be equipped with lightning strike protection, and carbon reinforced RTLs can be supplied with a thin glass top layer to protect a partly metallic assembly against galvanic corrosion. Glass scrim is also applicable in structures made from UD tape.

*Standard PEEK processes at temperatures up to 400°C (752°F)

FEATURES

- **Superior processability as a result of low-melt viscosity and relatively low processing temperature**
- **Form freedom—suited for overmolding with neat or short fiber reinforced PEEK**
- **Relatively low processing temperature enables shorter cycle times and less energy consumption**
- **Excellent mechanical performance, also at elevated temperatures**
- **Excellent toughness—demonstrated by high compression after impact strengths and fracture toughness values**
- **Very low moisture absorption (high hot/wet property retention)**
- **Outstanding chemical and solvent resistance**
- **Indefinite shelf life at ambient temperature storage**
- **Excellent FST performance**

PRODUCT TYPE

LMPAEK™ (Low-Melt PolyArylEtherKetone)
Thermoplastic Resin System

TYPICAL APPLICATIONS

- Primary and secondary aircraft structures
- High-load aircraft interiors applications
- Access panels, rib stiffeners, brackets
- Radome
- Medical
- Oil and gas

TYPICAL NEAT RESIN PROPERTIES

Density (specific gravity)	1.30 g/cm^3 (81.2 lb/ft^3)
T_g (glass transition)	147°C (297°F)
T_m (melt)	305°C (581°F)
T_c (crystallinity)	263°C (505°F)
T_p (processing)	340–385°C (644–725°F)

SHELF LIFE

Out Life:	Indefinite at ambient temperature storage
Frozen Storage Life:	Not applicable—product does not require freezing

PRODUCT DATA SHEET

PHYSICAL PROPERTIES—CARBON

Property	Standard Modulus Carbon UD Tape	5 Harness Satin (T300JB Carbon Woven Prepreg)
Fiber areal weight (FAW)	145 g/m^2 (4.28 oz/yd^2)	281 g/m^2 (8.29 oz/yd^2)
Weight per ply (PAW)	221 g/m^2 (6.52 oz/yd^2)	489 g/m^2 (14.42 oz/yd^2)
Resin content by weight (RC)	34%	43%
Consolidated ply thickness (CPT)	0.14 mm (0.0054 in.)	0.31 mm (0.0122 in.)
Density	1.59 g/cm^3 (99.3 lb/ft^3)	1.53 g/cm^3 (95.51 lb/ft^3)

These reinforcements are available as rolls of semi-preg or as RTLs. Lightning-strike protection layers can be incorporated into RTLs. A glass scrim can also be added to the surface of carbon fiber based laminates. This glass scrim is often used to protect against galvanic corrosion in assemblies where carbon fiber composites are in contact with metal components.

PHYSICAL PROPERTIES—GLASS (STRUCTURAL USE)

Property	US Style 7781 8 Harness Satin (EC6 Glass Woven Prepreg)	US Style 6781 8 Harness Satin (S2 C9 Glass Woven Prepreg)
Fiber areal weight (FAW)	296 g/m^2 (8.73 oz/yd^2)	298 g/m^2 (8.79 oz/yd^2)
Weight per ply (PAW)	448 g/m^2 (13.21 oz/yd^2)	452 g/m^2 (13.33 oz/yd^2)
Resin content by weight (RC)	34%	34%
Consolidated ply thickness (CPT)	0.24 mm (0.009 in.)	0.24 mm (0.009 in.)
Density	1.92 g/cm^3 (119.8 lbs/ft^3)	1.87 g/cm^3 (116.7 lbs/ft^3)

The reinforcements above are available as rolls of semi-preg or as RTLs. RTLs can consist of glass plies only or can incorporate UD carbon tapes or woven carbon tapes as required.

PHYSICAL PROPERTIES—GLASS SCRIM

Property	US Style 0120 4 Harness Satin (EC5 Glass Woven Prepreg)	US Style 1080 Plain Weave (EC5 Glass Woven Prepreg)
Fiber areal weight (FAW)	105 g/m^2 (3.10 oz/yd^2)	48 g/m^2 (1.42 oz/yd^2)
Weight per ply (PAW)	210 g/m^2 (6.19 oz/yd^2)	120 g/m^2 (3.54 oz/yd^2)
Resin content by weight (RC)	50%	60%
Consolidated ply thickness (CPT)	0.12 mm (0.005 in.)	0.08 mm (0.003 in.)
Density	1.71 g/cm^3 (106.8 lbs/ft^3)	1.61 g/cm^3 (100.5 lbs/ft^3)

The reinforcements above are available as rolls of semi-preg or can be added to the surface of RTLs of carbon UD tape or carbon woven fabric to act as a barrier to prevent galvanic corrosion.

MECHANICAL PROPERTIES

Standard Modulus Carbon 145gsm UD Tape 34% RC

Property	Condition	Test Method	Results	
Tensile Strength 0°	RTD	ASTM D 3039	2410 MPa	350 ksi
Tensile Modulus 0°	RTD	ASTM D 3039	135 GPa	19.5 Msi
Tensile Strength 90°	RTD	ASTM D 3039	86 MPa	12.5 ksi
Tensile Modulus 90°	RTD	ASTM D 3039	10 GPa	1.4 Msi
Compression Strength 0°	RTD	ASTM D 6641	1300 MPa	189 ksi
Compression Modulus 0°	RTD	ASTM D 6641	124 GPa	18 Msi
In-Plane Shear Strength	RTD	ASTM D 3518	152 MPa	22 ksi
In-Plane Shear Strength 2% Offset	RTD	ASTM D 3518	42.0 MPa	6.1 ksi
In-Plane Shear Modulus	RTD	ASTM D 3518	4.3 GPa	0.62 Msi
Flexural Strength 90°	RTD	ASTM D 790	152 MPa	22 ksi
Interlaminar Shear Strength (SBS) 0°/90°	RTD	ASTM D 2344	96.5 MPa	14 ksi
Open-Hole Tensile Strength	RTD	ASTM D 5766	448 MPa	65 ksi
Open-Hole Tensile Strength	CTD	ASTM D 5766	448 MPa	65 ksi
Open-Hole Compression Strength	RTD	ASTM D 6484	310 MPa	45 ksi
Open-Hole Compression Strength	ETD	ASTM D 6484	262 MPa	38 ksi
Compression After Impact Strength 30.5 J (270 in/lb) Impact Energy	RTD	ASTM D 7137	310 MPa	45 ksi
Mode I Interlaminar Fracture Toughness (G_{IC} Strain Energy Release Rate)	RTD	ASTM D 5528	2.1 kJ/m^2	12.0 in-lb/in^2
Mode II Interlaminar Fracture Toughness (G_{IIC} Strain Energy Release Rate)	RTD	ASTM D 7905	2.6 kJ/m^2	15.0 in-lb/in^2

Room Temperature Dry (RTD)
Cold Temperature Dry (CTD) is -54°C (-65°F)
Elevated Temperature Dry (ETD) is 121°C (250°F)

Intermediate Modulus Carbon 145gsm FAW UD Tape Laminate 34% RC

Property	Condition	Test Method	Results	
Tensile Strength 0°	RTD	ASTM D 3039	3100 MPa	450 ksi
Tensile Modulus 0°	RTD	ASTM D 3039	159 GPa	23 Msi
Tensile Strength 90°	RTD	ASTM D3039	86 MPa	12.5 ksi
Tensile Modulus 90°	RTD	ASTM D 3039	10 GPa	1.5 Msi
Compressive Strength 0°	RTD	ASTM D 6641	1300 MPa	189 ksi
Compressive Modulus 0°	RTD	ASTM D 6641	138 GPa	20 ksi
Flexural Strength 90°	RTD	ASTM D 7264	162 MPa	23.5 ksi
Interlaminar Shear Strength (SBS) 0°/ 90°	RTD	ASTM D 2344	96.5 MPa	14 ksi
Open-Hole Tensile Strength	RTD	ASTM D 5766	655 MPa	95 ksi
Open-Hole Compressive Strength	RTD	ASTM D 6484	303 MPa	44 ksi
Compression After Impact Strength 30.5 J (270 in/lb) Impact Energy	RTD	ASTM D 7137	338 MPa	49 ksi

Room Temperature Dry (RTD)

High Strength T300JB 3K Carbon 281gsm 5HS Woven Fabric Reinforced Laminate 43% RC

Property	Condition	Methods	Results	
Tensile Strength 0°	RTD	EN 2597B	805 MPa	117 ksi
Tensile Modulus 0°	RTD	EN 2597B	58.0 GPa	8.4 Msi
Tensile Strength 90°	RTD	EN 2597B	739 MPa	107 ksi
Tensile Modulus 90°	RTD	EN 2597B	59.0 GPa	8.6 Msi
In-Plane Shear Strength	RTD	AITM 1.0002	159 MPa	23 ksi
In-Plane Shear Modulus	RTD	AITM 1.0002	3.90 GPa	0.57 Msi
Compression Strength 0°	RTD	ASTM D6641	628 MPa	91 ksi
Compression Modulus 0°	RTD	ASTM D6641	52.0 GPa	7.5 Msi
Compression Strength 90°	RTD	ASTM D6641	676 MPa	98 ksi
Compression Modulus 90°	RTD	ASTM D6641	53 GPa	7.7 Msi
Flexural Strength 0°	RTD	EN 2562A	1100 MPa	160 ksi
Flexural Modulus 0°	RTD	EN 2562A	61 GPa	9 Msi
Flexural Strength 90°	RTD	EN 2562A	874 MPa	127 ksi
Flexural Modulus 90°	RTD	EN 2562A	48 GPa	7 Msi
Open-Hole Compressive Strength	RTD	AITM 1.0008	291 MPa	42 ksi
Compression After Impact Strength 30 J (266 in/lb) Impact Energy	RTD	ASTM D7137-12	314 MPa	45.6 ksi
Mode I Interlaminar Fracture Toughness (G_{IC} Strain Energy Release Rate)	RTD	ASTM D5528	2249 J/m^2	12.8 in-lb/in^2

Room Temperature Dry (RTD) is 21°C (69.8°F)
50% fiber by volume (Vf)
The mechanical data provided are average values from a limited dataset. For additional data please contact Toray Advanced Composites.

US Style 7781 EC6 Glass 296gsm 8HS Woven Fabric Reinforced Laminate 34% RC

Property	Condition	Methods	Results	
Tensile Strength 0°	RTD	ASTM D3039	480 MPa	70 ksi
Tensile Modulus 0°	RTD	ASTM D3039	23.7 GPa	3.4 Msi
Tensile Strength 90°	RTD	ASTM D3039	424 MPa	61 ksi
Tensile Modulus 90°	RTD	ASTM D3039	22.0 GPa	3.2 Msi
Compression Strength 0°	RTD	ASTM D6641	365 MPa	53 ksi
Compression Modulus 0°	RTD	ASTM D6641	26.7 GPa	3.9 Msi
Compression Strength 90°	RTD	ASTM D6641	332 MPa	48 ksi
Compression Modulus 90°	RTD	ASTM D6641	25.7 GPa	3.7 Msi
In Plane Shear Strength	RTD	ASTM D3518	47 MPa	7 ksi
In Plane Shear Modulus	RTD	ASTM D3518	2.70 GPa	0.39 Msi
Flexural Strength 0°	RTD	ISO 178	544 MPa	79 ksi
Flexural Modulus 0°	RTD	ISO 178	24 GPa	3.4 Msi
Flexural Strength 90°	RTD	ISO 178	454 MPa	66 ksi
Flexural Modulus 90°	RTD	ISO 178	20.0 GPa	2.9 Msi
Tensile Strength 0°	ETW	ASTM D3039	333 MPa	48 ksi
Tensile Modulus 0°	ETW	ASTM D3039	22.0 GPa	3 Msi
Tensile Strength 90°	ETW	ASTM D3039	289 MPa	42 ksi
Tensile Modulus 90°	ETW	ASTM D3039	20.3 GPa	3 Msi
Compression Strength 0°	ETW	ASTM D6641	197 MPa	29 ksi
Compression Modulus 0°	ETW	ASTM D6641	25.0 GPa	3.6 Msi
Compression Strength 90°	ETW	ASTM D6641	171 MPa	25 ksi
Compression Modulus 90°	ETW	ASTM D6641	23.0 GPa	3.3 Msi
In Plane Shear Strength	ETW	ASTM D3518	26 MPa	4 ksi
In Plane Shear Modulus	ETW	ASTM D3518	1.43 GPa	0.21 Msi

Room Temperature Dry (RTD) is 23°C (73.4°F)
Elevated Temperature Wet (ETW) is tested at 80°C/dry after 1000 hours of conditioning at 70°C/85% RH
50% fiber by volume (Vf)
For additional data please contact Toray Advanced Composites.

Continued on page 7

PRODUCT DATA SHEET

US Style 7781 EC6 Glass 296gsm FAW 8HS Woven Fabric Reinforced Laminate 34% RC				
Property	**Condition**	**Methods**	**Results**	
Tensile Strength 0°	HD	ASTM D3039	431 MPa	63 ksi
Tensile Modulus 0°	HD	ASTM D3039	23.0 GPa	3.3 Msi
Tensile Strength 90°	HD	ASTM D3039	338 MPa	49 ksi
Tensile Modulus 90°	HD	ASTM D3039	20.0 GPa	2.9 Msi
Compression Strength 0°	HD	ASTM D6641	312 MPa	45 ksi
Compression Modulus 0°	HD	ASTM D6641	26.0 GPa	3.8 Msi
Compression Strength 90°	HD	ASTM D6641	254 MPa	37 ksi
Compression Modulus 90°	HD	ASTM D6641	24.0 GPa	3.5 Msi
In Plane Shear Strength	HD	ASTM D3518	40 MPa	6 ksi
In Plane Shear Modulus	HD	ASTM D3518	2.33 GPa	0.34 Msi

Hot Dry (HD) is tested at 80°C (194°F)/dry
50% fiber by volume (Vf)
For additional data please contact Toray Advanced Composites.

PRODUCT DATA SHEET

US Style 6781 S2 Glass 298gsm 8HS Woven Fabric Reinforced Laminate 34% RC				
Property	**Condition**	**Methods**	**Results**	
Tensile Strength 0°	RTD	ASTM D3039	660 MPa	96ksi
Tensile Modulus 0°	RTD	ASTM D3039	25.0 GPa	3.6 Msi
Tensile Strength 90°	RTD	ASTM D3039	597 MPa	87 ksi
Tensile Modulus 90°	RTD	ASTM D3039	23.5 GPa	3.4 Msi
Compression Strength 0°	RTD	ASTM D6641	256.5 MPa	37 ksi
Compression Modulus 0°	RTD	ASTM D6641	29.5 GPa	4.3 Msi
Compression Strength 90°	RTD	ASTM D6641	257 MPa	37 ksi
Compression Modulus 90°	RTD	ASTM D6641	27.5 GPa	4.0 Msi
In Plane Shear Strength	RTD	ASTM D3518	37 MPa	5 ksi
In Plane Shear Modulus	RTD	ASTM D3518	1.85 GPa	0.27 Msi
Flexural Strength 0°	RTD	ISO 178	459 MPa	67 ksi
Flexural Modulus 0°	RTD	ISO 178	27 GPa	3.8 Msi
Flexural Strength 90°	RTD	ISO 178	399 MPa	58 ksi
Flexural Modulus 90°	RTD	ISO 178	23 GPa	3.3 Msi
Tensile Strength 0°	ETW	ASTM D3039	519 MPa	75 ksi
Tensile Modulus 0°	ETW	ASTM D3039	25.0 GPa	3.6 Msi
Tensile Strength 90°	ETW	ASTM D3039	463 MPa	67 ksi
Tensile Modulus 90°	ETW	ASTM D3039	23.5 GPa	3.4 Msi
Compression Strength 0°	ETW	ASTM D6641	171 MPa	25 ksi
Compression Modulus 0°	ETW	ASTM D6641	28.0 GPa	4.1 Msi
Compression Strength 90°	ETW	ASTM D6641	165 MPa	24 ksi
Compression Modulus 90°	ETW	ASTM D6641	26.0 GPa	3.8 Msi
In Plane Shear Strength	ETW	ASTM D3518	24 MPa	3 ksi
In Plane Shear Modulus	ETW	ASTM D3518	1.10 GPa	0.16 Msi

Room Temperature Dry (RTD) is 23°C (73.4°F)
Elevated Temperature Wet (ETW) is tested at 80°C/dry after 1000 hours of conditioning at 70°C/85% RH
50% fiber by volume (Vf)
For additional data please contact Toray Advanced Composites.

Continued on page 9

PRODUCT DATA SHEET

US Style 6781 S2 Glass 298gsm 8HS Woven Fabric Reinforced Laminate 34% RC				
Property	**Condition**	**Methods**	**Results**	
Tensile Strength 0°	HD	ASTM D3039	623 MPa	90 ksi
Tensile Modulus 0°	HD	ASTM D3039	25.0 GPa	3.6 Msi
Tensile Strength 90°	HD	ASTM D3039	544 MPa	79 ksi
Tensile Modulus 90°	HD	ASTM D3039	24.0 GPa	3.5 Msi
Compression Strength 0°	HD	ASTM D6641	233 MPa	34 ksi
Compression Modulus 0°	HD	ASTM D6641	29.0 GPa	4.2 Msi
Compression Strength 90°	HD	ASTM D6641	219 MPa	32 ksi
Compression Modulus 90°	HD	ASTM D6641	27.0 GPa	3.9 Msi
In Plane Shear Strength	HD	ASTM D3518	32 MPa	5 ksi
In Plane Shear Modulus	HD	ASTM D3518	1.60 GPa	0.23 Msi

Hot Dry (HD) is tested at 80°C (194°F)/dry
50% fiber by volume (Vf)
For additional data please contact Toray Advanced Composites.